INFORMATION TO USERS

The most advanced technology has been used to photograph and reproduce this manuscript from the microfilm master. UMI films the text directly from the original or copy submitted. Thus, some thesis and dissertation copies are in typewriter face, while others may be from any type of computer printer.

The quality of this reproduction is dependent upon the quality of the copy submitted. Broken or indistinct print, colored or poor quality illustrations and photographs, print bleedthrough, substandard margins, and improper alignment can adversely affect reproduction.

In the unlikely event that the author did not send UMI a complete manuscript and there are missing pages, these will be noted. Also, if unauthorized copyright material had to be removed, a note will indicate the deletion.

Oversize materials (e.g., maps, drawings, charts) are reproduced by sectioning the original, beginning at the upper left-hand corner and continuing from left to right in equal sections with small overlaps. Each original is also photographed in one exposure and is included in reduced form at the back of the book.

Photographs included in the original manuscript have been reproduced xerographically in this copy. Higher quality 6" x 9" black and white photographic prints are available for any photographs or illustrations appearing in this copy for an additional charge. Contact UMI directly to order.

U·M·I

University Microfilms International
A Bell & Howell Information Company
300 North Zeeb Road, Ann Arbor, MI 48106-1346 USA
313/761-4700 800/521-0600

Order Number 9108128

Distortion mitigation theory and techniques for multidimensional wideband data transmission via linear/nonlinear dispersive channels

Karabinis, Peter D., Ph.D.

City University of New York, 1990

U·M·I
300 N. Zeeb Rd.
Ann Arbor, MI 48106

A

DISTORTION MITIGATION THEORY AND TECHNIQUES FOR MULTIDIMENSIONAL WIDEBAND DATA TRANSMISSION VIA LINEAR/NONLINEAR DISPERSIVE CHANNELS

by

Peter D. Karabinis

A dissertation submitted to the Graduate Faculty in Engineering in partial fulfillment of the requirements for the degree of Doctor of Philosophy, The City University of New York

1990

This manuscript has been read and accepted for the Graduate Faculty in Engineering in satisfaction of the dissertation requirement for the degree of Doctor of Philosophy.

7/17/90
Date

Frederick E. Thau
Professor Frederick Thau
Chair of Examining Committee

7/17/90
Date

Gerard G. Lowen
Professor Gerard G. Lowen
Executive Officer

Professor Paul Karmel

Professor Tarek Saadawi

Professor Donald Schilling

Dr. Dimitrios Kokkinos (Nynex S&T)
Examination Committee

The City University of New York

ABSTRACT

DISTORTION MITIGATION THEORY AND TECHNIQUES FOR MULTIDIMENSIONAL WIDEBAND DATA TRANSMISSION VIA LINEAR/NONLINEAR DISPERSIVE CHANNELS

by

Peter D. Karabinis

Advisor: Professor Fred E. Thau

A unified distortion mitigation theory for multidimensional, linearly/nonlinearly dispersive data transmission systems is presented. The analysis starts with fundamental principles of linear systems theory, and linear digital communications systems modeling and optimization, and gradually generalizes until a mathematical framework emerges that unifies the behavior, analysis and optimization of the general system, containing an arbitrary combination of linear and/or nonlinear set of dispersive elements. The optimum receiver architectures and adaptive control laws that we derive and evaluate subject to the general linear/nonlinear system are channel distortion and nonlinearity model independent, and substantially superior to previously reported techniques, particularly during stressful channel conditions characterized by large amounts of linear and/or nonlinear distortion (Intersymbol Interference (ISI) limited channels).

A new approach to the ISI cancellation issue is postulated, analyzed, verified by computer simulation and shown to substantially mitigate against the limitations of conventional ISI cancellers. The new technique is generic and, besides lending itself to the linear/nonlinear ISI cancellation issue, it can also be applied to the

purely linear channel decision-feedback equalizer situation to substantially resolve the long-standing error propagation problem associated with decision-feedback equalizers. Due to the importance and central role played by the transversal filter (as the building block in forming the optimal receivers developed and analyzed in this dissertation), an experimental effort has been undertaken to study digital implementations of the multitap synchronously/fractionally spaced transversal filter. Several key properties and results predicted by the analysis are verified and presented, together with the supporting experimental observations.

ΑΦΙΕΡΩΜΑ

Ἡ ἐργασία αὐτὴ εἶναι ἀφιερωμένη μὲ πολλὴ ἀγάπη εἰς τοὺς γονεῖς μου Νίκη καὶ Δημήτρη ὡς μία μικρὴ ἀμοιβὴ γιὰ ὅλες τους τὶς προσπάθειες καὶ κόπους.

Ἐπίσης, εἶναι ἀφιερωμένη καὶ εἰς τὴν ἀγαπημένη μου σύζυγον Ἑρμιόνη διὰ τὴν συνπαράστασὴν της καὶ διὰ τὴν ἀκούραστην καθοδήγησην πού προσφέρει εἰς τὰ παιδιά μας Νίκη καὶ Δημήτρη. Εὔχομαι ὅπως μία ἡμέρα οἱ μικροὶ Νίκη καὶ Δημήτρης νὰ διαβάσουν τὶς λέξεις αὐτὲς καί, μελετῶντας τὸ ἔργον τοῦτο, νὰ καταλάβουν μόνοι τους γιατὶ ὁ μπαμπᾶς δὲν ἐδύναντο νὰ παίξῃ μαζί τους ὅλα ἐκεῖνα τὰ σαββατοκύριακα...

Π. Δ. Κ.

"Don't keep forever on the public road, going only where others have gone. Leave the beaten track occasionally and dive into the woods. You will be certain to find something you have never seen before. Of course, it will be a little thing, but do not ignore it. Follow it up, explore all around it; one discovery will lead to another ..."

Alexander Graham Bell

ACKNOWLEDGMENTS

I am grateful to Messrs. D. D. Falconer, E. Biglieri, A. Gersho, R. D. Gitlin and T. L. Lim (posthumously) for having provided me with invaluable mental stimulation and food for thought through their published work. I am also grateful to Tom L. Osborne for his enormous support and encouragement during the planting of the initial seeds of this work (during my tenure at AT&T Bell Laboratories). In general, I am indebted to both AT&T Bell Laboratories and Raytheon Company management for their enthusiastic and continuing support, which has enabled me, over the years, to pursue the Ph.D. degree. The investment made by AT&T Bell Laboratories in the "Visiting Professor Program", allowing me to serve at The City College of New York during the 1983 to 1984 academic year, is greatly appreciated! It was while I was on campus that some important elements of this work were refined.

Lately, the support of Tom J. Gluszczak (Director of the Communication Systems Directorate at Raytheon Comapny and a City College graduate himself) has been great and is much appreciated! Also at Raytheon Company, the very efficient Publications Department, managed by Thomas J. Trainor, and the superb typing skills of Pamela Meleones have proved invaluable in finalizing this manuscript.

An enormous amount of credit goes to my wife, daughter and son, who have patiently spent many weekends, holidays and evenings alone during the course of formulating and developing this work. Last, but by no means least, I wish to express my gratitude to Professors and Pillars of CCNY (many of whom are now retired) Morris Ettenberg, Carl Shulman (posthumously), George Eichmann, M. Javid, R. Mekel (posthumously), D. Schilling and Paul R. Karmel for having provided much needed guidance

and academic stimulation over the years at CCNY. Particularly, however, I am very grateful to Professors George M. Kranc and Fred E. Thau (my advisor) for their inspiration and for teaching me important mathematical skills.

P. D. K.

TABLE OF CONTENTS

TABLE OF CONTENTS (CONTINUED)

LIST OF ILLUSTRATIONS

LIST OF ILLUSTRATIONS (CONTINUED)

CHAPTER 1

INTRODUCTION AND EXECUTIVE SUMMARY

CHAPTER 1

INTRODUCTION AND EXECUTIVE SUMMARY

This dissertation presents a unified distortion mitigation theory for multi-dimensional, linearly/nonlinearly dispersive, data transmission systems utilizing Quadrature Amplitude Modulation (QAM). QAM has been chosen in this work since it represents a very high capacity/density modulation format in terms of the bit rate per unit bandwidth that it can accommodate (particularly when used with vestigial sideband filtering[1]) and because it has found wide applications in high capacity commercial communications systems.[2-4] Our approach, concepts and results, however, are (by intent) quite general and may readily be applied to a variety of other situations.

The analysis begins with fundamental principles of linear systems theory, and linear digital communications systems modeling and optimization, and gradually generalizes until a mathematical framework emerges that unifies the behavior, analysis and optimization of the general system, containing an arbitrary combination of linear and/or nonlinear set of dispersive elements. The optimum receiver architectures and adaptive control laws that we derive and evaluate subject to the general linear/nonlinear system are channel distortion and nonlinearity model independent, and substantially superior to previously reported techniques[5-11], particularly during stressful channel conditions characterized by large amounts of linear and/or nonlinear distortion (Intersymbol Interference (ISI) limited channels).

In References 5 through 7, the basic architecture of Figure 1-1 and some closely related variations thereof have been used as the means for cancelling ISI.

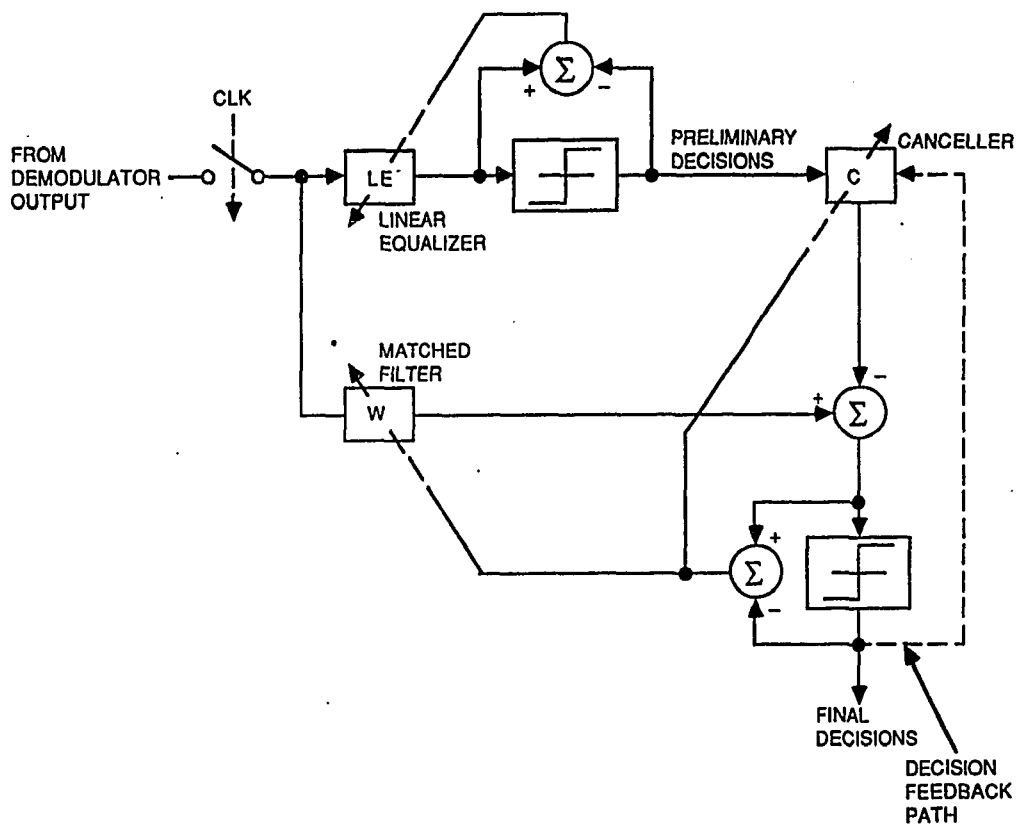

Figure 1-1. Conventional Canceller Architecture

The Linear Equalizer (LE) shown in this receiver is used to provide preliminary estimates of the transmitted data symbols, which are subsequently used by a canceller structure (C) to adaptively form the prevailing ISI estimate. The ISI estimate, thus formed, is subtracted from the matched filter (W) output, producing (in principle) an ISI-free quantity, which then serves as the basis for forming a final decision regarding the corresponding transmitted symbol value.

The generic ISI canceller of Figure 1-1 is quite flexible and lends itself to ISI cancellation resulting from arbitrary combinations of linear and/or nonlinear system impairments, provided that an appropriate configuration/architecture exists within the canceller block, C.[5-7] For a type of system containing a nonlinearity at the transmitter (a nonlinear power amplifier) followed by a linearly dispersive (multipath fading) channel, the ISI in the received data stream will, in general, contain a "linear" as well as a "nonlinear" component*. Given a channel memory of, say, N symbol (baud) intervals, the canceller (C) of Figure 1-1 must process a sequence of N preliminary decisions per signaling interval and be able to form (from such a sequence) the necessary linear and/or nonlinear symbol combinations reflecting the currently received ISI (as it exists at the matched filter output).

The signal processing (ISI cancellation) methodology outlined above has been argued as representing the ultimate in receiver processing, with performance approaching that of the isolated pulse matched filter bound[6]. Indeed, as long as the preliminary decisions (as provided by the LE) are correct, the canceller matched filter combination performance does approach the "isolated pulse matched filter

* The linear ISI component is defined by a linear combination of transmitted data symbols, while the nonlinear ISI term reflects a nonlinear combination of the transmitted data elements.

bound" claimed in Reference 6, but, if the preliminary decisions are correct, what is the need for the canceller matched filter combination? It is argued in Reference 7 (and substantiated, to some extent, by computer simulation) that, as long as only a small number of errors occur in the preliminary decisions, the canceller should still be capable of providing near optimum performance, since most of the symbols used in forming the ISI estimates are still correct. This, however, may not be true (in general), particularly when the ISI is strongly dependent on a relatively small number of symbols, some of which are represented in error by the preliminary decisions. For the line-of-sight multipath fading channel considered in this work, we have indeed observed considerable canceller degradations brought about by a relatively small number of errors made by the preliminary estimator (a consequence of the ISI being strongly dependent on a relatively small number of transmitted symbols).

In Chapter 3 of this dissertation, a new approach to the canceller decision making strategy and methodology is postulated, analyzed, verified by computer simulation and shown to substantially mitigate against the limitations of the conventional canceller algorithm.[12] The new technique is generic in nature and, besides lending itself to the ISI cancellation issue, it can also be applied to the purely linear channel decision feedback equalizer situation to substantially resolve the long standing error propagation problem associated with decision feedback equalizers.[9-11] The work presented in Chapter 3 also addresses the issue of ISI equalization for the general linear/nonlinear system. A baseband equivalent model is derived for the generalized QAM system, containing linear as well as nonlinear distortion, showing that the impulse response of such a system is not only distortion dependent, but data-sequence-dependent as well. Since the classical adaptive

equalizer operation relies on the assumption that the system's impulse response be quasistatic with respect to the system's transmission interval, this assumption breaks down completely for the general linear/nonlinear system, rendering the classical equalizer approach impotent (a data-sequence-dependent impulse response changes at the signaling rate). The development of Chapter 3 resolves this issue. A generalized equalizer structure (and associated control algorithm) is developed involving data-sequence-dependent coefficients that allow the equalizer to properly operate on the system's data-sequence-dependent impulse response.

Chapter 2, in conjunction with Appendices A through D, lays down the fundamental mathematical framework for the purely linear QAM system. These fundamentals are drawn upon heavily and serve as the basis for the generalized discussions of Chapter 3, as outlined above. In Appendix D, where a discussion of linear receivers in the Nyquist sense is presented, a new adaptive receiver architecture in the "optimum Nyquist sense" is developed (Figure D-4). This receiver configuration and associated control strategy is capable of forming adaptively a transfer function resulting in minimum probability of error subject to the zero ISI constraint. Prior published work involving an adaptive Nyquist receiver[2] used an arrangement resulting in suboptimum performance during channel fading.

Because of the importance and central role played by the transversal filter as the building block in forming the optimal receivers developed herein, a limited experimental effort has been undertaken to study digital implementations of the multitap synchronously/fractionally spaced transversal filter. Chapter 4 reports on these findings. Certain key properties/results predicted by analysis regarding the behavior of synchronously spaced as well as fractionally spaced transversal filters

are verified, and are presented and discussed in Chapter 4, together with the supporting experimental observations.

We close in Chapter 5 with a synopsis of the central theme of this work and with a detailed enumeration of contributions made throughout this dissertation. Several important observations/developments that have surfaced during the course of the present work, but have not been central to the theme of this dissertation, have not been expanded upon in Chapters 2 through 4, but are cited in some detail in Chapter 5. These concepts[1, 13] identify areas for further work aimed at improving the capabilities of the QAM system.

We close this chapter by presenting (systematically) a list of the major contributions made. The contributions are rated in importance (according to the author's judgement) using the following "three-star" method:

*** ≡ New and Very Important
** ≡ New and Moderately Important
* ≡ New, Interesting

* Several baseband equivalent mathematical models are derived for the QAM system illustrating its two-dimensional character (Chapter 2). The models are used in the analysis and optimization of the system to derive optimum linear receivers (Appendices C and D) in the:

a. Minimum mean-squared error sense

b. Minimum probability of error sense subject to the zero ISI constraint

** A new adaptive receiver architecture and associated control algorithm is derived which forms the optimum transfer function in the Nyquist sense yielding minimum probability of error subject to the zero ISI constraint (Appendix D).

** The general nonlinearly dispersive QAM system is shown equivalent to a system whose impulse response is data-sequence-dependent and, therefore, represents a baud-interval-by-baud-interval changing waveform (Chapter 3). This result illustrates why the classical adaptive equalization techniques (which involve data-sequence-independent coefficients) become highly suboptimum for the system containing nonlinearities.

** An equalizer receiver configuration is derived that can optimally mitigate against linear and/or nonlinear distortion (Chapter 3). This equalizer arrangement requires only a factor of two increase in the number of taps (over those that would be required in a purely linear system application) and is independent of the order of the nonlinearity. A new performance index for optimum decision making based on the equalizer output is also presented and illustrated (via simulation) to work well.

*** A new and generic algorithm/methodology for cancelling ISI is presented (Chapter 3). The algorithm is applicable to a variety of canceller arrangements and/or equalizers using decision feedback, and substantially resolves the problem of error propagation. Numerical results are presented illustrating the capabilities of the new algorithm.

* Experimental results are presented confirming the performance insensitivity of the digitally implemented fractionally spaced equalizer to timing phase errors and showing that a fractionally spaced equalizer with only five taps is capable of

forming the receiver matched filter adaptively for a PAM system employing a half-Nyquist transmitter filter (Chapter 4). The digitally implemented synchronously spaced equalizer performance is shown highly sensitive to timing phase errors and incapable of forming the receiver matched filter adaptively.

** Several new signal processing techniques, relating to the transmitter and receiver processing of the QAM system, have been identified during the course of developing the central theme of this dissertation. These new techniques/algorithms, not being central to the main theme of this work, have not been amplified in the main text. Instead, they are cited and discussed in some detail in Chapter 5 as areas for further work aimed at strengthening the capabilities of the communications system. They involve:

a. Transmitter and receiver processing enabling vestigial sideband filtering to be imposed on a QAM waveform (to achieve higher spectral efficiencies)

b. A nondata directed algorithm for adjusting the coefficients of adaptive equalizers during start-up periods (thus avoiding the need for a training sequence)

REFERENCES

[1] P. D. Karabinis, "Suppressed Double-Sideband Communication System", U.S. Patent No. 4,780,884, October 25, 1988

[2] J. Fenderson, S. R. Shepard and M. A. Skinner, "Adaptive Transversal Equalizer for 90-Mb/s 16-QAM System in the Presence of Multipath Propagation", International Conference on Communications (ICC), June 19 to 22, 1983, Boston, MA, Paper C8.7

[3] T. Murase, K. Morita and S. Komaki, "200 Mb/s 16-QAM Digital Radio System with New Countermeasure Techniques for Multipath Fading", ICC, 1981, Denver, CO, Paper 46.1

[4] S. Komaki, Y. Okamoto and K. Jajima, "Performance of 16-QAM Digital Radio System Using New Space Diversity", ICC, June 8 to 12, 1980, Seattle, WA, Paper 52.2

[5] D. D. Falconer, "Adaptive Equalization of Channel Nonlinearities in QAM Data Transmission Systems", Bell System Technical Journal, September 1978, Volume 57, No. 7

[6] A. Gersho and T. L. Lim, "Adaptive Cancellation of Intersymbol Interference for Data Transmission", Bell System Technical Journal, November 1981, Volume 60, No. 9

[7] E. Biglieri, A. Gersho, R. D. Gitlin and T. L. Lim, "Adaptive Cancellation of Nonlinear Intersymbol Interference for Voiceband Data Transmission", IEEE Journal on Selected Areas in Communications, September 1984, Volume SAC-2, No. 5

[8] R. D. Gitlin and S. B. Weinstein, "Fractionally Spaced Equalization: An Improved Digital Transversal Equalizer", Bell System Technical Journal, February 1981, Volume 60, No. 2

[9] P. Monsen, "Theoretical and Measured Performance of a DFE Modem on a Fading Multipath Channel", IEEE Transactions on Communications, October 1977, Volume COM-25, No. 10

[10] J. J. O'Reilly and A. M. de Oliveira Duarte, "Error Propagation in Decision Feedback Receivers", IEE Proceedings, December 1985, Volume 132, Part F, No. 7

[11] S. U. H. Qureshi, "Adaptive Equalization", Proceedings of the IEEE, September 1985, Volume 73, No. 9

[12] P. D. Karabinis and F. E. Thau, "An Adaptive Algorithm for Linear/Nonlinear Distortion Cancellation in Digital Communications Systems", ICC, 1990, Volume 4, Paper 337.5

[13] P. D. Karabinis, "Asynchronous and Non-Data Decision Directed Equalizer Adjustment", U.S. Patent No. 4,635,276, January 6, 1987

CHAPTER 2

MATHEMATICAL PRELIMINARIES AND THE LINEAR QAM SYSTEM

CHAPTER 2

MATHEMATICAL PRELIMINARIES AND THE LINEAR QAM SYSTEM

2.1 NOTATIONAL REMARKS

In this work, we will deal extensively with symbols that denote complex-valued quantities. Such symbols will invariably appear with a bar "‾" over them to emphasize their complex-valued significance. Thus, symbols such as $\bar{a}$, $\bar{\xi}$, $\bar{f}(x)$, $\bar{g}(\bar{n})$, etc., will be utilized in the representation of complex-valued entities. The form of the first two ($\bar{a}$, $\bar{\xi}$) will be used to represent complex-valued constants, while that of the third, $\bar{f}(x)$, will be appropriate for the representation of a complex-valued function of the real-valued argument x. The form of the fourth entry, $\bar{g}(\bar{n})$, will be used to denote a complex-valued function of the complex-valued argument $\bar{n}$.

Uppercase letters will be used to denote nondeterministic quantities (unless explicitly specified to the contrary). Accordingly, a form such as $\bar{A}$ will be used to specify a complex-valued random variable, while the form $\bar{N}(t)$ will designate a random process. One exception to the above notational convention will occur when the argument of the function, which is being designated by an uppercase letter, is $j\omega$. In that case, the function in question will always denote a Fourier transform. That is, given the functional form $\bar{N}(j\omega)$, $\bar{N}(j\omega)$ will always be interpreted as the Fourier transform of $n(t)$, never as a complex-valued process.

Vector quantities will be identified via an underbar, while a double underbar will be reserved for matrices. Hence, the symbols $\underline{\bar{v}}$ and $\underline{\underline{\bar{h}}}$ will, for example, be used to denote a complex-valued deterministic vector and matrix, respectively, while

uppercase symbols such as $\underline{\overline{V}}$ and $\underline{\overline{H}}$ will typically be reserved for nondeterministic (complex-valued as per the overbar) vectors and matrices, respectively. Of course, in some situations, exceptions to the above rules will occur, but, when this happens, it will always be clear from the context as to the meaning of the symbology being used (e.g., T will be used to denote the baud interval, J will be used as a performance index, etc.).

Finally, for the sake of simplicity, we will adhere to the infinite summation notational equivalence $\sum_{k=-\infty}^{\infty} \equiv \sum_{k}$ and the operator * will, at times, be used to represent convolution. The operator * will also be used as a superscript to denote complex conjugation.

2.2 COMPLEX-VALUED IMPULSE SEQUENCES AND SAMPLING THEORY

Let $\overline{x}(t)$ denote a complex-valued function of the independent (real-valued) argument t. We assume $\overline{x}(t)$ to be band-limited, with $\overline{X}(j\omega)$ denoting its Fourier transform $\Im$: $|\overline{X}(j\omega)| = 0$ for $\forall|\omega| \geq \omega_M$, $0 < \omega_M < \infty$. Given that $\overline{x}(t)$ undergoes ideal sampling, by being multiplied with the impulse train $\sum_k \delta(t-kT)$, $0 < T < \infty$, the following impulse sequence results:

$$\{\overline{x}(kT)\} \equiv \sum_k \overline{x}(kT)\delta(t-kT). \tag{2-1}$$

Fourier transforming the above, we have

$$F[\{\overline{x}(kT)\}] \equiv \int_{-\infty}^{\infty} \{\overline{x}(kT)\}e^{-j\omega t}dt = \sum_k \overline{x}(kT)e^{-j\omega kT} \equiv \overline{X}(e^{j\omega T}). \tag{2-2}$$

Having $\overline{X}(e^{j\omega T})$ as defined above, the n^{th} element of the sequence $\{\overline{x}(kT)\}$ may be regenerated via the following operation:

$$\bar{x}(nt) = \frac{T}{2\pi}\int_{-\pi/T}^{\pi/T}\bar{X}(e^{j\omega T})e^{j\omega nT}d\omega;\ n = 0, \pm1, \pm2, \ldots. \tag{2-3}$$

This can be verified in a straightforward fashion by substituting $\sum_k \bar{x}(kT)e^{-j\omega kT}$ in place of $\bar{X}(e^{j\omega T})$ and performing the indicated operations. Having established the above, we now observe that $\bar{x}(nT)$ may also be expressed as

$$\bar{x}(nT) \equiv \bar{x}(t)|_{t=nT} = \frac{1}{2\pi}\int_{-\infty}^{\infty}\bar{X}(j\omega)e^{j\omega nT}d\omega, \tag{2-4}$$

where we have utilized the continuous-time inverse Fourier transform relationship. Equation (2-4) may be rewritten in the following equivalent form:

$$\bar{x}(nT) = \frac{1}{2\pi}\sum_k \int_{(2k-1)\omega_0}^{(2k+1)\omega_0}\bar{X}(j\omega)e^{j\omega nT}d\omega;\ 0 < \omega_0 < \infty. \tag{2-5}$$

Letting $\omega_0 = \frac{\pi}{T}$, $0 < T < \infty$ and performing the following change of variable:

$$\xi \equiv \omega - 2k\omega_0, \tag{2-6}$$

we attain

$$\begin{aligned}\bar{x}(nT) &= \frac{1}{2\pi}\sum_k \int_{-\pi/T}^{\pi/T}\bar{X}(j\xi+j\frac{2\pi k}{T})e^{j\xi nT}d\xi \\ &= \frac{T}{2\pi}\int_{-\pi/T}^{\pi/T}[\frac{1}{T}\sum_k \bar{X}(j\xi+j\frac{2\pi k}{T})]e^{j\xi nT}d\xi.\end{aligned} \tag{2-7}$$

Comparing equation (2-7) with equation (2-3) and invoking the uniqueness property of the inverse Fourier transform, we conclude

$$\overline{X}(e^{j\omega T}) \equiv \frac{1}{T}\sum_k \overline{X}(j\omega + j\frac{2\pi k}{T}), \quad |\omega| \leq \frac{\pi}{T}. \tag{2-8}$$

Owing to our band-limited assumption regarding $\overline{x}(t)$, we see that, if the sampling interval T is chosen such that $\frac{2\pi}{T} \geq 2\omega_M$, only the k = 0 term in the above summation will assume nonzero values over the frequency band $|\omega| \leq \frac{\pi}{T}$. Hence, given that $T \leq \frac{\pi}{\omega_M}$, we can write

$$\overline{X}(j\omega) \equiv T\,\overline{X}(e^{j\omega T}), \quad |\omega| \leq \frac{\pi}{T}, \tag{2-9}$$

or, equivalently,

$$\overline{x}(t) = T\{\overline{x}(kT)\} * h(t) = \sum_k \overline{x}(kT)\,\frac{\text{Sin}\,\frac{\pi}{T}(t-kT)}{\frac{\pi}{T}(t-kT)}, \tag{2-10}$$

where "*" denotes convolution and

$$h(t) = \frac{1}{T}\left[\frac{\text{Sin}\left(\frac{\pi}{T}\right)t}{\left(\frac{\pi}{T}\right)t}\right], \tag{2-11}$$

represents the impulse response of an ideal low pass filter band-limited to $\omega = \frac{\pi}{T}$. Equations (2-9) and (2-10) summarize the well-established result of the sampling theorem.

2.3 BASEBAND EQUIVALENT REPRESENTATIONS OF THE LINEAR QAM SYSTEM

Baseband equivalent representations of passband communications systems are often used to facilitate the analysis and/or computer simulation of such systems. In this section, we develop several baseband equivalent representations of the

linear passband QAM system. These representations are used later on in this work as the bases for further analysis and to facilitate numerical computations.

Figure 2-1 shows the elements of a basic QAM communications system comprising a modulator, a passband channel and a demodulator*. At the modulator input, two independent impulse data sequences, {a(nT)} and {b(nT)}, are assumed to exist on the In-phase (I) and Quadrature (Q) "rails" of the system, respectively**. Following low pass filtering of the input data sequences by identical I- and Q-rail transmitter filters, the resulting I- and Q-rail signals, i(t) and q(t), respectively, are used to amplitude modulate two carrier waveforms that are in phase-quadrature. Superposition of the two modulated carriers, as shown in Figure 2-1, yields the QAM waveform, s(t). The waveform s(t) propagates through the passband channel and, at the receiver, it is once again decomposed into baseband I- and Q-rail components, i'(t) and q'(t), respectively, via the coherent demodulation process shown in Figure 2-1.

In arriving at the first baseband equivalent representation of the system, we first associate Fourier transforms $\overline{I}(j\omega)$ and $\overline{Q}(j\omega)$ with i(t) and q(t), respectively, and trace these transforms through the system of Figure 2-1. At the receiver, at points D and D', we find transforms corresponding to i'(t) and q'(t), that are explicitly related to the transmitted spectra by baseband transfer functions. These

* Thermal noise effects are neglected for the purposes of this discussion. Additive thermal noise is not relevant in calculating the baseband equivalent of a linear passband communications system. The input passband thermal noise is treated later on in conjunction with the optimization of the receiver processing. At that juncture, a baseband equivalent representation for the input passband thermal noise is developed.

** These data sequences are taken to be deterministic for the purposes of this discussion.

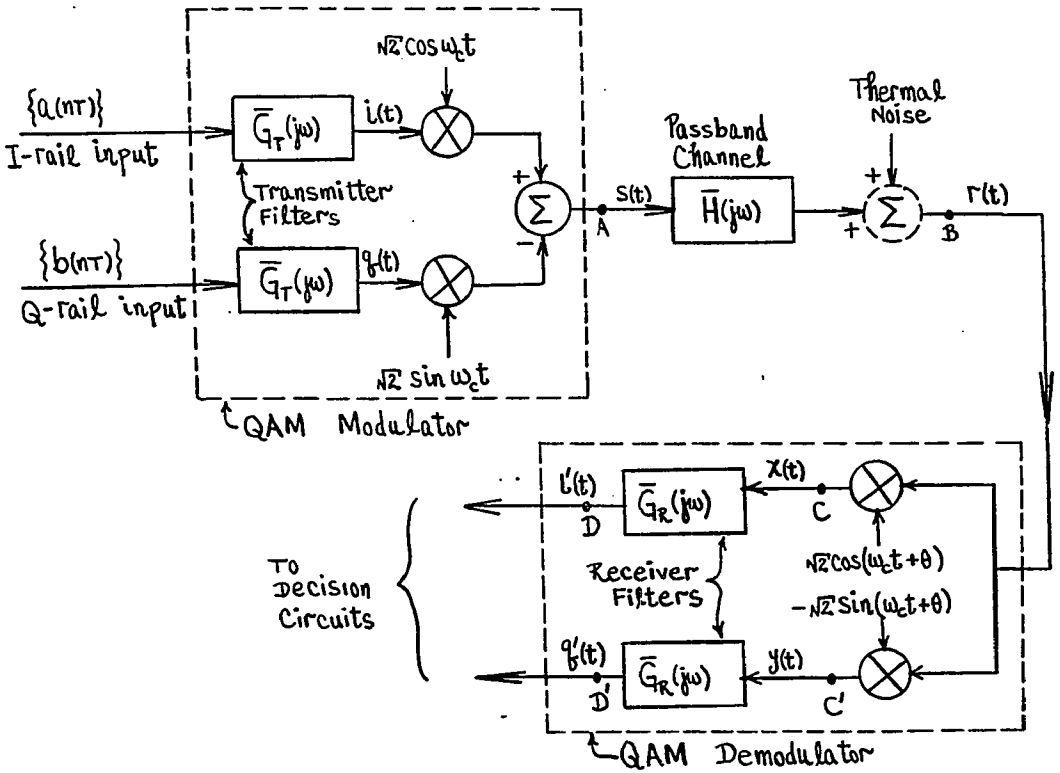

$$\{a(nT)\} \equiv \sum_k a(kT)\delta(t-kT) \;,\; i(t) = \sum_k a(kT) g_T(t-kT) \;;\; g_T(t) \equiv \mathcal{F}^{-1}\left[\bar{G}_T(j\omega)\right]$$

$$\{b(nT)\} \equiv \sum_k b(kT)\delta(t-kT) \;,\; q(t) = \sum_k b(kT) g_T(t-kT)$$

Figure 2-1. Basic QAM Communications System

baseband transfer functions enable us to define a baseband equivalent model for the passband QAM system.

At point A in the system (see Figure 2-1), we have

$$s(t) = \sqrt{2}\,[i(t)\cos\omega_c t - q(t)\sin\omega_c t], \tag{2-12}$$

or, in the frequency domain,

$$\overline{S}(j\omega) = \frac{1}{\sqrt{2}}[\overline{I}(j\omega-j\omega_c) + \overline{I}(j\omega+j\omega_c)] + \frac{j}{\sqrt{2}}[\overline{Q}(j\omega-j\omega_c) - \overline{Q}(j\omega+j\omega_c)], \tag{2-13}$$

where, as usual, $j \equiv \sqrt{-1}$. At the passband channel output (at point B of the system), we therefore have the signal transform $\overline{R}(j\omega) = \overline{H}(j\omega)\,\overline{S}(j\omega)$. Using the identities

$$2\cos(\omega_c t+\theta) = e^{j\theta}e^{j\omega_c t} + e^{-j\theta}e^{-j\omega_c t}, \tag{2-14}$$

and

$$-2\sin(\omega_c t+\theta) = je^{j\theta}e^{j\omega_c t} - je^{-j\theta}e^{-j\omega_c t}, \tag{2-15}$$

the signal transform at point C may be expressed as

$$\overline{X}(j\omega) = \frac{1}{2} e^{j\theta}\overline{H}(j\omega-j\omega_c)[\overline{I}(j\omega-j2\omega_c) + \overline{I}(j\omega)]$$

$$+ \frac{j}{2} e^{j\theta}\overline{H}(j\omega-j\omega_c)[\overline{Q}(j\omega-j2\omega_c) - \overline{Q}(j\omega)]$$

$$+ \frac{1}{2} e^{-j\theta}\overline{H}(j\omega+j\omega_c)[\overline{I}(j\omega) + \overline{I}(j\omega+j2\omega_c)]$$

$$+ \frac{j}{2} e^{-j\theta}\overline{H}(j\omega+j\omega_c)[\overline{Q}(j\omega) - \overline{Q}(j\omega+j2\omega_c)].$$

Similarly, at point C', we have

$$\overline{Y}(j\omega) = \frac{j}{2} e^{j\theta}\overline{H}(j\omega-j\omega_c)[\overline{I}(j\omega-j2\omega_c) + \overline{I}(j\omega)]$$

$$- \frac{1}{2} e^{j\theta}\overline{H}(j\omega-j\omega_c)[\overline{Q}(j\omega-j2\omega_c) - \overline{Q}(j\omega)]$$

$$- \frac{j}{2} e^{-j\theta}\overline{H}(j\omega+j\omega_c)[\overline{I}(j\omega) + \overline{I}(j\omega+j2\omega_c)]$$

$$+ \frac{1}{2} e^{-j\theta}\overline{H}(j\omega+j\omega_c)[\overline{Q}(j\omega) - \overline{Q}(j\omega+j2\omega_c)].$$

Finally, in order to specify the signal spectra at points D and D', we assume that the receiver filter characteristic, $\overline{G}_R(j\omega)$, being of a low pass nature, is going to eliminate all passband signal components existing at points C and C'. We can thus specify the signal spectrum at point D as

$$\overline{I}'(j\omega) = \frac{1}{2} [\overline{H}(j\omega-j\omega_c)e^{j\theta} + \overline{H}(j\omega+j\omega_c)e^{-j\theta}]\overline{G}_R(j\omega)\ \overline{I}(j\omega)$$

$$+ \frac{j}{2} [-\overline{H}(j\omega-j\omega_c)e^{j\theta} + \overline{H}(j\omega+j\omega_c)e^{-j\theta}]\overline{G}_R(j\omega)\ \overline{Q}(j\omega),$$

and the signal spectrum at point D' as

$$\overline{Q}'(j\omega) = \frac{j}{2}\left[\overline{H}(j\omega-j\omega_c)e^{j\theta} - \overline{H}(j\omega+j\omega_c)e^{-j\theta}\right]\overline{G}_R(j\omega)\ \overline{I}(j\omega)$$

$$+ \frac{1}{2}\left[\overline{H}(j\omega-j\omega_c)e^{j\theta} + \overline{H}(j\omega+j\omega_c)e^{-j\theta}\right]\overline{G}_R(j\omega)\ \overline{Q}(j\omega).$$

Letting

$$\overline{H}_{11}(j\omega) \equiv \overline{H}_{22}(j\omega) \equiv \frac{1}{2}\left[\overline{H}(j\omega-j\omega_c)e^{j\theta} + \overline{H}(j\omega+j\omega_c)e^{-j\theta}\right], \tag{2-16}$$

and

$$\overline{H}_{12}(j\omega) \equiv -\overline{H}_{21}(j\omega) \equiv \frac{j}{2}\left[-\overline{H}(j\omega-j\omega_c)e^{j\theta} + \overline{H}(j\omega+j\omega_c)e^{-j\theta}\right], \tag{2-17}$$

the I- and Q-rail signal transforms at the demodulator output may be written as

$$\overline{I}'(j\omega) = \overline{G}_R(j\omega)\left[\overline{H}_{11}(j\omega)\ \overline{I}(j\omega) + \overline{H}_{12}(j\omega)\ \overline{Q}(j\omega)\right], \tag{2-18}$$

and

$$\overline{Q}'(j\omega) = \overline{G}_R(j\omega)\left[\overline{H}_{21}(j\omega)\ \overline{I}(j\omega) + \overline{H}_{22}(j\omega)\ \overline{Q}(j\omega)\right], \tag{2-19}$$

or, more compactly, in terms of a complex-valued vector matrix equation as

$$\begin{bmatrix} \overline{I}'(j\omega) \\ \overline{Q}'(j\omega) \end{bmatrix} = \overline{G}_R(j\omega)\begin{bmatrix} \overline{H}_{11}(j\omega) & \overline{H}_{12}(j\omega) \\ \overline{H}_{21}(j\omega) & \overline{H}_{22}(j\omega) \end{bmatrix}\begin{bmatrix} \overline{I}(j\omega) \\ \overline{Q}(j\omega) \end{bmatrix}. \tag{2-20}$$

Defining the vectors

$$\underline{\overline{S}}_B(j\omega) \equiv \begin{bmatrix} \overline{I}(j\omega) \\ \overline{Q}(j\omega) \end{bmatrix} \text{ and } \underline{\overline{S}}_B'(j\omega) \equiv \begin{bmatrix} \overline{I}'(j\omega) \\ \overline{Q}'(j\omega) \end{bmatrix}, \tag{2-21}$$

and the matrix

$$\underline{\overline{H}}_B(j\omega) \equiv \begin{bmatrix} \overline{H}_{11}(j\omega) & \overline{H}_{12}(j\omega) \\ \overline{H}_{21}(j\omega) & \overline{H}_{22}(j\omega) \end{bmatrix}, \tag{2-22}$$

equation (2-20) may be rewritten as

$$\underline{\overline{S}}_B'(j\omega) = \overline{G}_R(j\omega)\, \underline{\overline{H}}_B(j\omega)\, \underline{\overline{S}}_B(j\omega). \tag{2-23}$$

These relationships highlight the two-dimensional character of the QAM system. The complex-valued matrix transfer function, $\underline{\overline{H}}_B(j\omega)$, as specified above, defines the *two-dimensional baseband equivalent transfer characteristic* of the QAM system. Figure 2-2 shows a block diagram representation of this baseband equivalent model.

An examination of equation (2-20), which is equivalent to the two scalar equations of (2-18) and (2-19), reveals that the signals transmitted on the two orthogonal dimensions of the system (the I and Q rails) will interfere with one another unless $\overline{H}_{12}(j\omega)$ is identically zero or is otherwise properly behaved. Furthermore, unless $\overline{H}_{11}(j\omega)$ is properly behaved, self-rail (intersymbol) interference will also be present in the received waveform. In addition, the baseband equivalent form of equation (2-20) suggests that a receiver architecture as shown in Figure 2-3 may (in principle) be employed, following the demodulator stage, in order to negate the effect of the channel. Although this is theoretically and practically feasible, it is typically attained at the expense of thermal noise enhancement, as will be quantified later on.

Having established the first baseband equivalence of the linear passband QAM system, we now derive a second equivalence incorporating a baseband channel model with complex-valued impulse response instead of the real-valued matrix impulse

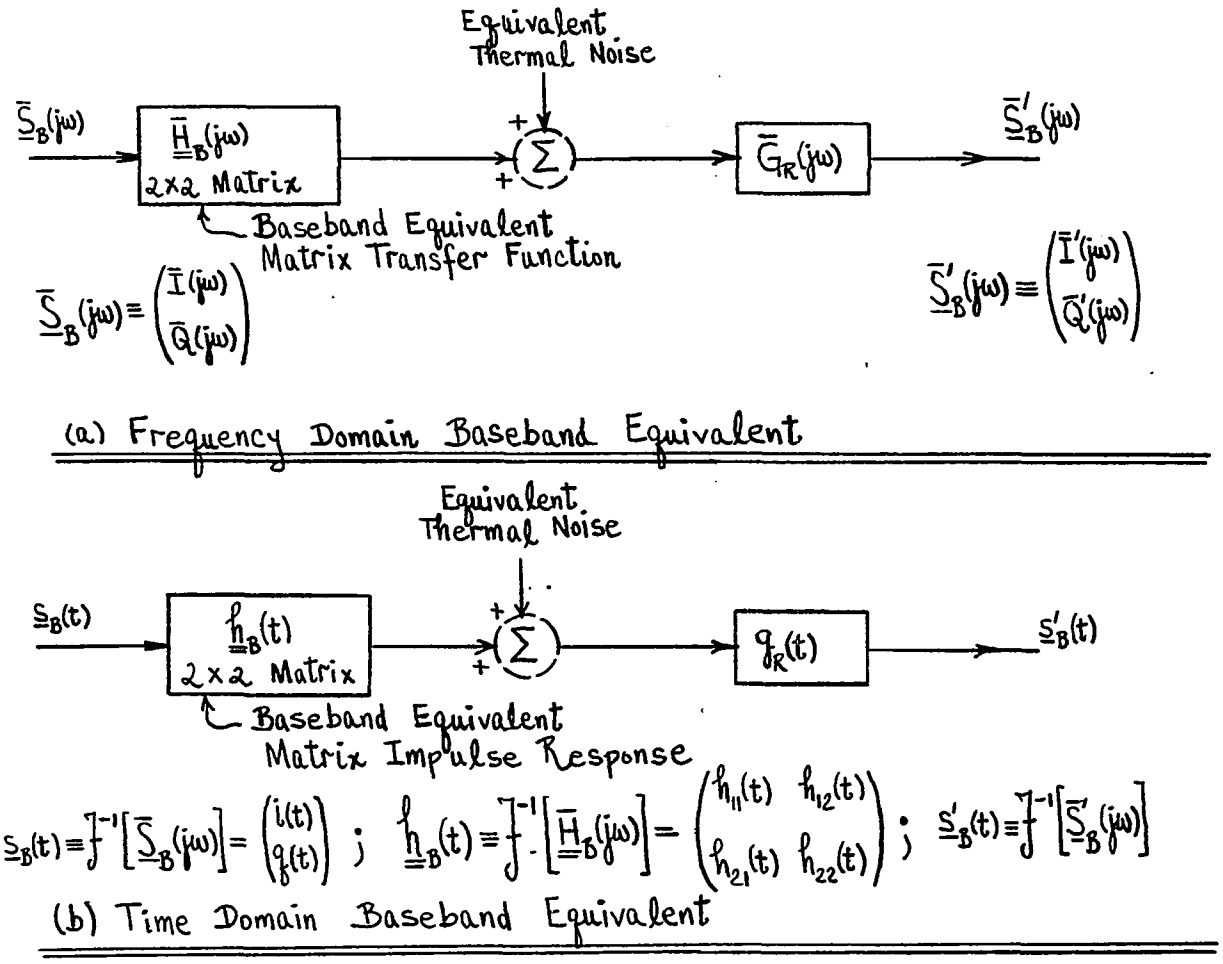

Figure 2-2. Baseband Equivalent Representation of the Linear QAM System (Matrix Formulation)

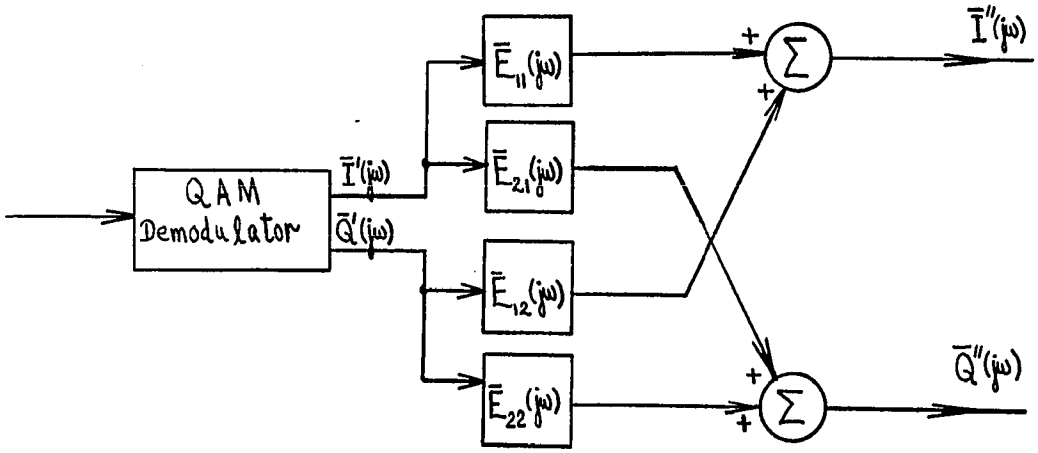

$$\begin{pmatrix}\bar{I}''(j\omega)\\ \bar{Q}''(j\omega)\end{pmatrix} = \begin{pmatrix}\bar{E}_{11}(j\omega) & \bar{E}_{12}(j\omega)\\ \bar{E}_{21}(j\omega) & \bar{E}_{22}(j\omega)\end{pmatrix}\begin{pmatrix}\bar{I}'(j\omega)\\ \bar{Q}'(j\omega)\end{pmatrix} = \bar{G}_R(j\omega)\underbrace{\begin{pmatrix}\bar{E}_{11}(j\omega) & \bar{E}_{12}(j\omega)\\ \bar{E}_{21}(j\omega) & \bar{E}_{22}(j\omega)\end{pmatrix}}_{\underline{\underline{\bar{E}}}(j\omega)}\underbrace{\begin{pmatrix}\bar{H}_{11}(j\omega) & \bar{H}_{12}(j\omega)\\ \bar{H}_{21}(j\omega) & \bar{H}_{22}(j\omega)\end{pmatrix}}_{\underline{\underline{\bar{H}}}_B(j\omega)}\begin{pmatrix}\bar{I}(j\omega)\\ \bar{Q}(j\omega)\end{pmatrix}$$

$\underline{\underline{\bar{E}}}(j\omega)$ can be chosen $\ni$: $\underline{\underline{\bar{E}}}(j\omega)\,\underline{\underline{\bar{H}}}_B(j\omega) = \text{Identity Matrix}$

Figure 2-3. Baseband Receiver Filtering for Channel Inversion

response utilized above. Considering the block diagram of Figure 2-4, we let the input complex-valued signal $\overline{s}_B(t)$ be

$$\overline{s}_B(t) \equiv i(t) + jq(t), \tag{2-24}$$

and define the complex-valued impulse response $\overline{h}_B(t)$ as

$$\overline{h}_B(t) \equiv h_1(t) + jh_2(t). \tag{2-25}$$

Based on these definitions, the complex-valued output, $\overline{s}'_B(t)$, may be written as (neglecting thermal noise)

$$\overline{s}'_B(t) = g_R(t) * \overline{h}_B(t) * \overline{s}_B(t) \equiv i''(t) + jq''(t). \tag{2-26}$$

Substituting equations (2-24) and (2-25) into equation (2-26) gives

$$\begin{aligned} \overline{s}'_B(t) &= g_R(t)*[h_1(t) + jh_2(t)]*[i(t) + jq(t)] \\ &= g_R(t)*[h_1(t)*i(t) - h_2(t)*q(t)] \\ &\quad + jg_R(t)*[h_1(t)*q(t) + h_2(t)*i(t)]. \end{aligned} \tag{2-27}$$

Equating the real and imaginary parts on both sides of equation (2-27) results in

$$i''(t) = g_R(t)*[h_1(t)*i(t) - h_2(t)*q(t)], \tag{2-28}$$

and

$$q''(t) = g_R(t)*[h_1(t)*q(t) + h_2(t)*i(t)]. \tag{2-29}$$

We now observe that equations (2-28) and (2-29) become indistinguishable from equations (2-18) and (2-19), respectively, provided that

$$h_1(t) = h_{11}(t) \text{ and } h_2(t) = -h_{12}(t). \tag{2-30}$$

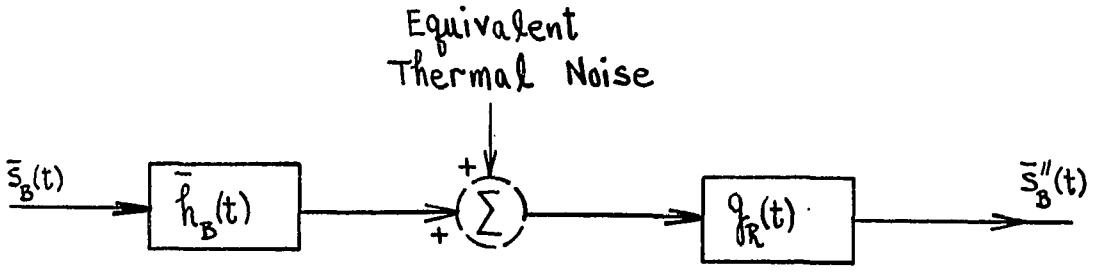

$$\bar{s}_B(t) = i(t) + jq(t)$$

$$\bar{s}''_B(t) \equiv i''(t) + jq''(t)$$

$$\bar{h}_B(t) \equiv h_1(t) + jh_2(t) \begin{cases} h_1(t) \equiv h_{11}(t) \\ h_2(t) \equiv -h_{12}(t) \end{cases}$$

Figure 2-4. Baseband Equivalent Representation of the Linear QAM System (Complex-Valued Impulse Response Formulation)

Hence, subject to the constraint of equation (2-30), an equivalence exists between the two baseband models of Figures 2-2 and 2-4, and, consequently, an isomorphism between 2 x 2 real-valued matrices and complex-valued quantities.

The baseband equivalent models described above serve in characterizing the overall communications system from an input/output standpoint. That is, given baseband inputs to the system, one of the two baseband equivalent models derived thus far may be used to predict the corresponding baseband system outputs (at points D and D' of Figure 2-1). These baseband models, however, are incapable of specifying signal values at intermediate (passband) system points, such as at point B of Figure 2-1. To provide for such a capability, an alternate baseband equivalent representation for the QAM system is derived based on the complex envelope principle. The method of representing passband signals and systems via corresponding "complex envelopes" is developed in Appendix A.

Refer to Figure 2-5a, which, just as in Figure 2-1, shows a basic linear QAM system. Figure 2-5a, however, expands on Figure 2-1 in that a receiver filter is postulated to exist in the passband prior to the demodulation process and, after the demodulator, a receiver sampler is shown, followed by a decision-making process. The modulator and demodulator blocks shown in Figure 2-5a are assumed structurally identical to those shown in Figure 2-1. The receiver filter with impulse response g(t), shown in the passband in Figure 2-5a, is mathematically equivalent to having a baseband structure (after the demodulator) as that shown in Figure 2-3 (see Appendix B for the details of this equivalence).

We begin the mathematical development of the "complex envelope" based baseband equivalent of the physical system shown in Figure 2-5a by considering the narrowband

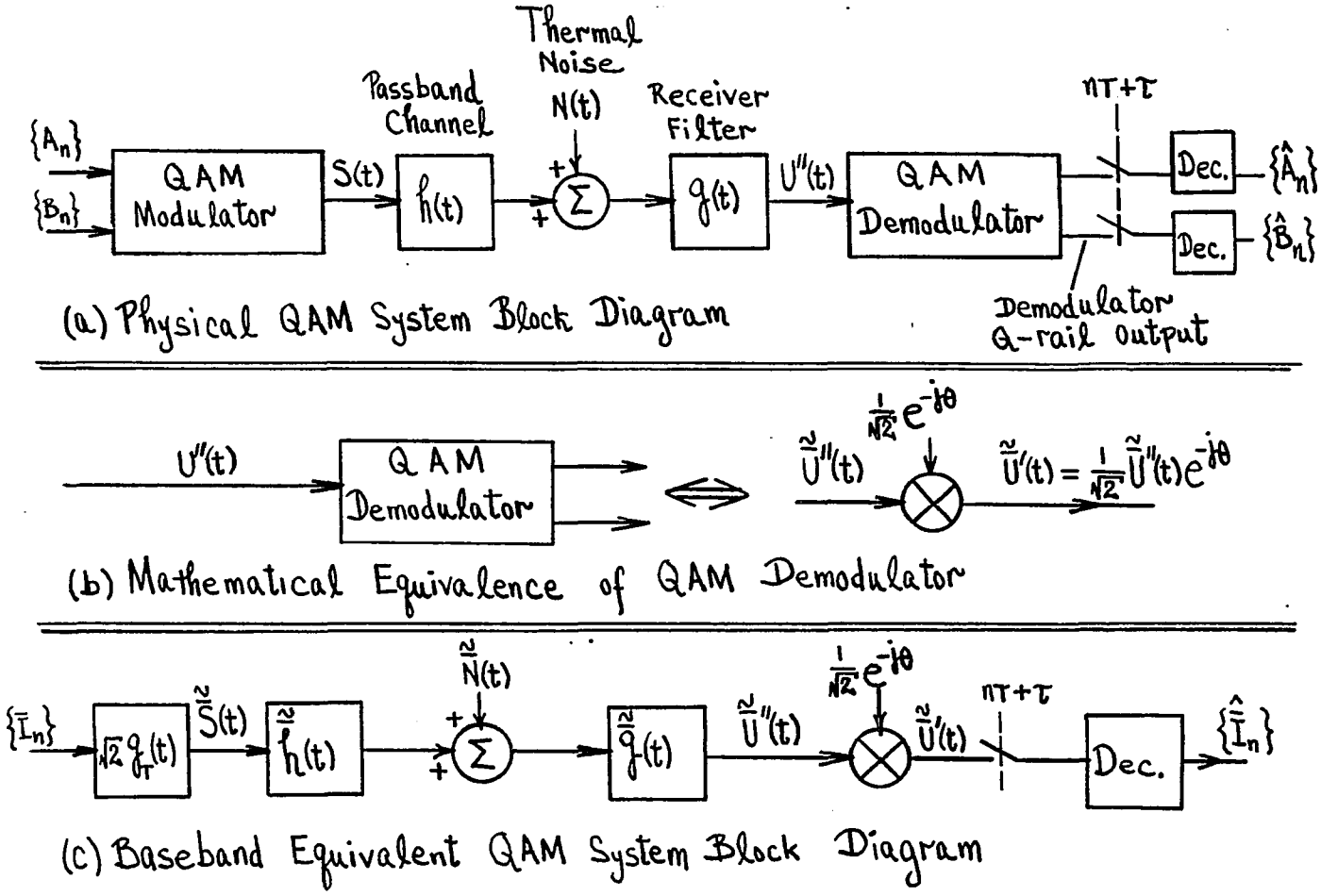

Figure 2-5. QAM System Modeling Based on the Complex Envelope Principle

passband process signal U"(t), which we assume to exist at the QAM demodulator input. Since, by design, U"(t) is a narrowband* passband random process (owing to the band-limited nature of the receiver filter), it can be represented in terms of I and Q components, relative to the carrier frequency ω_c, as

$$U''(t) = U_c''(t) \cos \omega_c t - U_s''(t) \sin \omega_c t, \tag{2-31}$$

where $U_c''(t)$ and $U_s''(t)$ denote the I and Q components of U"(t), respectively. Thus, the I-rail output of the QAM demodulator will be**

$$\begin{aligned} \begin{pmatrix}\text{Demodulator}\\ \text{(I-Rail Output)}\end{pmatrix} &= [\{\sqrt{2} \cos (\omega_c t+\theta)\} \\ &\quad \cdot \{U_c''(t) \cos \omega_c t - U_s''(t) \sin \omega_c t\}]_B \qquad (2\text{-}32) \\ &= \frac{1}{\sqrt{2}} U_c''(t) \cos \theta + \frac{1}{\sqrt{2}} U_s''(t) \sin \theta, \end{aligned}$$

where $[\cdot]_B$ denotes the low pass (baseband) components of the expression inside the brackets. Similarly, the Q-rail component at the demodulator output will be

$$\begin{aligned} \begin{pmatrix}\text{Demodulator}\\ \text{(Q-Rail Output)}\end{pmatrix} &= [\{-\sqrt{2} \sin (\omega_c t+\theta)\} \\ &\quad \cdot \{U_c''(t) \cos \omega_c t - U_s''(t) \sin \omega_c t\}]_B \qquad (2\text{-}33) \\ &= \frac{1}{\sqrt{2}} U_s''(t) \cos \theta - \frac{1}{\sqrt{2}} U_c''(t) \sin \theta. \end{aligned}$$

* Relative to the system's carrier frequency

** The I- and Q-rail filters that are part of the QAM demodulator (see Figure 2-1) are taken here to be ideal low pass filters defined over the system bandwidth.

Next, we consider the decomposition into real and imaginary parts of the low pass complex-valued waveform $\frac{1}{\sqrt{2}}\tilde{\tilde{U}}''(t)e^{-j\theta}$, where $\tilde{\tilde{U}}''(t)$ denotes the complex envelope (see Appendix A) of $U''(t)$. We have

$$\begin{aligned}\frac{1}{\sqrt{2}}U''(t)e^{-j\theta} &= \frac{1}{\sqrt{2}}\{U_c''(t) + jU_s''(t)\}\{\cos\theta - j\sin\theta\} \\ &= \frac{1}{\sqrt{2}}U_c''(t)\cos\theta + \frac{1}{\sqrt{2}}U_s''(t)\sin\theta \\ &\quad + j\{\frac{1}{\sqrt{2}}U_s''(t)\cos\theta - \frac{1}{\sqrt{2}}U_c''(t)\sin\theta\}.\end{aligned} \tag{2-34}$$

From the above, we observe that the real and imaginary parts of $\frac{1}{\sqrt{2}}\tilde{\tilde{U}}''(t)e^{-j\theta}$ are isomorphic to the I- and Q-rail waveforms, respectively, of the demodulator output, hence, allowing us to state the mathematical equivalence of Figure 2-5b. Furthermore, since the waveform at the QAM modulator output may be expressed as

$$S(t) = \sqrt{2}\,I(t)\cos\omega_c t - \sqrt{2}\,Q(t)\sin\omega_c t, \tag{2-35}$$

where

$$I(t) = \sum_k A_k g_T(t-kT), \tag{2-36}$$

and

$$Q(t) = \sum_k B_k g_T(t-kT), \tag{2-37}$$

the complex envelope of $S(t)$ may be expressed as

$$\tilde{\tilde{S}}(t) = \sqrt{2}\,\{I(t)+jQ(t)\} = \sqrt{2}\sum_k (A_k+jB_k)g_T(t-kT) \equiv \sqrt{2}\sum_k \bar{I}_k g_T(t-kT), \quad (2\text{-}38)$$

with $\bar{I}_k \equiv A_k + jB_k$ ($k = 0, \pm1, \pm2, \ldots$) denoting the k^{th} complex-valued input data element. Using the above, the physical QAM system of Figure 2-5a, which encompasses both passband and baseband signals, and system sections, may mathematically and equivalently be replaced by the nonphysical purely baseband model shown in Figure 2-5c. At each stage of the baseband equivalent block diagram of Figure 2-5c, a complex waveform represents, via its real and imaginary parts, the I- and Q-rail (or in-phase and quadrature) components, respectively, of the corresponding signal on the physical QAM system diagram of Figure 2-5a. Thus, the real and imaginary parts of $\tilde{\tilde{S}}(t)$ map onto the I and Q components, respectively, of $S(t)$. The same can be said regarding the relationship between $\tilde{\tilde{U}}''(t)$ and $U''(t)$.

Continuing on with our mathematical modeling, we refer now to Figure 2-6. In Figure 2-6a, we have equivalently rearranged the mathematical QAM demodulator model (from the way it appears in Figure 2-5c) to being distributed between the system's noise input and channel characteristic. In Figure 2-6b, a mathematical equivalence is depicted between sampling the waveform $\tilde{\tilde{U}}'(t)$ at the discrete points in time $nT + \tau$ ($n = 0, \pm1, \pm2, \ldots$) to form the sequence $\{\tilde{\tilde{U}}'(nT+\tau)\}$, versus delaying $\tilde{\tilde{U}}'(t)$ by $-\tau$ seconds to yield $\tilde{\tilde{U}}'(t+\tau)$, and then sampling $\tilde{\tilde{U}}'(t+\tau)$ at the points nT ($n = 0, \pm1, \pm2, \ldots$) to produce the same sequence $\{\tilde{\tilde{U}}'(nT+\tau)\}$. Incorporating the results of the sampler equivalence of Figure 2-6b into the configuration of Figure 2-6a and accounting for the noncausal delay element $-\tau$ (by modifying the noise input and channel characteristic), the simplified baseband equivalent model of Figure 2-6c results.

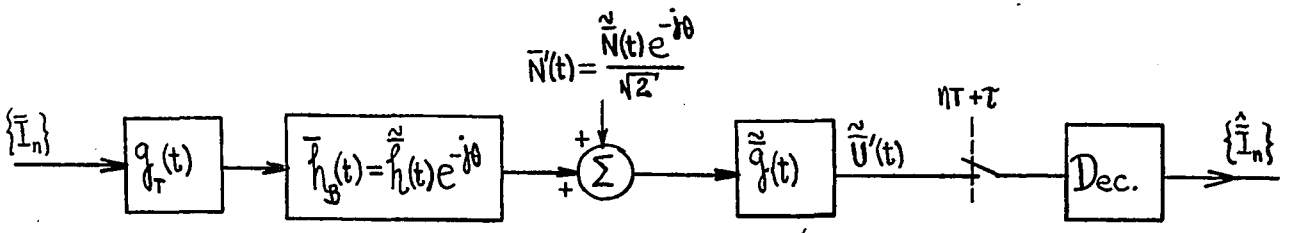

(a) Baseband Equivalent QAM System Model (Equivalent to Fig. 2-5 c)

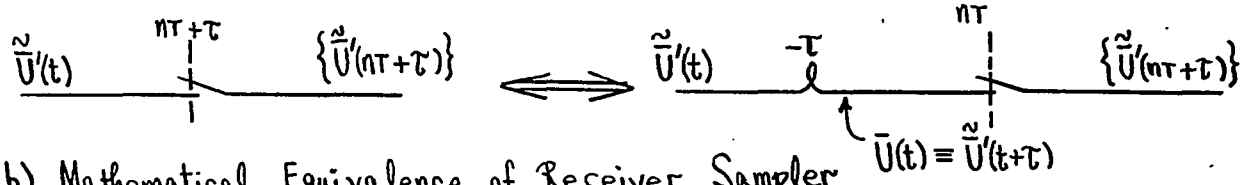

(b) Mathematical Equivalence of Receiver Sampler

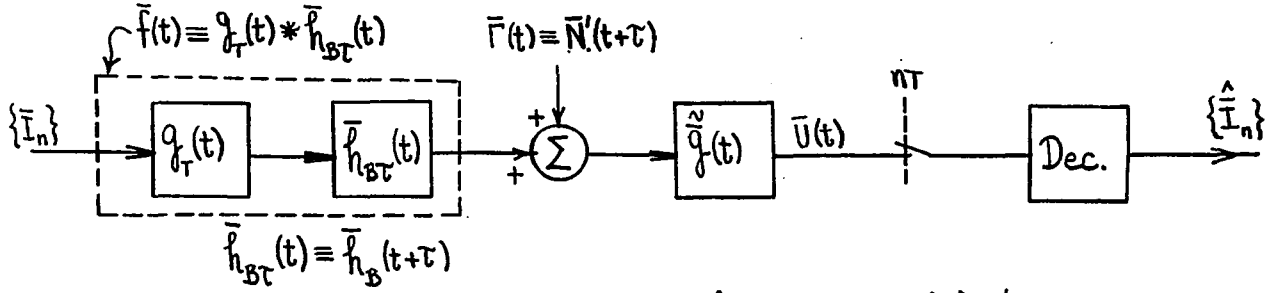

(c) Baseband Equivalent QAM System Model in Simplified Form

Figure 2-6. QAM System Modeling Continued

In summary, the physical passband QAM system model of Figure 2-5a has been shown to be mathematically equivalent to the purely baseband (nonphysical) model of Figure 2-5c, which, in turn, is equivalent to the simplified baseband models of Figures 2-6a and 2-6c. Since the relationships between the simplest model of Figure 2-6c and the other alternatives shown in Figures 2-5 and 2-6 are straightforward, we chose to analyze the configuration of Figure 2-6c in determining the "best" receiver filter response, $\tilde{\tilde{g}}^{\circ}(t)$, which optimizes some (as yet undefined) relevant performance index.

2.4 A NYQUIST ZERO INTERSYMBOL INTERFERENCE CONDITION FOR THE QAM SYSTEM

In reference to the baseband equivalent model of Figure 2-6c, we let $\bar{x}(t)$ denote the overall baseband equivalent impulse response of the system; that is, we let

$$\bar{x}(t) \equiv \bar{f}(t) * \tilde{\tilde{g}}(t). \tag{2-39}$$

In terms of $\bar{x}(t)$, the received waveform $\bar{U}(t)$ may be expressed as

$$\bar{U}(t) = \sum_k \bar{I}_k \bar{x}(t-kT) + \bar{V}(t), \tag{2-40}$$

where $\bar{V}(t)$ denotes the filtered noise process $\tilde{\tilde{g}}(t) * \bar{r}(t)$. Evaluating equation (2-40) at the n^{th} receiver sampling instant gives

$$\bar{U}(nT) = \sum_k \bar{I}_k \bar{x}(nT-kT) + \bar{V}(nT). \tag{2-41}$$

As can readily be seen from equation (2-41), intersymbol-interference-free transmission will occur provided that

$$\bar{x}(mT) = \begin{cases} 1 + j0 \text{ for } m = 0 \\ 0 + j0 \text{ for } m = \pm 1, \pm 2, \pm 3, \ldots. \end{cases} \tag{2-42}$$

That is, provided that the overall system impulse response satisfies the constraints imposed by equation (2-42), the received waveform at the n^{th} receiver observation instant will be

$$\bar{U}(nT) = \bar{I}_n + \bar{V}(nT), \tag{2-43}$$

thus being influenced only by the n^{th} transmitted symbol (and, of course, noise) with all other future and past transmitted symbols (relative to the n^{th} signaling interval) not effecting its value.

Since the overall system impulse response, $\bar{x}(t)$, may be expressed in terms of its Fourier transform, $\bar{X}(j\omega)$, via the inverse Fourier transform relationship,

$$\bar{x}(t) = \frac{1}{2\pi} \int_{-\infty}^{\infty} \bar{X}(j\omega) e^{j\omega t} d\omega, \tag{2-44}$$

$\bar{x}(mT)$ may be evaluated from

$$\bar{x}(mT) = \frac{1}{2\pi} \int_{-\infty}^{\infty} \bar{X}(j\omega) e^{j\omega mT} d\omega. \tag{2-45}$$

Rearranging and placing equation (2-45) in the form of

$$\bar{x}(mT) = \frac{1}{2\pi} \sum_k \int_{(2k-1)\omega_0}^{(2k+1)\omega_0} \bar{X}(j\omega) e^{j\omega mT} d\omega; \ \omega_0 > 0, \tag{2-46}$$

followed by changing the variable of integration in accordance with

$$\nu \equiv \omega - 2k\omega_0, \tag{2-47}$$

setting ω_0 equal to $\frac{\pi}{T}$, and reversing the order of summation and integration gives

$$\bar{x}(mT) = \frac{T}{2\pi}\int_{-\pi/T}^{\pi/T}\left[\frac{1}{T}\sum_k \bar{X}(j\nu+j\frac{2\pi k}{T})\right]e^{j\nu mT}d\nu. \tag{2-48}$$

Since $\bar{x}(mT)$ can be envisioned as representing the m^{th} element of the sequence $\{\bar{x}(mT)\}$, we may also write

$$\bar{x}(mT) = \frac{T}{2\pi}\int_{-\pi/T}^{\pi/T} X(e^{j\omega T})e^{j\omega mT}d\omega, \tag{2-49}$$

where

$$\bar{X}(e^{j\omega T}) \equiv F[\{\bar{x}(mT)\}] = \sum_k \bar{X}(kT)e^{-j\omega kT} = 1, \tag{2-50}$$

where equation (2-42) was invoked in writing the last equality above. Comparing equations (2-49) and (2-48), and using the uniqueness properties of the Fourier and inverse Fourier transformations, we conclude (with the help of equation (2-50)) that

$$\sum_k \bar{X}(j\omega+j\frac{2\pi k}{T}) = T \text{ for } |\omega| \leq \frac{\pi}{T}. \tag{2-51}$$

The constraint imposed by equation (2-51) on the overall system transfer function $\bar{X}(j\omega)$ is typically referred to as the frequency domain zero intersymbol interference condition, which, when satisfied by $\bar{X}(j\omega)$, yields received waveform performance in accordance with equation (2-43). Mathematically equivalent to the frequency domain constraint of equation (2-51) is the time domain constraint of equation (2-42), typically referred to as the time domain zero intersymbol interference condition.

CHAPTER 3

THE GENERALIZED LINEAR/NONLINEAR QAM SYSTEM

CHAPTER 3

THE GENERALIZED LINEAR/NONLINEAR QAM SYSTEM

3.1 INTRODUCTION AND REVIEW OF LINEAR SYSTEM FUNDAMENTALS

Thus far, we have focused on and dealt with issues related to the mitigation of linear system distortions. Despite all linear distortion mitigation efforts, however, nonlinearities in state-of-the-art communications systems (albeit typically controlled by sophisticated component designs and substantially maintained at fairly low levels) are rapidly assuming a major role in limiting the further increase in reliable data rates. The pioneering works of D. D. Falconer[1] and E. Biglieri, et al[2], established and characterized a class of adaptive receiver structures capable of mitigating nonlinear channel distortions in multidimensional data communications systems, at the expense, however, of substantial hardware complexities (a large number of tap coefficients is typically required in these structures to compensate for the effects of the nonlinear dispersive channel). As a consequence of such practical limitations, alternatives such as adaptive baseband predistortion at the transmitter have been explored.[3] Adaptive baseband predistortion, however, may not always be desirable or even feasible, particularly in multihop nonregenerative digital communications systems. It therefore becomes highly desirable to have adaptive capability of mitigating nonlinear channel impairments at the receiver of a communications system without having to resort to unreasonable hardware complexities.

The work outlined in this chapter addresses this issue. We show that, indeed, it is possible to define relatively simple receiver structures (representing not

more than a factor of two increase in the number of tap coefficients over those required in the linear channel applications) that can effectively mitigate channel nonlinearities. The adaptive receiver structures that we propose and study represent generalizations on the classical techniques that have been developed subject to the linear channel assumption. We show that the general nonlinear channel can be modeled equivalently by one whose impulse response is data-sequence-dependent and, in this sense, represents a baud-interval-by-baud-interval changing waveform. That is, we show that the channel's impulse response assumes values from an ensemble of waveforms, with a possibly different waveshape being assumed once every signaling interval. This simple observation leads to the data-sequence-dependent channel concept, which is the key to defining relatively simple extensions of the classical adaptive receiver structures that are capable of effectively combating channel nonlinearities. Before embarking on this venture, however, a synopsis of the techniques developed thus far for the linear QAM system (in Chapter 2, and Appendices A, B, C and D) is in order.

A simplified block diagram of the basic QAM communications system is shown in Figure 3-1a. As shown, two statisically independent discrete-valued (typically, zero mean) random data sequences, $\{A_k\}$ and $\{B_k\}$, are each low pass filtered by a transmitter filter with impulse response $p_T(t)$. Then, the filtered random information processes corresponding to $\{A_k\}$ and $\{B_k\}$ [I(t) and Q(t), respectively] amplitude modulate two phase quadrature carriers, $\sqrt{2}\cos\omega_c t$ and $\sqrt{2}\sin\omega_c t$, respectively. Hence, following the summation of the modulated carrier signals, the passband QAM random process signal, S(t), is formed. We therefore have

$$S(t) = \sqrt{2}\, I(t)\cos\omega_c t - \sqrt{2}\, Q(t)\sin\omega_c t, \qquad (3\text{-}1a)$$

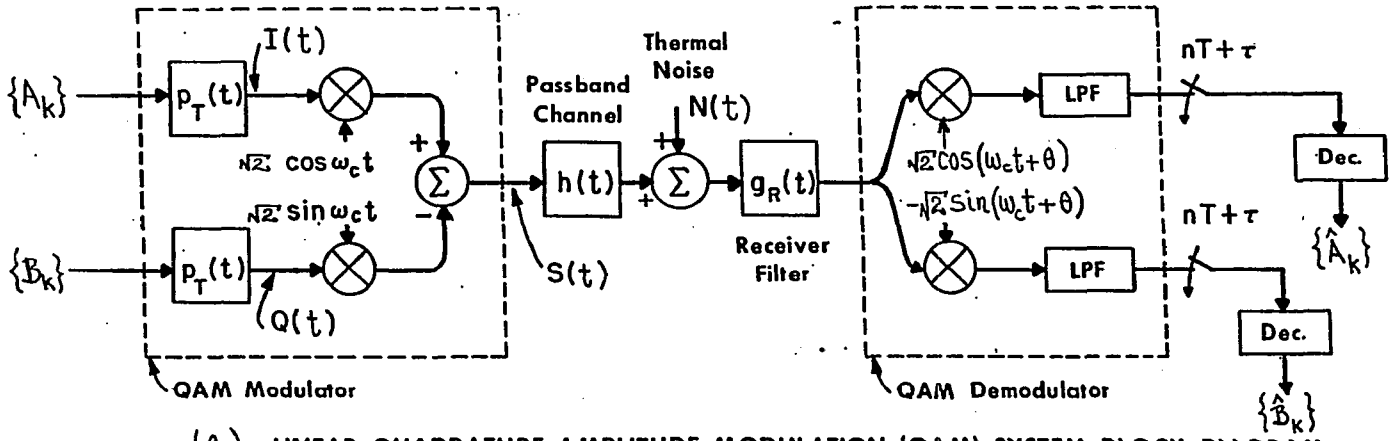

(a) LINEAR QUADRATURE AMPLITUDE MODULATION (QAM) SYSTEM BLOCK DIAGRAM

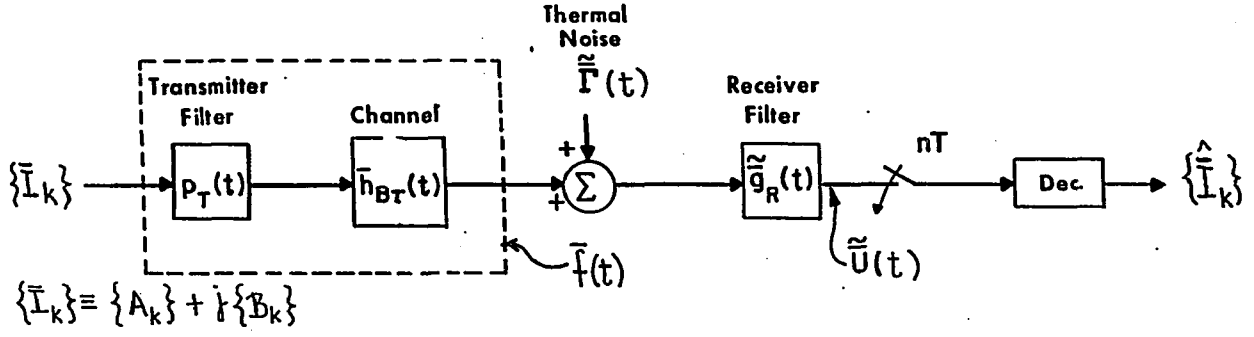

(b) BASEBAND EQUIVALENT MATHEMATICAL MODEL FOR THE LINEAR QAM SYSTEM

Figure 3-1. Linear QAM System Block Diagram and Baseband Equivalent Model

where

$$I(t) = \sum_k A_k p_T(t-kT), \tag{3-1b}$$

$$Q(t) = \sum_k B_k p_T(t-kT), \tag{3-1c}$$

$$\{A_k\} \equiv \sum_k A_k \delta(t-kT) \tag{3-1d}$$

and

$$\{B_k\} \equiv \sum_k B_k \delta(t-kT), \tag{3-1e}$$

where T denotes the signaling interval. The passband channel (the propagation medium) is characterized by the impulse response $h(t)$. This impulse response is assumed unknown and, in general, time varying, but substantially quasistatic with respect to the transmission rate (the baud rate) $1/T$. At the output of the channel, a thermal noise process, $N(t)$, is added to the received information carrying random process signal. Following this, we postulate a passband receiver filter with impulse response $g_R(t)$. The purpose of this filter is to optimize (minimize) some performance index of the system, such as, for example, the Mean Squared Error (MSE) at the sampling times, or the probability of error subject to the zero Intersymbol Interference (ISI) constraint, etc. Finally, demodulation of the received noisy process by the phase orthogonal carrier signals $\sqrt{2}\cos(\omega_c t + \theta)$ and $\sqrt{2}\sin(\omega_c t + \theta)$ followed by sampling at $t = nT + \tau$, $n = 0, \pm 1, \pm 2, \ldots$, and decision making produces estimates, $\{\hat{A}_k\}$ and $\{\hat{B}_k\}$, of the transmitted random data sequences. The parameters θ and τ denote the receiver's carrier phase and timing phase values, respectively.

Using the complex envelope representation of passband signals and systems (see Appendix A), a mathematical equivalence can be established between the passband QAM system of Figure 3-1a and the purely baseband equivalent mathematical system depicted in Figure 3-1b. In the representation of Figure 3-1b, a complex-valued random data sequence, $\{\overline{I}_k\}$, defined as

$$\{\overline{I}_k\} \equiv \sum_k \overline{I}_k \delta(t-kT) \equiv \sum_k [A_k+jB_k]\delta(t-kt) \tag{3-2}$$

is low pass filtered by a transmitter filter having real-valued impulse response $p_T(t)$. The effect of the channel, receiver carrier phase θ and receiver timing phase τ, is accounted for by the complex-valued low pass filter entity having impulse response $\overline{h}_{B\tau}(t)$, where

$$\overline{h}_{B_\tau}(t) \equiv \tilde{\tilde{h}}(t+\tau)e^{-j\theta}. \tag{3-3}$$

Thermal noise is accounted for by the complex envelope $\tilde{\tilde{\Gamma}}(t)$, where

$$\tilde{\tilde{\Gamma}}(t) \equiv \frac{1}{\sqrt{2}} \tilde{\tilde{N}}(t+\tau)e^{-j\theta} \tag{3-4}$$

and the receiver filter function is represented by the complex envelope $\tilde{\tilde{g}}_R(t)$. We stress that, in the mathematical model of Figure 3-1b, although the demodulation functions are not shown explicitly, they are mathematically and equivalently accounted for by the channel's response as given by equation (3-3).

The baseband equivalent model described above for the linear QAM system can readily be analyzed and optimized (see Appendices C and D) by finding the optimum receiver filter impulse response, $g_R^\circ(t)$, which minimizes some mathematically

tractable performance index, such as, for example, the MSE at the sampling times. That is, letting $\tilde{\tilde{U}}(t)$ denote the random process signal at the output of the receiver filter, we can define the MSE at the n^{th} sampling time as

$$\varepsilon_n \equiv E[|\tilde{\tilde{U}}(nT) - \bar{I}_n|^2], \tag{3-5}$$

where the expectation operator, $E[\cdot]$, denotes ensemble averaging with respect to all possible complex-valued data sequences and noise waveforms. Minimizing such a performance index (see Appendix C) results in an optimum receiver filter transfer function given by (see equation (C-45))

$$\tilde{\tilde{G}}_R^o(j\omega) \equiv F[\tilde{\tilde{g}}_R^o(t)] = \frac{\bar{F}^*(j\omega)}{\frac{1}{T}\sum_k \left|\bar{F}(j\omega + j\frac{2\pi k}{T})\right|^2 + \frac{N_o}{\sigma_I^2}}, \tag{3-6a}$$

where

$$\bar{F}(j\omega) \equiv F[p_T(t) * \bar{h}_{B\tau}(t)], \tag{3-6b}$$

$$\sigma_I^2 \equiv E[|\bar{I}_k|^2], \tag{3-6c}$$

and

$$N_o = S_\Gamma(j\omega) \equiv F[\phi_\Gamma(\tau)] \equiv F[E[\tilde{\tilde{\Gamma}}(t)\,\tilde{\tilde{\Gamma}}^*(t+\tau)]], \tag{3-6d}$$

where the power spectral density of the equivalent noise, $S_\Gamma(j\omega)$, has been assumed constant over the system bandwidth and $F[\cdot]$ denotes the Fourier transformation, $F[\cdot] \equiv \int_{-\infty}^{\infty} [\cdot] e^{-j\omega t} dt$.

Similarly, if the performance index to be minimized is the well known "probability of error subject to the zero ISI constraint", it can readily be shown that an appropriate performance index in the frequency domain is (see Appendix D)

$$J = \frac{1}{2\pi}\int_{-\pi/T}^{\pi/T}\sum_k S_\Gamma(j\omega+j\frac{2\pi k}{T})\left|\tilde{\tilde{G}}_R(j\omega+j\frac{2\pi k}{T})\right|^2 d\omega$$

$$+ \lambda[\sum_k \overline{X}(j\omega+j\frac{2\pi k}{T}) - T], \tag{3-7a}$$

where λ denotes a Lagrange multiplier, with

$$\overline{X}(j\omega) \equiv \overline{F}(j\omega)\tilde{\tilde{G}}_R(j\omega) \tag{3-7b}$$

denoting the overall transfer characteristic of the system. Minimizing J with respect to $\tilde{\tilde{G}}_R(j\omega)$ gives

$$\tilde{\tilde{G}}_R^{\circ}(j\omega) = \frac{\overline{F}^*(j\omega)}{\frac{1}{T}\sum_k\left|\overline{F}(j\omega+j\frac{2\pi k}{T})\right|^2} \tag{3-8}$$

We observe that $\tilde{\tilde{G}}_R^{\circ}(j\omega)$, as defined by equation (3-8), yields an overall system characteristic that is Nyquist, satisfying the zero ISI constraint. Furthermore, observe that, in the limit, as the thermal noise becomes vanishingly small, the two optimum receivers as defined by equations (3-8) and (3-6) become indistinguishable.

In practice, the optimum linear receivers represented by equations (3-6) and (3-8) are implemented (approximated) by fractionally spaced transversal filter structures (see Appendices C and D). The basic elements of a (2N + 1) tap, T' spaced, fractionally spaced transversal filter are shown in Figure 3-2. The delay

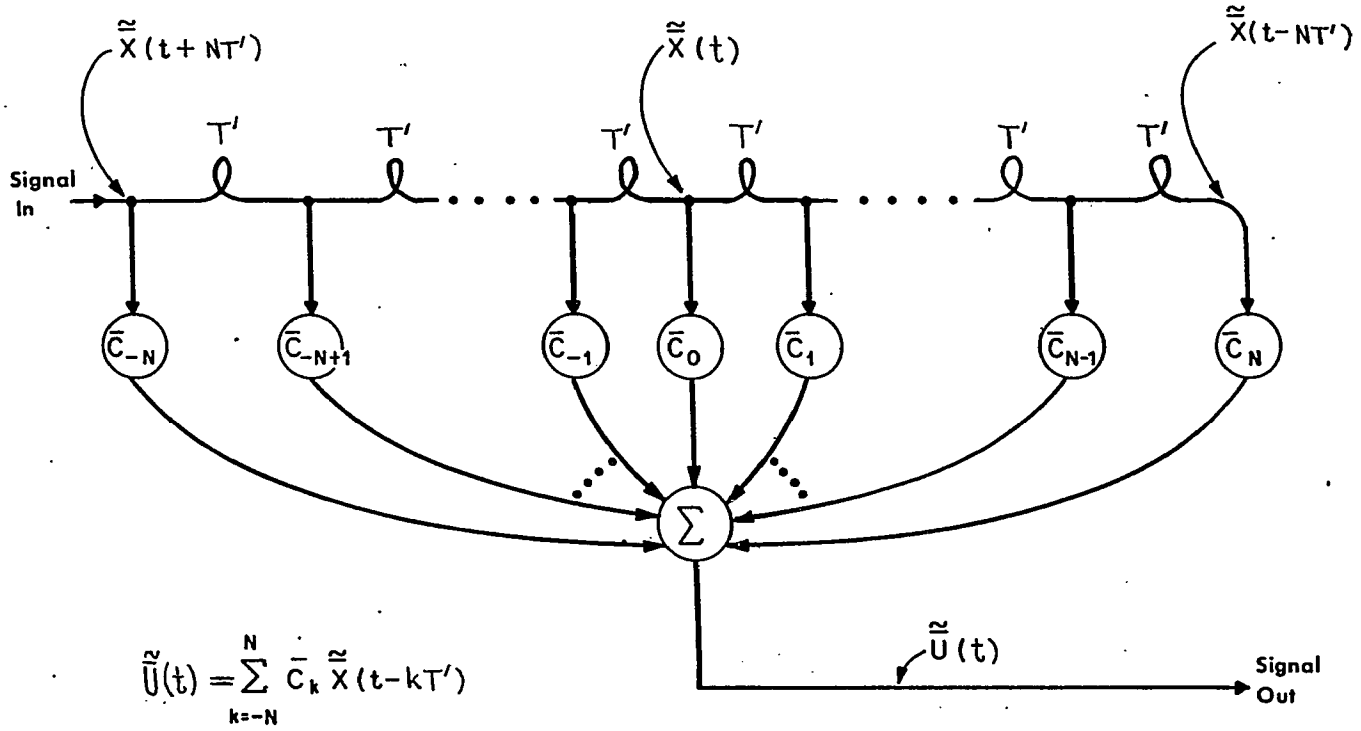

Figure 3-2. A 2N + 1 Tap, T' Spaced, Fractionally Spaced Filter with Complex-Valued Coefficients

line elements are typically chosen such that T' = T/2. However, T' need not be set equal to T/2, as long as it is chosen so that the periodic transfer characteristic formed by the structure spans the entire system bandwidth, which is typically defined (according to the Nyquist school of thought) to extend over the frequency interval $|\omega| \leq \frac{\pi}{T}(1+\alpha)$, $0 < \alpha < 1$. A T/2 tap spacing, however, does represent a preferred embodiment for practical reasons, particularly when the filter is implemented digitally. The filter coefficients are assumed complex-valued (as shown in Figure 3-2), since the complex-valued impulse response $\tilde{\tilde{g}}_R(t)$ is being approximated. It is readily seen that in terms of the complex random process signals defined along the delay line of the filter, the complex-valued output signal at t = nT can be written as

$$\tilde{\tilde{U}}(nT) = \overline{C}_{-N}\tilde{\tilde{X}}(nT+NT') + \overline{C}_{-N+1}\tilde{\tilde{X}}(nT+NT'-T') + \ldots$$

$$+ \overline{C}_0\tilde{\tilde{X}}(nT) + \overline{C}_1\tilde{\tilde{X}}(nT-T') + \ldots + \overline{C}_N\tilde{\tilde{X}}(nT-NT'), \qquad (3\text{-}9a)$$

or, more compactly, in terms of an inner product of complex-valued vector quantities,

$$\tilde{\tilde{U}}(nT) = \underline{\overline{C}}^T\underline{\tilde{\tilde{X}}}_n, \qquad (3\text{-}9b)$$

where

$$\underline{\bar{C}} \equiv \begin{bmatrix} \bar{C}_{-N} \\ \bar{C}_{-N+1} \\ \vdots \\ \bar{C}_0 \\ \bar{C}_1 \\ \vdots \\ \bar{C}_N \end{bmatrix} \quad \text{and} \quad \underline{\tilde{\tilde{X}}}_n \equiv \begin{bmatrix} \tilde{\tilde{X}}(nT+NT') \\ \tilde{\tilde{X}}(nT+NT'-T') \\ \vdots \\ \tilde{\tilde{X}}(nT) \\ \tilde{\tilde{X}}(nT-T') \\ \vdots \\ \tilde{\tilde{X}}(nT-NT') \end{bmatrix}, \tag{3-9c}$$

with T used as a superscript on a vector to denote transposition. For the case where the performance index to be minimized is the MSE at the n^{th} sampling time, we have

$$\varepsilon_n = E[|\tilde{\tilde{U}}(nT) - \bar{I}_n|^2]$$

$$= \underline{\bar{C}}^T \underline{\tilde{\tilde{R}}} \underline{\bar{C}}^* - \underline{\bar{C}}^T \underline{\bar{P}} - \underline{\bar{C}}^{*T} \underline{\bar{P}}^* + \sigma_I^2, \tag{3-10a}$$

where

$$\underline{\tilde{\tilde{R}}} \equiv E[\underline{\tilde{\tilde{X}}}_n \underline{\tilde{\tilde{X}}}_n^{*T}], \tag{3-10b}$$

$$\underline{\bar{P}} \equiv E[\bar{I}_n^* \underline{\tilde{\tilde{X}}}_n] \tag{3-10c}$$

and

$$\sigma_I^2 \equiv E[\bar{I}_n \bar{I}_n^*]. \tag{3-10d}$$

To find the optimum complex-valued coefficient vector, $\underline{\bar{C}}^{o}$, which minimizes ε_n, we take the gradient of ε_n with respect to $\underline{\bar{C}}$, set the result to zero and solve for $\underline{\bar{C}}$. That is,

$$\nabla_{\underline{\bar{C}}}\varepsilon_n \equiv \frac{\partial \varepsilon_n}{\partial \underline{\bar{C}}} = 0. \tag{3-11}$$

Evaluating equation (3-11) gives

$$\underline{\bar{C}}^{o*} = \underline{\underline{\tilde{R}}}^{-1}\underline{\bar{P}}. \tag{3-12}$$

In practice, the optimum coefficient vector predicted by equation (3-12) is found adaptively using some control law such as the well known stochastic gradient algorithm (see Appendix C)

$$\underline{\bar{C}}^{*}_{k+1} = \underline{\bar{C}}^{*}_{k} + \mu \bar{E}^{*}_{n}\underline{\tilde{X}}_{n}, \tag{3-13}$$

where $\bar{E}_n \equiv \bar{I}_n - \tilde{\bar{U}}_n$, the subscript k specifies the adaptation index, and n pertains to receiver sampling time. It can readily be shown that

$$\lim_{k\to\infty} E[\underline{\bar{C}}^{*}_{k+1}] = \underline{\bar{C}}^{o*} = \underline{\underline{\tilde{R}}}^{-1}\underline{\bar{P}}. \tag{3-14}$$

That is, the control law (3-13) finds $\underline{\bar{C}}^{o}$ in the mean in the limit as $k \to \infty$. Similar techniques exist for finding the coefficient vector that minimizes the performance index J (see Appendix D).

Below, the mathematical model for the nonlinear QAM system is derived, leading to the data-sequence-dependent channel concept. Following this, an optimum in the

Least MSE (LMSE) sense receiver structure is defined for the nonlinear QAM system, together with its associated adaptive control algorithm. The issue of nonlinear ISI equalization versus cancellation is also examined. An ISI canceller is defined for the nonlinear QAM system and its performance examined via computer simulation.

3.2 A BASEBAND EQUIVALENT REPRESENTATION FOR THE NONLINEAR SYSTEM

The overall structure of the nonlinear QAM system to be considered here is assumed substantially the same as that of the linear QAM system described in Chapter 2 and reviewed above. As shown in Figure 3-3, however, a nonlinear device is postulated at the output of the QAM modulator. Following Heiter's approach[4], the assumed J^{th} order nonlinearity is modeled by the input/output relationship

$$v_o(t) = g_1 v_i(t-\tau_1) + g_2 v_i^2(t-\tau_2) + \ldots + g_J v_i^J(t-\tau_J), \tag{3-15}$$

where $v_i(t)$ and $v_o(t)$ denote the input and output signals, respectively. The nonlinearity model defined by equation (3-15) is capable of predicting nonlinear distortions in both amplitude and phase. As specified above, we assume that the only nonlinearity in the system exists at the modulator output (accounting perhaps for the effects of a transmitter power amplifier). However, this need not be the case. The system model may be further generalized to account for a multiplicity of nonlinearities distributed throughout it. This, however, is not attempted at this point for the sake of simplicity and clarity. Furthermore, in order to keep the analytical results more easily interpretable and manageable, we consider, in detail, the $J = 3$ case. That is, we assume a third order nonlinearity at the modulator output.

Subject to the above simplifications, the passband random signal process at the output of the nonlinearity, $S'(t)$, may be expressed as

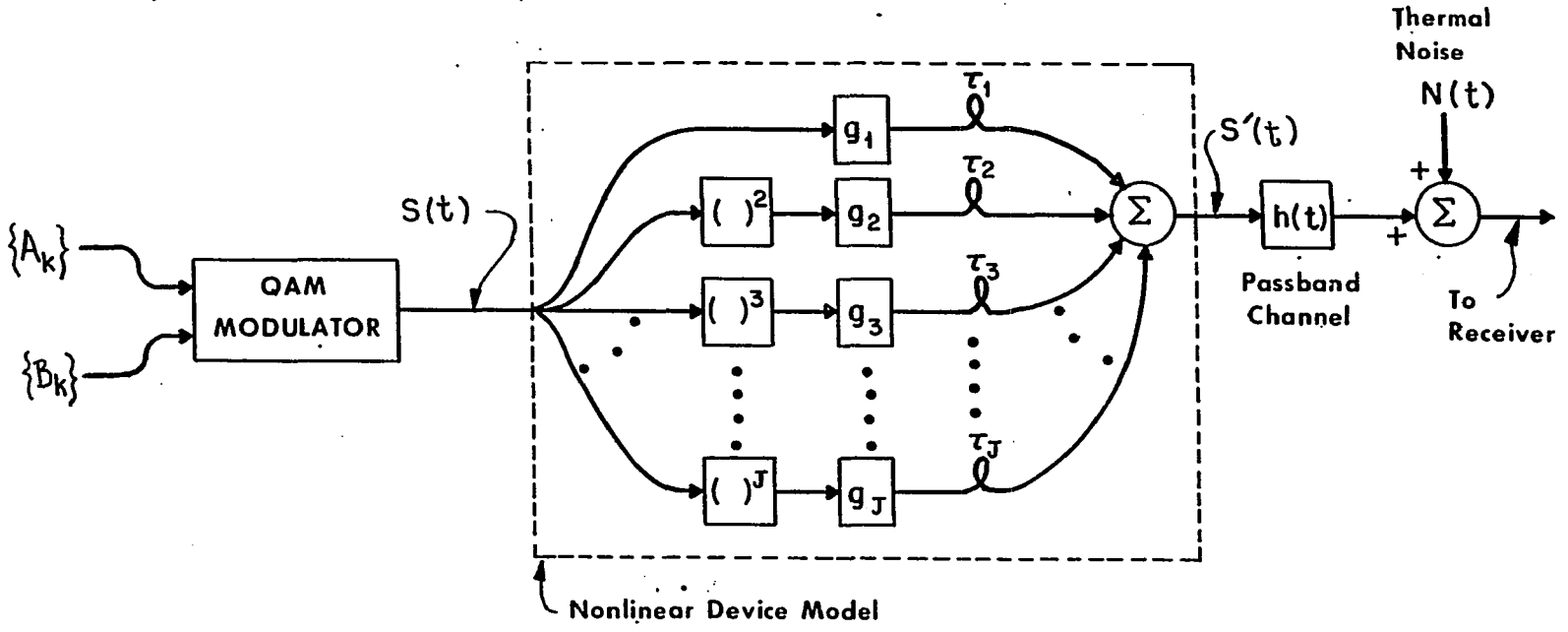

Figure 3-3. Nonlinear QAM System Block Diagram

$$S'(t) = g_1 S(t-\tau_1) + g_2 S^2(t-\tau_2) + g_3 S^3(t-\tau_3), \tag{3-16}$$

where $S(t)$ represents the QAM signal as defined by equation (3-1). Assuming that the passband system bandwidth is small compared to the carrier frequency, $S^2(t-\tau_2)$ will exist entirely outside the band of interest and will, hence, not appear at the receiver. The term $S^3(t-\tau_3)$ will contribute, however, an inband as well as an out-of-band component. The component of $S^3(t-\tau_3)$ in the passband will be denoted by $S^3_{PB}(t-\tau_3)$. Straightforward algebraic manipulations give

$$\begin{aligned} S^3_{PB}(t-\tau_3) = {} & K_{C3}\, \Xi(t-\tau_3)\, I(t-\tau_3)\, \sqrt{2} \cos \omega_c t \\ & + K_{S3}\, \Xi(t-\tau_3)\, Q(t-\tau_3)\, \sqrt{2} \cos \omega_c t \\ & - K_{C3}\, \Xi(t-\tau_3)\, Q(t-\tau_3)\, \sqrt{2} \sin \omega_c t \\ & + K_{S3}\, \Xi(t-\tau_3)\, I(t-\tau_3)\, \sqrt{2} \sin \omega_c t \end{aligned} \tag{3-17a}$$

where

$$K_{C3} \equiv \cos \omega_c \tau_3, \quad K_{S3} \equiv \sin \omega_c \tau_3 \tag{3-17b}$$

and

$$\Xi(t) \equiv \frac{3}{2} [I^2(t) + Q^2(t)]. \tag{3-17c}$$

Using equations (3-1c) and (3-1d), equation (3-17a) above may be rewritten in terms of the transmitted random data sequences, $\{A_k\}$ and $\{B_k\}$, and the transmitter filter impulse response, $p_T(t)$, as

$$S^3_{PB}(t-\tau_3) = \left\{\frac{3}{2} K_{C3} \sum_k A_k \sum_\ell \sum_m [A_\ell A_m + B_\ell B_m]\right.$$

$$\left. \cdot\, p_T(t-\tau_3-kT)p_T(t-\tau_3-\ell T)p_T(t-\tau_3-mT)\right\} \sqrt{2} \cos \omega_c t$$

$$+ \left\{\frac{3}{2} K_{S3} \sum_k B_k \sum_\ell \sum_m [A_\ell A_m + B_\ell B_m]\right.$$

$$\left. \cdot\, p_T(t-\tau_3-kT)p_T(t-\tau_3-\ell T)p_T(t-\tau_3-mT)\right\} \sqrt{2} \cos \omega_c t$$

$$- \left\{\frac{3}{2} K_{C3} \sum_k B_k \sum_\ell \sum_m [A_\ell A_m + B_\ell B_m]\right.$$

$$\left. \cdot\, p_T(t-\tau_3-kT)p_T(t-\tau_3-\ell T)p_T(t-\tau_3-mT)\right\} \sqrt{2} \sin \omega_c t$$

$$+ \left\{\frac{3}{2} K_{S3} \sum_k A_k \sum_\ell \sum_m [A_\ell A_m + B_\ell B_m]\right.$$

$$\left. \cdot\, p_T(t-\tau_3-kT)p_T(t-\tau_3-\ell T)p_T(t-\tau_3-mT)\right\} \sqrt{2} \sin \omega_c t. \qquad (3\text{-}18)$$

The total passband (inband) component of $S'(t)$ will therefore be

$$S'_{PB}(t) = g_1 S(t-\tau_1) + g_3 S^3_{PB}(t-\tau_3). \qquad (3\text{-}19)$$

Hence, we can write

$$
\begin{aligned}
S'_{PB}(t) = & \Bigg\{\sum_k A_k\Big[\frac{3}{2} K_{C3} g_3 \sum_\ell \sum_m (A_\ell A_m + B_\ell B_m) p_T(t-\tau_3-kT) \\
& \cdot p_T(t-\tau_3-\ell T) p_T(t-\tau_3-mT) + K_{C1} g_1 P_T(t-\tau_1-kT)\Big] \\
& + \sum_k B_k\Big[\frac{3}{2} K_{S3} g_3 \sum_\ell \sum_m (A_\ell A_m + B_\ell B_m) p_T(t-\tau_3-kT) \\
& \cdot p_T(t-\tau_3-\ell T) p_T(t-\tau_3-mT) + K_{S1} g_1 P_T(t-\tau_1-kT)\Big]\Bigg\} \sqrt{2} \cos \omega_c t \\
& - \Bigg\{\sum_k B_k\Big[\frac{3}{2} K_{C3} g_3 \sum_\ell \sum_m (A_\ell A_m + B_\ell B_m) p_T(t-\tau_3-kT) \\
& \cdot p_T(t-\tau_3-\ell T) p_T(t-\tau_3-mT) + K_{C1} g_1 P_T(t-\tau_1-kT)\Big] \\
& - \sum_k A_k\Big[\frac{3}{2} K_{S3} g_3 \sum_\ell \sum_m (A_\ell A_m + B_\ell B_m) p_T(t-\tau_3-kT) \\
& \cdot p_T(t-\tau_3-\ell T) p_T(t-\tau_3-mT) + K_{S1} g_1 P_T(t-\tau_1-kT)\Big]\Bigg\} \sqrt{2} \sin \omega_c t, \qquad (3\text{-}20a)
\end{aligned}
$$

where

$$
K_{C1} \equiv \cos \omega_c \tau_1 \text{ and } K_{S1} \equiv \sin \omega_c \tau_1. \qquad (3\text{-}20b)
$$

At this point, we make the assumption that, at any one particular point in time, only M' preceding and N' succeeding data values play a role in determining the value of $S'_{PB}(t)$. We, hence, write

$$S'_{PB}(t) \equiv \left\{\sum_k A_k f_1(t-kT, \{\overline{I}_\ell\}_{k-M'}^{k+N'}) + \sum_k B_k f_2(t-kT, \{\overline{I}_\ell\}_{k-M'}^{k+N'})\right\} \sqrt{2} \cos \omega_c t$$

$$- \left\{\sum_k B_k f_1(t-kT, \{\overline{I}_\ell\}_{k-M'}^{k+N'}) - \sum_k A_k f_2(t-kT, \{\overline{I}_\ell\}_{k-M'}^{k+N'})\right\} \sqrt{2} \sin \omega_c t, \quad (3\text{-}21)$$

where

$$f_1(t, \{\overline{I}_\ell\}_{-M'}^{N'}) \equiv \frac{3}{2} K_{C3} g_3 \sum_{\ell=-M'}^{N'} \sum_{m=-M'}^{N'} (A_\ell A_m + B_\ell B_m) p_T(t-\tau_3) \cdot p_T(t'-\tau_3-\ell T) p_T(t'-\tau_3-mT) + K_{C1} g_1 p_T(t-\tau_1) \quad (3\text{-}22a)$$

and

$$f_2(t, \{\overline{I}_\ell\}_{-M'}^{N'}) \equiv \frac{3}{2} K_{S3} g_3 \sum_{\ell=-M'}^{N'} \sum_{m=-M'}^{N'} (A_\ell A_m + B_\ell B_m) p_T(t-\tau_3) \cdot p_T(t'-\tau_3-\ell T) p_T(t'-\tau_3-mT) + K_{S1} g_1 p_T(t-\tau_1). \quad (3\text{-}22b)$$

Note that, in the above expressions, $t' = t$. The only reason for using t' in the places where we have is for clarity of the definition of $f_1(t - kT, \{\overline{I}_\ell\}_{-M'}^{N'})$ and $f_2(t - kT, \{\overline{I}_\ell\}_{-M'}^{N'})$ above. In light of equation (3-21), and definitions (3-22a) and (3-22b), we can now define an equivalent data-sequence-dependent transmitter filter as illustrated in Figure 3-4. The data-sequence-dependent transmitter filter is

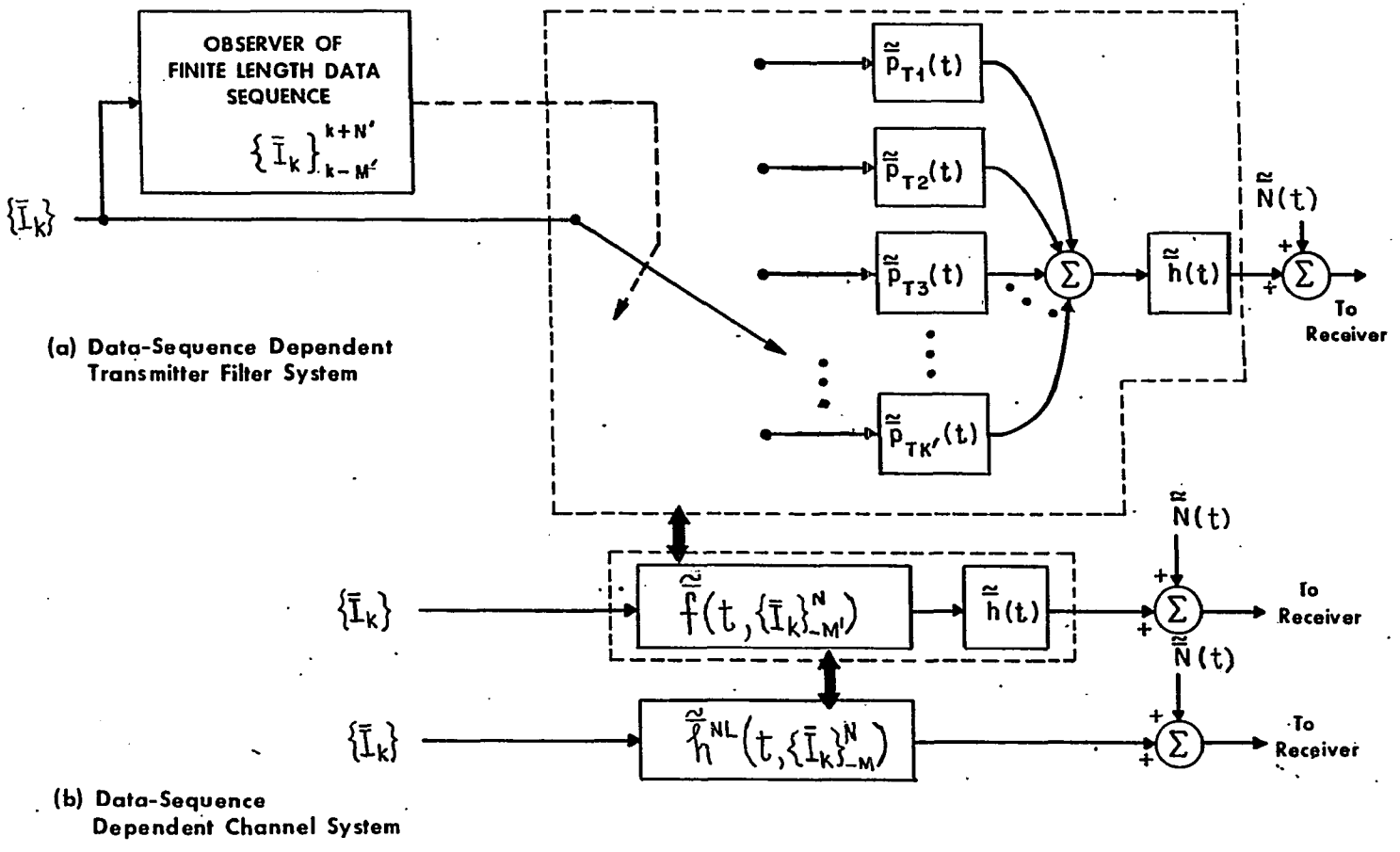

Figure 3-4. Various Equivalent Forms of the Nonlinear QAM System

modeled mathematically by associating with it the complex envelope $\tilde{\tilde{f}}(t, \{I_\ell\}_{-M'}^{N'})$, where

$$\tilde{\tilde{f}}(t, \{\bar{I}_\ell\}_{-M'}^{N'}) \equiv f_1(t, \{\bar{I}_\ell\}_{-M'}^{N'}) + jf_2(t, \{\bar{I}_\ell\}_{-M'}^{N'}). \tag{3-22c}$$

Letting $\tilde{\tilde{S}}'_{PB}(t)$ denote the complex envelope of $S'_{PB}(t)$, we can write

$$\begin{aligned}
\tilde{\tilde{S}}'_{PB}(t) &= \sum \bar{I}_k \tilde{\tilde{f}}(t-kT, \{\bar{I}_\ell\}_{k-M'}^{k+N'}) \\
&= \sum_k (A_k+jB_k)[f_1(t-kT, \{\bar{I}_\ell\}_{k-M'}^{k+N'}) + jf_2(t-kT, \{\bar{I}_\ell\}_{k-M'}^{k+N'})] \\
&= \sum_k \{A_k f_1(t-kT, \{\bar{I}_\ell\}_{k-M'}^{k+N'}) - B_k f_2(t-kT, \{\bar{I}_\ell\}_{k-M'}^{k+N'})\} \\
&\quad + j\sum_k \{B_k f_1(t-kT, \{\bar{I}_\ell\}_{k-M'}^{k+N'}) + A_k f_2(t-kT, \{\bar{I}_\ell\}_{k-M'}^{k+N'})\}.
\end{aligned} \tag{3-23}$$

As expected, equation (3-23) gives $S'_{PB}(t) = \mathrm{Re}[\tilde{\tilde{S}}'_{PB}(t)e^{j\omega_c t}]$, as per equation (3-21). Next, allowing $\tilde{\tilde{S}}'_{PB}(t)$ to propagate through the passband channel (with complex envelope $\tilde{\tilde{h}}(t)$), the signal $\tilde{\tilde{S}}'_{PB}(t) * \tilde{\tilde{h}}(t)$ is generated. We let

$$\tilde{\tilde{S}}'(t) * \tilde{\tilde{h}}(t) \equiv \sum_k \bar{I}_k \tilde{\tilde{h}}^{NL}(t-kT, \{\bar{I}_\ell\}_{k-M}^{k+N}), \tag{3-23a}$$

where

$$\tilde{\tilde{h}}^{NL}(t, \{\overline{I}_\ell\}_{-M}^{N}) \equiv \tilde{\tilde{f}}(t, \{\overline{I}_\ell\}_{-M'}^{N'}) * \tilde{\tilde{h}}(t). \tag{3-23b}$$

The equation above serves as the defining equation for the data-sequence-dependent channel. Since it is the convolution of $\tilde{\tilde{h}}(t)$ with $\tilde{\tilde{f}}(t, \{\overline{I}_\ell\}_{-M'}^{N'})$ that determines the impulse response of the data-sequence-dependent channel, we let $\tilde{\tilde{h}}^{NL}(\cdot)$ depend on a data sequence of length $M + N + 1 \geq M' + N' + 1$, in general. The equivalence of the data-sequence-dependent transmitter filter (followed by the passband channel) with the data-sequence-dependent channel is illustrated in Figure 3-4. Finally, accounting for the demodulator recovered carrier phase and sampling time phase parameters, θ and τ, respectively (just as we did for the linear QAM system case), gives the data-sequence-dependent baseband equivalent channel model with impulse response $\overline{h}_{B\tau}^{NL}(t, \{\overline{I}_\ell\}_{-M}^{N})$, where

$$\overline{h}_{B\tau}^{NL}(t, \{\overline{I}_\ell\}_{-M}^{N}) \equiv \tilde{\tilde{h}}^{NL}(t+\tau, \{\overline{I}_\ell\}_{-M}^{N})e^{-j\theta}. \tag{3-24}$$

This data-sequence-dependent baseband equivalent channel model for the nonlinear QAM system is illustrated in Figure 3-5.

3.3 THE DATA-SEQUENCE-DEPENDENT IMPULSE RESPONSE

In this section, computer simulation results are presented illustrating the nonlinear behavior of the assumed QAM communications system (impaired by a third order nonlinearity at the modulator output (see Figure 3-3)). The pulse shaping transmitter filter, $p_T(t)$, is assumed half-Nyquist, with the following frequency domain transfer characteristic[5]:

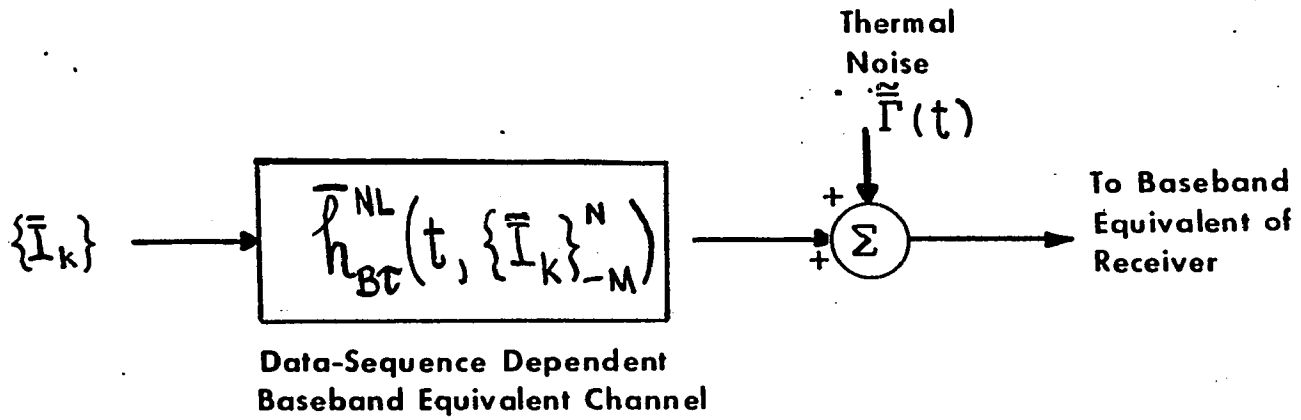

Figure 3-5. Nonlinear QAM System Baseband Equivalent Model

$$\overline{P}_T(j\omega) \equiv F[p_T(t)] \equiv \begin{cases} \sqrt{T} \text{ for } 0 \leq \omega \leq \frac{\pi}{T}(1-\alpha) \\ \sqrt{\frac{T}{2}}\{1 - \sin[\frac{T}{2\alpha}(\omega - \frac{\pi}{T})]\}^{1/2} \\ \text{for } \frac{\pi}{T}(1-\alpha) \leq \omega \leq \frac{\pi}{T}(1+\alpha), \end{cases} \tag{3-25}$$

where α denotes the "roll-off" factor, $0 \leq \alpha \leq 1$. Here, we have set $\alpha = 0.5$. The baud interval (the signaling interval) has been set to 66.67×10^{-9} seconds $\equiv$ 66.67 ns, corresponding to an assumed baud rate (number of transmitted data symbols per second) of $15 \times 10^6 \equiv 15$ Mbaud.

The passband channel transfer characteristic is assumed to exist over the frequency interval $\omega_c - \frac{\pi}{T}(1 + \alpha) \leq \omega \leq \omega_c + \frac{\pi}{T}(1 + \alpha)$, where $\omega_c = 2\pi(4 \times 10^9)$ rads/second. The passband channel transfer function, $\overline{H}(j\omega)$, is chosen to represent a line-of-sight multipath fading tropospheric medium.[6-9] We let

$$\overline{H}(j\omega) = a(1 - be^{-j(\omega-\omega_f)\tau}) = a(1 + be^{-j\omega\tau}) \tag{3-26}$$

in accordance with the Rummler model.[7] In equation (3-26), the parameter ω_f denotes the frequency at which the magnitude of $\overline{H}(j\omega)$ is at a minimum (thus, ω_f defines the "fade notch" frequency). At the fade notch frequency, we have $e^{j\omega_f\tau} = -1$, by definition, with τ set equal to 6.3 ns, according to the Rummler model. The parameter "a" represents frequency independent attenuation (or gain) over the entire band and "b" determines the maximum attenuation of $\overline{H}(j\omega)$ at $\omega = \omega_f$ due to the frequency dependent factor $(1 + be^{-j\omega\tau})$. The quantity 20 log $|1 - b|$, expressed in dB, is used as a measure of the frequency dependent factor of the passband channel's

transfer function and serves as an indicator of transmission quality, since it is the frequency dependent factor of $\overline{H}(j\omega)$ that is responsible for generating ISI.

In Section 3.2, we derived an expression for the inband (passband) random signal process at the nonlinearity output, just prior to propagation through the passband channel (the expression is repeated below for convenience):

$$\begin{aligned} S'_{PB}(t) \equiv & \{\sum_k A_k f_1(t-kT, \{\overline{I}_\ell\}_{k-M'}^{k+N'}) \\ & + \sum_k B_k f_2(t-kT, \{\overline{I}_\ell\}_{k-M'}^{k+N'})\} \sqrt{2} \cos \omega_c t \\ & - \{\sum_k B_k f_1(t-kT, \{\overline{I}_\ell\}_{k-M'}^{k+N'}) \\ & - \sum_k A_k f_2(t-kT, \{\overline{I}_\ell\}_{k-M'}^{k+N'})\} \sqrt{2} \sin \omega_c t, \end{aligned}$$

where

$$\begin{aligned} f_1(t, \{\overline{I}_\ell\}_{k-M'}^{k+N'}) \equiv & \frac{3}{2} K_{C3} g_3 \sum_{\ell=k-M'}^{k+N'} \sum_{m=k-M'}^{k+N'} (A_\ell A_m + B_\ell B_m) p_T(t-\tau_3-kT) \\ & \cdot p_T(t-\tau_3-\ell T) p_T(t-\tau_3-mT) + K_{C1} g_1 p_T(t-\tau_1-kT), \end{aligned}$$

with a similar equation defining $f_2(t - kT, \{\overline{I}_\ell\}_{k-M'}^{k+N'})$.

With k and τ_3 set to zero (for simplicity and without loss of generality), we have evaluated the triplet $p_T(t)\, p_T(t - \ell T)\, p_T(t - mT)$ for various integer values of

ℓ and m. Some results are shown in Figure 3-6a. First, as a point of reference, the half-Nyquist pulse, $p_T(t)$, is shown with its peak amplitude normalized to unity. Also shown, and correspondingly labeled, are the half-Nyquist pulse triplets generated by (k = 0, ℓ = 0, m = 0), (k = 0, ℓ = 0, m = 1) and (k = 0, ℓ = 1, m = 2). Observe the rapid decay of triplet peak magnitude as a function of the distance of m and ℓ away from k. For example, we see that the triplet $p_T(t)\ p_T(t - T)\ p_T(t - 2T)$, generated by (k = 0, ℓ = 1, m = 2), never exceeds 0.04 in magnitude, whereas the peak magnitude of triplet $p_T^2(t)\ p_T(t - T)$, corresponding to (k = 0, ℓ = 0, m = 1), is about 0.17.

The superposition of $p_T(t)$ with all such pulse triplets (appropriately weighted by corresponding transmitted data values) forms what we have referred to as the "data-sequence-dependent" transmitter filter impulse response. Assuming an ideal passband channel characteristic (that is, $\overline{H}(j\omega) = 1$) and a half-Nyquist receiver filter (in conjunction with ideal coherent demodulation), the received triplet waveforms corresponding to those depicted in Figure 3-6a are shown in Figure 3-6b. First, the solid curve represents the "full-Nyquist" pulse shape corresponding to the transmitted half-Nyquist pulse, $p_T(t)$. The other three (nonsolid) curves of Figure 3-6b correspondingly show the effect that the ideal band-limited passband channel and half-Nyquist filtering (at the receiver) have on the transmitted triplets $p_T^3(t)$, $p_T^2(t)\ p_T(t - T)$ and $p_T(t)\ p_T(t - T)\ p_T(t - 2T)$. Similar results are presented in Figures 3-7a and 3-7b. Observe that all numerical results discussed thus far suggest that a symbol sequence of length 3 is adequate to accurately describe the data-sequence-dependent transmitter filter impulse response.

Results similar to those presented in Figures 3-6 and 3-7 (for the ideal channel case) have been attained subject to a dispersive (fading) passband channel.

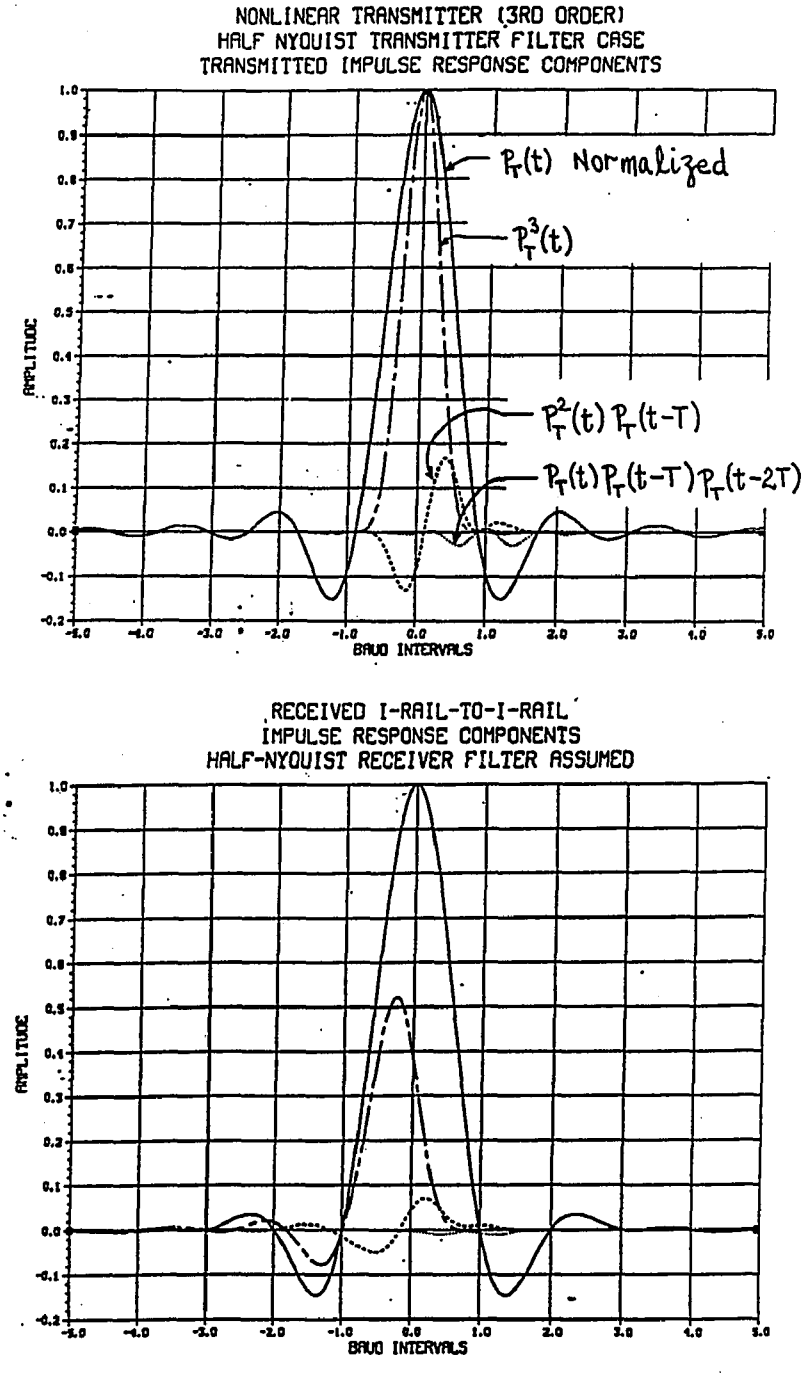

Figure 3-6. Transmitted and Received Impulse Response Components (Ideal Channel Case)

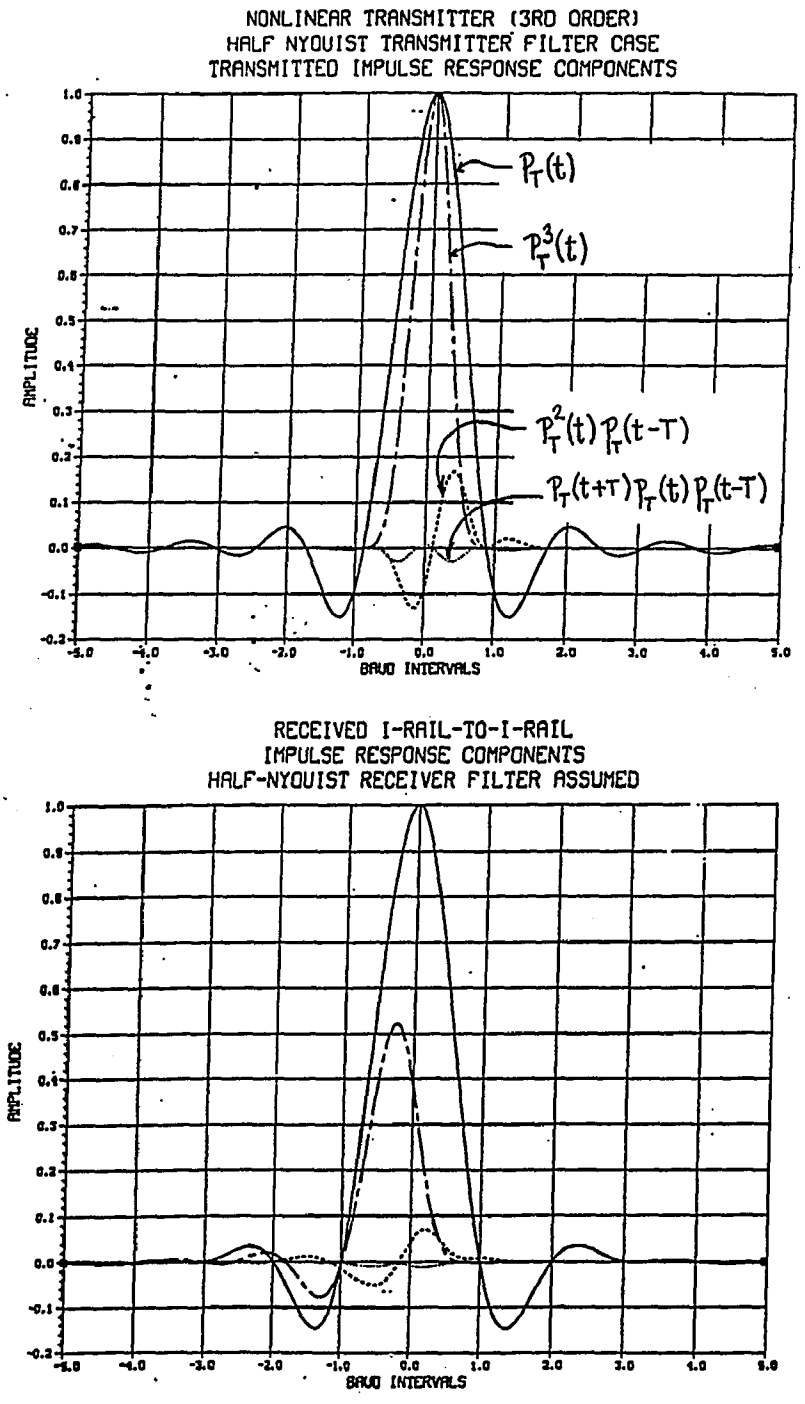

Figure 3-7. Transmitted and Received Impulse Response Components (Ideal Channel Case)

With a 20-dB selective fade (20 log $|1 - b|$ = -20 dB, with b = 0.9) assumed at the center of the channel, $\omega_f = \omega_c$ (with a = 1 and τ = 6.3 ns. Figures 3-8 and 3-9 illustrate the effect of dispersion on the transmitted pulse triplets and on $p_T(t)$. Interestingly enough, we observe that, even under largely dispersive channel conditions, the nonlinear ISI, caused by the received pulse triplets, extends roughly over the same number of baud intervals as it does subject to the ideal channel assumption. The same statement is clearly not true relative to the linear ISI components, as can be seen from the figures.

The overall system data-sequence-dependent impulse response, as defined by equation (3-24), may be broken up into two components, a first component that is completely data independent (as per the linear channel case) and a second component that is data-sequence-dependent as well as channel dependent (this second component is generated by the transmitter filter impulse response triplets discussed above). The data-sequence-dependent component of the overall system's impulse response generates nonlinear ISI, thus rendering the optimal receivers (which we have already discussed relative to the linear system) incapable of functioning optimally. Figures 3-10 and 3-11 illustrate two possible wave shapes that the data-sequence-dependent component of the overall system's impulse response may assume from one signaling interval to the next. These results have been generated assuming an ideal passband channel, with the following values characterizing the third order nonlinearity (see equation (3-15)): $g_1 = 1$, $g_2 = 0$, $g_3 = 0.05$, τ_1 = 15 ns and τ_3 = 25 ns. A 16-state QAM system utilizing full-Nyquist filtering at the transmitter with a roll-off factor of 0.45 and operating at 15 Mbaud was assumed. The results of Figures 3-10 and 3-11 point out how drastically the channel's impulse response can change from one signaling interval to the next. Since the classical adaptive

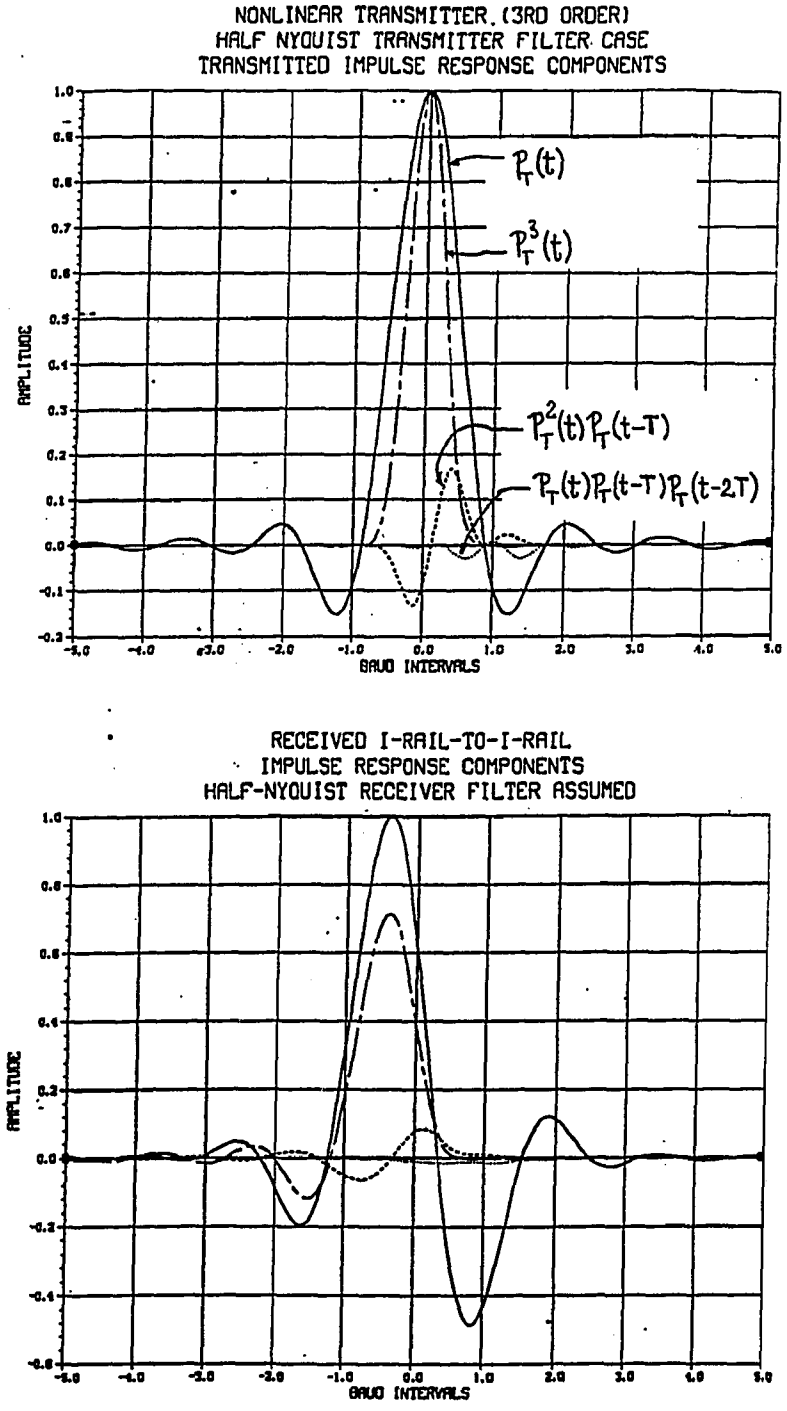

Figure 3-8. Transmitted and Received Impulse Response Components (Faded Channel Case; 20-dB Fade Notch at Channel Center)

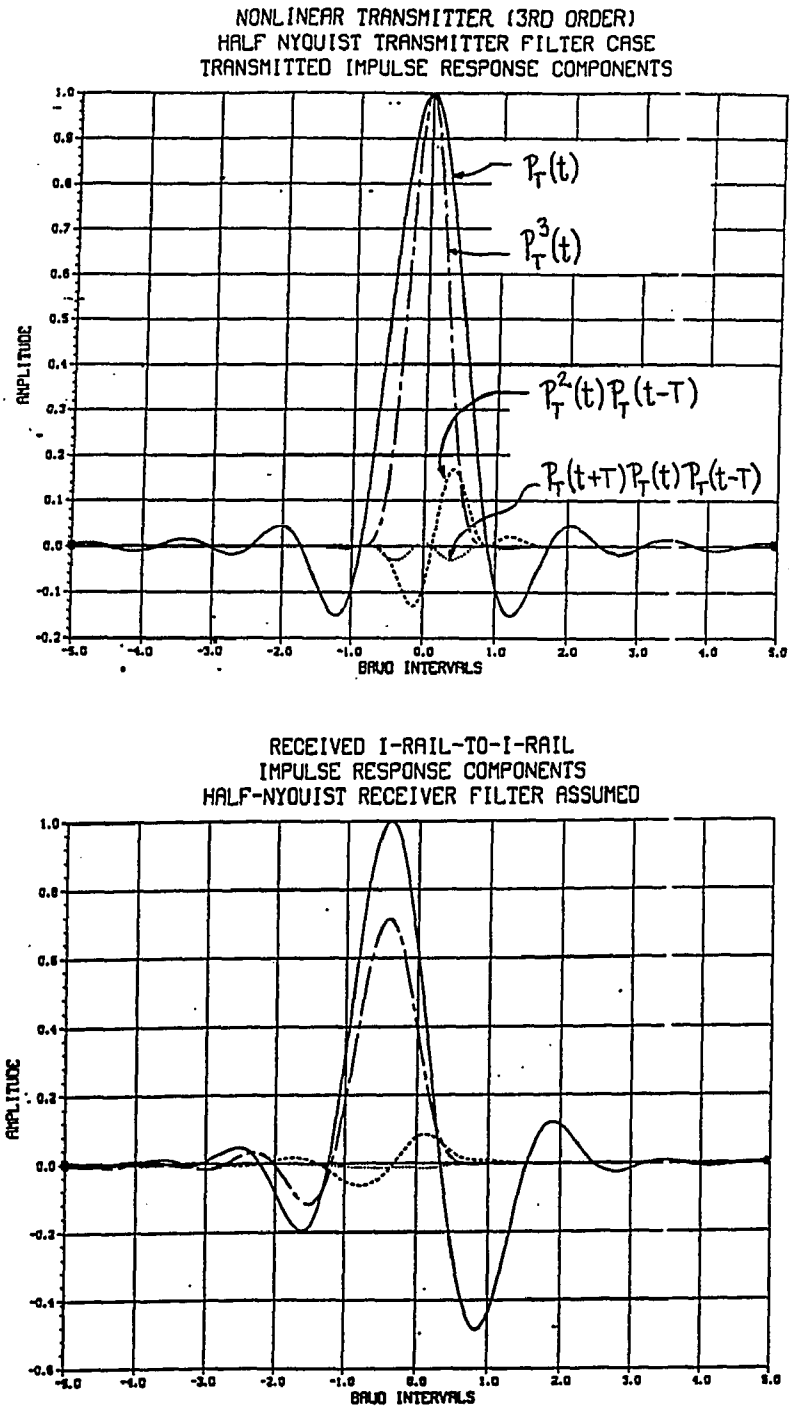

Figure 3-9. Transmitted and Received Impulse Response Components (Faded Channel Case; 20-dB Fade Notch at Channel Center)

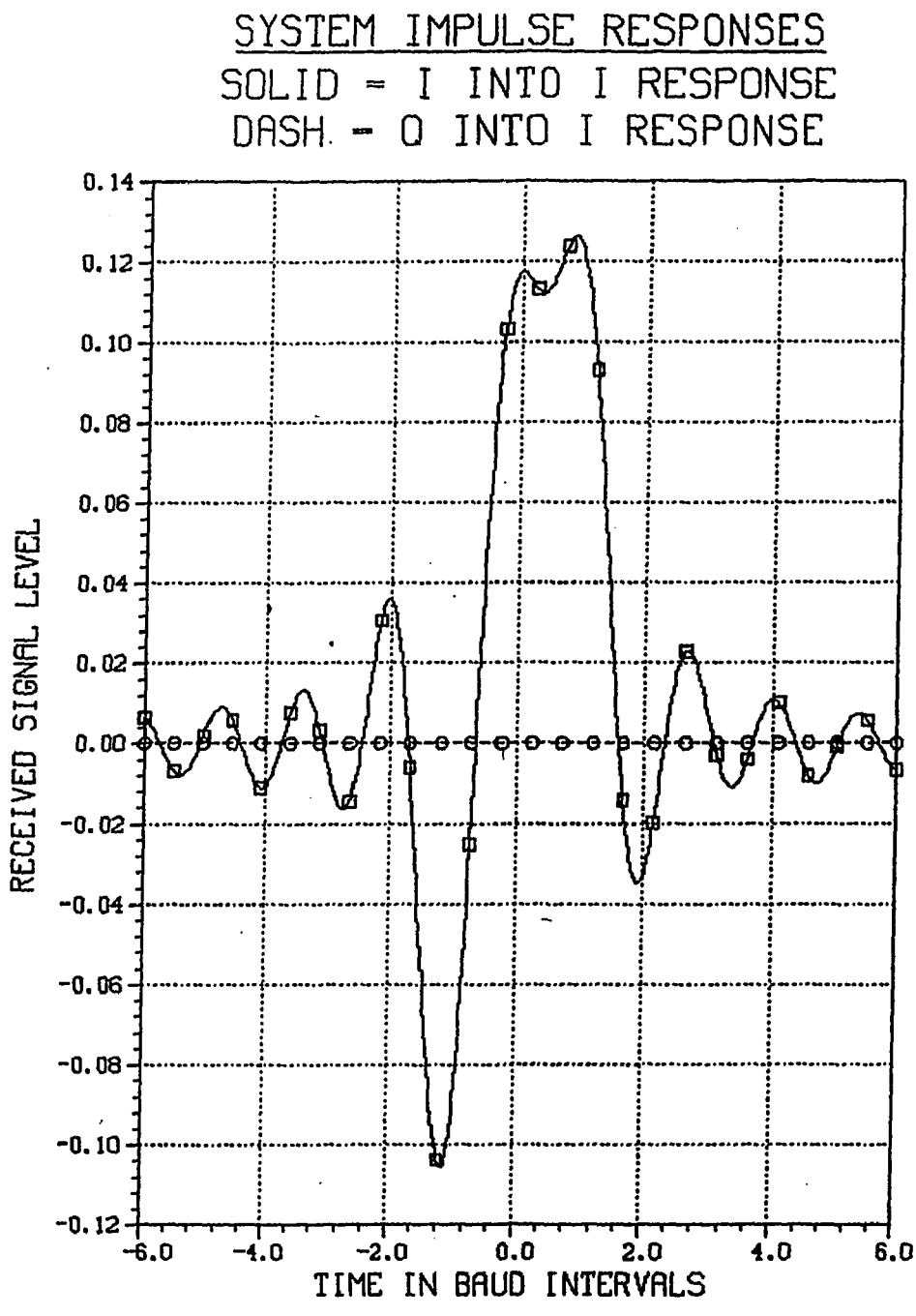

Figure 3-10. Composite Data-Sequence-Dependent Component of Overall System Impulse Response

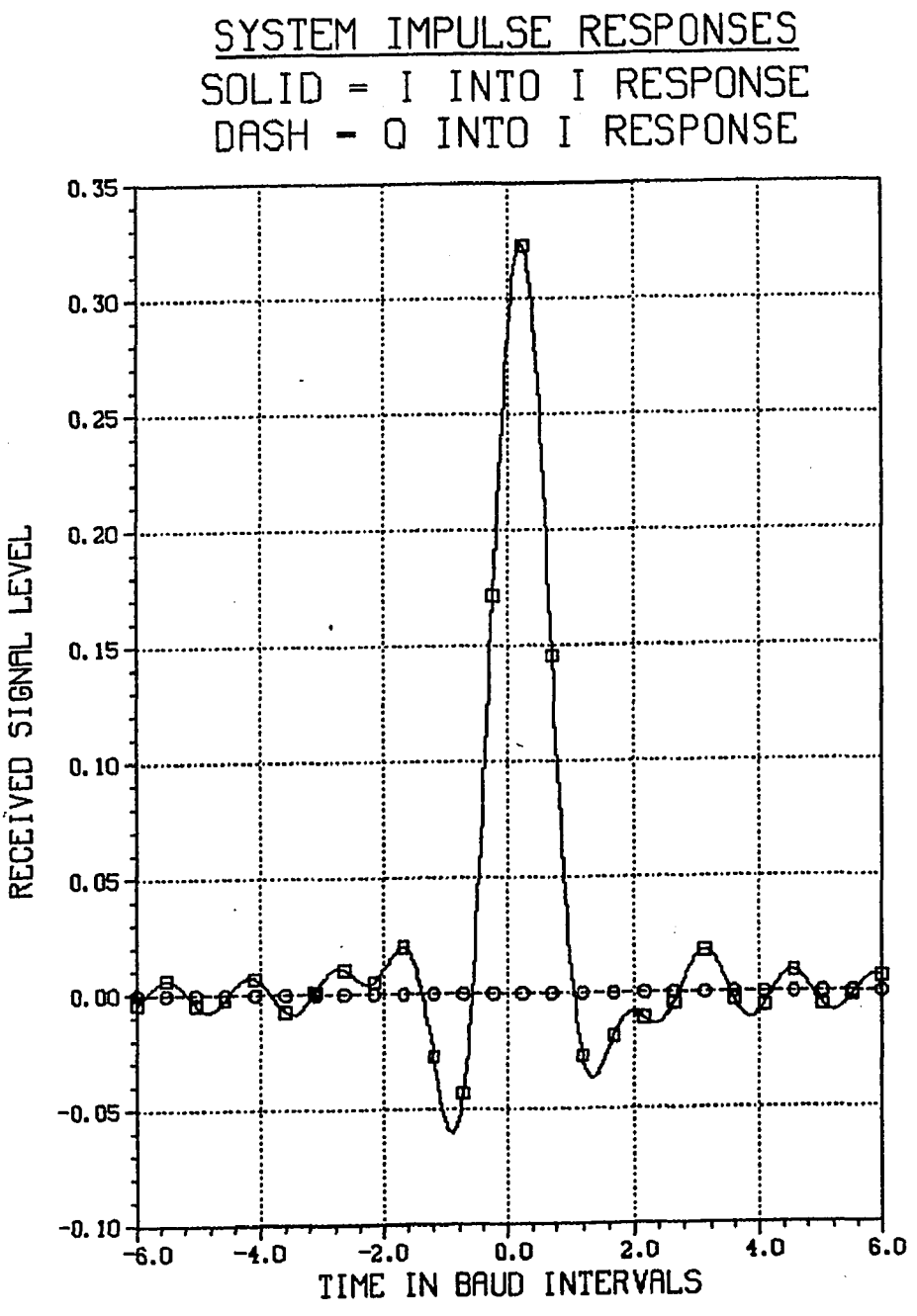

Figure 3-11. Composite Data-Sequence-Dependent Component of Overall System Impulse Response

receiver techniques (particularly the ones utilizing stochastic gradient type algorithms) rely on a quasistatic (with respect to the signaling interval) assumption regarding the channel, they cannot be expected to function properly here and they don't.

3.4 TRANSVERSAL FILTER ARCHITECTURES FOR LINEAR/NONLINEAR INTERSYMBOL INTERFERENCE MITIGATION

Having established a mathematical equivalence between the nonlinear QAM system and a linear one that involves a data-sequence-dependent channel (or a data-sequence-dependent transmitter filter), it becomes apparent that a receiver filter that is also data-sequence-dependent is required in order to "match" the received pulse shapes and also combat ISI. This realization leads us to propose the receiver structure of Figure 3-12, where, in response to an estimate of the finite length data sequence $\{\bar{I}_n\}_{n-M''}^{n+N''}$, a corresponding linear receiver filter with impulse response $\tilde{g}_{Rj}(t)$, $1 \leq j \leq K''$, is chosen. The output of the chosen receiver filter is observed at $t = nT$ to yield an optimal estimate of the transmitted data symbol $\bar{I}_n$. Having assumed that the data-sequence-dependent transmitter filter and the transmitter filter-channel combination depend on $M' + N' + 1$ and $M + N + 1$ length data sequences, respectively, we postulate that the receiver filter is determined by an $M'' + N'' + 1 \geq M + N + 1 \geq M' + N' + 1$ length data sequence. Accordingly, we may say that the overall impulse response of the system is determined by an $M'' + N'' + 1$ length data sequence.

A practical embodiment of the receiver structure proposed in Figure 3-12 is shown in Figure 3-13. A $(2L + 1)$ tap fractionally spaced transversal filter implementation is assumed, where the $(2L + 1)$ tap coefficients are allowed to be data-sequence-dependent. A finite length data sequence estimator (assumed here to be a

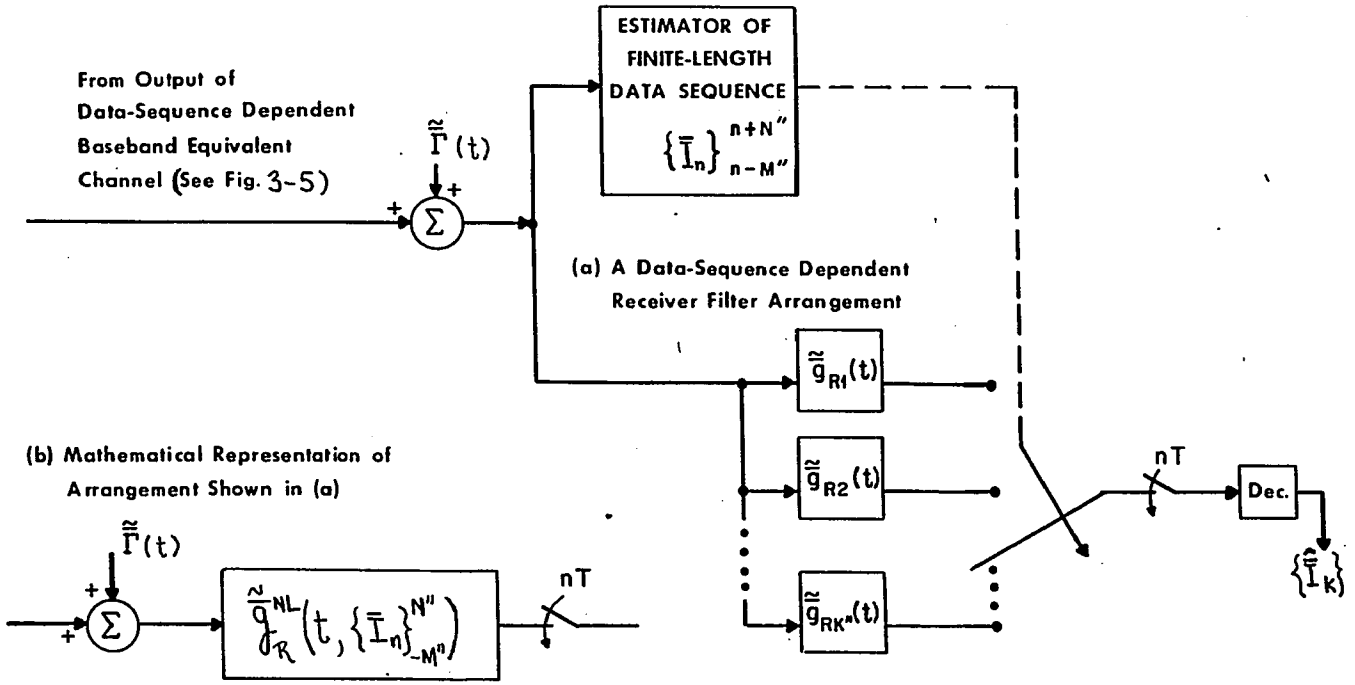

Figure 3-12. Data-Sequence-Dependent Receiver Filter for the Nonlinear QAM System

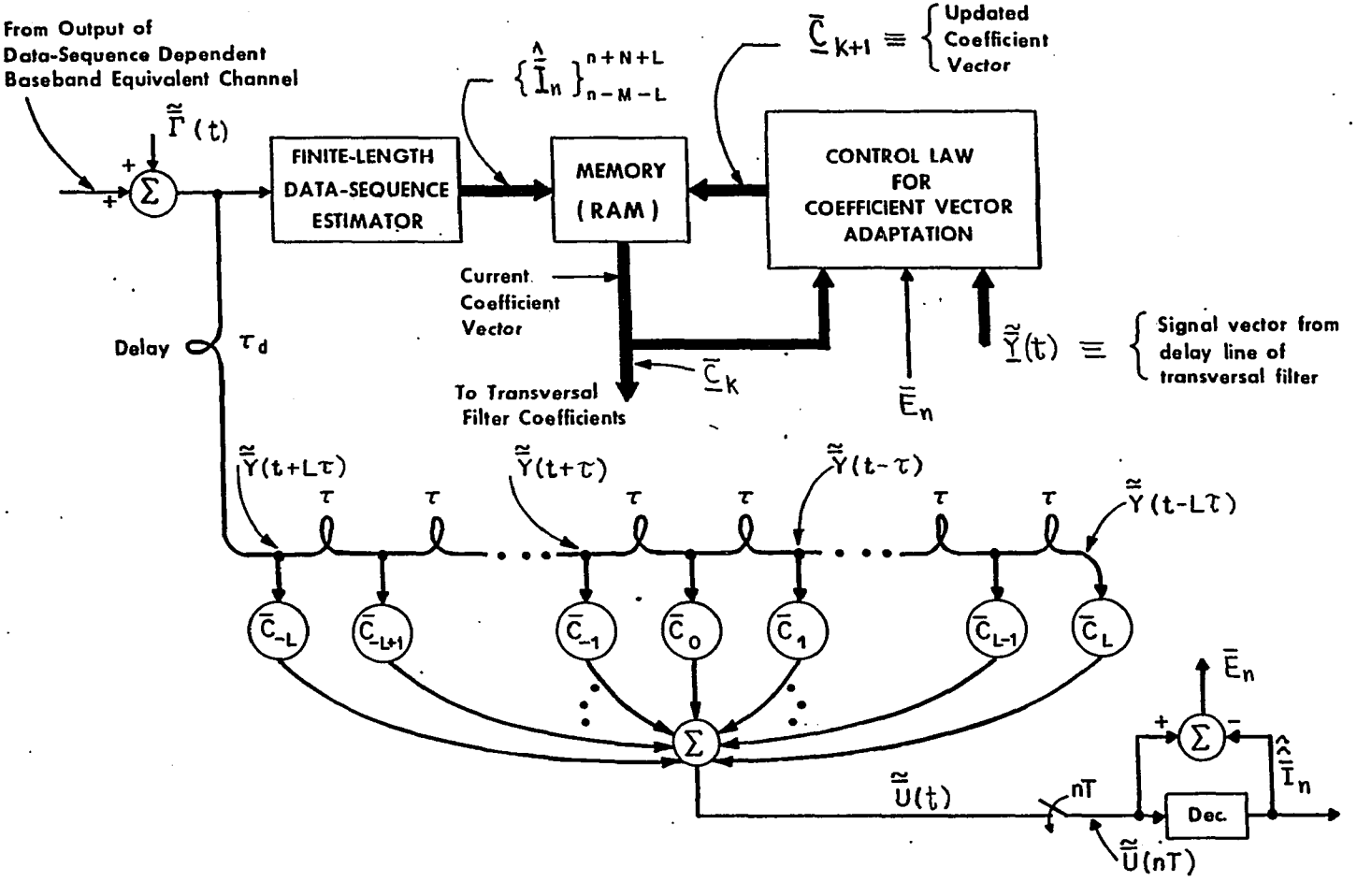

Figure 3-13. Transversal Equalizer Arrangement with Data-Sequence-Dependent Coefficient Set

conventional equalizer) generates the sequence estimate $\{\hat{\bar{I}}_n\}_{n-M-L}^{n+N+L}$. This estimate serves as an address to a Random Access Memory (RAM) device, which, in turn, provides an appropriate coefficient vector to the transversal filter. The value of this coefficient vector is distributed among the (2L + 1) tap coefficients and is subsequently updated in accordance with some control law, such as, for example, the stochastic gradient algorithm of equation (3-13). Then, the updated value of the coefficient vector is stored back in memory to be accessed the next time the same data sequence estimate is made.

The number of distinct data sequences that can be generated by an (M + N + 2L + 1)T long transmission interval grows very rapidly, however, with the length of the transmission interval. For example, assuming a 64-QAM system (where each member of the transmitted data sequence $\{\bar{I}_\ell\}$ can assume values from a 64-element set), even for (M + N + 2L + 1) = 5, corresponding to M = N = L = 1, we have $\approx 10^9$ distinct data sequences to contend with. Consequently, the receiver structure of Figure 3-13, although (in principle) feasible, may require a very large memory (RAM) for storing all coefficient vectors. The receiver structure of Figure 3-13, however, may be simplified (from a memory requirement standpoint), as is described next. In reference to Figure 3-14, a finite length data sequence estimator is, as before, used, but now to generate the estimated data sequence $\{\hat{\bar{I}}_n\}_{n-1-L}^{n+1+L}$ of length 2(L + 1) + 1. Then, subsequences of this estimated data sequence are generated, each of length 3 and overlapping with adjacent subsequences by one data element. It is these (2L + 1) overlapping subsequences that are used (as shown in Figure 3-14) as addresses to access, from (2L + 1) different RAMs, the (2L + 1) corresponding coefficients of the transversal filter. Following such a methodology, the i^{th} equalizer

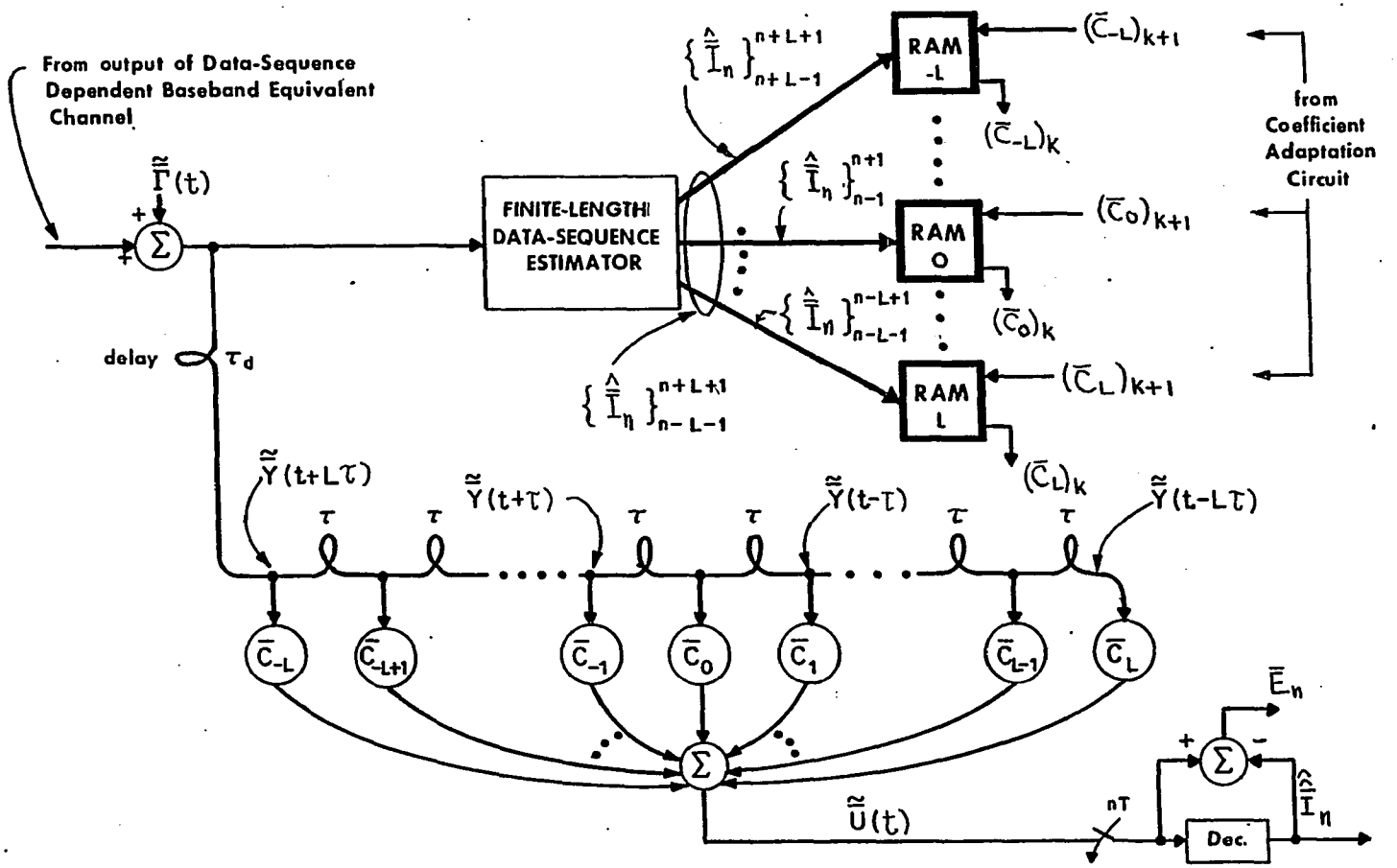

Figure 3-14. Alternate Transversal Equalizer Arrangement with Data-Sequence-Dependent Coefficient Set

coefficient, $-L \leq i \leq L$, depends on the i^{th} generated subsequence $\{\hat{\bar{I}}_n\}_{n-i-1}^{n-i+1}$ of length 3.

Since the subsequence $\{\hat{\bar{I}}_n\}_{n-i-1}^{n-i+1}$ is of length 3, even for 64 QAM, we have $64^3 = 262{,}144$, a number that is quite manageable with current RAM technology. Letting the i^{th} equalizer coefficient depend on the estimated data sequence $\{\hat{\bar{I}}_n\}_{n-i-1}^{n-i+1} \equiv \{\hat{\bar{I}}_{n-i-1}, \hat{\bar{I}}_{n-i}, \hat{\bar{I}}_{n-i+1}\}$ instead of letting the entire coefficient vector (and, hence, each coefficient) depend on the entire sequence $\{\hat{\bar{I}}_n\}_{n-M-L}^{n+N+L}$ may somewhat hinder the performance of the equalizer, depending on the channel's memory. For the type of channel considered here, however, the length of the data sequence that determines the nonlinear part of the impulse response of the baseband equivalent channel (or the transmitter filter characteristic) is substantially confined to a span of three baud intervals, as has already been demonstrated by the computer simulation results of the previous section.

The baseband equivalent nonlinear QAM system as depicted in Figure 3-5 has been simulated, in conjunction with the receiver architecture of Figure 3-13. In the simulation, 16-state QAM transmission was assumed, at a baud rate of 15 Mbaud, with full-Nyquist pulse shaping at the transmitter involving a roll-off factor of 0.45. The receiver was formed in terms of two nine-tap synchronously spaced transversal filters (one forming the finite length data sequence estimator and the second forming the transversal filter with data-sequence-dependent coefficients). The following approach was used to evaluate the "error correction" capability of the proposed receiver.

Given that the third order nonlinearity in the system and the fading channel parameters were defined, the adaptive receiver was initially allowed to converge and reach steady state using an a priori known transmitted data sequence (a training sequence). Once convergence had taken place, the transition from a priori known to random transmission of data commenced. Based on the estimates of the transmitted symbols made by the data sequence estimator, corresponding coefficient sets were accessed from memory and transferred to the transversal filter of Figure 3-13. The simulated algorithm involved an examination of five different coefficient sets per signaling interval: one coefficient set corresponding to the actual finite length data sequence estimated by the estimator, with the remaining four coefficient sets reflecting the four nearest neighbors of the data estimate in the middle of the finite length estimated data sequence. In response to these five coefficient sets, five decisions and five error quantities were derived. The one error quantity found smallest in magnitude was used as a pointer in outputting the corresponding decision.

Table 3-1 shows typical examples of symbol errors made by the sequence estimator that were corrected by the proposed receiver and associated control algorithm. In the first example shown in Table 3-1, QAM state 2 is transmitted (see Figure 3-15), but the estimator decides on QAM state 1. In response to this initial estimate (state 1) and the other $\pm$four symbol estimates surrounding the current estimate, five coefficient sets are accessed and used to yield the output error magnitudes of 0.68 ..., 0.86 ..., 0.92 ..., 0.08 ... and 1.13 .... The first error magnitude of 0.68 ... is generated by the coefficient set that is accessed in response to the estimate of "state 1", and the other four prior and four future estimates that surround it. The next four error magnitudes (0.86 ... through 1.13 ...) are

Table 3-1. Examples of Symbol Errors Corrected by the Receiver of Figure 3-13

```
TRANSMITTED STATE =  2     INITIAL ESTIMATE =  1
TRUE ERROR MAGNITUDE OF ESTIMATOR =   1.29563518
ERROR MAGNITUDE =     .68155310      J =  1
ERROR MAGNITUDE =     .86652108      J =  5
ERROR MAGNITUDE =     .92537704      J =  9
ERROR MAGNITUDE =     .08971078      J =  2
ERROR MAGNITUDE =    1.13657887      J =  3
TR I-RAIL =  1.0   RCV I-RAIL =  1.0
TR Q-RAIL =  3.0   RCV Q-RAIL =  3.0
```

QAM States

Transmitted symbol

Final Decision

```
TRANSMITTED STATE = 10     INITIAL ESTIMATE =  9
TRUE ERROR MAGNITUDE OF ESTIMATOR =   1.24334568
ERROR MAGNITUDE =     .55419788      J =  9
ERROR MAGNITUDE =     .88121349      J =  1
ERROR MAGNITUDE =     .98945793      J = 13
ERROR MAGNITUDE =     .22461724      J = 10
ERROR MAGNITUDE =    1.13907366      J = 11
TR I-RAIL = -1.0   RCV I-RAIL = -1.0
TR Q-RAIL =  3.0   RCV Q-RAIL =  3.0
```

```
TRANSMITTED STATE =  9     INITIAL ESTIMATE = 11
TRUE ERROR MAGNITUDE OF ESTIMATOR =   1.33788920
ERROR MAGNITUDE =     .43521941      J = 11
ERROR MAGNITUDE =     .80178276      J =  3
ERROR MAGNITUDE =     .95361105      J = 15
ERROR MAGNITUDE =     .24128944      J =  9
ERROR MAGNITUDE =     .82211778      J = 12
TR I-RAIL = -1.0   RCV I-RAIL = -1.0
TR Q-RAIL =  1.0   RCV Q-RAIL =  1.0
```

Nonliniarity: $g_1 = 1$, $g_2 = 0$, $g_3 = 0.03$; $\tau_1 = 15$ ns, $\tau_2 = 25$ ns

Channel: 14 dB fade at 5 MHz from carrier

$E_b/N_0 = 27$ dB

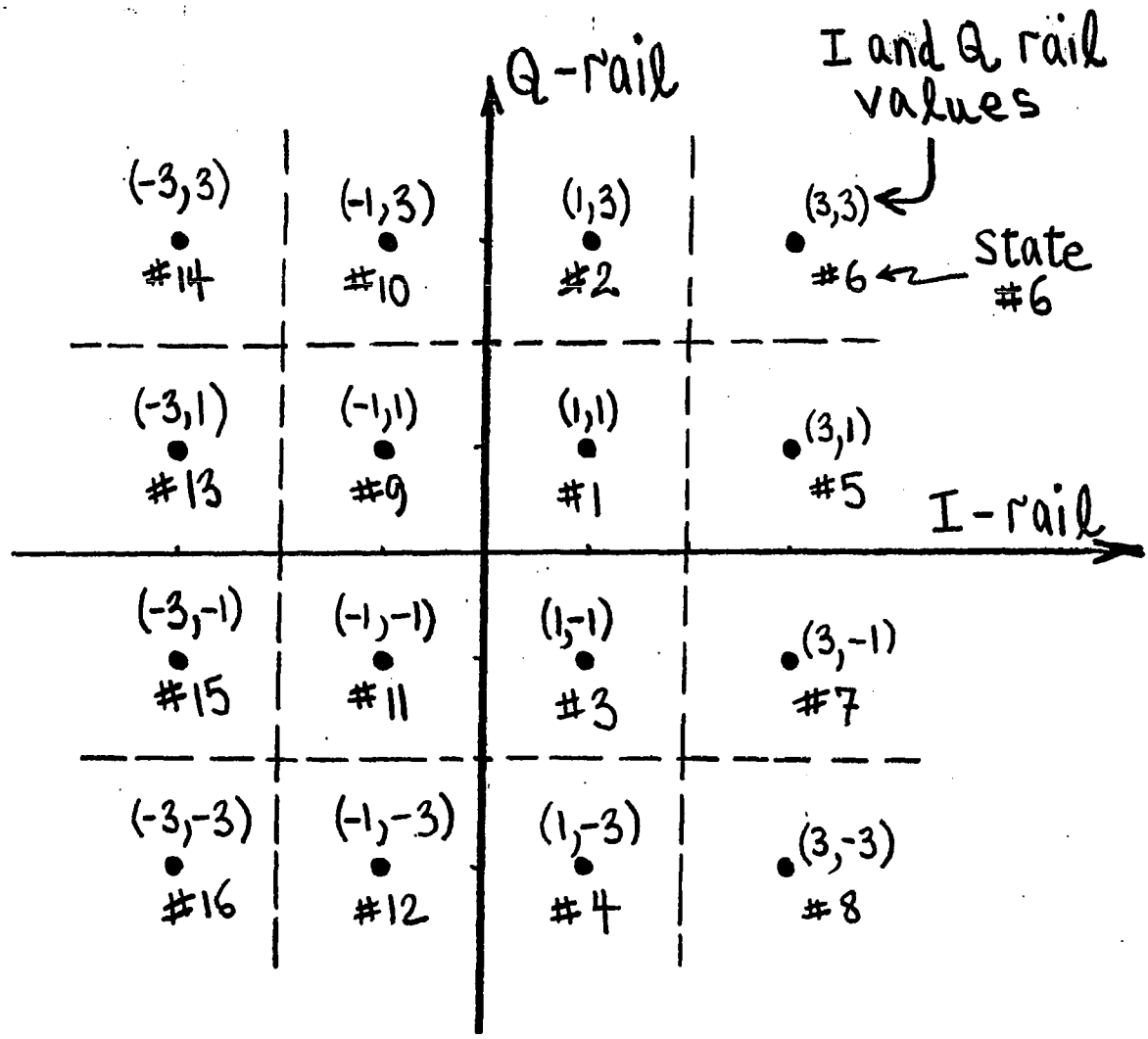

Figure 3-15. Definition of 16-State QAM Constellation Used in Simulations

generated by the coefficient sets that are accessed in response to the four nearest neighbors of "state 1", and the same four prior and four future symbols that surround it. The proposed receiver decides correctly on state 2, since the coefficient set corresponding to this choice (of center symbol estimate) yields the minimum error magnitude. In generating the above results, a nonlinearity with $g_1 = 1$ and $g_3 = 0.03$ has been assumed, in conjunction with an rf channel fade of 14 dB at a frequency of 5 MHz above the carrier frequency of 4 GHz. The unfaded E_b/N_0 was assumed to be 27 dB.

3.5 LINEAR/NONLINEAR INTERSYMBOL INTERFERENCE CANCELLATION

In this section, an adaptive distortion cancellation algorithm is described that can be used in the receiver of a digital communications system to cancel ISI without increasing the noise level already present in the received signal. The algorithm is similar to previously reported techniques[1, 10, 2] in that it uses tentative decisions to form noiseless ISI estimates. It is, however, substantially different in its decision making strategy and, as a consequence, is more resilient to tentative decision errors as compared to the previously reported methods. The new algorithm described herein is generic and can be used with a variety of canceller architectures in mitigating ISI caused by arbitrary combinations of linear and nonlinear system impairments. Computer simulation results illustrating the performance capabilities of the algorithm subject to a severely distorted channel are presented.

The basic structure shown in Figure 3-16 (and various variations thereof) has been used in previous investigations (as cited above) as the means of cancelling ISI introduced in the received data stream by linear and/or nonlinear system distortion.

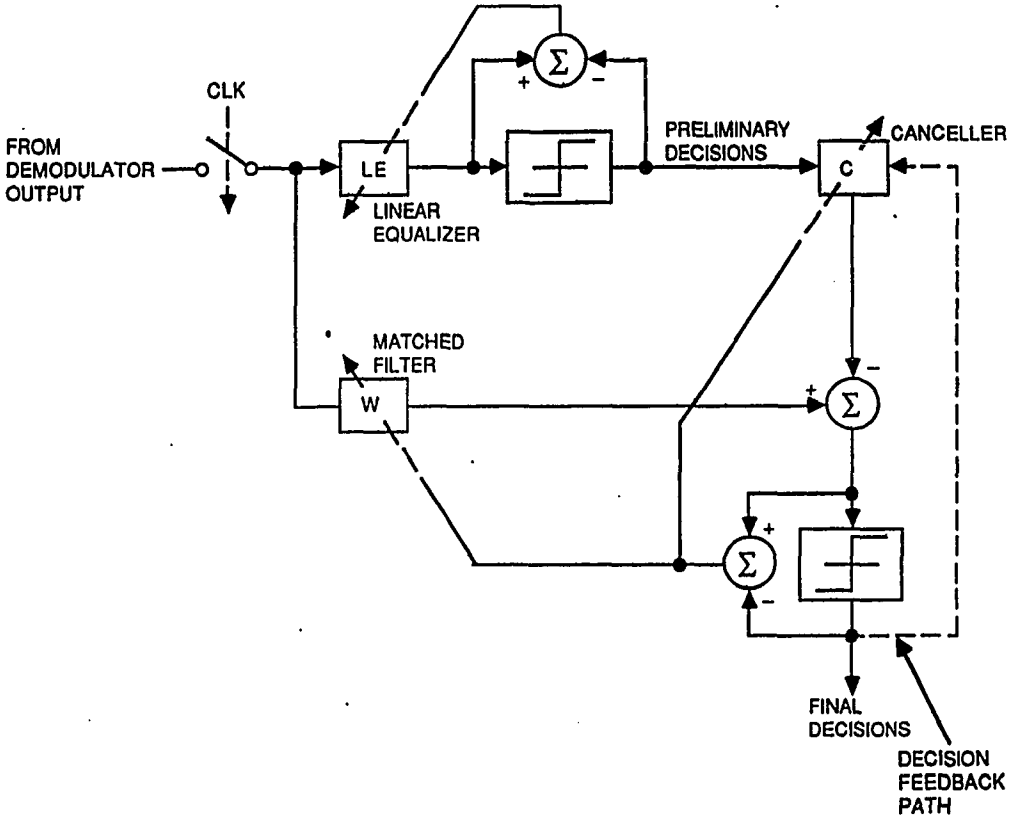

Figure 3-16. Conventional Canceller Architecture

As shown, a Linear Equalizer (LE), which may be configured as synchronously or fractionally spaced[11], is used to provide preliminary estimates of the transmitted data elements. These preliminary estimates serve as inputs to a canceller structure C, which, in response, adaptively forms an estimate of ISI and subtracts it from the output of the matched filter W. Based on the assumption that the final decisions will be better (more of them will be correct) than the preliminary estimates, it has been argued[2] that existing final decisions may be used by the canceller C, in lieu of the corresponding preliminary estimates, to improve performance. A fundamental problem associated with the above technique, however, stems from the way in which the preliminary estimates and final decisions are utilized by the canceller C in forming the ISI estimate. No provision is made to question the validity of the preliminary estimates (or that of the final decisions), which are being used by the canceller C in forming the current ISI estimate. That is, the preliminary estimates and final decisions are utilized blindly. When the channel is substantially noisy and/or highly dispersive, erroneous preliminary estimates and/or final decisions may adversely affect the canceller's ability to form the proper ISI estimates, thus leading to more errors in final decisions and, hence, to error propagation and deterioration in performance. This effect has long been recognized with regard to the operation of decision feedback equalizers.[12, 13, 14]

Below, an adaptive algorithm is described that substantially mitigates against this problem. The algorithm can be applied to the conventional decision feedback equalizer to improve its robustness properties (by substantially resolving the problem of error propagation), and can also be used within the framework of the linear and nonlinear cancellers of References 10 and 2, respectively, to achieve added performance gains there. Computer simulation results of a particular canceller

structure, governed by the new algorithm, are presented, subject to a combination of linear and nonlinear system impairments. A comparison of the new canceller algorithm performance against the conventional one is also made.

3.5.1 DISTORTION CANCELLATION PRELIMINARIES

Consider a digital communications system and let the n^{th} transmitted data element be denoted by A_n. Furthermore, assume that a new data element is transmitted once every T seconds and that each data element assumes values from an L element alphabet, i.e., $A_n \in \{a_1, a_2, \ldots, a_L\}$ for $\forall n$. In such a system, irrespective of the modulation format being used, the n^{th} receiver sample, following the demodulation process, may be represented by the following generic form:

$$R_n = \xi_n A_n + I_n + N_n, \tag{3-27}$$

where R_n represents the observable (the n^{th} receiver sample), N_n denotes Gaussian thermal noise, the value of I_n reflects the ISI that may have been generated by a variety of system imperfections, and ξ_n denotes frequency independent channel attenuation or gain. Clearly, in an ideal system, we would expect $I_n = 0$ and $\xi_n = 1$ for $\forall n$, and the variance of N_n to be as small as possible (approaching the matched filter limit).

In general, the value of ISI at the n^{th} sampling time, I_n, will depend on the overall system characteristic (i.e., impulse response) and on a finite length data sequence, $\{A_n\}_{-M}^{N}$, that includes A_n as one of its elements, and extends M symbol periods before A_n and N symbol periods after A_n. We define $\{A_n\}_{-M}^{N}$ as follows:

$$\{A_n\}_{-M}^{N} \equiv \{A_{n-M}, A_{n-M+1}, \ldots, A_{n-1}, A_n, A_{n+1}, \ldots, A_{n+N}\}, \qquad (3\text{-}28)$$

where the length of $\{A_n\}_{-M}^{N}$ is determined by the system's memory. Assuming a linear system, the dependency of I_n on the elements of $\{A_n\}_{-M}^{N}$ is a linear one. However, for the nonlinear system, this relationship becomes nonlinear. For a linear system, the attenuation/gain parameter, ξ_n, will only depend on the system characteristic, while, for a nonlinear system, ξ_n will also depend (in some nonlinear fashion) on the elements of $\{A_n\}_{-M}^{N}$.

In cancelling the system induced distortion, the objective is to add a noiseless term to the observable R_n such as to force $\xi_n A_n + I_n$ to become A_n without enhancing the variance of thermal noise already present in the received waveform. That is, we desire to find a cancellation parameter C such that

$$R_n + C = \xi_n A_n + I_n + N_n + C = A_n + N_n. \qquad (3\text{-}29)$$

The above equation implies that the distortion cancelling term, C, must assume the value of

$$C = A_n(1-\xi_n) - I_n. \qquad (3\text{-}30)$$

Distortion cancellation, as outlined above, has been investigated for linear and nonlinear systems using various canceller embodiments[1, 10, 2]. In each reported case, a preliminary estimate of the data sequence $\{A_n\}_{-M}^{N}$ is used to generate the value of C. This preliminary estimate of $\{A_n\}_{-M}^{N}$, however, is used blindly and is not questioned in any way regarding the possibility of containing erroneous

components. Clearly, since C is dependent on the system characteristic and on $\{A_n\}_{-M}^{N}$ (since, in general, ξ_n and I_n are), errors made in estimating $\{A_n\}_{-M}^{N}$ will result in a distortion cancellation term, say C', which will not, in general, be equal to C (the desired value). Therefore, given that errors have been made in estimating $\{A_n\}_{-M}^{N}$, we will, in general, have

$$C' = C + \varepsilon; \; |\varepsilon| \geq 0, \tag{3-31}$$

with the magnitude of ε depending, in general, on the number of errors made and on the system characteristic prevailing at the time the errors were made. Subject to the above hypothesis, the canceller's performance will degrade, since

$$R_n + C' = A_n + \varepsilon + N_n, \tag{3-32}$$

with ε denoting the residual distortion. That is,

$$\Pr\left[\begin{matrix}\text{Final}\\ \text{Decision}\\ \text{Error}\end{matrix}\,\middle|\, R_n + C'\right] \geq \Pr\left[\begin{matrix}\text{Final}\\ \text{Decision}\\ \text{Error}\end{matrix}\,\middle|\, R_n + C\right]; \; |\varepsilon| \geq 0. \tag{3-33}$$

3.5.2 A NEW CANCELLER ALGORITHM

Having established the above, we now extend the canceller's scope by providing for a mechanism via which checks on the original estimate of $\{A_n\}_{-M}^{N}$ may be performed. Given an original estimate of $\{A_n\}_{-M}^{N}$, a series of subsequent estimates may be made by modifying the elements of the original estimate of the sequence $\{A_n\}_{-M}^{N}$. Then, each new generated sequence of data elements may be used as an input to the canceller structure to yield a corresponding distortion cancellation quantity C. The value of each generated C may be added to the receiver observable, R_n, thus generating a sequence of values of $R_n + C$. The one element of the $R_n + C$ sequence that

is found closest (Euclidian-distance-wise) to an ideal element of the alphabet $\{a_1, a_2, \ldots, a_L\}$ may be used to determine the best canceller estimate of A_n. That is, the one element of the $R_n + C$ sequence found closest to an element of $\{a_1, a_2, \ldots, a_L\}$ will (most likely) correspond to a distortion cancellation coefficient C, which yields $R_n + C = A_n + N_n$. Note that, in generating the various different estimates of the sequence $\{A_n\}_{-M}^{N}$ (based on the original estimate of $\{A_n\}_{-M}^{N}$), only the nearest neighbors of the elements of $\{A_n\}_{-M}^{N}$ should be considered in order to maintain manageable the number of resulting possibilities that will have to be examined, particularly when dealing with large signal constellations (i.e., 64 QAM).

The flowchart of Figure 3-17 further illustrates the algorithm outlined above. This algorithm has been investigated via computer simulation (in conjunction with a particular canceller architecture) and the results are presented below, together with a more in-depth analysis of the required functions and hardware/software implications of the proposed distortion cancellation algorithm.

For the purpose of investigating the capabilities of the distortion cancellation algorithm outlined above, a FORTRAN computer program has been developed that simulates a 15-Mbaud, 16-state, QAM carrier system, where (for simplicity) we have assumed full-Nyquist pulse shaping at the transmitter, with a roll-off factor of 0.45. Following the QAM modulation stage, a third order nonlinearity is imposed on the QAM waveform in order to model the effects of a transmitter power amplifier. The input/output characteristic of this nonlinearity is specified as[4]

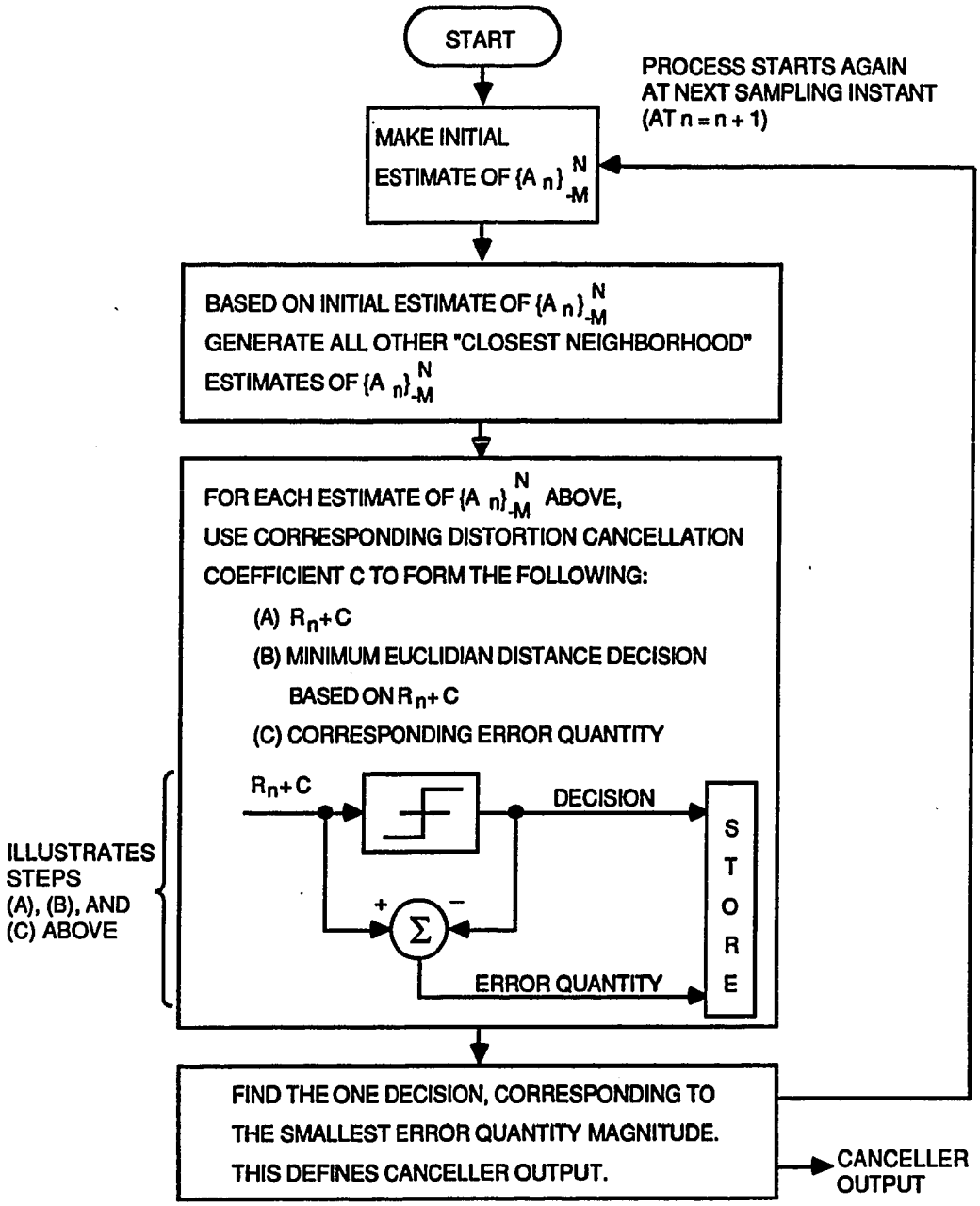

Figure 3-17. Outline of Distortion Cancellation Algorithm

$$v_o(t) = g_1 v_i(t-\tau_1) + g_2 v_i^2(t-\tau_2) + g_3 v_i^3(t-\tau_3), \qquad (3\text{-}34)$$

where $v_i(t)$ and $v_o(t)$ denote the input and output signals, respectively, and the coefficients g_2 and g_3 are set in accordance with the degree of nonlinear distortion that we wish to model in the system. The value of g_1 is always set to unity, with τ_1, τ_2, and τ_3 representing delays. Following the transmitter amplifier stage, a fading line-of-sight radio link (the channel) is simulated in accordance with the Rummler model[7] and propagation at an rf of 4 GHz is assumed. At the receiver baseband section, Gaussian thermal noise is added to the demodulated waveform, and the canceller embodiment of Figure 3-18 is used in conjunction with the control algorithm presented above and outlined in Figure 3-17. Preliminary estimates of the received data sequence are made using a conventional nine-tap synchronously spaced transversal filter whose coefficients are controlled by the classical "stochastic gradient" LMS algorithm. Initially, a training sequence (known to the receiver) is used to achieve rapid convergence in the transversal filter and canceller coefficients. Then, random (unknown to the receiver) data transmission commences.

As shown in Figure 3-18, the sampled demodulator output serves as the input to a nine-tap synchronously spaced transversal filter whose output is used to form a preliminary estimate of the finite length sequence $\{A_n\}_{-M}^{N}$. For the type of channel and system considered here, the extent of ISI has (to a large degree of accuracy) been found not to exceed $\pm$two baud intervals about any given signaling epoch. Thus, corresponding to the n^{th} signaling interval, the transmitted sequence

$$\{A_n\}_{-2}^{2} = \{A_{n-2}, A_{n-1}, A_n, A_{n+1}, A_{n+2}\}, \qquad (3\text{-}35)$$

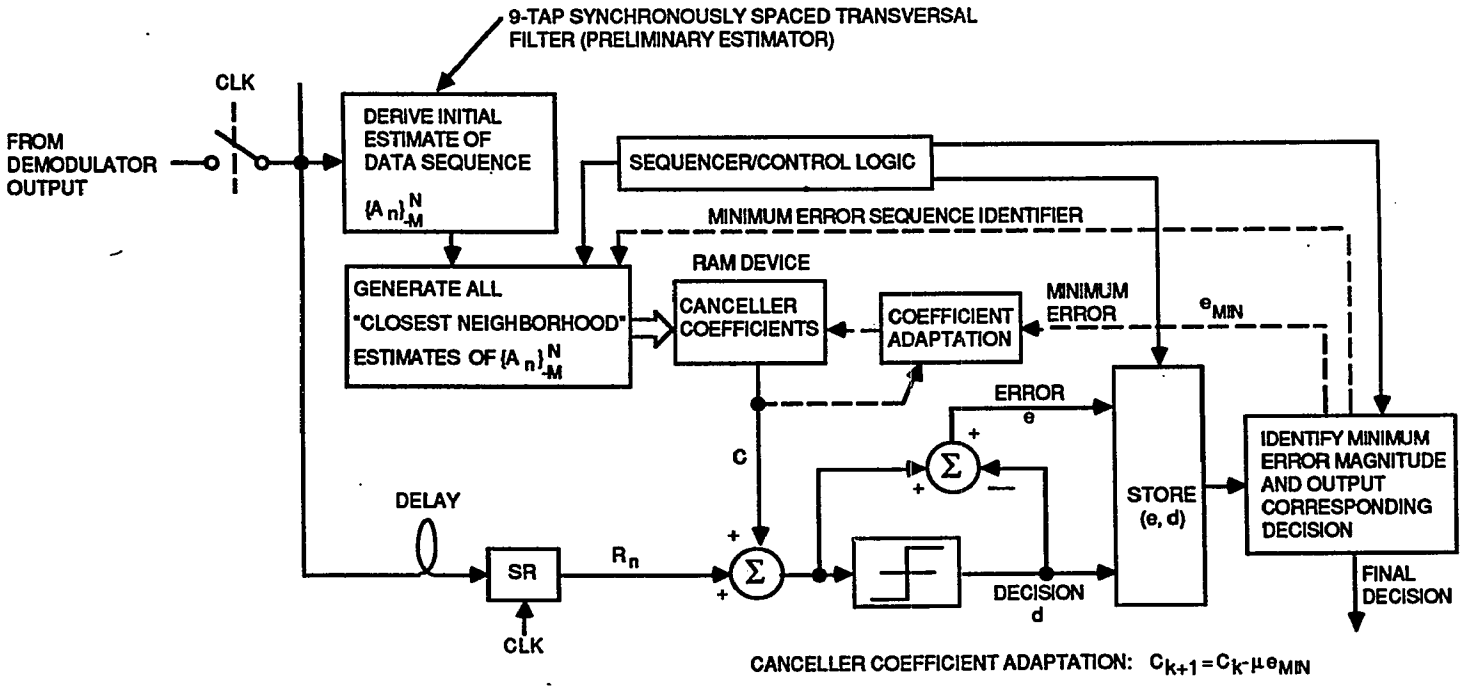

Figure 3-18. Simulated Canceller Architecture and Algorithm

in conjunction with the channel characteristic, defines the ISI that exists within the corresponding receiver observation. As a consequence, in this simulation we have used the transversal filter in providing a preliminary estimate of $\{A_n\}_{-2}^{2}$, a sequence of length 5. The preliminary estimate of $\{A_n\}_{-2}^{2}$ is then used to define a "nearest neighborhood" region that involves, at most, $5^5 = 3125$ distinct possibilities for the sequence $\{A_n\}_{-2}^{2}$. This is true since, for 16-QAM signaling, a given constellation point has, at most, four nearest neighbors (diagonally adjacent points excluded). In the interest of minimizing computation, however, and in light of the fact that the distortion is strongly dependent on the A_{n-1}, A_n, A_{n+1} elements, with weak dependency on the elements A_{n-2} and A_{n+2}, the simulated algorithm has been restricted to consider only a subset of all nearest neighbors of the original estimate of $\{A_n\}_{-2}^{2}$. That is, we only consider all nearest neighbors of $\{A_n\}_{-1}^{1}$ and take $A_{n\pm2}$ as originally estimated by the transversal filter. Consequently, at each receiver sampling epoch, an estimate of $\{A_n\}_{-2}^{2}$ is made by the transversal filter and is then used to generate only $5^3 = 125$ nearest neighbors to the original sequence estimate. Then, these 5^3 distinct sequence possibilities are used sequentially to access from a RAM device corresponding distortion cancellation coefficients. As shown in Figure 3-18, each distortion cancellation coefficient, C, which is fetched from memory, is added to the observable R_n to yield a decision d and a corresponding error quantity, e. The 5^3 (e, d) twoples thus created are stored in temporary memory and, at the end of the baud interval, the one associated with a minimum error magnitude is identified. The identified "minimum error" twople defines the system output in terms of a final decision on A_n. Furthermore, the identified minimum error twople serves as an index in identifying the particular sequence estimate and, hence, distortion cancellation coefficient that has given rise to it. That distortion

cancellation coefficient (resulting in the minimum error twople) is updated in accordance with

$$C_{k+1} = C_k - \mu e_{MIN}, \tag{3-36}$$

where μ is the step size and e_{MIN} denotes the minimum error. After adaptation, the coefficient is stored back in its corresponding memory location.

A few words are in order now regarding the size requirements of the RAM device, which contains the distortion cancellation values. For the channel and system that we have studied, a sequence of length 5 is sufficient to define the distortion present at any one receiver sampling instant. Hence, in general, there will be $16^5 = 1{,}048{,}576$ distinct distortion possibilities. At first glance, therefore, it appears that there must be 16^5 distinct memory locations within the RAM device to accommodate, in general, the 16^5 distinct distortion possibilities. Some thought, however, reveals that one-half of these distortion values will be the negatives of the remaining one-half, assuming a symmetrical QAM signal state constallation (for any arbitrary linear and/or nonlinear channel condition). Hence, only $16^5/2 = 524{,}288$ distinct memory locations need to be provided in conjunction with the capability of changing the distortion cancellation coefficient sign external to the RAM. If the above memory based canceller requirement is still prohibitive, one may substitute the RAM device and associated coefficient adaptation algorithm of Figure 3-18 with a hardware based canceller approach such as the one described in Reference 2. The overall scheme of Figure 3-18, however, remains invariant relative to the strategy utilized in arriving at the final decisions.

Relative to the purely memory based canceller approach, it is worth mentioning that a generally suboptimal (but one requiring substantially less memory capacity)

configuration may be pursued, whereby the single RAM device of Figure 3-18 is replaced by an arrangement such as that shown in Figure 3-19. In utilizing the arrangement of Figure 3-19, the assumption is that at any one signaling instant the overall system impulse response (for the general system where nonlinearities exist) is strongly dependent on the currently transmitted data element, A_n, and on its two adjacent neighbors, $A_{n\pm1}$. This, to a large extent, is true and has been verified for the subject system. Hence, still assuming an overall system memory of 5, five RAMs, each containing $16^3/2 = 2048$ memory locations, may be configured as shown in Figure 3-19 to "approximately" (subject to the assumptions) replace the function of the single $16^5/2$ size RAM. Before leaving the subject, we point out that, for a purely linear system, the size of each of the five RAMs in Figure 3-19 becomes 16/2 (or, in general, M/2, where M is the number of QAM constellation states).

3.5.3 NUMERICAL RESULTS

Turning our attention now to some numerical results, Figure 3-20 illustrates performance for a system impaired by linear and nonlinear distortion with the nonlinearity characteristics and channel state as defined in the figure. The top trace represents the transversal filter's (the estimator's) performance, with a script E placed over a point to indicate that an incorrect decision in received QAM constellation state has been made by the estimator. The bottom trace illustrates the performance of the new canceller algorithm described above using the embodiment of Figure 3-18. The canceller algorithm has corrected all incorrect decisions found in the preliminary estimates while maintaining relatively small error magnitudes at its output as compared to the transversal filter output error magnitudes. The middle (dotted) trace in the figure illustrates how the canceller embodiment of Figure 3-18 would have performed if it were controlled by a conventional algorithm where the

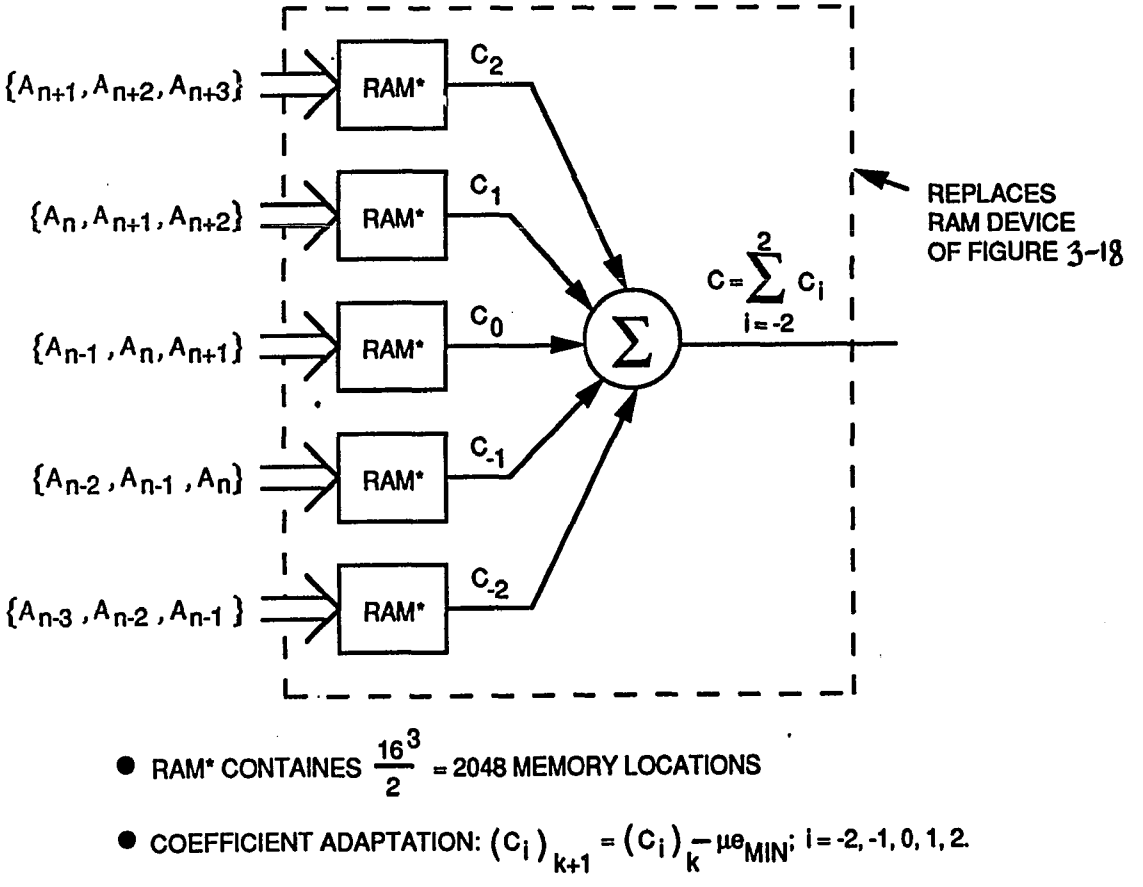

Figure 3-19. Reduced Complexity Memory Based Canceller Configuration

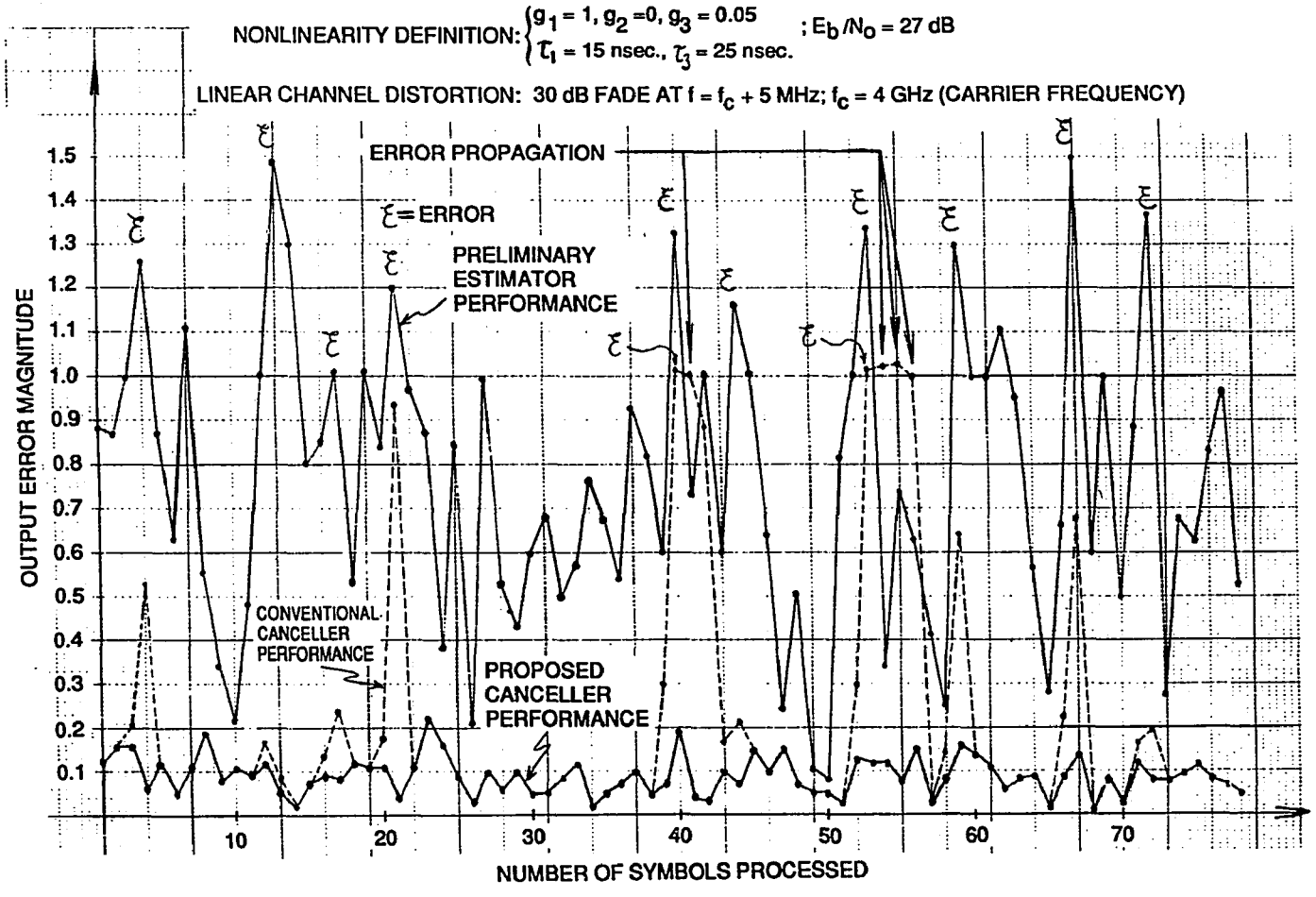

Figure 3-20. Performance of Canceller Arrangement of Figure 3-18

original set of preliminary estimates are used unequivocally without generating and examining "closest neighborhood" variations. In generating this middle trace of Figure 3-20, a decision feedback canceller mechanism has been postulated whereby the canceller's output is utilized in generating ISI estimates (see Figure 3-16). Because of the assumed decision feedback canceller approach, it is seen that error propagation does occur at two different instances where the conventional canceller algorithm makes errors.

The new distortion cancellation strategy presented above appears to represent an optimum technique designed to achieve isolated pulse, matched filter performance. Our simulation results confirm that there is improvement to be gained by using this technique over the conventional canceller strategies. The precise error rates achievable with the new approach, however, can only be estimated with extremely long and costly computer runs, which, up until now, have proved prohibitive. Actual experimentation may ultimately be the preferred approach toward a detailed characterization of the proposed signal processor.

REFERENCES

[1] D. D. Falconer, "Adaptive Equalization of Channel Nonlinearities in QAM Data Transmission Systems", Bell System Technical Journal, September 1978, Volume 57, No. 7

[2] E. Biglieri, A. Gersho, R. D. Gitlin and T. L. Lim, "Adaptive Cancellation of Nonlinear Intersymbol Interference for Voiceband Data Transmission", IEEE Journal on Selected Areas in Communications, September 1984, Volume SAC-2, No. 5

[3] A. A. M. Saleh and J. Salz, "Adaptive Linearization of Power Amplifiers in Digital Radio Systems", Bell System Technical Journal, April 1983, Volume 62, No. 4

[4] G. L. Heiter, "Characterization of Nonlinearities in Microwave Devices and Systems", IEEE Transactions on Microwave Theory and Techniques, December 1973, Volume MTT-21, No. 12

[5] R. W. Lucky, J. Salz and E. J. Weldon, Jr., "Principles of Data Communication", McGraw-Hill, 1968, Chapter 4

[6] M. Emshwiller, "Characterization of the Performance of PSK Digital Radio Transmission in the Presence of Multipath Fading", International Conference on Communications (ICC), 1978

[7] W. D. Rummler, "A New Selective Fading Model: Application to Propagation Data", Bell System Technical Journal, May to June 1979, Volume 58, No. 5, pages 1037 to 1071

[8] L. W. Pickering and J. K. DeRosa, "Refractive Multipath Model for Line-of-Sight Microwave Relay Links", IEEE Transactions on Communications, August 1979, Volume COM-27, No. 8, pages 1174 to 1182

[9] L. J. Greenstein and B. A. Czekaj, "A Polynomial Model for Multipath Fading Channel Responses", Bell System Technical Journal, September 1980, Volume 59, No. 7

[10] A. Gersho and T. L. Lim, "Adaptive Cancellation of Intersymbol Interference for Data Transmission", Bell System Technical Journal, November 1981, Volume 60, No. 9

[11] R. D. Gitlin and S. B. Weinstein, "Fractionally Spaced Equalization: An Improved Digital Transversal Equalizer", Bell System Technical Journal, February 1981, Volume 60, No. 2

[12] P. Monsen, "Theoretical and Measured Performance of a DFE Modem on a Fading Multipath Channel", IEEE Transactions on Communications, October 1977, Volume COM-25, No. 10

[13] J. J. O'Reilly and A. M. de Oliveira Duarte, "Error Propagation in Decision Feedback Receivers", IEE Proceedings, December 1985, Volume 132, Part F, No. 7

[14] S. U. H. Qureshi, "Adaptive Equalization", Proceedings of the IEEE, September 1985, Volume 73, No. 9

CHAPTER 4

EXPERIMENTAL RESULTS ON DIGITAL TRANSVERSAL FILTER IMPLEMENTATIONS

CHAPTER 4

EXPERIMENTAL RESULTS ON DIGITAL TRANSVERSAL FILTER IMPLEMENTATIONS

4.1 INTRODUCTION AND SUMMARY

As we have seen in Chapters 2 and 3, and Appendices C and D, adaptive optimal receivers rely heavily on transversal filter structures for their implementations. In this chapter, we examine, from an experimental standpoint, various key issues regarding the implementation (and, in particular, the digital implementation) of the basic optimal receiver building block - the transversal filter.

Below, the digital implementation of an adaptive baseband transversal filter (equalizer) is described in which the filter is configured and evaluated in both the fractionally and synchronously spaced modes of operation. The filter coefficients are updated using the "zero-forcing" version of the Least Mean-Squared (LMS) error algorithm* and the performance is evaluated in terms of Bit Error Rate (BER) measurements during fade-free and faded channel conditions. A four-level pseudorandom symbol sequence at a symbol rate of 5.5 Mbaud is used as the test signal.

In the synchronously spaced mode of operation, the sensitivity of the filter to the receiver timing phase error is investigated. The measurements show that, for a synchronously spaced equalizer, the BER curve degrades very rapidly for large timing phase errors (timing phase errors approaching 90°). This degradation can be explained in terms of the effects of spectrum aliasing that occur at the output of the receiver sampler (the Analog-to-Digital (A/D) converter, in this case) as a result

* The zero-forcing LMS algorithm represents a variation of the exact LMS algorithm, where only sign information is used in calculating the adaptation increments.

of a sampling rate that, for the synchronous tap spacing, is less than twice the bandwidth of the baseband signal. As a result of the spectrum aliasing, a spectrum null can occur at one-half the Nyquist frequency. This spectrum null must then be compensated (inverted) by the equalizer, resulting in a degradation of the received Signal-to-Noise Ratio (SNR). In contrast, the performance of the fractionally spaced equalizer is found only mildly dependent on timing phase errors. In principle, a fractionally spaced equalizer should be completely insensitive to timing phase errors[1-3]. Our experimental model showed slight variations in BER performance (about 0.5-dB shift of the BER curve) as the timing phase error was varied, starting from optimum, through a 360° excursion. This is attributed to nonideal low pass filtering of the baseband spectrum preceding the equalizer, as will be discussed in more detail in a later section. Furthermore, the equalizer in the fractionally spaced mode was shown capable of synthesizing the receiver matched filter adaptively for a 50-percent roll-off half-Nyquist transmit filter. This property of fractionally spaced equalizers is predicted from theoretical considerations of Appendix C. What is perhaps more important, however, from a practical standpoint, is the finding that only five fractionally spaced taps can synthesize the receiver matched filter with sufficient accuracy. This was verified by comparing the theoretical BER curve (assuming ideal transmitter and receiver 50-percent roll-off half-Nyquist filters) with measurements corresponding to the fractionally spaced equalizer preceded only by a simple low pass filter. The measured BER curve showed an average degradation of less than 0.4 dB from the theoretical one. To investigate the effect of adding more taps for the purpose of improving the receiver matched filter synthesis, two more fractionally spaced taps were added to the equalizer (giving a total of seven fractionally spaced taps) and the BER measurements were

repeated. No observable improvement was noticed in the BER curve over that obtained with only five fractionally spaced taps.

Section 4.2 describes the digital implementation of the transversal filter structure and the "zero-forcing" version of the LMS control algorithm. In Section 4.3, an analysis of the A/D converter sampling process is presented, showing how spectrum aliasing arises and how, as a result of the aliasing and a suboptimum sampling time, a null can occur in the sampled spectrum at a frequency equal to one-half the symbol rate. The analysis is substantiated by laboratory measurements that also illustrate the response of the synchronously spaced equalizer to the sampled spectrum containing a null. In Section 4.4, the BER measurements comparing the performance of the filter in the two modes of operation are presented.

4.2 CIRCUIT DESCRIPTION

Figure 4-1 shows a block diagram of the transversal equalizer circuit. The received analog symbol sequence, {x}, is sampled by an A/D converter that provides at its output an 8-bit representation of the sampled data. The sampling rate of the A/D converter was equal to the symbol rate for the synchronously spaced configuration and was made equal to twice the symbol rate for the fractionally spaced case. The elements of the delay line following the A/D converter were implemented by conventional 4-bit shift registers (two 4-bit shift registers were needed per delay element section) and clocked by the same clock signal strobing the A/D converter. Thus, it is the clock rate that determines the delay introduced by each shift register stage. This means that, in a digital implementation of a transversal equalizer, the mode of operation of the equalizer can be changed from synchronously spaced to fractionally spaced simply by doubling the clock rate of the system.

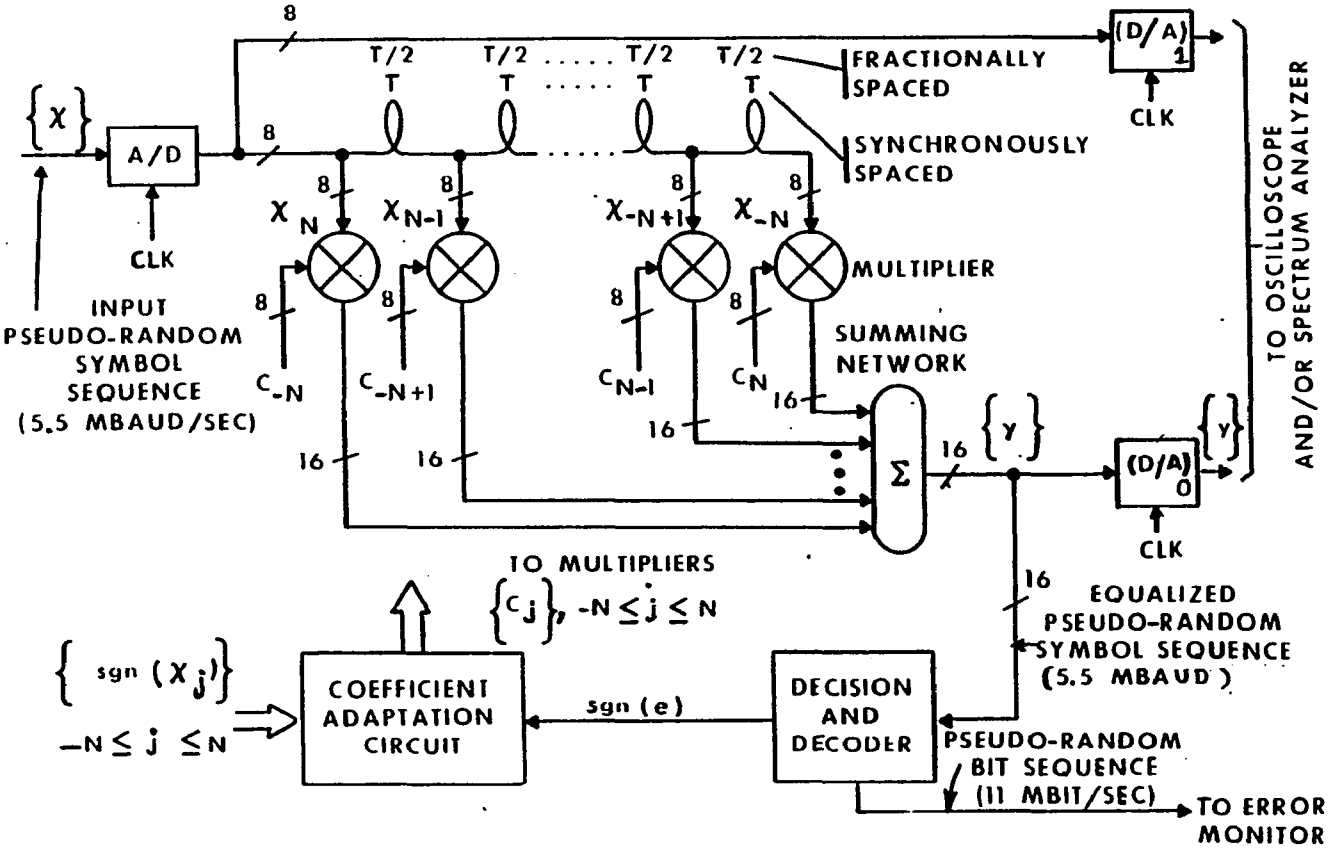

Figure 4-1. Block Diagram of Transversal Equalizer Circuit

Digital 8- by 8-bit multipliers were used for weighting the sampled data values $\{x_N, x_{N-1}, \ldots, x_0, \ldots, x_{-N+1}, x_{-N}\}$ residing on the delay line by the corresponding coefficient values $\{C_{-N}, C_{-N+1}, \ldots, C_0, \ldots, C_{N-1}, C_N\}$ generated by the coefficient adaptation circuit. The Motorola 8- by 8-bit multiplier (MC 10901), having a 20-ns typical multiply time, was used in this implementation. The result of each 8- by 8-bit multiplication is a 16-bit word that represents the product $C_j x_{-j}$ for $-N \leq j \leq N$. All elements of the product set, $\{C_{-N}x_N, C_{-N+1}x_{N-1}, \ldots, C_0x_0, \ldots, C_{N-1}x_{-N+1}, C_Nx_{-N}\}$, are added in the summing network as shown in Figure 4-1. The result of this summation is a 16-bit word representing the equalized symbol value.

The equalized symbol samples, $\{y\}$, are processed by a decision and decoder circuit that generates a digital error sequence, $\{e\}$, and also decodes the equalized symbol sequence, $\{y\}$, to its corresponding bit sequence for the purpose of bit error detection. The error, e, is generated by assigning to each equalized symbol value an ideal state (that state which is found closest to the equalized symbol value) and then taking the difference between the equalized symbol value and its assigned ideal state. Note that, in forming the "zero-forcing" version of the LMS algorithm, only the Most Significant Bit (MSB) of the error quantity, e, is required by the coefficient adaptation circuit.* In addition, the coefficient adaptation circuit requires the set of binary values, $\{\text{sgn}(x_N), \text{sgn}(x_{N-1}), \ldots, \text{sgn}(x_0), \ldots, \text{sgn}(x_{-N+1}), \text{sgn}(x_{-N})\}$, in order to form the gradients, $\Delta\ \text{sgn}(e)\ \text{sgn}(x_j)$, $-N \leq j \leq N$, and update the coefficient set according to the rule $C_j^{k+1} = C_j^k - \Delta\ \text{sgn}(e)\ \text{sgn}(x_{-j})$, $-N \leq j \leq N$. In implementing the algorithm as defined above, the increment quantity Δ was

* In the two's complement representation of binary numbers, the MSB of e is equivalent to the operation sgn(e).

made equal to one Least Significant Bit (LSB). That is, Δ = 0000 0001 in two's complement representation, assuming 8-bit wide coefficient values.

Since the equalizer is implemented entirely in the digital domain, meaning that all signals within the equalizer are represented by binary words, Digital-to-Analog (D/A) converters were attached at the output of the A/D and summing network (as shown in Figure 4-1) in order to display analog waveforms (eyes) corresponding to the digital signals at these points.

Implementing the transversal equalizer structure in the straightforward conventional fashion as depicted in Figure 4-1 (i.e., delay line, followed by multipliers, followed by the summing network), it was soon realized that the amount of hardware required to synthesize the various equalizer functions grows very rapidly as a function of the number of taps, especially in forming the summing network. This proved to be a serious limitation of this approach, not only from an economic standpoint, but also from a circuit reliability and management aspect. We originally intended to implement 11 taps, N = 5, so that we may have ample freedom to evaluate the performance of the equalizer as a function of a sufficiently large number of taps. To illustrate the circuit complexity required to digitally form the summing network of Figure 4-1 for 11 taps, consider Figure 4-2. Figure 4-2 shows a summing tree that accepts 11 16-bit multiplier outputs and sequentially sums them (two at a time) to form the final sum output. The dashed lines show how the circuit was subdivided and built onto six different boards. Each summing junction appearing in Figure 4-2 was implemented using Motorola ECL 10,000 series devices, as shown in Figure 4-3. The shift registers (the boxes labeled SR) appearing in Figure 4-2 between the various functional stages of the circuit were used for retiming of the digital signals to maintain alignment between them as they propagated through the summing tree. The

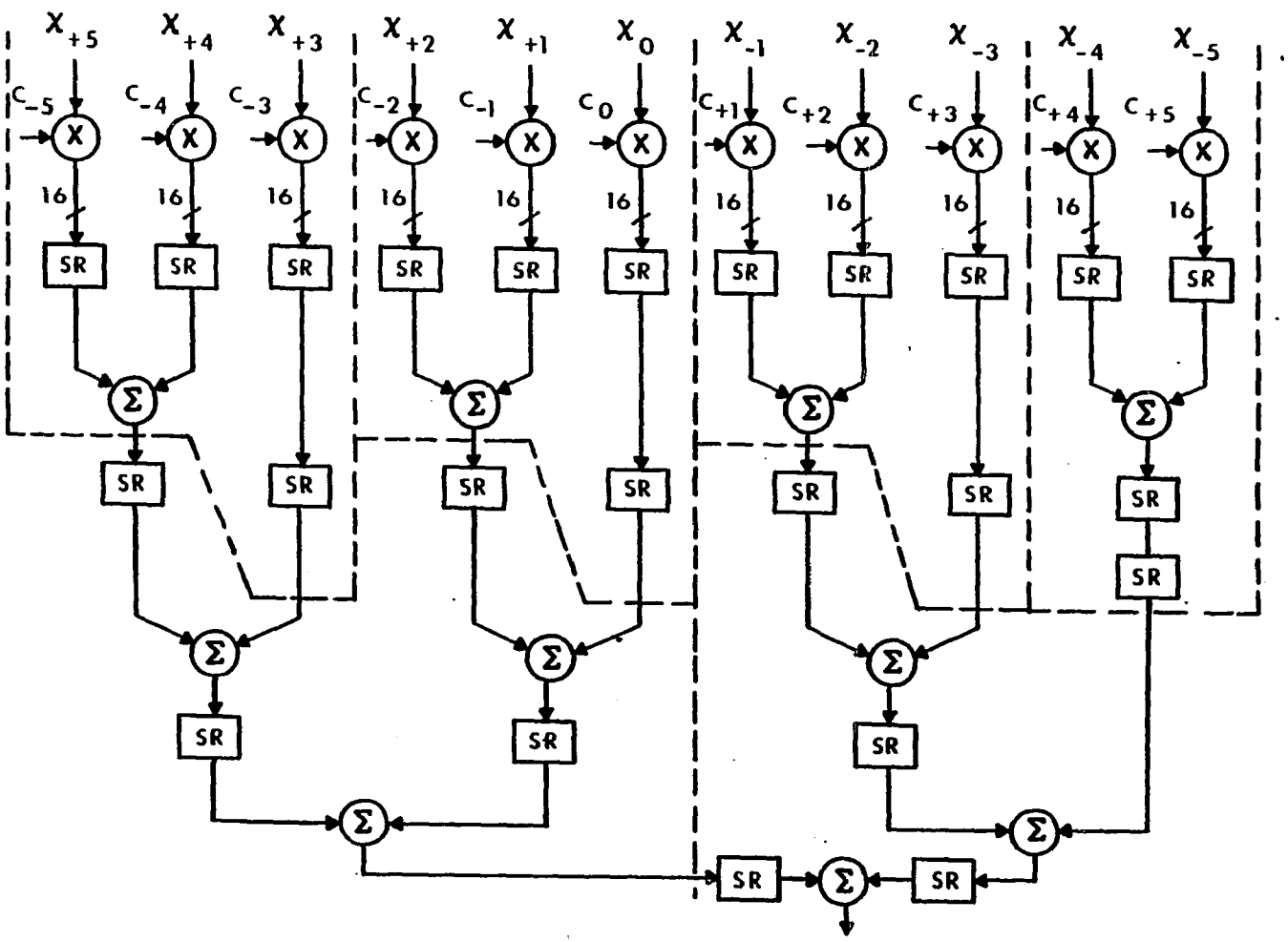

Figure 4-2. Implementation of Summing Network of Figure 4-1

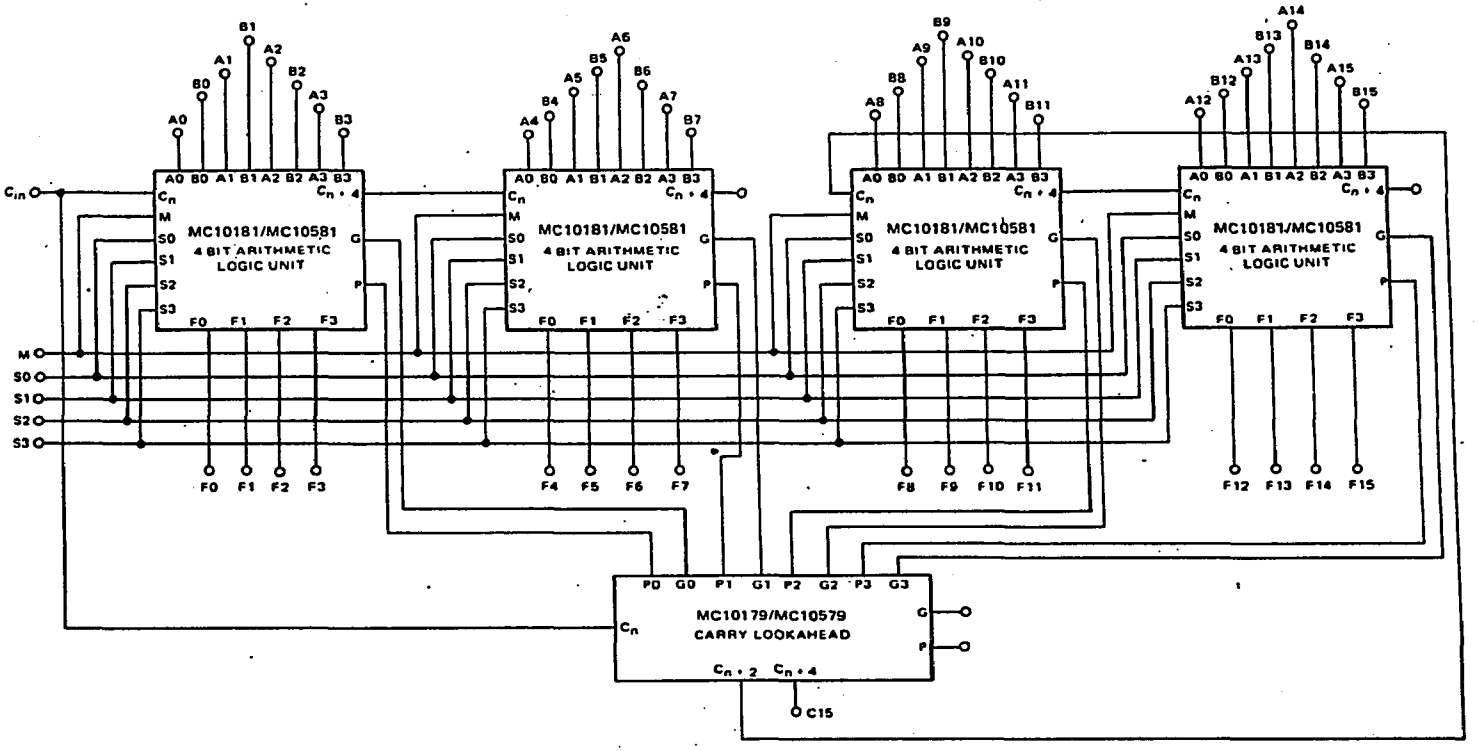

Figure 4-3. Summation of Two 16-Bit Words

sheer bulk and density of the digital circuit required to form the summing tree presented us with insurmountable clock and signal cross-coupling problems. We were able to maintain error-free operation with a maximum of seven consecutive taps (out of the possible 11) at a maximum equalizer clock frequency of 11 MHz. This meant that the equalizer could operate synchronously spaced at a maximum signal baud rate of 11 Mbaud or fractionally spaced at a maximum signal baud rate of 5.5 Mbaud. For consistency and ease of comparing the results, we chose to evaluate the equalizer's performance in both modes of operation at the lower baud rate of 5.5 Mbaud.

The approach of implementing the "zero-forcing" version of the LMS algorithm is illustrated by the simplified block diagram of Figure 4-4. The circuit shown is time-shared between all coefficient values, thus minimizing the amount of hardware required for the adaptation process. This was possible since distortions in the channel changed at a rate much lower than the baud rate. A detailed description of its operation follows.

Eleven exclusive-OR gates were used to equivalently form the products, $\mathrm{sng}(e)\ \mathrm{sng}(x_{-j})$, $-5 \leq j \leq 5$, by forming the operations, $\mathrm{MSB}(e) \oplus \mathrm{MSB}(x_{-j})$, $-5 \leq j \leq 5$, with $\oplus$ denoting the exclusive-OR operation. Then, the outputs of the 11 exclusive-OR gates were processed sequentially. A multiplexer was used, as shown in Figure 4-4, to accomplish this. The multiplexer output at any one time is a binary signal (logic level 0 or 1) that indicates whether the tap coefficient corresponding to the particular multiplexer output under consideration needs to be incremented or decremented by an amount Δ (an LSB). However, many indications of each multiplexer output signal need to be considered (averaged out or integrated) before a decision to update the corresponding tap coefficient is made. This minimizes random fluctuations of coefficients due to random noise effects. Accordingly, the output of the

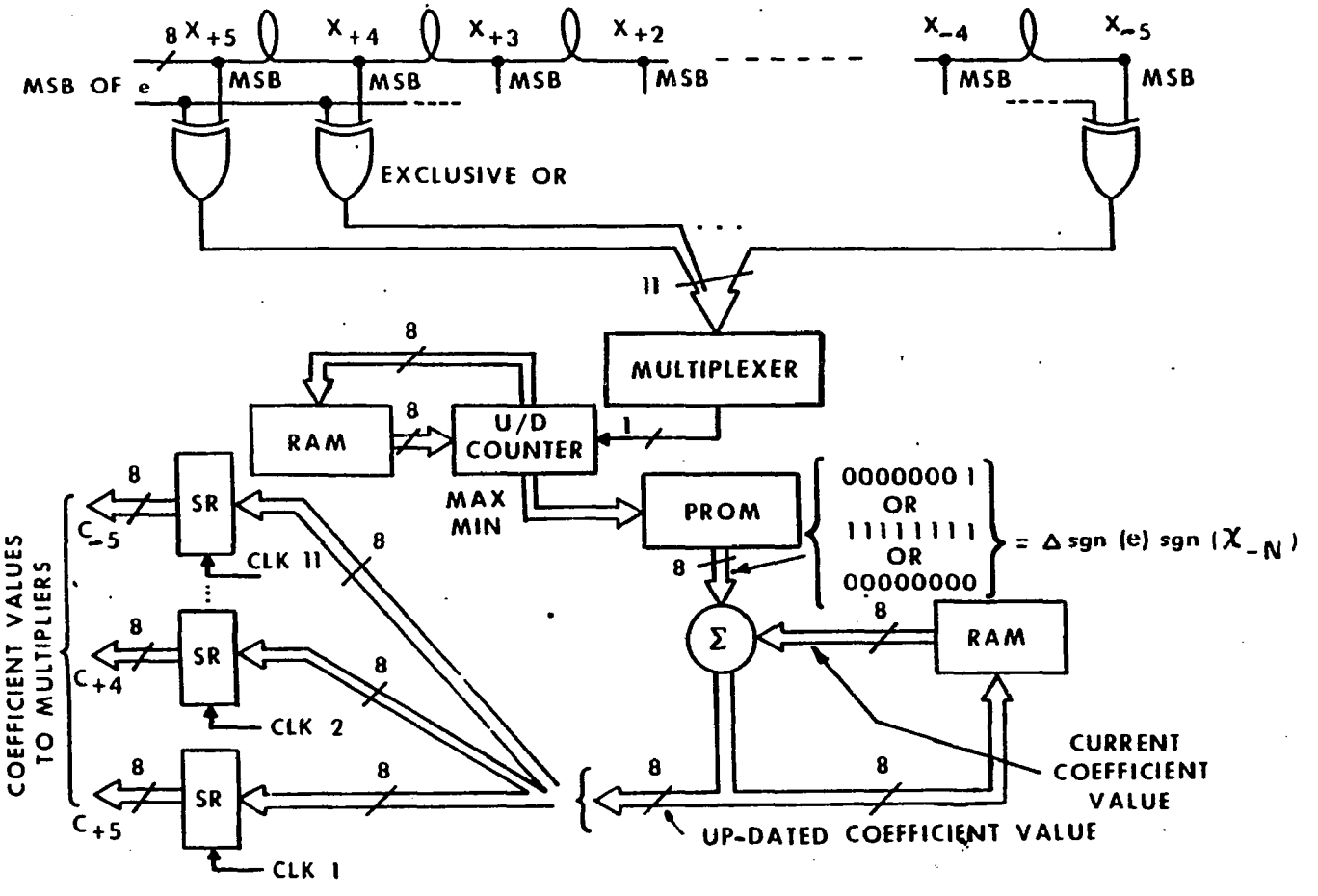

Figure 4-4. Simplified Block Diagram of Memory Based Time-Shared "Zero-Forcing" Version of the LMS Algorithm $C_N^{K+1} = C_N^K - \Delta \text{ sgn}(e) \text{ sgn}(x_{-N})$

multiplexer was fed into an 8-bit Up/Down (U/D) counter, which was initialized to reflect all past indications of the current multiplexer output signal. The initial value of the U/D counter was accessed from a Random Access Memory (RAM) shown attached to it. Depending on the logic state of the multiplexer output signal, the initial value of the U/D counter was incremented or decremented by an LSB. The result was stored back in RAM to be accessed again, as an initial value, at the next cycle when the same multiplexer output signal would again be under evaluation. If, at some point (as a result of an increment or decrement), the U/D counter value corresponding to some particular tap coefficient reached an overflow or underflow condition, then it was time to update, by an LSB, the corresponding coefficient value. That is, at this point, we updated the coefficient value corresponding to the multiplexer output signal, which, over many cycles, had provided enough correlated indications resulting in the overflow or underflow condition of the U/D counter. When an overflow or underflow condition occurred, the mid-range value of the U/D counter was stored back in RAM and the Max, Min output leads of the counter (corresponding to overflow and underflow, respectively) were activated (in the absence of an extreme condition of the U/D counter, the Max, Min outputs are both at logic level 0). The Max, Min outputs served as an address to a Programmable Read Only Memory (PROM) that provided, at its output, the appropriate adaptation word for the coefficient value under consideration. All current coefficient values were stored in a RAM, as shown in Figure 4-4. At the appropriate point in time, when the PROM had provided an output corresponding to the outcome of the gradient, Δ sgn(e) sgn(x_{-j}), coefficient C_j was accessed and updated by the gradient value. Subsequently, it was stored back in its corresponding memory location in RAM and was also simultaneously sent to 11 parallel shift register stages corresponding to the 11 coefficients. Only one of the 11 shift register stages was clocked, however (the one corresponding

to the tap whose coefficient value had just been updated). This transferred the updated coefficient value to the appropriate tap multiplier.

4.3 ANALYSIS OF A/D CONVERTER SAMPLING

The A/D converter preceding the delay line of the digitally implemented transversal equalizer (see Figure 4-1) serves as a sampler and quantizer for the system. That is, the A/D converter samples the received symbol sequence, {x}, at some predetermined rate and provides, at its output, a sequence of binary words (each word being 8 bits wide in our case). The binary word sequence represents, to within one-half of an LSB of accuracy, the values of an analog sample sequence that would be seen at the output of an analog sampling circuit if such a circuit were to replace the A/D converter. In this section, we analyze the sampling operation of the A/D converter and the resulting sampled waveforms as they relate to the performance of the transversal equalizer.

Consider Figure 4-5 and let m(t), an arbitrary function of time, be the input to the sampler (the A/D converter). The analog waveform, m(t), is to be sampled once every T seconds by strobing the sampler with the periodic impulse train, p(t), shown in Figure 4-5. A characteristic of the A/D converter sampling process is that the output word, corresponding to a particular sample of the input waveform, is held constant for the entire duration of a sampling interval. Thus, the analog waveform corresponding to the binary word samples appearing at the output of the A/D converter, given that m(t) is the input, would be a random staircase-type function such as that designated as $f_s(t)$ in Figure 4-5. It is the digital representation of $f_s(t)$ that the transversal equalizer operates on. By associating a spectrum with the input waveform, m(t), we will evaluate the spectrum of $f_s(t)$ in terms of the

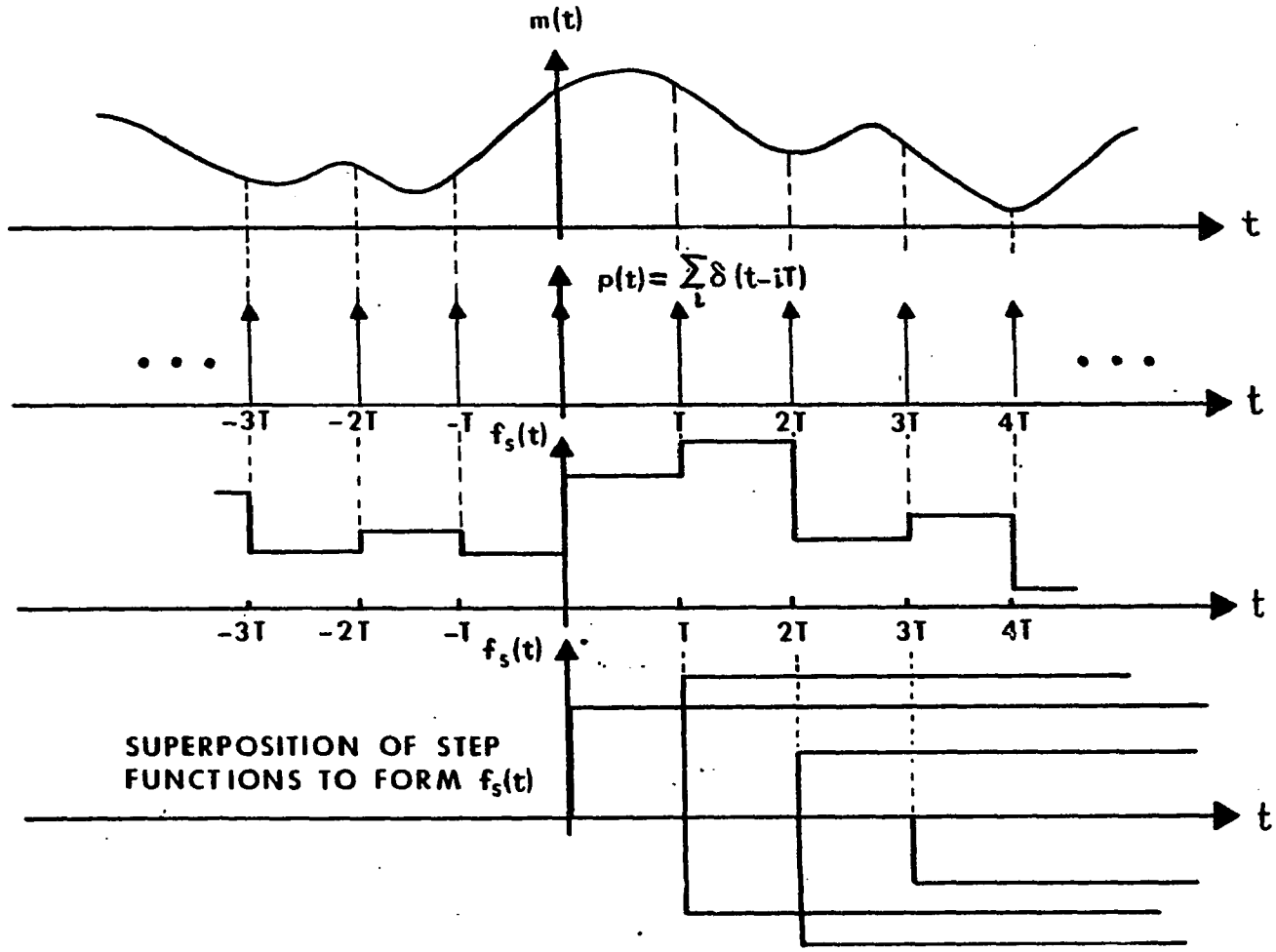

Figure 4-5. Waveforms Pertinent to A/D Sampling Analysis

spectrum of m(t). Then, we will show that linear distortion in the spectrum of $f_S(t)$ can arise as a consequence of a time displacement (a timing phase error) of the sampling impulse train, p(t), given that the spectral density of m(t) extends beyond 1/2T Hz (i.e., the case where m(t) represents a sequence of Nyquist pulses at a baud rate of 1/T and with a roll-off factor greater than zero). Since the transversal equalizer is operating on $f_S(t)$, it will naturally attempt to compensate for the linear distortion on $f_S(t)$ induced by the sampling process. This, we will show, can lead to a degradation of the received SNR, affecting the BER performance of the receiver at the equalizer output. Applying our analytical results to the fractionally spaced case (with a sampling rate of 2/T), we show that all sampling related problems are circumvented.

In reference to the bottom sketch of Figure 4-5, which illustrates the function $f_S(t)$ in terms of a superposition of weighted and delayed step functions, we can write

$$f_S(t) = \ldots -[m(-3T) - m(-2T)]u(t + 2T) - [m(-2T) - m(-T)]u(t + T) - [m(-T) - m(0)]u(t) - [m(0) - m(T)]u(t - T) - \ldots, \quad (4\text{-}1)$$

where m(kT) represents the value of m(t) at t = kT and u(t) denotes the unit step function defined as

$$u(t) \equiv \begin{cases} 1 \text{ for } t > 0. \\ 0 \text{ for } t \leq 0 \end{cases} \quad (4\text{-}2)$$

Note that $f_S(t)$ can be expressed succinctly as

$$f_S(t) = -\sum_i [m((i-1)T) - m(iT)]u(t-iT). \quad (4\text{-}3)$$

Differentiating $f_s(t)$ with respect to time, we find

$$\frac{df_s(t)}{dt} = -\sum_i [m((i-1)T) - m(iT)]\delta(t-iT), \tag{4-4}$$

where $\delta(t)$ denotes the impulse "function". Equation (4-4) can be rewritten as

$$\frac{df_s(t)}{dt} = -[m(t-T) - m(t)]p(t), \tag{4-5}$$

where

$$p(t) = \sum_i \delta(t-iT), \tag{4-6}$$

representing the impulse train shown in Figure 4-5. Expanding the periodic impulse train, $p(t)$, in terms of a Fourier series, we find

$$p(t) = \frac{1}{T}\sum_{k=-\infty}^{\infty} e^{jk(\frac{2\pi}{T})t}. \tag{4-7}$$

Substituting equation (4-7) into equation (4-5) yields

$$\frac{df_s(t)}{dt} = \frac{1}{T}[m(t) - m(t-T)]\sum_{k=-\infty}^{\infty} e^{jk(\frac{2\pi}{T})t}. \tag{4-8}$$

Letting $\overline{M}(j\omega)$ denote the Fourier transform of $m(t)$,

$$m(t) \leftrightarrow \overline{M}(j\omega), \tag{4-9}$$

it is easily seen that

$$\frac{1}{T}[m(t) - m(t-T)] \leftrightarrow j\omega \bar{M}(j\omega)\left[\frac{\sin(\frac{\omega T}{2})}{(\frac{\omega T}{2})}\right] e^{-j(\frac{\omega T}{2})}. \tag{4-10}$$

Using expressions (4-8) and (4-10), the Fourier transform of $\frac{df_s(t)}{dt}$ can be written as

$$F\left[\frac{df_s(t)}{dt}\right] = j\sum_{k=-\infty}^{\infty}(\omega - k\frac{2\pi}{T})\,\bar{M}(j\omega - jk\frac{2\pi}{T})$$

$$\cdot\left[\frac{\sin\left[(\omega - k\frac{2\pi}{T})\frac{T}{2}\right]}{(\omega - k\frac{2\pi}{T})\frac{T}{2}}\right] e^{-j(\omega - k\frac{2\pi}{T})\frac{T}{2}}, \tag{4-11}$$

where the operator F[ ] denotes the Fourier transformation.

We seek an expression for the Fourier transform of $f_s(t)$. Having the Fourier transform of $df_s(t)/dt$, we can use the relationship

$$F[f_s(t)] = \frac{1}{j\omega} F\left[\frac{df_s(t)}{dt}\right]. \tag{4-12}$$

Therefore, the Fourier transform of $f_s(t)$ can be written as

$$F[f_s(t)] = \sum_{k=-\infty}^{\infty}\left[\frac{\omega - k\frac{2\pi}{T}}{\omega}\right]\bar{M}(j\omega - jk\frac{2\pi}{T})$$

$$\cdot\left[\frac{\sin\left[(\omega - k\frac{2\pi}{T})\frac{T}{2}\right]}{(\omega - k\frac{2\pi}{T})\frac{T}{2}}\right] e^{-j(\omega - k\frac{2\pi}{T})\frac{T}{2}}. \tag{4-13}$$

Equation (4-13) is a superposition of an infinite number of spectral harmonics [of $\overline{M}(j\omega)$], with each harmonic in the summation representing a weighted and translated version of the input spectral density $\overline{M}(j\omega)$. Taking m(t) to be a sequence of Nyquist pulses transmitted at a baud rate of 1/T and with a roll-off factor $\alpha > 0$ (meaning that the spectrum of m(t) is nonzero for all $|\omega| \leq \frac{(1 + \alpha)\pi}{T}$), we see that $F[f_s(t)]$ contains aliased spectra of m(t). That is, the harmonics forming the infinite summation (4-13) overlap to some degree. To illustrate this further, the magnitudes of the fundamental and first harmonic (corresponding to k = 0 and k = 1, respectively) are plotted in Figure 4-6. The dashed curve labeled k = 0 represents the magnitude of the fundamental component of the summation. The dashed curve marked k = 1 represents the magnitude of the first harmonic of the summation, excluding the effect of the multiplicative factor $(\omega - k\frac{2\pi}{T})/\omega$. The dotted curve shown for k = 1 takes into account the effect of this factor. Therefore, the overall baseband spectrum over the Nyquist equivalent channel $(0 \leq |\omega| \leq \frac{\pi}{T})$ corresponds to the superposition of the dashed curve for k = 0 and the dotted curve for k = 1. Thus, it becomes apparent that the relative phase between overlapping spectral components of the fundamental and first harmonics of $F[f_s(t)]$ is of paramount importance over the frequency interval $\frac{(1 - \alpha)\pi}{T} \leq \omega \leq \frac{\pi}{T}$. In particular, note that complete cancellation between overlapping spectral components can occur at $\omega = \frac{\pi}{T}$ (at the half-Nyquist frequency, where the overlapping spectra are equal in amplitude) given a π-radian phase differential between them. It is easily seen from equation (4-13) that, for the assumed clock signal, $p(t) = \sum_i \delta(t - iT)$, the overlapping spectral components between the fundamental and first hamonics of $F[f_s(t)]$ add coherently for all frequencies in the interval $\frac{(1 - \alpha)\pi}{T} \leq \omega \leq \frac{(1 + \alpha)\pi}{T}$. This assumes a spectrum $\overline{M}(j\omega)$ of the form $\overline{M}(j\omega) = M_0(\omega)e^{j\phi(\omega)}$, where $\phi(\omega) = 0$ for $0 \leq \omega \leq$

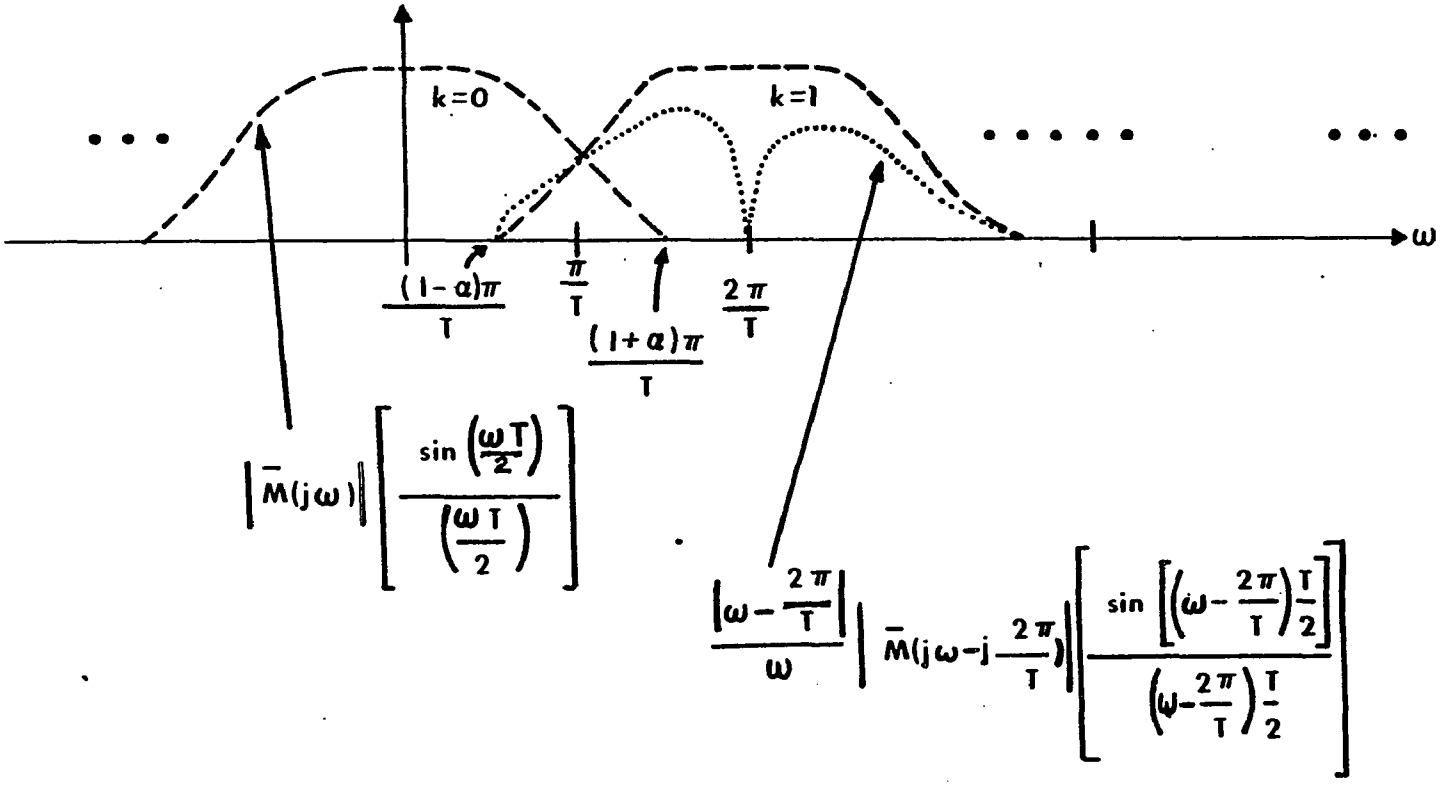

Figure 4-6. Superposition of Spectra at A/D Converter Output

$\frac{(1+\alpha)\pi}{T}$. However, if we assume a clock signal containing an arbitrary time shift τ, as expressed by $p(t) = \sum_i \delta(t - iT - \tau)$, we find

$$F[f_s(t)] = \sum_{k=-\infty}^{\infty} \left[\frac{\omega - k\frac{2\pi}{T}}{\omega} \right] \bar{M}(j\omega - jk\frac{2\pi}{T}) \cdot \left[\frac{\sin\left[(\omega - k\frac{2\pi}{T})\frac{T}{2} \right]}{(\omega - k\frac{2\pi}{T})\frac{T}{2}} \right] e^{-j(\omega - k\frac{2\pi}{T})\frac{T}{2}} e^{-jk(\frac{2\pi}{T})\tau}. \quad (4\text{-}14)$$

Having assumed an arbitrary timing offset, τ, we see that the fundamental component of $F[f_s(t)]$ is unaffected,

$$F[f_s(t)]_{k=0} = \bar{M}(j\omega) \left[\frac{\sin(\frac{\omega T}{2})}{(\frac{\omega T}{2})} \right] e^{-j(\frac{\omega T}{2})}, \quad (4\text{-}15)$$

but its first harmonic becomes

$$F[f_s(t)]_{k=1} = \left[\frac{\omega - \frac{2\pi}{T}}{\omega} \right] \bar{M}(j\omega - j\frac{2\pi}{T}) \cdot \left[\frac{\sin\left[(\omega - \frac{2\pi}{T})\frac{T}{2} \right]}{(\omega - \frac{2\pi}{T})\frac{T}{2}} \right] e^{-j(\omega - \frac{2\pi}{T})\frac{T}{2}} e^{-j(\frac{2\pi}{T})\tau}. \quad (4\text{-}16)$$

It is easily seen that a choice of $\tau = \frac{T}{2}$ yields π-radian phase difference between $F[f_s(t)]_{k=0}$ and $F[f_s(t)]_{k=1}$ at $\omega = \frac{\pi}{T}$, thus resulting in a spectrum null at one-half the Nyquist frequency of the signal spectrum entering the equalizer delay line. To substantiate further the effect of spectrum aliasing when the sampling rate equals

the baud rate of a Pulse Amplitude Modulated (PAM) waveform, the sampled spectrum was experimentally measured as a function of the clock timing offset parameter, τ. The results are shown in Figure 4-7. The photograph at the top of the figure shows the spectrum at the A/D converter output for the case of optimum sampling, corresponding to $\tau = 0$.* The first spectrum null occurs at $\omega = \frac{2\pi}{T}$, which is at the Nyquist frequency, as is predicted by equation (4-13) and Figure 4-6. The Nyquist equivalent channel $(0 \leq |\omega| \leq \frac{\pi}{T})$ is relatively flat, which is representative of a distortion-free signal. As τ is allowed to depart from its optimum value, a spectrum null appears at the edge of the Nyquist equivalent channel and becomes more pronounced as τ approaches T/2. The photograph at the bottom of Figure 4-7 shows the aliased spectrum for a clock timing offset, τ, equal to T/2. The spectrum null created at $\omega = \frac{\pi}{T}$ is at its maximum depth, representing substantial distortion in the sampled data sequence entering the delay line of the transversal filter. When presented with such a dispersive input condition, the transversal filter will respond by attempting to flatten out the Nyquist equivalent channel, thus greatly enhancing the noise level in the vicinity of the spectrum null. The response of the synchronously spaced transversal equalizer to a dispersive input condition generated by a suboptimum timing offset, τ, has been measured. A value of τ was chosen such that the BER at the output of the equalizer reached a steady state value of 10^{-3}. Under these conditions, the spectral density at the A/D converter output is shown by the top photograph of Figure 4-8. The spectrum at the output of the equalizer (operating with five taps) was also measured and is shown by the bottom photograph of Figure 4-8. As is evident from the latter photograph, the five-tap equalizer has formed a transfer function that has, to a large extent, compensated for the input

* The 8-bit word sequence provided by the A/D converter is passed through an 8-bit D/A converter to recover the corresponding analog sample sequence.

SPECTRUM AT A/D CONVERTER OUTPUT.
OPTIMUM TIMING; $\hat{\tau} = 0$.
NULL OCCURS AT $\omega = \frac{2\pi}{T}$.
SPECTRUM IS RELATIVELY FLAT OVER THE NYQUIST EQUIVALENT CHANNEL, $0 \leq |\omega| \leq \frac{\pi}{T}$.

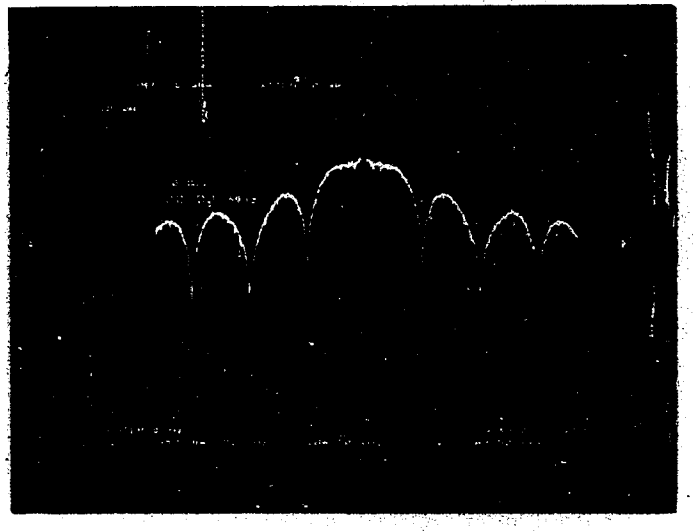

SPECTRUM AT A/D CONVERTER OUTPUT.
SUBOPTIMUM TIMING; $\hat{\tau} = \frac{T}{2}$.
A SPECTRUM NULL OCCURS AT $\omega = \frac{\pi}{T}$.

Figure 4-7. Aliased Spectra at the A/D Converter Output as a Function of the Clock Timing Offset, τ (Baud $\equiv \frac{1}{T}$ = 5.5 Mbaud; Roll-Off Factor $\equiv \alpha$ = 0.5)

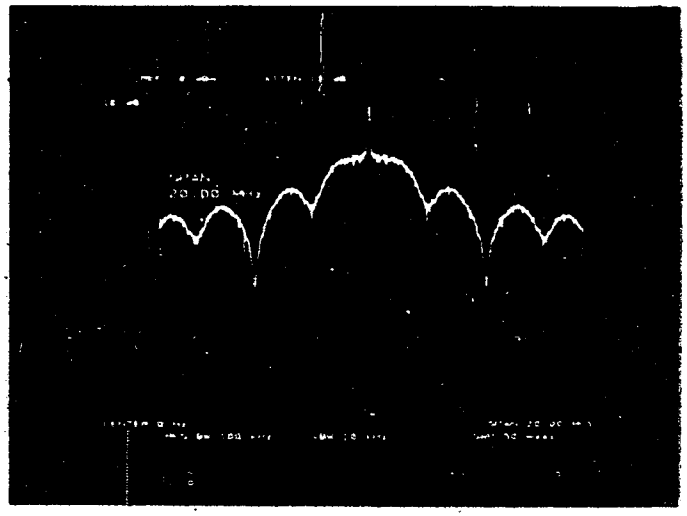

SPECTRAL DENSITY AT
A/D CONVERTER OUTPUT

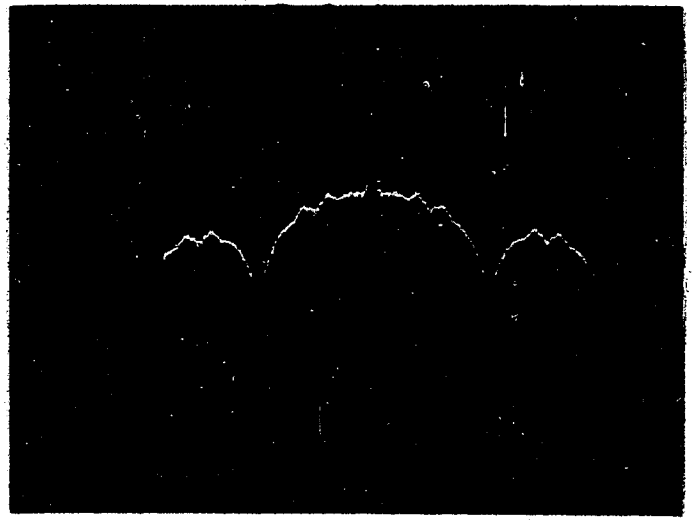

SPECTRAL DENSITY AT
5-TAP SYNCHRONOUSLY-SPACED
EQUALIZER OUTPUT, BER=10^{-3}

Figure 4-8. Spectral Densities at the Output of the A/D Converter and at the Output of a Five-Tap Synchronously Spaced Equalizer Corresponding to a Suboptimum Timing Offset τ (BER = 10^{-3} at the Equalizer Output)

spectrum null at $\omega = \frac{\pi}{T}$. The four-level eyes corresponding to the input and output spectral density curves of Figure 4-8 are shown by the first and second traces, respectively, of the first photograph of Figure 4-9. For comparison, the bottom photograph of Figure 4-9 shows undistorted (ideal) four-level eyes at the output of the A/D converter and at the output of the five-tap equalizer, respectively.

We have seen the effect of a suboptimum sampling time on the performance of a synchronously spaced transversal equalizer. Because of the sensitivity of the synchronously spaced equalizer to timing phase errors, adaptive timing techniques would have to be used with such equalizers to track perturbations of the optimum sampling time due to changing characteristics of the channel. To circumvent such timing related complications, a fractionally spaced equalizer can be used instead. It has been shown, and is well recognized, that a fractionally spaced equalizer is insensitive to timing phase errors, no matter how severe.[3] Here, we illustrate this property by resorting to equation (4-14), which expresses the spectral density at the output of the sampler (the A/D converter) as a function of the sampling offset parameter, τ.

Assume that, for a fractionally spaced equalizer, a sampling rate of $1/T'$ (where $T' < T$) is used to sample a sequence of half-Nyquist pulses that are being received at a baud rate of $1/T$. Then, the spectral density of the sample sequence at the output of the A/D converter will have the form

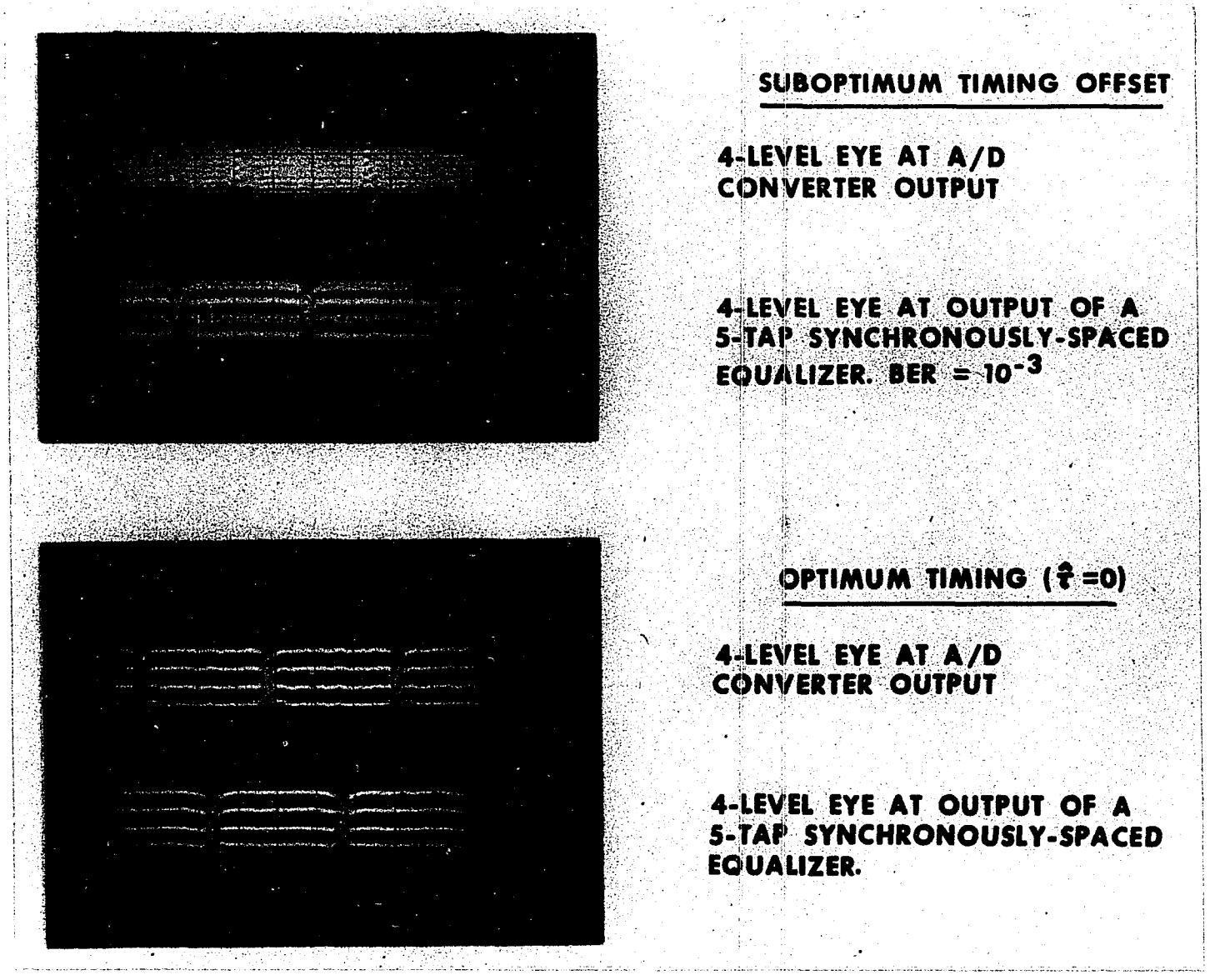

Figure 4-9. Four-Level Eyes at the Output of the A/D Converter and at the Output of a Five-Tap Synchronously Spaced Equalizer

$$F[f_s(t)] = \sum_{k=-\infty}^{\infty} \left[\frac{\omega - k\frac{2\pi}{T'}}{\omega} \right] \bar{M}(j\omega - jk\frac{2\pi}{T'}) \cdot \left[\frac{\sin\left[(\omega - k\frac{2\pi}{T'})\frac{T'}{2} \right]}{(\omega - k\frac{2\pi}{T'})\frac{T'}{2}} \right] e^{-j(\omega - k\frac{2\pi}{T'})\frac{T'}{2}} e^{-jk(\frac{2\pi}{T'})\tau}. \quad (4\text{-}17)$$

Letting $T' = \frac{T}{2}$ yields

$$F[f_s(t)] = \sum_{k=-\infty}^{\infty} \left[\frac{\omega - k\frac{4\pi}{T}}{\omega} \right] \bar{M}(j\omega - jk\frac{4\pi}{T}) \cdot \left[\frac{\sin\left[(\omega - k\frac{4\pi}{T})\frac{T}{4} \right]}{(\omega - k\frac{4\pi}{T})\frac{T}{4}} \right] e^{-j(\omega - k\frac{4\pi}{T})\frac{T}{4}} e^{-jk(\frac{4\pi}{T})\tau}. \quad (4\text{-}18)$$

It is evident from equation (4-18) that, for a band-limited input waveform, m(t) (band-limited to $0 \leq |\omega| \leq \frac{(1+\alpha)\pi}{T} \leq \frac{2\pi}{T}$), no spectrum aliasing between the harmonics of $\bar{M}(j\omega)$ will result at the output of the sampler. Therefore, the baseband spectrum at the output of the sampler (over the frequency interval $0 \leq |\omega| \leq \frac{(1+\alpha)\pi}{T}$) is determined solely by the fundamental harmonic of the summation and is thus completely independent of the timing offset parameter, τ. That is,

$$F[f_s(t)] = \bar{M}(j\omega)\left[\frac{\sin(\frac{\omega T}{4})}{(\frac{\omega T}{4})} \right], \quad 0 \leq |\omega| \leq \frac{(1+\alpha)\pi}{T}. \quad (4\text{-}19)$$

This was verified experimentally by converting the equalizer to fractionally spaced with a sampling rate equal to twice the baud rate. Figure 4-10 shows photographs of the sampled waveforms at the A/D converter output and at the equalizer output. The

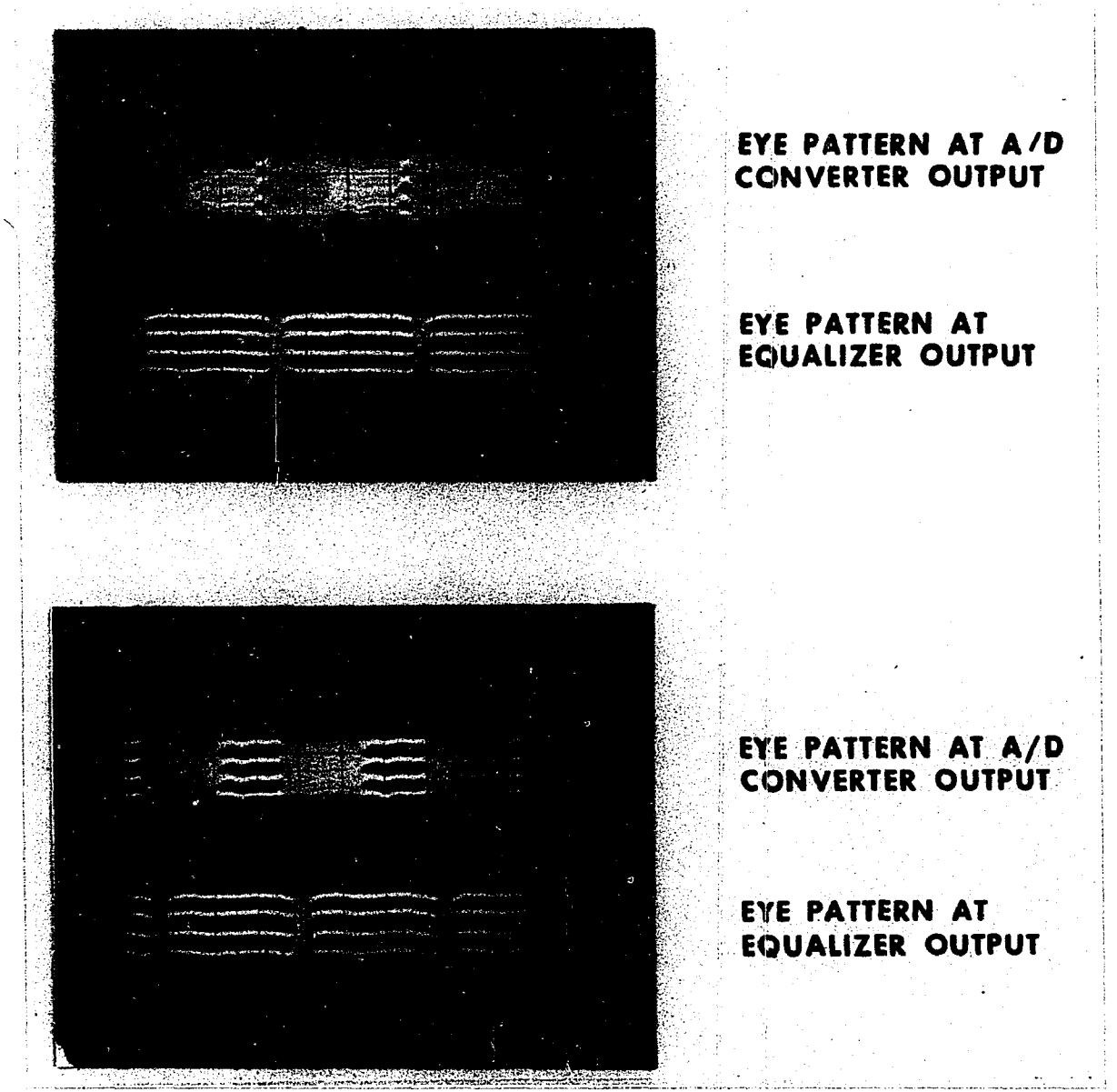

Figure 4-10. Eye Patterns Associated with a Five-Tap Fractionally Spaced Equalizer (A/D Converter Sampling Rate = $\frac{2}{T}$)

first trace of each photograph shows the "eye" pattern that appears at the output of the A/D converter, having sampled the input eye (corresponding to a sequence of half-Nyquist pulses with roll-off factor, α, equal to 0.5) at twice the baud rate. The second trace on each photograph corresponds to the four-level eye appearing at the output of the fractionally spaced qualizer operating with five taps. Clearly, the measurements show the insensitivity of the fractionally spaced configuration to the timing offset (compare the top picture of Figure 4-10 with the top picture of Figure 4-9). Even when both A/D converter samples (per baud interval) are far from optimum (in the sense that they represent samples of the input eye pattern at the transition regions), as is the case shown by the first trace of the top photograph of Figure 4-10, the equalizer output seems unaffected. The spectral density corresponding to the sample waveforms at the output of the A/D converter (shown in Figure 4-10) is shown in Figure 4-11. This spectral density clearly shows the absence of spectrum aliasing and was found insensitive to the timing offset parameter, τ, as is predicted by equation (4-19).

4.4 BIT ERROR RATE MEASUREMENTS

BER measurements were taken in both the synchronously and fractionally spaced modes of operation. The laboratory arrangement used for these measurements is shown in Figure 4-12. A Pseudorandom Word Generator (PRWG) was used to provide a binary sequence, which was subsequently encoded into a four-level PAM sequence of symbols. A digitally implemented pulse synthesizer circuit was used to perform the encoding and half-Nyquist transmit filtering operations. The transmitter filter, shown after the pulse synthesizer circuit, was used solely for the purpose of rejecting the higher order sidebands generated by the pulse synthesizer. This filter was chosen to be a fifth order Chebyshev low pass filter with a cutoff radian frequency of

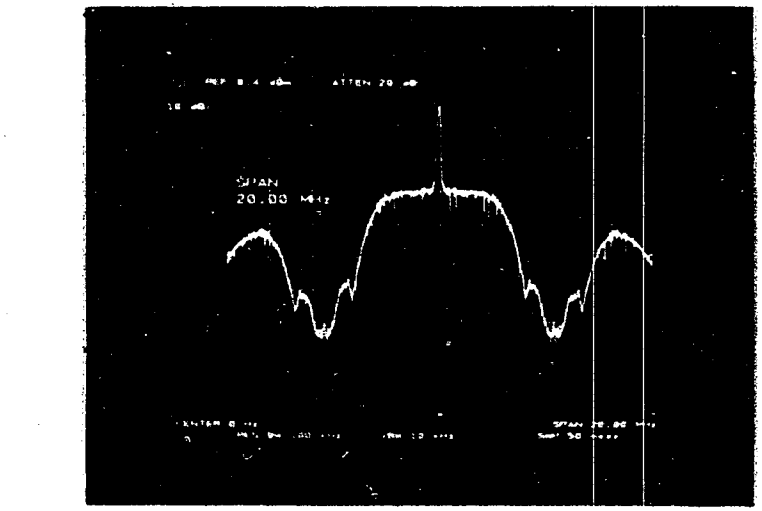

Figure 4-11. Spectral Density at A/D Converter Output (Sampling Rate = $\frac{2}{T}$)

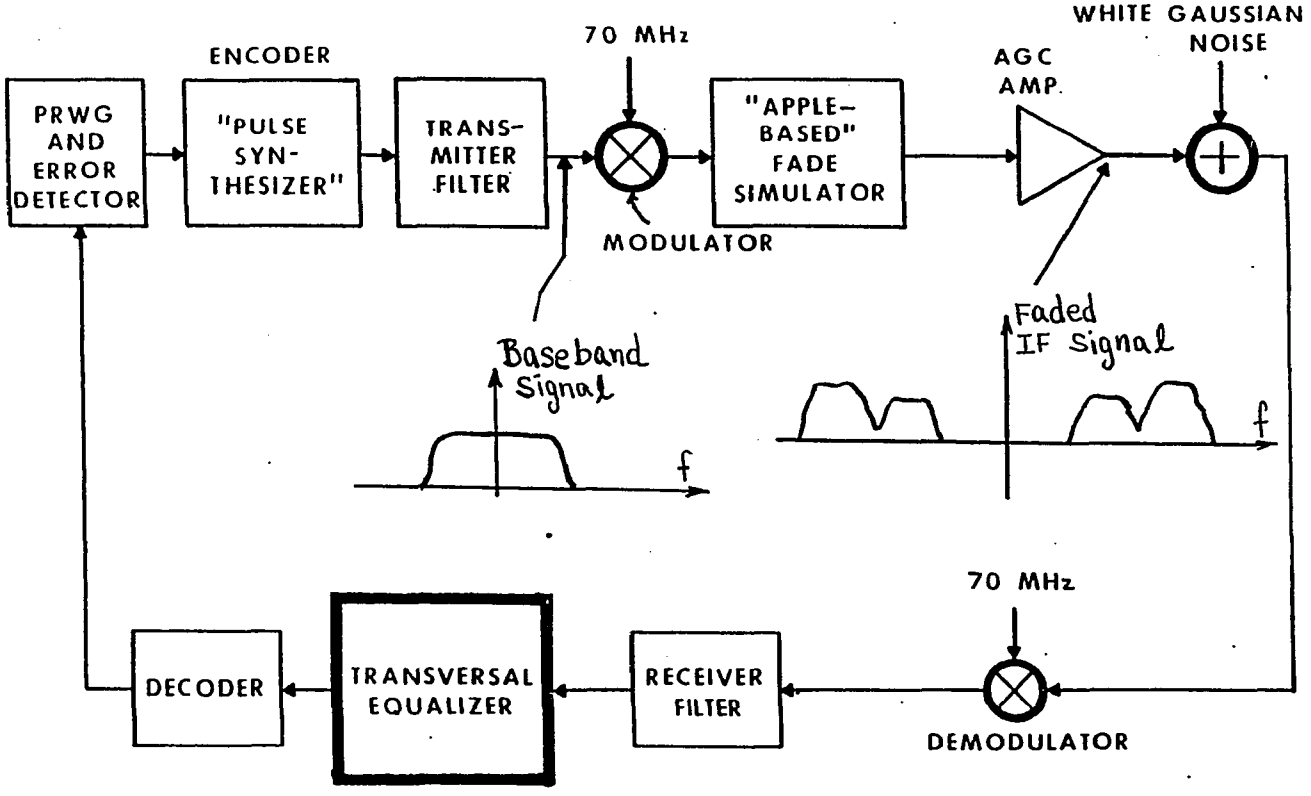

Figure 4-12. Laboratory Arrangement for Evaluation of Transversal Equalizer Performance

$\frac{(1+\alpha)\pi}{T}$, where T defines the baud interval and α is the roll-off factor of the Nyquist pulse. In this experiment, an α of 0.5 was chosen and the baud rate was set at 5.5 Mbaud (as mentioned earlier).

The baseband PAM signal was upconverted to an Intermediate Frequency (IF) of 70 MHz (as shown in Figure 4-12), where a fade simulator was used to generate Intersymbol Interference (ISI). An Automatic Gain Control (AGC) amplifier following the fade simulator was used to maintain the power level at the receiver input fixed. Also, at the input of the receiver, Additive White Gaussion Noise (AWGN) was introduced to the signal. Following this, the signal plus AWGN was demodulated and filtered by a receiver filter and the transversal equalizer. The receiver filter shown prior to the transversal equalizer was chosen identical to the low pass Chebyshev filter following the pulse synthesizer. Having a half-Nyquist filter at the transmitter, but not one at the receiver, the receiver frequency characteristic was no longer matched to that of the transmitter. This translated into a BER degradation, which was reflected in our measurements, as will become evident shortly. In a way, however, this shortcoming proved advantageous, since it served as a measure of the fractionally spaced equalizer's ability to synthesize the receiver matched filter adaptively.

Figure 4-13 presents BER measurements illustrating the performance of the equalizer in the two modes of operation and as a function of the clock phase error. The curves presented in Figure 4-13 correspond to the nonfaded channel case. That is, the "APPLE based" fade simulator was removed from the system loop of Figure 4-12. All measured BER versus SNR curves of Figure 4-13 correspond to SNR values as measured at the input of the transversal equalizer. As a point of reference, the

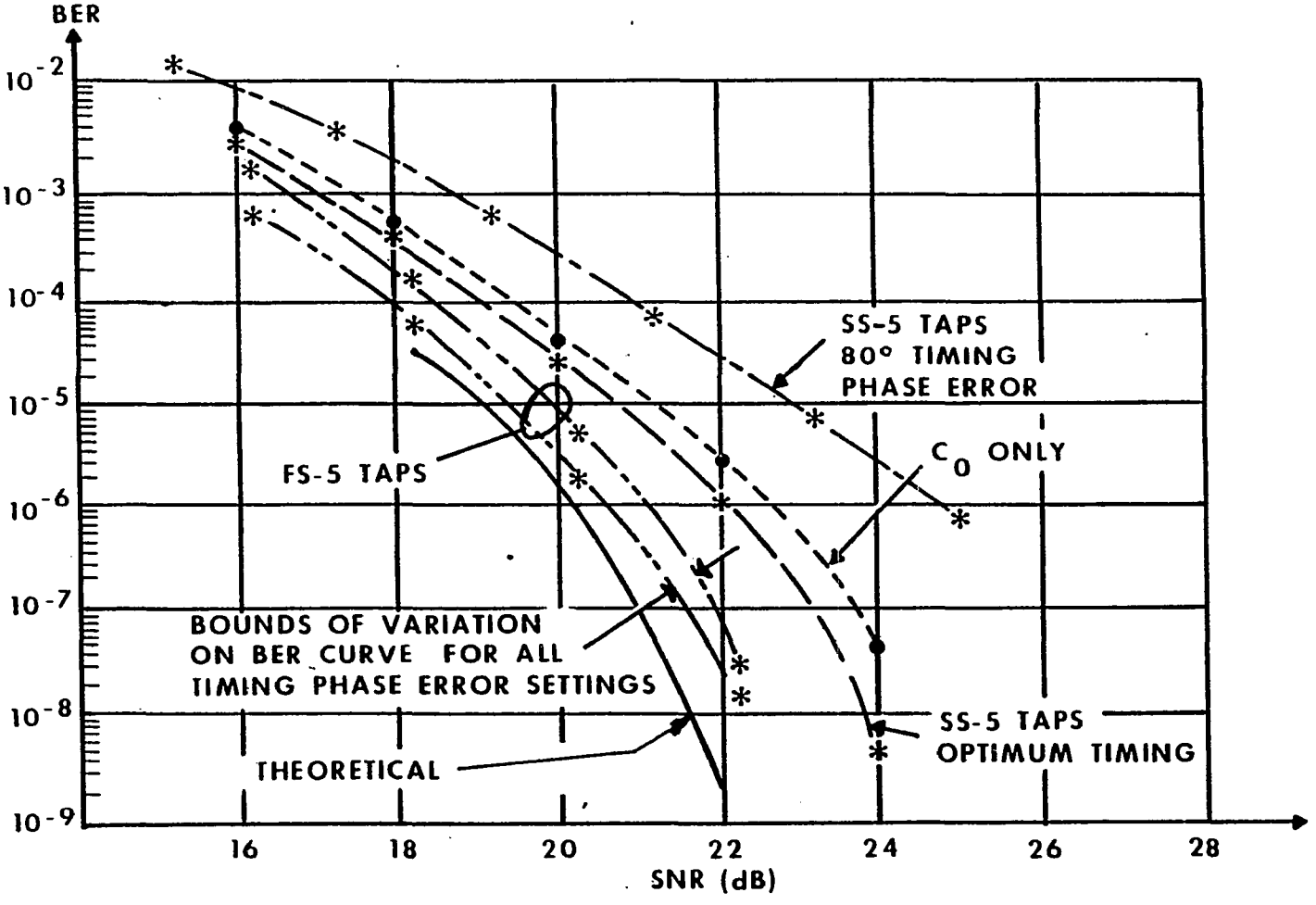

Figure 4-13. Measured BER Curves for Various Equalizer Configurations (Nonfaded Channel Case)

BER of the "unequalized" system was measured first. This curve is labeled "C_0 only" and corresponds to a transversal equalizer where all tap values except the C_0 tap have manually been forced to zero. The center (C_0) tap is allowed to operate normally, providing flat AGC over the channel bandwidth, but is incapable of mitigating any ISI that may exist. Next, all equalizer taps (C_{-2} through C_{+2}) are allowed to operate normally, with the equalizer in the synchronously spaced mode, resulting in the curve (immediately to the left of the "C_0 only" curve) labeled "SS-5 taps optimum timing". As indicated, this curve corresponds to optimum sampling timing, meaning that the input four-level eye is sampled at its maximum eye opening. As discussed earlier, the synchronously spaced equalizer is sensitive to the timing phase error. To verify the degradation in BER performance as a function of a suboptimum timing phase, the measurement was repeated for several timing phase error values. A curve corresponding to a timing phase error of 80° is shown in Figure 4-13. Note that, at a BER of 10^{-6}, a degradation of 3 dB in SNR is observed.

The BER versus SNR performance of the equalizer in the fractionally spaced mode is illustrated by the curves labeled "FS-5 taps". We immediately notice two striking differences comparing these curves with those corresponding to the synchronously spaced configuration. First, we note that the BER performance of the fractionally spaced equalizer is highly insensitive to the choice of sampling time. All BER curves measured, corresponding to various timing phase values ranging from "optimum" to $\pm 180°$, were bounded by the two curves shown in Figure 4-13. At a BER of 10^{-6}, the two bounds differ by only 0.5 dB. Even this small variation, however, is surprising, since it is not anticipated by the analysis. It is possible that, due to a nonideal low pass filter characteristic, a nonzero noise spectral density existed beyond the radian frequency $\frac{2\pi}{T}$. Subject to this, aliasing of the noise spectrum

would result, given a sampling rate of 2/T. As we have seen, cancellation or enhancement of certain spectral components can take place, depending on the particular value of the sampling offset parameter, τ, thus resulting in a fluctuation of the average noise power over the interval $0 \leq |\omega| \leq \frac{2\pi}{T}$.

The second interesting aspect regarding the fractionally spaced equalizer curves is the improvement in BER performance that they display over the synchronously spaced equalizer curve with optimum timing. In both cases, the number of equalizer tap coefficients is the same, $\{C_{-2}, C_{-1}, C_0, C_{+1}, C_{+2}\}$. With five tap coefficients, the delay line of the synchronously spaced equalizer spans four baud intervals, while the delay line of the fractionally spaced equalizer (operating at a sampling rate of 2/T) spans only two baud intervals. Even so, as our measurements show, the five-tap fractionally spaced equalizer outperforms the synchronously spaced arrangement. As can be seen from the curves of Figure 4-13, the improvement in performance at a BER of 10^{-6} is about 1.3 dB (taking an average over the two curves representing the performance bounds).

In Appendix C, we show, analytically, that a fractionally spaced equalizer forms the optimum linear receiver in the sense that it forms a transfer function that is equivalent to a matched filter, followed by a synchronously spaced transversal filter. The BER curve corresponding to the synchronously spaced equalizer (with optimum timing) represents the performance of an unmatched receiver, given the transmitter and receiver filter arrangements described earlier. The degradation in BER performance of such an unmatched receiver over one that is perfectly matched to the transmitter characteristic was evaluated numerically. The degradation in BER performance was found to be 1.54 dB (assuming that the transmitter and receiver filters shown in Figure 4-12 were ideal low pass filters with a cutoff radian

frequency of $\frac{(1 + \alpha)\pi}{T}$). In other words, we predicted, by computer simulation, a 1.54-dB improvement in BER performance afforded by a receiver that is ideally matched to the overall transmitter filter characteristic, followed by a synchronously spaced transversal equalizer, as compared to the transmitter/receiver arrangement shown in Figure 4-12, with the transversal equalizer operating synchronously spaced. The transmitter/receiver arrangement shown in Figure 4-12, with the transversal equalizer operating fractionally spaced, provided an average measured improvement in the BER curve ranging from 1.2 to 1.3 dB over the case involving the synchronously spaced equalizer. We, therefore, conclude that the fractionally spaced equalizer, with only five taps, was able to adaptively form the receiver matched filter with sufficient accuracy (our experimental error in measuring the SNRs was approximately 0.2 dB). To see whether increasing the number of fractionally spaced taps could improve the matched filter synthesis (bringing us closer to the theoretical 1.54-dB improvement), the fractionally spaced equalizer was extended to seven taps. The measurements were repeated, with no observable deviation from those corresponding to the five-tap fractionally spaced case. It would thus appear that five fractionally spaced taps suffice in forming the receiver matched filter adaptively with sufficient accuracy.

To observe the performance of the two equalizer configurations under faded channel conditions, the computer controlled fade simulator was used, as shown in Figure 4-12, to introduce a 20-dB frequency selective fade centered at the carrier frequency (70 MHz). With the channel faded, the BER versus SNR curves corresponding to the five-tap synchronously and fractionally spaced equalizers were measured. The results are shown in Figure 4-14. The superiority of the five-tap fractionally spaced equalizer is again evident. The "FS-5 taps" curve of Figure 4-14 represents

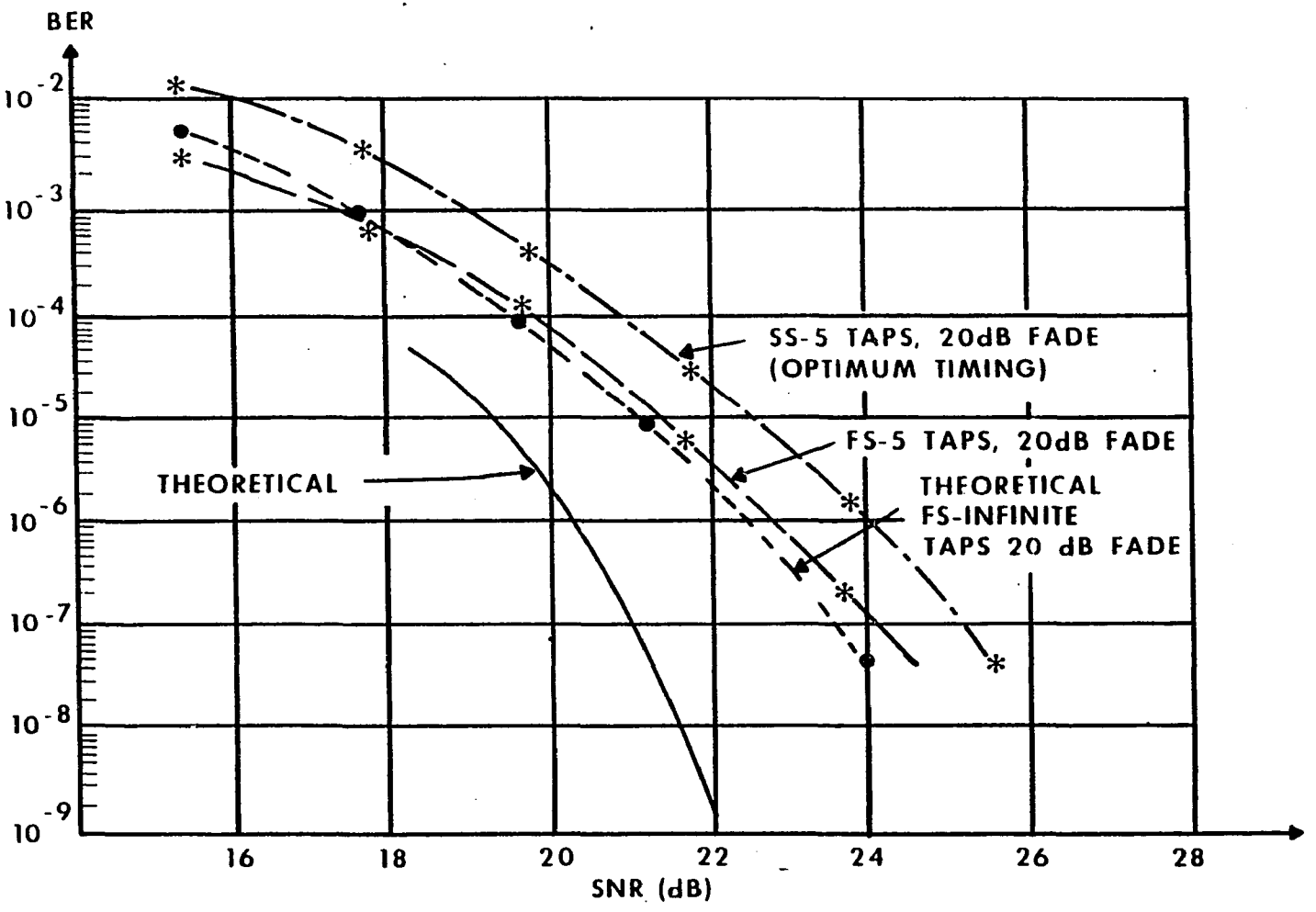

Figure 4-14. Measured BER Curves for Fractionally and Synchronously Spaced Equalizer Configurations (Faded Channel Case)

an average taken over all timing phase errors. As can be seen from the figure, this measured curve falls very close to a theoretically predicted curve that assumes ideal matched filtering followed by an infinitely long synchronously spaced equalizer. This again supports the claim that five fractionally spaced taps yield performance that very closely approximates the optimum attainable (for the type of channel used here). Computer simulations showed that the receiver mismatching due to the 20-dB faded channel, given a four-level 5.5-Mbaud signal with 50-percent roll-off factor, is negligible (only 0.05-dB degradation of the BER curve). Thus, the improvement in BER performance afforded by the fractionally spaced equalizer, as shown in Figure 4-14, is still due to the fact that the receiver filter is not matched to the transmitter filter. At higher baud rates, however, the mismatching due to a faded channel becomes more significant. At a baud rate of 20 Mbaud, a 20-dB notch centered fade will cause an 0.5-dB degradation in the BER curve due to receiver mismatching. At a baud rate of 50 Mbaud, the same fade will cause a 3.5-dB BER curve degradation due to the same effect. We see that, at the higher baud rates, a fractionally spaced equalizer can provide appreciable BER improvements during faded channel conditions by adaptively maintaining a receiver characteristic that is matched to the overall transfer function of the transmitter filter plus the channel.

REFERENCES

[1] S. U. H. Qureshi and G. D. Forney, Jr., "Performance and Properties of a T/2 Equalizer", NTC'77

[2] G. Ungerboeck, "Fractional Tap-Spacing Equalizer and Consequences for Clock Recovery in Data Modems", IEEE Transactions on Communications, August 1976, Volume COM-24, No. 8

[3] R. D. Gitlin and S. B. Weinstein, "Fractionally Spaced Equalization: An Improved Digital Transversal Equalizer", Bell System Technical Journal, February 1981, Volume 60, No. 2, pages 275 to 296

CHAPTER 5

CLOSING REMARKS

CHAPTER 5

CLOSING REMARKS

5.1 SYNOPSIS OF DISSERTATION

We have presented a distortion mitigation theory (and techniques for implementing the theoretical results) for a generalized two-dimensional digital communications system that is corrupted by additive thermal noise and contains, throughout its transmission path, linear as well as nonlinear dispersive elements. The modulation format assumed for the communications system has been QAM, chosen for its two-dimensional nature and high density (spectral efficiency), and because it poses challenges due to that it is very fragile to system imperfections (linear and nonlinear distortion).

Following a brief historical introduction and preview of the main theme and contributions of this work, presented in Chapter 1, in Chapter 2 we established the mathematical framework and baseband equivalent modeling tools that enabled us to derive detailed descriptions of two classes of optimal linear receivers for the linear QAM system. Using one of the baseband equivalent models established in Chapter 2, in Appendix C we derived optimal linear receivers, in the minimum mean-squared error sense, in conjunction with adaptive control laws and transversal filter architectures for adaptively forming the optimal solutions. Using the same baseband equivalent representation, the QAM system was optimized in Appendix D in the Nyquist sense, resulting in a second class of optimal linear receivers, control laws and transversal filter architectures, for adaptively forming the necessary transfer characteristics. A new receiver configuration and adaptive signal processing

methodology was derived, capable of forming the minimum probability of error (linear) receiver, subject to the zero ISI constraint. In Appendices A and B, mathematical arguments/derivations and equivalence relations were presented complementing the baseband equivalent model developments of Chapter 2.

Having established a supporting mathematical framework and proper baseband equivalent modeling methodology, in Chapter 3 we embarked on the main theme of this dissertation and began to develop a logical generalization and extension of the concepts established in Chapter 2. A baseband equivalent model for the generalized QAM system (containing linear as well as nonlinear distortion) was developed showing that the impulse response of such a system is not only distortion dependent, but data-sequence-dependent as well, thus showing explicitly why the classical adaptive equalizer (transversal filter) receiver fails to function when subjected to the nonlinear channel environment. The shortcoming of the classical equalizer receiver was resolved by developing an equalizer structure (and associated control algorithm) involving data-sequence-dependent coefficients, controlled appropriately, such as to allow the equalizer to optimally operate on the system's data-sequence-dependent characteristic. We resorted to a computer simulation of the new equalizer/algorithm arrangement and illustrated proper operation.

Having developed a solution for the equalization of ISI, stemming from a combination of linear and nonlinear system impairments, we focused next (in Chapter 3) on the issue of ISI cancellation for the generalized QAM system. Cancellation of ISI is, in general, a more complex process (requiring more hardware) as compared to ISI equalization. However, cancellation of ISI avoids the receiver thermal noise enhancement problem and, hence, becomes important during periods of deep channel

fading*. In Chapter 3, we developed a strategically new algorithm for the ISI cancellation issue (perhaps the most important contribution of the dissertation). The algorithm was shown to be generic and, hence, applicable to a variety of canceller configurations and also to decision feedback equalizers (recall that a decision feedback equalizer performs partial ISI cancellation). The strength of the algorithm was shown to lie in that it optimally mitigates against the problem of "error propagation" that has plagued the operation of decision feedback equalizers and ISI cancellers using decision feedback. Furthermore, for ISI cancellers not using decision feedback (relying solely on preliminary decisions to form ISI estimates), the new algorithm was shown beneficial by resolving errored preliminary decisions, hence maintaining optimum ISI estimates. The ISI cancellation strategy developed in Chapter 3 was shown optimum, designed to achieve the isolated pulse, matched filter performance bound (the ultimate performance bound for any communications system). Our computer simulation results of the new algorithm confirmed that there is substantial improvement to be gained by using this technique over conventional canceller strategies.

Because of the importance and central role played by the transversal filter, as the building block in forming the optimal receivers developed in Appendices C and D, and Chapter 3, an experimental effort was undertaken to study digital implementations of multitap synchronously/fractionally spaced transversal filters. We reported on our findings in Chapter 4. Experimental results were presented confirming the performance insensitivity of the digital implemented fractionally spaced

* For the same reason decision feedback equalizers have been developed to mitigate against the thermal noise penalty incurred by the classical adaptive equalizer during periods of deep channel fading. A decision feedback equalizer performs partial ISI cancellation in conjunction with some channel equalization.

equalizer to timing phase errors and showing that a fractionally spaced equalizer, with only five taps, is capable of forming the receiver matched filter adaptively for a PAM system employing a half-Nyquist transmitter filter. The digitally implemented synchronously spaced equalizer performance was shown highly sensitive to timing phase errors and incapable of forming the receiver matched filter adaptively.

5.2 EXTENSIONS AND TOPICS FOR FURTHER WORK

Several important tangential observations/signal processing techniques that surfaced during the course of developing the central theme of this dissertation have not been expanded upon in the main text, but are presented in some detail below. They may be viewed as means of defining areas for further work, aimed at improving the capabilities of the QAM system.

5.2.1 SUPPRESSED SIDEBAND QAM SYSTEM

Consider the conventional QAM signal

$$s(t) = i(t) \cos \omega_c t - q(t) \sin \omega_c t, \tag{5-1}$$

where ω_c denotes the carrier frequency, and i(t) and q(t) denote the I- and Q-rail baseband information waveforms, respectively. Let the QAM carrier, s(t), be passed through a low pass filter in order to suppress one of the sidebands, say the upper. This filtering function is depicted in Figure 5-1.

At the output of the filter, the single sideband waveform $[s(t)]_{ss}$ can be expressed as

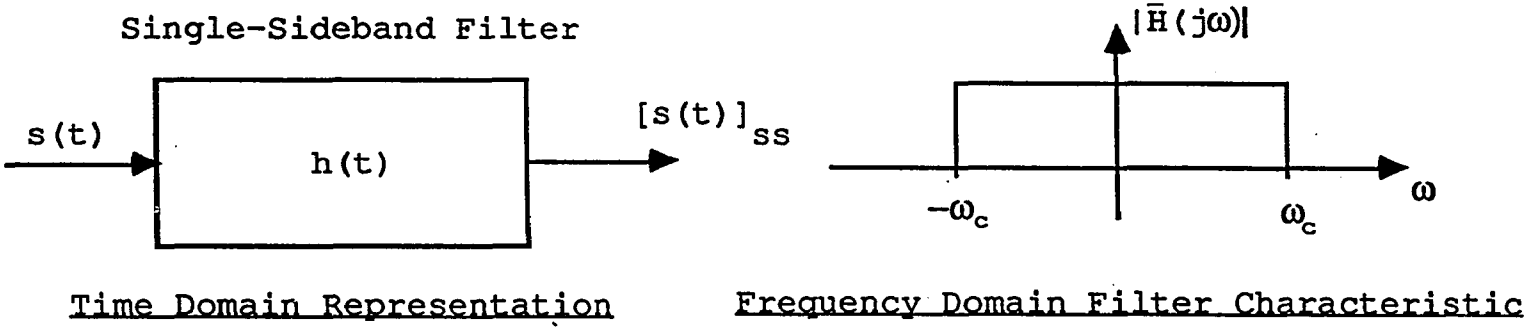

Figure 5-1. Suppressing One Sideband of a QAM Signal

$$[s(t)]_{ss} = \int_{-\infty}^{\infty} h(\tau)\, i(t-\tau) \cos [\omega_c(t-\tau)]d\tau$$

$$- \int_{-\infty}^{\infty} h(\tau)\, q(t-\tau) \sin [\omega_c(t-\tau)]d\tau. \qquad (5\text{-}2)$$

Using the trigonometric identities

$$\left.\begin{aligned} 2 \cos [\omega_c(t-\tau)] &= \cos \omega_c t \cos \omega_c \tau + \sin \omega_c t \sin \omega_c \tau \\ \text{and} & \\ 2 \sin [\omega_c(t-\tau)] &= \sin \omega_c t \cos \omega_c \tau - \cos \omega_c t \sin \omega_c \tau, \end{aligned}\right\} \quad (5\text{-}3)$$

equation (5-2) can be rewritten as

$$[s(t)]_{ss} = \left\{\int_{-\infty}^{\infty} h(\tau)\, i(t-\tau) \cos (\omega_c \tau)d\tau \right.$$

$$\left. + \int_{-\infty}^{\infty} h(\tau)\, q(t-\tau) \sin (\omega_c \tau)d\tau\right\}\cos \omega_c t$$

$$+ \left\{\int_{-\infty}^{\infty} h(\tau)\, i(t-\tau) \sin (\omega_c \tau)d\tau \right.$$

$$\left. - \int_{-\infty}^{\infty} h(\tau)\, q(t-\tau) \cos (\omega_c \tau)d\tau\right\}\sin \omega_c t \qquad (5\text{-}4)$$

or as

$$[s(t)]_{SS} = \frac{1}{2}\left\{i(t) + \overset{v}{q}(t)\right\}\cos \omega_c t - \frac{1}{2}\left\{q(t) - \overset{v}{i}(t)\right\}\sin \omega_c t, \qquad (5\text{-}5)$$

where $\overset{v}{i}(t)$ and $\overset{v}{q}(t)$ denote the Hilbert transforms of i(t) and q(t), respectively.

We see that $[s(t)]_{SS}$, as expressed by equation (5-5), has the same form as the conventional QAM signal expressed by equation (5-1). However, it occupies half the bandwidth of s(t) and, as a result, the I- and Q-rail information waveforms i(t) and q(t) are contaminated by $\overset{v}{q}(t)$ and $-\overset{v}{i}(t)$, respectively. Thus, if $[s(t)]_{SS}$ is to be transmitted, received and demodulated intelligibly, means must be provided at the receiver for cancelling $\overset{v}{q}(t)$ and $-\overset{v}{i}(t)$ from the I and Q rails, respectively. We now illustrate how this may be done.

Consider the block diagram shown in Figure 5-2, which depicts the transmitter and receiver portions of the SSQAM system. As shown, the single sideband waveform $[s(t)]_{SS}$ is transmitted through a linear (dispersive) channel. At the receiver, after coherent demodulation, the baseband waveforms appearing on the I and Q rails will have the form

$$i'(t) = [i(t) + \overset{v}{q}(t)] + \text{ISI} + \text{X-Rail ISI} + n_I(t) \qquad (5\text{-}6)$$

and

$$q'(t) = [q(t) - \overset{v}{i}(t)] + \text{ISI} + \text{X-Rail ISI} + n_Q(t), \qquad (5\text{-}7)$$

respectively. The terms "ISI" and "X-Rail ISI" appearing in i'(t) and q'(t), respectively, denote the ISI and cross-rail ISI that may have been generated in the I

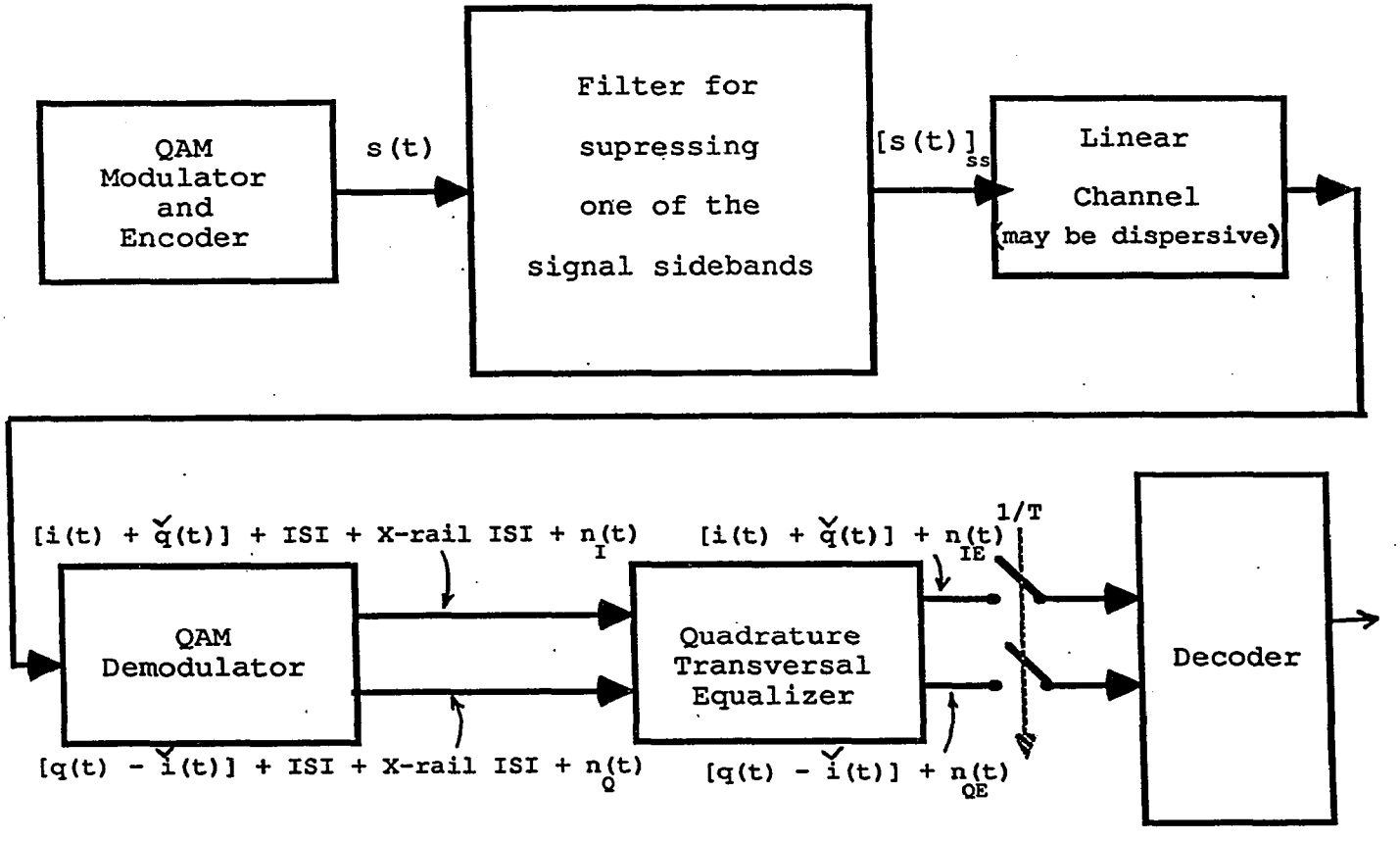

Figure 5-2. A Single Sideband QAM System

and Q rails by a dispersive channel. The waveforms $n_I(t)$ and $n_Q(t)$ represent the additive Gaussian thermal noise.

A conventional quadrature transversal equalizer can be configured to operate on $i'(t)$ and $q'(t)$ as if $[i(t) + \overset{v}{q}(t)]$ and $[q(t) - \overset{v}{i}(t)]$ are the desired pulse shapes, thus mitigating the ISI and X-rail ISI terms. At the equalizer output, we assume all channel induced distortion has been eliminated, yielding the I- and Q-rail waveforms

$$i_E(t) = [i(t) + \overset{v}{q}(t)] + n_{IE}(t) \tag{5-8}$$

and

$$q_E(t) = [q(t) - \overset{v}{i}(t)] + n_{QE}(t). \tag{5-9}$$

These waveforms are sampled at the symbol rate (at T-second intervals), with the k^{th} sample being

$$i_E(kT) = [i(kT) + \overset{v}{q}(kT)] + n_{IE}(kT) \tag{5-10}$$

for the I rail and

$$q_E(kT) = [q(kT) + \overset{v}{i}(kT)] + n_{QE}(kT) \tag{5-11}$$

for the Q rail. The samples must now be processed to extract the information carrying components $i(kT)$ and $q(kT)$. That is, the terms $-\overset{v}{i}(kT)$ and $\overset{v}{q}(kT)$ must be eliminated.

The terms $\overset{v}{i}(kT)$ and $\overset{v}{q}(kT)$ can assume a limited number of a priori known values. For example, in a 16-QAM system with i(kT) and q(kT) assuming the values ± 1 and ± 3, it can be shown[1] that the quantities $\overset{v}{i}(kT)$ and $\overset{v}{q}(kt)$ can take on values only from the set {0, -1, -2, -3, 1, 2, 3}, provided that raised cosine Nyquist filtering with 50-percent roll-off is used for the transmitter (pulse shaping) filter and that the sideband suppressing filter of Figure 5-1 is made a vestigial sideband filter having a roll-off factor of 0.5. That is, subject to the stated filtering, the terms $\overset{v}{i}(kT)$ and $\overset{v}{q}(kT)$ can assume one of seven possible values. Realizing this, the decoder circuit shown in Figure 5-3 can be used for the detection of $i(kT)$ and $q(kT)$. The decoding will be illustrated for the I rail only. The Q-rail information can be decoded in a similar fashion.

The seven a priori known values of $\overset{v}{q}(kT)$, $\{\overset{v}{q}_1(kT), \overset{v}{q}_2(kT), \ldots, \overset{v}{q}_7(kT)\}$, are subtracted, one at a time, from the input sample, $i_E(kT) = [i(kT) + \overset{v}{q}(kT)]$, resulting in the following set of possibilities: $\{i_{En}(kT)\} = \{i(kT) + \overset{v}{q}(kT) - \overset{v}{q}_n(kT) + n_{IE}(kT)\}$, $1 \leq n \leq 7$. These seven values are then compared to the ideal levels that i(kT) can assume, $\{\pm 1, \pm 3\}$. The one value found to be closest to an ideal level from the set $\{\pm 1, \pm 3\}$ is used in determining the best estimate, $\overset{v}{i}(kT)$, of the transmitted I-rail symbol. The best estimate of i(kT) is represented by the ideal level, which is found to have a minimum Euclidian distance from some element of $\{i_{En}(kT)\}$, $1 \leq n \leq 7$. In the absence of noise $[n_{iE}(kT) = 0]$, the minimum distance between an ideal state of i(kT) and an element of $\{i_{En}(kT)\}$ should be zero. However, only one element of $\{i_{En}(kT)\}$ should be found to coincide (having a distance of zero) with an ideal state of i(kT). Unless this is true, an unambiguous decision as to the state of i(kT) cannot be made. We have shown that such ambiguities can arise with a

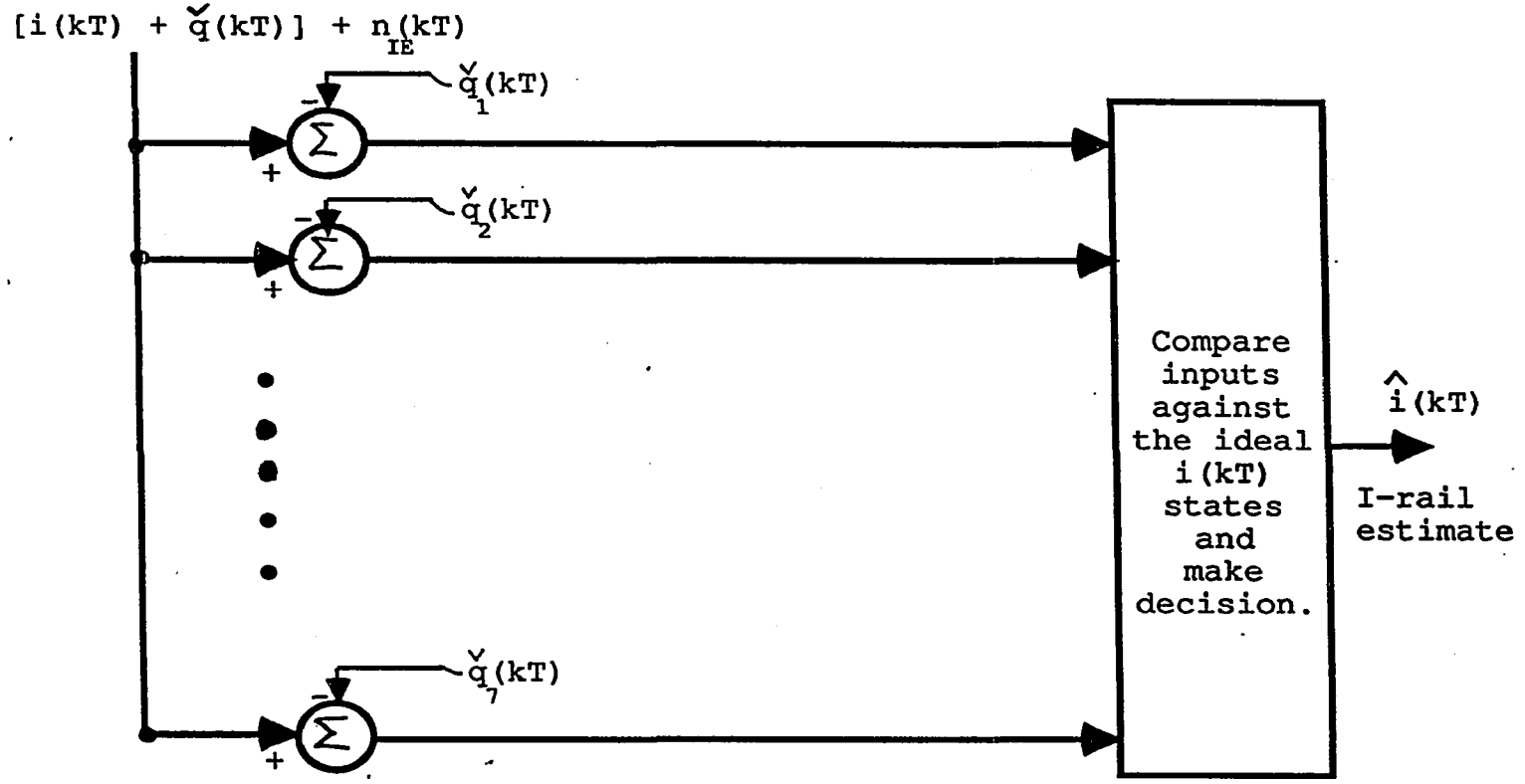

Figure 5-3. Vestigial Sideband QAM Decoder Architecture

16-QAM constellation, where i(kT) and q(kT) are allowed to take on values from the set $\{\pm 1, \pm 3\}$. To circumvent this problem, the QAM constellation can be modified such that the I- and Q-rail samples do not share values from a common set. As an example, if we let $i(kT) \in \{\pm 1, \pm 3\}$ and $q(kT) \in \{\pm 1.5, \pm 4.5\}$, it can be shown that the detection procedure described above will always determine only one of the members of $\{i_{En}(kT)\}$, $1 \leq n \leq 7$, as having the minimum distance from an ideal state of i(kT) and, thus, a decision regarding the best estimate, $\hat{i}(kT)$, can always be made unambiguously.

5.2.2 NON-DATA DIRECTED EQUALIZER ALGORITHM

Recently, there has been considerable effort towards developing "nondata directed" adaptive algorithms for the control of tap weight coefficients of equalizers and/or cross-polarization (x-pol) cancellers.[2-5] Such algorithms are desirable for use during periods of time when the receiver's demodulation processes (carrier, timing recovery and estimation of the transmitted data) become unreliable or break down completely. Use of a nondata directed algorithm when the receiver is experiencing outage allows an equalizer and/or an x-pol canceller to maintain reasonably proper coefficient sets, thus substantially aiding reacquisition of the data directed carrier and time recovery processes, and, hence, of the data estimation process itself.

In this section, we briefly describe an LMS error adaptive algorithm that is carrier synchronization independent and, hence, nondata directed in the conventional sense.[6] Furthermore, we show that the algorithm intrinsically derives its own optimal clock signal; thus, it is completely independent of the receiver timing synchronization issue. This nondata directed algorithm represents a special case of

the classical stochastic gradient LMS adaptive algorithm, in both theory and means of implementation. Therefore, it is robust and relatively simple to implement. Since the algorithm's adaptations utilize (by design) a select subset of the received signal states (in contrast to the classical LMS adaptations, which utilize all states of the QAM signal constellation), the derived coefficient set will, in general, be suboptimum in minimizing the mean-squared error with respect to the ensemble of all data sequences.

In Figure 5-4, we show a representative baseband arrangement of an x-pol canceller and a copolarization equalizer. The circuit shown is for operating on the received vertically polarized QAM signal. An identical arrangement (not shown) would have to be provided in order to similarly treat the horizontally polarized received QAM signal. The demodulator and carrier recovery architecture shown advantageously maintains a frequency alignment between the (V and H polarized) baseband spectra that is identical to that existing between them in the passband where the interference has occurred.

The nondata directed LMS algorithm that we postulate operates on the following simple principle. A peak in the QAM signal envelope occurs every time two successive QAM constellation states involve the same outer corner state. Furthermore, this peak in the ideal QAM signal envelope will occur at a point in time that is halfway between these two successive constellation states. Using these two simple observations, a circuit is provided for identifying the points in time at which the QAM signal envelope peaks at the equalizer/canceller output of Figure 5-4. These points in time are denoted by the set $\{t_0\}$. Once a point in time from the set $\{t_0\}$ has been identified, it is known what, ideally, the signal envelope must be at $t = t_0 \pm T/2$. Using this information and the actual value of the QAM signal envelope at

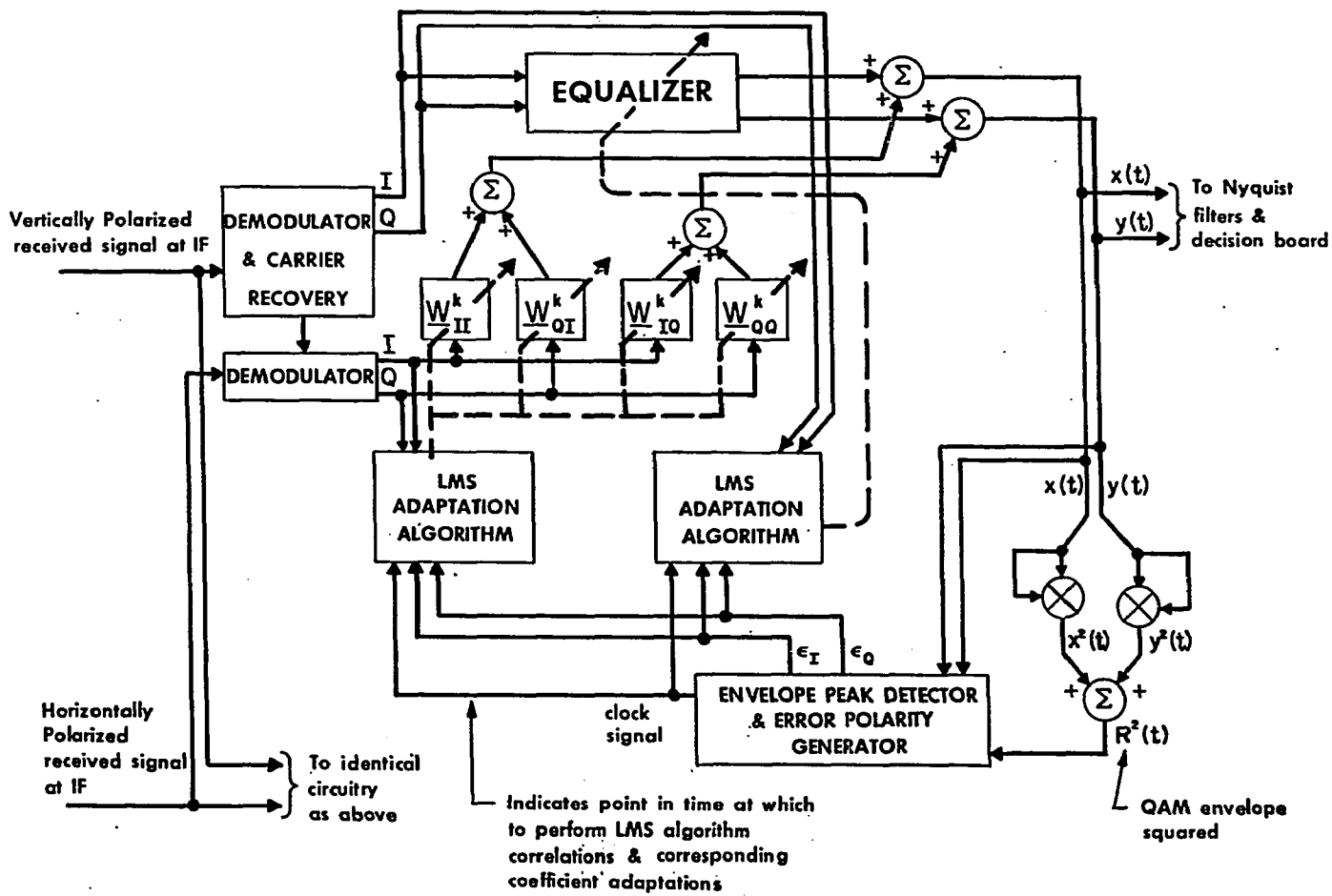

Figure 5-4. Baseband System Utilizing Nondata Directed LMS Algorithm

$t = t_0 \pm T/2$, reliable error quantities can be associated with the I- and Q-rail signals at these points. These error quantities can be used in a conventional LMS adaptation algorithm. The details of the "peak envelope detector and error polarity generator" circuit used to achieve the above are shown in Figure 5-5. The heart of the circuit involves a statistical technique for adaptively tracking the peak of the QAM signal envelope. It can easily be verified that the expected number of QAM envelope peaks per second, assuming, for example, 15-Mbaud 64-QAM transmission, is 7,324 (where statistical independence between successive constellation states is postulated). Hence, a voltage reference, V_R, is adaptively found and compared with the actual signal envelope so that this number of peaks is, on the average, satisfied. The circuit details are shown in Figure 5-5. Since the QAM signal envelope characteristics are not affected by either carrier recovery or timing recovery operation, the acquisition algorithm described above is carrier and timing synchronization independent, and is, furthermore, self-synchronizing in the sense that it creates its own optimal timing signal.

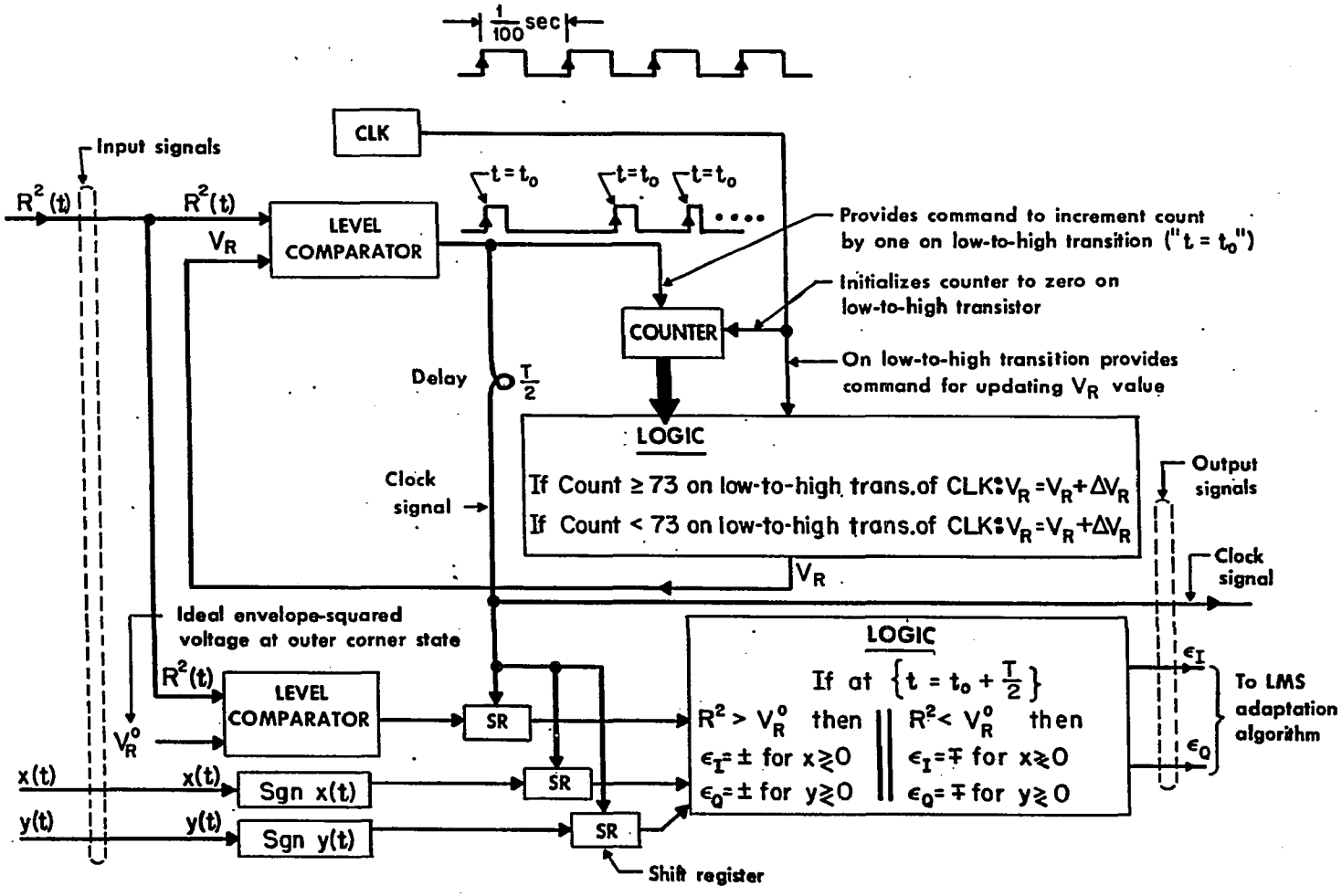

Figure 5-5. Peak Envelope Detector and Error Polarity Generator

REFERENCES

[1] P. D. Karabinis, "Suppressed Double-Sideband Communication System", U.S. Patent No. 4,780,884, October 25, 1988

[2] Y. Bar-Ness, J. W. Carlin and M. L. Steinberger, "Bootstrapping Adaptive Cross-Pol Cancelers for Satellite Communications", ICC 1982, pages 4F.5.1 to 4F.5.5

[3] D. N. Godard, "Self-Recovering Equalization and Carrier Tracking in Two-Dimensional Data Communication Systems", IEEE Transactions on Communications, November 1980, Volume COM-28, No. 11

[4] A. Benveniste and M. Goursat, "Blind Equalizers", IEEE Transactions on Communications, August 1984, Volume COM-32, No. 8

[5] Y. Sato, "A Method of Self-Recovering Equalization for Multilevel Amplitude Modulation Systems", IEEE Transactions on Communications, June 1975, Volume COM-23, pages 679 to 682

[6] P. D. Karabinis, "Asynchronous and Non-Data Decision Directed Equalizer Adjustment", U.S. Patent No. 4,635,276, January 6, 1987

APPENDIX A

BASEBAND EQUIVALENT FORMS FOR PASSBAND SIGNALS AND SYSTEMS (THE COMPLEX ENVELOPE PRINCIPLE)

APPENDIX A

BASEBAND EQUIVALENT FORMS FOR PASSBAND SIGNALS AND SYSTEMS (THE COMPLEX ENVELOPE PRINCIPLE)

In a multielement passband system, comprising a tandem interconnection of a plurality of linear passband subsystems, it may be required to mathematically optimize some subsystem element with respect to some overall system performance index, and/or evaluate and predict some signal state at an intermediate system point. Such a task (whether performed analytically or by computer simulation) is invariably facilitated via the use of a baseband equivalent modeling methodology that is convolutionally isomorphic (in passing from system element to system element) to the original physical passband system model. Owing to the wide use of this approach in this work, we develop, in this appendix, the necessary mathematical foundations.

We begin by defining the Hilbert transform of an arbitrary waveform, $x(t)$, as the waveform $\overset{v}{x}(t)$, where $\overset{v}{x}(t)$ is generated from $x(t)$ via a linear operation. This linear operation involves passing $x(t)$ through a system whose transfer function is $-j\text{sgn}(\omega)$. The transfer function $-j\text{sgn}(\omega)$ is defined as

$$-j\text{sgn}(\omega) \equiv \begin{cases} -j & \text{for } \omega > 0 \\ 0 & \text{for } \omega = 0. \\ +j & \text{for } \omega > 0 \end{cases} \tag{A-1}$$

Hence, if $x(t)$ has the transform $\overline{X}(j\omega)$, we may write

$$F[\overset{v}{x}(t)] = -j\text{sgn}(\omega)F[x(t)] = \begin{cases} -j\overline{X}(j\omega) & \text{for } \omega > 0 \\ 0 & \text{for } \omega = 0. \\ +j\overline{X}(j\omega) & \text{for } \omega < 0 \end{cases} \tag{A-2}$$

In general, we may also write

$$\overset{v}{x}(t) = x(t) * F^{-1}[-j\text{sgn}(\omega)], \tag{A-3}$$

where "*" denotes convolution.

Given now that x(t) is a narrowband passband signal whose frequency content is confined about some carrier frequency ω_c, x(t) may be represented generically in terms of I and Q components in the form of

$$x(t) = x_I(t) \cos \omega_c t - x_Q(t) \sin \omega_c t, \tag{A-4}$$

where $x_I(t)$ and $x_Q(t)$ represent the I and Q components of x(t), respectively. The generic form of equation (A-4) may always be invoked in representing an arbitrary narrowband passband waveform (whose spectrum exists about ω_c), since such a waveform may be envisioned as the result of having subjected a carrier to amplitude and/or phase modulation. In general, we may therefore write

$$\begin{aligned} x(t) &= a(t) \cos(\omega_c t + \phi(t)) \\ &= a(t)[\cos \phi(t) \cos \omega_c t - \sin \phi(t) \sin \omega_c t], \end{aligned} \tag{A-5}$$

where a(t) and $\phi(t)$ are assumed to be baseband (low pass) signals. Equation (A-5) above yields the generic form of equation (A-4), where $x_I(t) \equiv a(t) \cos \phi(t)$ and $x_Q(t) \equiv a(t) \sin \phi(t)$.

The I and Q components of x(t) may be evaluated from x(t) and its Hilbert transform. Given that $\overline{X}_I(j\omega)$ and $\overline{X}_Q(j\omega)$ represent the transforms of $x_I(t)$ and $x_Q(t)$, respectively, the transform of x(t) may be written as

$$F[x(t)] \equiv \overline{X}(j\omega) = [\tfrac{1}{2}\overline{X}_I(j\omega - j\omega_c) + \tfrac{1}{2}\overline{X}_I(j\omega + j\omega_c)]$$

$$- [-\tfrac{1}{2} j\overline{X}_Q(j\omega - j\omega_c) + \tfrac{1}{2} j\overline{X}_Q(j\omega + j\omega_c)]$$

$$= \tfrac{1}{2}[\overline{X}_I(j\omega - j\omega_c) + j\overline{X}_Q(j\omega - j\omega_c)]$$

$$+ \tfrac{1}{2}[\overline{X}_I(j\omega + j\omega_c) - j\overline{X}_Q(j\omega + j\omega_c)]. \qquad \text{(A-6)}$$

Since the first and second bracketed terms above represent the spectral content of $x(t)$ for positive and negative frequencies, respectively, utilization of equation (A-2) allows us to write, by inspection,

$$F[\overset{v}{x}(t)] = -\tfrac{1}{2} j[\overline{X}_I(j\omega - j\omega_c) + j\overline{X}_Q(j\omega - j\omega_c)]$$

$$+ \tfrac{1}{2} j[\overline{X}_I(j\omega + j\omega_c) - j\overline{X}_Q(j\omega + j\omega_c)], \qquad \text{(A-7)}$$

and, hence,

$$jF[\overset{v}{x}(t)] = \tfrac{1}{2}[\overline{X}_I(j\omega - j\omega_c) + j\overline{X}_Q(j\omega - j\omega_c)]$$

$$- \tfrac{1}{2}[\overline{X}_I(j\omega + j\omega_c) - j\overline{X}_Q(j\omega + j\omega_c)]. \qquad \text{(A-8)}$$

Adding equations (A-6) and (A-8) yields

$$F[x(t)] + jF[\overset{v}{x}(t)] = \overline{X}_I(j\omega - j\omega_c) + j\overline{X}_Q\,(j\omega - j\omega_c), \qquad \text{(A-9)}$$

or, equivalently,

$$x(t) + j\overset{v}{x}(t) = [x_I(t) + jx_Q(t)]e^{j\omega_c t}, \tag{A-10}$$

where the baseband complex-valued waveform $x_I(t) + jX_Q(t)$ defines the complex envelope, $\tilde{x}(t)$, of the passband narrowband signal $x(t)$. We let

$$\tilde{x}(t) \equiv x_I(t) + jX_Q(t). \tag{A-11}$$

The complex-valued quantity $x(t) + j\overset{v}{x}(t)$ defines the preenvelope, $\overline{x}_+(t)$, of $x(t)$. We therefore have

$$\overline{x}_+(t) \equiv x(t) + j\overset{v}{x}(t) = \tilde{x}(t)e^{j\omega_c t}. \tag{A-12}$$

We observe that the spectral content of the signal $\overline{x}_+(t)$ is nonzero for positive frequencies only, as is evident from equation (A-9). At this juncture, we also observe that, since

$$\begin{aligned}\tilde{x}(t)e^{j\omega_c t} &= [x_I(t) + jx_Q(t)][\cos \omega_c t + j \sin \omega_c t] \\ &= x_I(t) \cos \omega_c t - x_Q(t) \sin \omega_c t \\ &\quad + j[x_Q(t) \cos \omega_c t + x_I(t) \sin \omega_c t],\end{aligned} \tag{A-13}$$

conformance with equation (A-12) dictates that

$$\left.\begin{aligned} x(t) &= x_I(t) \cos \omega_c t - x_Q(t) \sin \omega_c t \text{ (as expected)} \\ &\text{and} \\ \overset{v}{x}(t) &= x_I(t) \sin \omega_c t + x_Q(t) \cos \omega_c t. \end{aligned}\right\} \tag{A-14}$$

Solving equations (A-14) simultaneously for $x_I(t)$ and $x_Q(t)$, we find

$$\left.\begin{aligned} x_I(t) &= x(t)\cos\omega_c t + \overset{v}{x}(t)\sin\omega_c t \\ \text{and} \\ x_Q(t) &= -x(t)\sin\omega_c t + \overset{v}{x}(t)\cos\omega_c t. \end{aligned}\right\} \quad \text{(A-15)}$$

We now turn our attention to the case of a linear, time invariant, passband narrowband system having an impulse response $h(t)$. Furthermore, we assume that the transform of $h(t)$ exists about the carrier frequency ω_c. As in the case of the narrowband passband signal $x(t)$, here too, $h(t)$ lends itself to the generic representation of equation (A-4); hence, we can write

$$h(t) = h_I(t)\cos\omega_c t - h_Q(t)\sin\omega_c t. \quad \text{(A-16)}$$

The complex envelope for the passband system case, however, will be defined as

$$\tilde{\tilde{h}}(t) \equiv \frac{1}{2}[h_I(t) + jh_Q(t)], \quad \text{(A-17)}$$

where the factor of $\frac{1}{2}$ has been introduced in order to preserve an isomorphism between $\tilde{\tilde{h}}(t) * \tilde{\tilde{x}}(t)$ and $h(t) * x(t)$, as will be established shortly. The preenvelope for the passband system will be defined as

$$\overline{h}_+(t) \equiv \frac{1}{2}[h(t) + j\overset{v}{h}(t)] = \tilde{\tilde{h}}(t)e^{j\omega_c t}. \quad \text{(A-18)}$$

Letting $y(t)$ represent the output of a linear, time invariant, passband system with impulse response $h(t)$ and with the passband input $x(t)$, we may write $y(t) =$

$h(t) * x(t)$. We now show that $\tilde{\tilde{h}}(t) * \tilde{\tilde{x}}(t)$ generates the complex envelope of $y(t)$, $\tilde{\tilde{y}}(t)$, and, hence, the convolution operation as performed between the complex envelopes of a passband signal and system is isomorphic to the convolution operation performed between the passband signal and the impulse response of the passband system. Towards establishing the above, we first show that

$$y(t) = \mathrm{Re}\left[\int_{-\infty}^{\infty} \overline{h}_+(\tau)\overline{x}_+(t-\tau)d\tau\right].$$

Using definitions (A-18) and (A-12), we have

$$\mathrm{Re}\left[\int_{-\infty}^{\infty} \overline{h}_+(\tau)\overline{x}_+(t-\tau)d\tau\right] = \mathrm{Re}\left[\frac{1}{2}\int_{-\infty}^{\infty} \{h(\tau) + j\overset{v}{h}(\tau)\}\right.$$

$$\left. \cdot \{x(t-\tau) + j\overset{v}{x}(t-\tau)\}d\tau\right]$$

$$= \frac{1}{2}\int_{-\infty}^{\infty} h(\tau)x(t-\tau)d\tau - \frac{1}{2}\int_{-\infty}^{\infty} \overset{v}{h}(\tau)\overset{v}{x}(t-\tau)d\tau. \qquad \text{(A-19)}$$

Fourier transforming equation (A-19) yields

$$F\left[\mathrm{Re}\left[\int_{-\infty}^{\infty} \overline{h}_+(\tau)\overline{x}_+(t-\tau)d\tau\right\}\right] = \frac{1}{2}\overline{H}(j\omega)\overline{X}(j\omega) - \frac{1}{2}F[\overset{v}{h}(t)]F[\overset{v}{x}(t)], \qquad \text{(A-20)}$$

where $\overline{H}(j\omega)$ and $\overline{X}(j\omega)$ denote the Fourier transforms of $h(t)$ and $x(t)$, respectively. Next, utilizing the result of equation (A-2), it becomes apparent that the right-hand side of equation (A-20) is equivalent to $\overline{H}(j\omega)\overline{X}(j\omega)$. Hence, we conclude

$$\mathrm{Re}\left[\int_{-\infty}^{\infty} \overline{h}_+(\tau)\overline{x}_+(t-\tau)d\tau\right] = \int_{-\infty}^{\infty} h(\tau)x(t-\tau)d\tau = y(t). \qquad \text{(A-21)}$$

Having established the above, we now observe that

$$\mathrm{Re}\left[\int_{-\infty}^{\infty} \overline{h}_+(\tau)\overline{x}_+(t-\tau)d\tau\right] = \mathrm{Re}\left[\int_{-\infty}^{\infty} \{\tilde{\tilde{h}}(\tau)e^{j\omega_c\tau}\}\{\tilde{\tilde{x}}(t-\tau)e^{j\omega_c(t-\tau)}\}d\tau\right]$$

$$= \mathrm{Re}\left[e^{j\omega_c t}\int_{-\infty}^{\infty} \tilde{\tilde{h}}(\tau)\tilde{\tilde{x}}(t-\tau)d\tau\right]. \qquad \text{(A-22)}$$

However, since $y(t)$ is also a passband signal, it may be written in terms of its complex envelope as

$$y(t) = \mathrm{Re}\left[\tilde{\tilde{y}}(t)e^{j\omega_c t}\right]. \qquad \text{(A-23)}$$

Combining equations (A-21) through (A-23), we arrive at the desired result

$$\tilde{\tilde{y}}(t) = \int_{-\infty}^{\infty} \tilde{\tilde{h}}(\tau)\tilde{\tilde{x}}(t-\tau)d\tau \equiv \tilde{\tilde{h}}(t) * \tilde{\tilde{x}}(t). \qquad \text{(A-24)}$$

Hence, the complex envelopes of $x(t)$ and $h(t)$ may be used via the convolution operation to evaluate the complex envelope of $y(t)$ and thus $y(t)$ itself. We have thus established that convolution involving passband waveforms is isomorphic to convolution involving complex-valued low pass waveforms provided that the aforementioned low pass waveforms represent the complex envelopes of the corresponding passband quantities.

APPENDIX B

AN EQUIVALENCE BETWEEN PASSBAND AND BASEBAND RECEIVER FILTERS

APPENDIX B

AN EQUIVALENCE BETWEEN PASSBAND AND BASEBAND RECEIVER FILTERS

The complex envelope principle developed in Appendix A is utilized herein to establish an equivalence between the operations of baseband and passband receiver filtering in a linear QAM communications system. In reference to Figure B-1b, depicting a (noiseless) linear QAM system, where a passband receiver filter with impulse response g(t) is being utilized, the passband signal r'(t) at the receiver filter output may be expressed as

$$r'(t) = r(t) * g(t), \tag{B-1}$$

where r(t) denotes the passband received waveform at the receiver filter input. In terms of the associated complex envelopes, we may also write

$$\tilde{r}'(t) = \tilde{r}(t) * \tilde{g}(t). \tag{B-2}$$

Letting (see Appendix A, equation (A-4))

$$\left.\begin{aligned} r(t) &= r_I(t)\cos\omega_c t - r_Q(t)\sin\omega_c t, \\ g(t) &= g_I(t)\cos\omega_c t - g_Q(t)\sin\omega_c t \end{aligned}\right\} \tag{B-3}$$

and

$$r'(t) = r'_I(t)\cos\omega_c t - r'_Q(t)\sin\omega_c t,$$

the associated complex envelopes may be expressed as

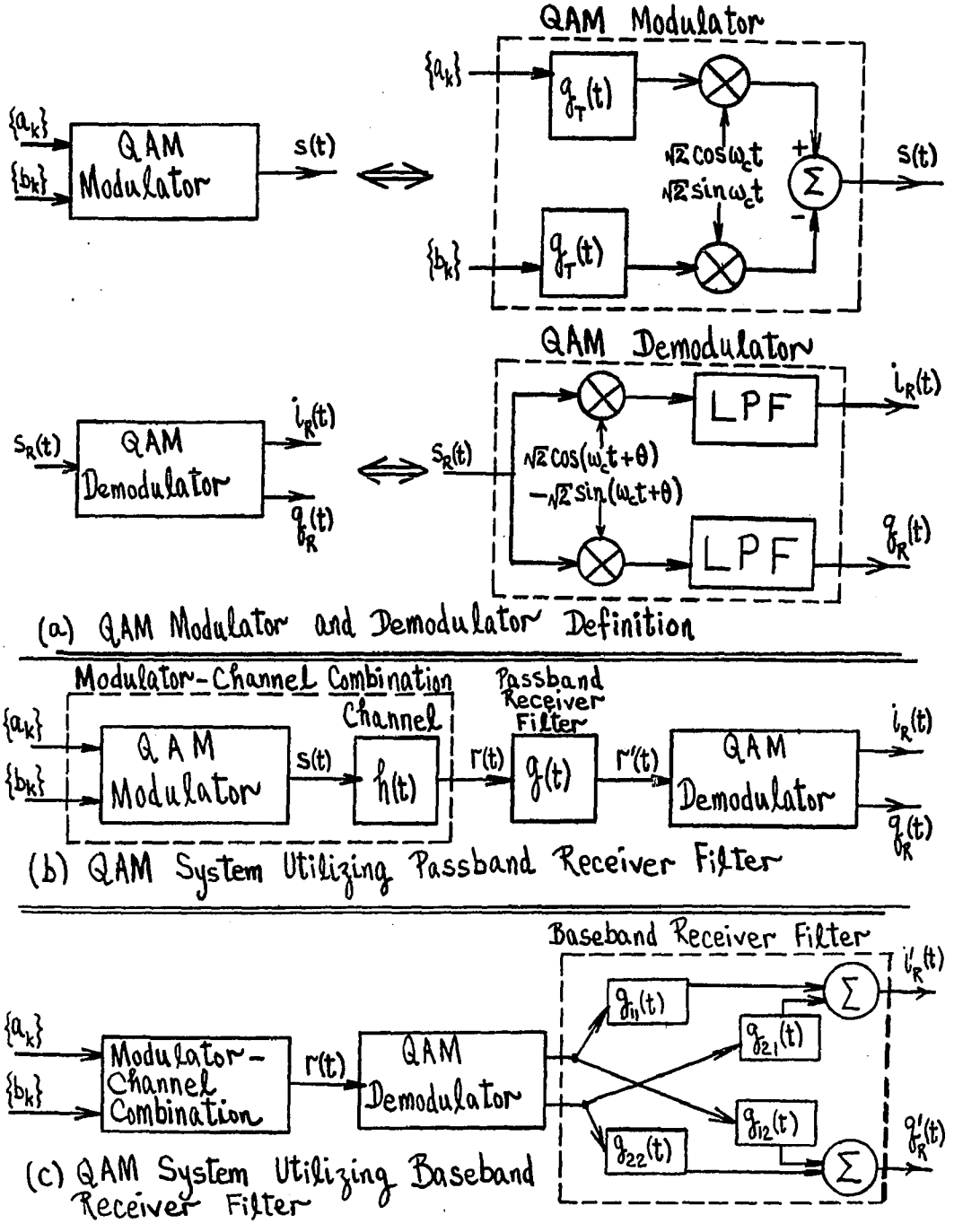

Figure B-1. Passband Versus Baseband Receiver Filters

$$\left.\begin{aligned} \tilde{r}(t) &= r_I(t) + jr_Q(t), \\ \tilde{g}(t) &= \tfrac{1}{2}\, g_I(t) + j\,\tfrac{1}{2}\, g_Q(t) \end{aligned}\right\} \quad \text{(B-4)}$$

and

$$\tilde{r}'(t) = r_I'(t) + jr_Q'(t).$$

Substituting equations (B-4) into equation (B-2), we have

$$r_I'(t) + jr_Q'(t) = \tfrac{1}{2}\,(r_I(t) + jr_Q(t)) * (g_I(t) + jg_Q(t)). \quad \text{(B-5)}$$

Or, equivalently,

$$\left.\begin{aligned} r_I'(t) &= \tfrac{1}{2}\, r_I(t) * g_I(t) - \tfrac{1}{2}\, r_Q(t) * g_Q(t) \end{aligned}\right\} \quad \text{(B-6)}$$

and

$$r_Q'(t) = \tfrac{1}{2}\, r_I(t) * g_Q(t) + \tfrac{1}{2}\, r_Q(t) * g_I(t).$$

Having established the I and Q components of r'(t) as per equation (B-6) above, the I and Q signal components at the QAM demodulator output, $i_R(t)$ and $q_R(t)$, respectively (see Figure B-1b), may readily be evaluated. Given the QAM demodulator structure of Figure B-1a (encompassing ideal low pass filters following the I- and Q-rail mixing processes), the output I component, $i_R(t)$, may be expressed as

$$i_R(t) = [\{\sqrt{2} \cos(\omega_c t + \theta)\} \cdot \{r_I'(t) \cos \omega_c t - r_Q'(t) \sin \omega_c t\}]_B, \quad \text{(B-7)}$$

where $[\cdot]_B$ indicates that we are keeping only the baseband component of the quantity in the brackets. Hence,

$$i_R(t) = \frac{1}{\sqrt{2}} r_I'(t) \cos \theta + \frac{1}{\sqrt{2}} r_Q'(t) \sin \theta. \tag{B-8}$$

Similarly, we have

$$q_R(t) = [\{-\sqrt{2} \sin (\omega_c t+\theta)\}\{r_I'(t) \cos \omega_c t - r_Q'(t) \sin \omega_c t\}]_B$$

$$= \frac{1}{\sqrt{2}} r_Q'(t) \cos \theta - \frac{1}{\sqrt{2}} r_I'(t) \sin \theta. \tag{B-9}$$

Equations (B-8) and (B-9), in conjunction with equations (B-6), specify the I and Q components at the demodulator output of the system of Figure B-1b in terms of the I and Q components of the received waveform r(t) and the characteristics of the pass-band receiver filter. Upon substitution of equations (B-6) into equations (B-8) and (B-9), straightforward algebraic manipulation yields the following explicit representations:

$$i_R(t) = \frac{1}{2\sqrt{2}} [r_I(t) \cos \theta + r_Q(t) \sin \theta] * g_I(t)$$

$$+ \frac{1}{2\sqrt{2}} [r_I(t) \sin \theta - r_Q(t) \cos \theta] * g_Q(t), \tag{B-10}$$

and

$$q_R(t) = \frac{1}{2\sqrt{2}}[r_I(t)\cos\theta + r_Q(t)\sin\theta] * g_Q(t)$$

$$+ \frac{1}{2\sqrt{2}}[r_Q(t)\cos\theta - r_I(t)\sin\theta] * g_I(t). \qquad \text{(B-11)}$$

Next, we turn our attention to the second receiver arrangement depicted in Figure B-1c. In this case, the I- and Q-rail signals at the demodulator output may be expressed as

$$\left[\begin{array}{l}\text{I-Rail Signal}\\ \text{at Demodulator}\\ \text{Output}\end{array}\right] = \frac{1}{\sqrt{2}}r_I(t)\cos\theta + \frac{1}{\sqrt{2}}r_Q(t)\sin\theta$$

and (B-12)

$$\left[\begin{array}{l}\text{Q-Rail Signal}\\ \text{at Demodulator}\\ \text{Output}\end{array}\right] = \frac{1}{\sqrt{2}}r_Q(t)\cos\theta - \frac{1}{\sqrt{2}}r_I(t)\sin\theta.$$

Utilizing the above expressions and referring to Figure B-1c, we can, by inspection, conclude that

$$i_R'(t) = \frac{1}{\sqrt{2}}[r_I(t)\cos\theta + r_Q(t)\sin\theta] * g_{11}(t)$$

$$+ \frac{1}{\sqrt{2}}[r_Q(t)\cos\theta - r_I(t)\sin\theta] * g_{21}(t), \qquad \text{(B-13)}$$

and

$$q'(t) = \frac{1}{\sqrt{2}}[r_Q(t) \cos \theta - r_I(t) \sin \theta] * g_{22}(t)$$

$$+ \frac{1}{\sqrt{2}}[r_I(t) \cos \theta + r_Q(t) \sin \theta] * g_{12}(t). \qquad \text{(B-14)}$$

Comparing equations (B-13) and (B-14) to equations (B-10) and (B-11), respectively, we conclude that, for the two sets to be indistinguishable, we must have

$$\left.\begin{aligned} g_{11}(t) &= \tfrac{1}{2}\, g_I(t),\ g_{21}(t) = -\tfrac{1}{2}\, g_Q(t), \\ g_{22}(t) &= \tfrac{1}{2}\, g_I(t), \text{ and } g_{12}(t) = \tfrac{1}{2}\, g_Q(t). \end{aligned}\right\} \text{(B-15)}$$

Furthermore, we observe that

$$g_{11}(t) = g_{22}(t), \text{ and } g_{12}(t) = -g_{21}(t). \qquad \text{(B-16)}$$

Consequently, provided that the relationships of equations (B-15) and (B-16) hold, the two receiver filtering methodologies of Figures B-1b and B-1c become mathematically equivalent. In practice, the baseband receiver filter architecture of Figure B-1c often represents a preferred embodiment, since baseband signal processing is typically easier to implement, particularly when using digital techniques. The passband receiver filter configuration of Figure B-1b, however, is often preferred in performing mathematical analysis and optimization of the system, since it lends itself to the complex envelope representation. Having demonstrated the equivalence between the two configurations, mathematical results derived relative to passband filtering may easily, via the use of equations (B-15) and (B-16), be transformed to reflect the properties of the corresponding baseband configuration.

APPENDIX C

OPTIMAL LINEAR RECEIVERS IN THE MINIMUM MEAN-SQUARED ERROR SENSE AND THE LEAST MEAN-SQUARED ERROR ALGORITHM

APPENDIX C

OPTIMAL LINEAR RECEIVERS IN THE MINIMUM MEAN-SQUARED ERROR SENSE AND THE LEAST MEAN-SQUARED ERROR ALGORITHM

C.1 INTRODUCTION

The baseband equivalent QAM system model, as derived in paragraph 2.3 and shown in Figure 2-6c, is repeated here (Figure C-1) for convenience. In this appendix, we derive and establish optimum linear receiver filter characteristics which minimize the Mean-Squared Error (MSE) at the receiver sampling instants nT, n = 0, ± 1, ± 2, ... Initially, we do so without imposing any constraints on the linear receiver filter architecture. This leads to the optimum linear receiver structure of a matched filter followed by a synchronously spaced transversal equalizer. This optimum linear receiver architecture is shown equivalent to a fractionally spaced transversal filter structure. The stochastic gradient Least MSE (LMSE) algorithm is derived and used to adjust the coefficients of the fractionally spaced transversal filter in order to adaptively form the linear optimal receiver in the presence of arbitrary channel conditions. An inferior (but still optimal in the MSE sense) linear receiver characteristic is also derived by imposing the additional constraint that the linear receiver be realized via a synchronously spaced transversal filter architecture.

C.2 THE OPTIMAL SOLUTION

We begin the analysis, relative to Figure C-1, by defining the MSE at the n^{th} receiver sampling instant as

$$\varepsilon_n = E[|\overline{U}(nT) - \overline{I}_n|^2], \qquad (C\text{-}1)$$

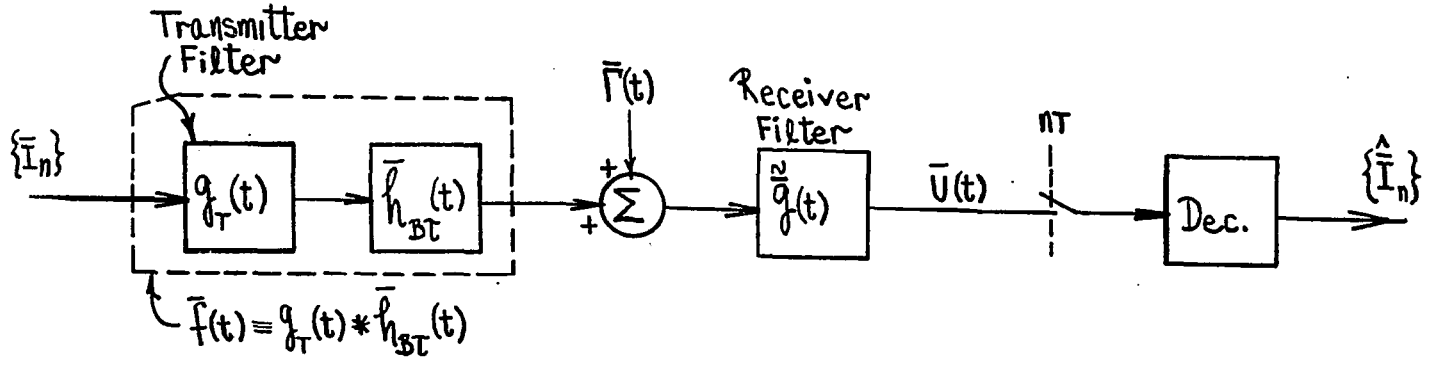

$\bar{h}_{BT}(t) \equiv \bar{h}_B(t+\tau) \equiv \tilde{\bar{h}}(t+\tau)e^{-j\theta}$ = Baseband Equivalent Channel

$\tilde{\bar{h}}(t) \equiv$ Complex Envelope of passband Channel

$\theta \equiv$ Demodulator Carrier phase

$\tau \equiv$ Receiver Sampler Phase

$\bar{\Gamma}(t) \equiv \bar{N}'(t+\tau) \equiv \frac{1}{\sqrt{2}} \tilde{\bar{N}}(t+\tau)e^{-j\theta}$ = Equivalent Thermal Noise

$\tilde{\bar{N}}(t) \equiv$ Complex Envelope of passband Thermal Noise

$\tilde{\bar{g}}(t) \equiv$ Complex Envelope of Passband Receiver Filter

Figure C-1. Baseband Equivalent QAM System Model

where $E[\cdot]$ denotes the statistical expectation (ensemble average) operator. The statistical expectation is taken over the entire ensemble of possible transmitted data sequences and thermal noise waveforms. Letting $\overline{x}(t)$ denote the overall impulse response of the system, we have

$$\overline{x}(t) \equiv \overline{f}(t) * \tilde{\overline{g}}(t) \equiv \int_{-\infty}^{\infty} \tilde{\overline{g}}(t)\overline{f}(t-\tau)d\tau, \tag{C-2}$$

where

$$\overline{f}(t) \equiv g_T(t) * \overline{h}_{B\tau}(t). \tag{C-3}$$

Using the above, the received random process waveform, $\overline{U}(t)$, may be written as

$$\overline{U}(t) = \sum_k \overline{I}_k \overline{x}(t-kT) + \overline{V}(t), \tag{C-4}$$

where

$$\overline{V}(t) \equiv \overline{r}(t) * \tilde{\overline{g}}(t) \tag{C-5}$$

denotes the filtered thermal noise process at the output of the receiver filter and where the input complex-valued data sequence, $\{\overline{I}_\eta\}$, has been assumed of the form

$$\{\overline{I}_\eta\} \equiv \sum_k \overline{I}_k \delta(t-kT). \tag{C-6}$$

Using equation (C-4), the n^{th} receiver observation may be expressed as

$$\overline{U}(nT) = \sum_k \overline{I}_k \overline{x}(nT-kT) + \overline{V}(nT), \tag{C-7}$$

or, in shorthand notation, as

$$\bar{U}_n = \sum_k \bar{I}_k \bar{x}_{n-k} + \bar{V}_n, \tag{C-8}$$

where $\bar{U}_n \equiv \bar{U}(nT)$, $\bar{x}_{n-k} \equiv \bar{x}(nT-kT)$, ..., etc.

Next, expanding equation (C-1) as

$$\begin{aligned} \varepsilon_n &= E[(\bar{U}_n - \bar{I}_n)(\bar{U}_n^* - \bar{I}_n^*)] \\ &= E[\bar{U}_n\bar{U}_n^* - \bar{I}_n^*\bar{U}_n - \bar{I}_n\bar{U}_n^* + \bar{I}_n\bar{I}_n^*], \end{aligned} \tag{C-9}$$

and substituting equation (C-8) into equation (C-9) yields

$$\begin{aligned} \varepsilon_n = E[&(\sum_k \bar{I}_k \bar{x}_{n-k} + \bar{V}_n)(\sum_m \bar{I}_m^* \bar{x}_{n-m}^* + \bar{V}_n^*) \\ &- \bar{I}_n^*(\sum_k \bar{I}_k \bar{x}_{n-k} + \bar{V}_n) - \bar{I}_n(\sum_k \bar{I}_k^* \bar{x}_{n-k}^* + \bar{V}_n^*) + \bar{I}_n\bar{I}_n^*]. \end{aligned} \tag{C-10}$$

To evaluate the above, the following assumptions are made:

a. $\bar{I}_k$ is identically distributed for $\forall k$, with zero mean and variance σ_I^2.

b. $\bar{I}_k$ and $\bar{I}_m$ are statistically independent for $\forall k \neq m$.

c. $\bar{I}_k$ and $\bar{V}_n$ are statistically independent for $\forall k, n$.

d. $\bar{V}_n$ is identically distributed for $\forall n$, with zero mean and variance σ_V^2.

Subject to the above assumptions, equation (C-10) may readily be evaluated to yield

$$\varepsilon_n = \sigma_I^2 \sum_k \bar{x}_{n-k}\bar{x}_{n-k}^* + \sigma_V^2 - \sigma_I^2\bar{x}_o - \sigma_I^2\bar{x}_o^* + \sigma_I^2. \tag{C-11}$$

Using equation (C-2) to evaluate the form of $\overline{x}_\ell$, followed by substitution into equation (C-11), results in

$$\varepsilon_n = \sigma_I^2 \int_{-\infty}^{\infty} \int_{-\infty}^{\infty} \tilde{g}(\tau)\tilde{g}^*(\eta) \sum_\ell \overline{f}(\ell T-\tau)\overline{f}^*(\ell T-\eta)d\tau d\eta$$

$$+ \int_{-\infty}^{\infty} \int_{-\infty}^{\infty} \tilde{g}(\tau)\tilde{g}^*(\eta)\phi_\Gamma(\tau-\eta)d\tau d\eta$$

$$- \sigma_I^2 \int_{-\infty}^{\infty} \tilde{g}(\tau)\overline{f}(-\tau)d\tau - \sigma_I^2 \int_{-\infty}^{\infty} \tilde{g}^*(\tau)\overline{f}^*(-\tau)d\tau + \sigma_I^2, \qquad \text{(C-12)}$$

where the following have been used in writing the above:

$$\sum_k |\overline{x}_{n-k}|^2 = \sum_\ell |\overline{x}_\ell|^2, \qquad \text{(C-13)}$$

and

$$\sigma_v^2 = E[\overline{V}_n \overline{V}_n^*] = \int_{-\infty}^{\infty} \int_{-\infty}^{\infty} \tilde{g}(\tau)\tilde{g}^*(\eta) E[\overline{\Gamma}(nT-\tau)\overline{\Gamma}^*(nT-\eta)]d\tau d\eta$$

$$\equiv \int_{-\infty}^{\infty} \int_{-\infty}^{\infty} \tilde{g}(\tau)\tilde{g}^*(\eta)\phi_\Gamma(\tau-\eta)d\tau d\eta. \qquad \text{(C-14)}$$

Also, we note that, in letting $E[\overline{\Gamma}(nT-\tau)\overline{\Gamma}^*(nT-\eta)]$ be represented by the autocorrelation function of the process $\overline{\Gamma}(t)$ evaluated at $\tau - \eta$, a stationarity assumption regarding the process $\overline{\Gamma}(t)$ has been invoked.

The MSE at the n^{th} sampling time, as expressed by equation (C-12), can be written more succinctly via the following definition. We let

$$\bar{a}(\tau,\eta) \equiv \sum_{\ell} \bar{f}(\ell T-\tau)\bar{f}^*(\ell T-\eta) + \frac{1}{\sigma_I^2}\phi_I(\tau-\eta), \tag{C-15}$$

thus placing ε_n in the form of

$$\varepsilon_n = \sigma_I^2\Big[\int_{-\infty}^{\infty}\int_{-\infty}^{\infty}\tilde{g}(\tau)\tilde{g}^*(\eta)\bar{a}(\tau,\eta)d\tau d\eta - \int_{-\infty}^{\infty}\tilde{g}(\tau)\bar{f}(-\tau)d\tau$$

$$- \int_{-\infty}^{\infty}\tilde{g}^*(\tau)\bar{f}^*(-\tau)d\tau + 1\Big]. \tag{C-16}$$

In order to determine the optimum receiver filter characteristic that minimizes ε_n, the first variation of ε_n with respect to the function $\tilde{g}$ must be taken, set to zero, and the value of $\tilde{g}$ satisfying the resulting equation must be evaluated. We have

$$\delta g_R(\varepsilon_n) = 0$$

$$\delta g_I(\varepsilon_n) = 0 \tag{C-17}$$

where g_R and g_I denote the real and imaginary parts of $\tilde{g}$, respectively.

Prior to performing the operations above, we rearrange equation (C-16) slightly; we have

$$\varepsilon_n = \sigma_I^2\Big\{\int_{-\infty}^{\infty}\Big[\int_{-\infty}^{\infty}\tilde{g}(\tau)\bar{a}(\tau,\eta)d\tau\Big]\tilde{g}^*(\eta)d\eta - \int_{-\infty}^{\infty}\tilde{g}(\tau)\bar{f}(-\tau)d\tau$$

$$- \int_{-\infty}^{\infty}\tilde{g}(\tau)\bar{f}^*(-\tau)d\tau + 1\Big\}, \tag{C-18}$$

or, more explicitly,

$$\varepsilon_n = \sigma_I^2\{\int_{-\infty}^{\infty}[\int_{-\infty}^{\infty}\overline{a}(\tau,\eta)(g_R(\tau)+jg_I(\tau))d\tau](g_R(\eta)-jg_I(\eta))d\eta$$

$$- \int_{-\infty}^{\infty}(g_R(\tau)+jg_I(\tau))\overline{f}(-\tau)d\tau - \int_{-\infty}^{\infty}(g_R(\tau)-jg_I(\tau))\overline{f}^*(-\tau)d\tau + 1\}. \qquad \text{(C-19)}$$

Hence,

$$\delta g_R(\varepsilon_n) = \sigma_I^2\{\int_{-\infty}^{\infty}[\int_{-\infty}^{\infty}\overline{a}(\tau,\eta)\tilde{\overline{g}}(\tau)d\tau + \tilde{\overline{g}}^*(\eta)\int_{-\infty}^{\infty}\overline{a}(\tau,\eta)d\tau]d\eta$$

$$- \int_{-\infty}^{\infty}\overline{f}(-\tau)d\tau - \int_{-\infty}^{\infty}\overline{f}^*(-\tau)d\tau\}, \qquad \text{(C-20)}$$

and

$$\delta g_I(\varepsilon_n) = \sigma_I^2\{\int_{-\infty}^{\infty}[-j\int_{-\infty}^{\infty}\overline{a}(\tau,\eta)\tilde{\overline{g}}(\tau)d\tau$$

$$+ j\tilde{\overline{g}}^*(\eta)\int_{-\infty}^{\infty}\overline{a}(\tau,\eta)d\tau]d\eta$$

$$- j\int_{-\infty}^{\infty}\overline{f}(-\tau)d\tau + j\int_{-\infty}^{\infty}\overline{f}^*(-\tau)d\tau\}. \qquad \text{(C-21)}$$

Setting equations (C-20) and (C-21) to zero and solving simultaneously yields

$$2\int_{-\infty}^{\infty}\int_{-\infty}^{\infty}\overline{a}(\tau,\eta)\tilde{\overline{g}}(\tau)d\tau d\eta - 2\int_{-\infty}^{\infty}\overline{f}^*(-\tau)d\tau = 0, \qquad \text{(C-22)}$$

where, to get equation (C-22), we have multiplied equation (C-21) by j and added the result to equation (C-20). Changing the dummy variable of integration of the second term of equation (C-22) from τ to η, we can write

$$\int_{-\infty}^{\infty}\left[\int_{-\infty}^{\infty}\overline{a}(\tau,\eta)\tilde{g}(\tau)d\tau - \overline{f}^*(-\eta)\right]d\eta = 0. \tag{C-23}$$

At this point, we observe that the integral with respect to η will vanish (as is required by the right-hand side of the equation) if we require that the integrand vanish. Hence, we require that*

$$\int_{-\infty}^{\infty}\overline{a}(\tau,\eta)\tilde{g}(\tau)d\tau - \overline{f}^*(-\eta) = 0. \tag{C-24}$$

Substituting definition (C-15) into equation (C-24) and slightly rearranging yields

$$\sum_{\ell}\overline{f}^*(\ell T-\eta)\int_{-\infty}^{\infty}\tilde{g}(\tau)\overline{f}(\ell T-\tau)d\tau - \overline{f}^*(-\eta) = \frac{1}{\sigma_I^2}\int_{-\infty}^{\infty}\tilde{g}(\tau)\phi_\Gamma(\eta-\tau)d\tau \tag{C-25}$$

or, equivalently, by using definition (C-2),

$$-\sum_{\ell}\overline{x}(\ell T)\overline{f}^*(\ell T-\eta) + \overline{f}^*(-\eta) = \frac{1}{\sigma_I^2}\int_{-\infty}^{\infty}\tilde{g}(\tau)\phi_\Gamma(\eta-\tau)d\tau. \tag{C-26}$$

* Note that the solution stemming from equation (C-24) may not be the only one satisfying equation (C-23) and, thus, the receiver filter characteristic minimizing ε_η may not be unique. This, however, is inconsequential at this point in the development.

Equation (C-26) is of the form

$$\sum_{\ell} \overline{\alpha}_{\ell} \overline{f}^{*}(\ell T - \eta) = \int_{-\infty}^{\infty} \tilde{\tilde{g}}(\tau) \phi_{\Gamma}(\eta - \tau) d\tau, \tag{C-27}$$

where

$$\alpha_{\ell} \equiv \begin{cases} -\sigma^2_{\overline{IX}}(0) + \sigma_I^2 \text{ for } \ell = 0 \\ -\sigma^2_{\overline{IX}}(\ell T), \text{ otherwise.} \end{cases} \tag{C-28}$$

Fourier transforming equation (C-27) with respect to η gives

$$\overline{F}^{*}(j\omega) \sum_{\ell} \overline{\alpha}_{\ell} e^{-j\omega \ell T} = \tilde{\tilde{G}}(j\omega) S_{\Gamma}(j\omega), \tag{C-29}$$

where $\overline{F}(j\omega) \equiv F[\overline{f}(\eta)]$, and $\tilde{\tilde{G}}(j\omega)$ and $S_{\Gamma}(j\omega)$ denote the transforms of $\tilde{\tilde{g}}(\tau)$ and $\phi_{\Gamma}(\eta)$, respectively. We are now in a position to examine the form of the optimum receiver filter characteristic that promises minimum MSE at the receiver observation instants. Assuming that the noise power spectral density does not vanish over the system bandwidth (a fair assumption), we may divide both sides of equation (C-29) by $S_{\Gamma}(j\omega)$, giving

$$\tilde{\tilde{G}}(j\omega) = \frac{\overline{F}^{*}(j\omega)}{S_{\Gamma}(j\omega)} \sum_{\ell} \overline{\alpha}_{\ell} e^{-j\omega \ell T}. \tag{C-30}$$

The term $\frac{\overline{F}^{*}(j\omega)}{S_{\Gamma}(j\omega)}$ may be envisioned as a noise whitener/matched filter combination (see Figure C-2 for interpretation), while the second term, $\sum_{\ell} \overline{\alpha}_{\ell} e^{-j\omega \ell T}$, represents a

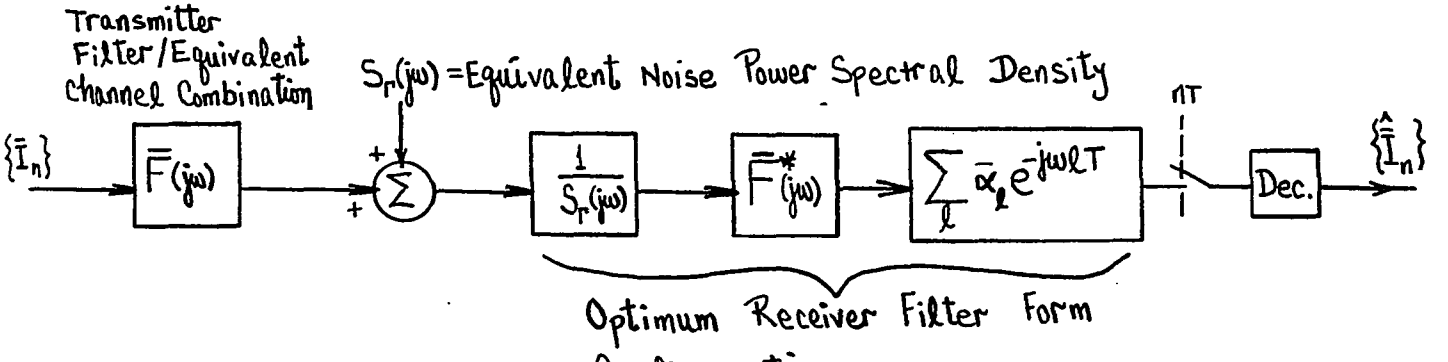

(a) Optimum Receiver Filter Configuration

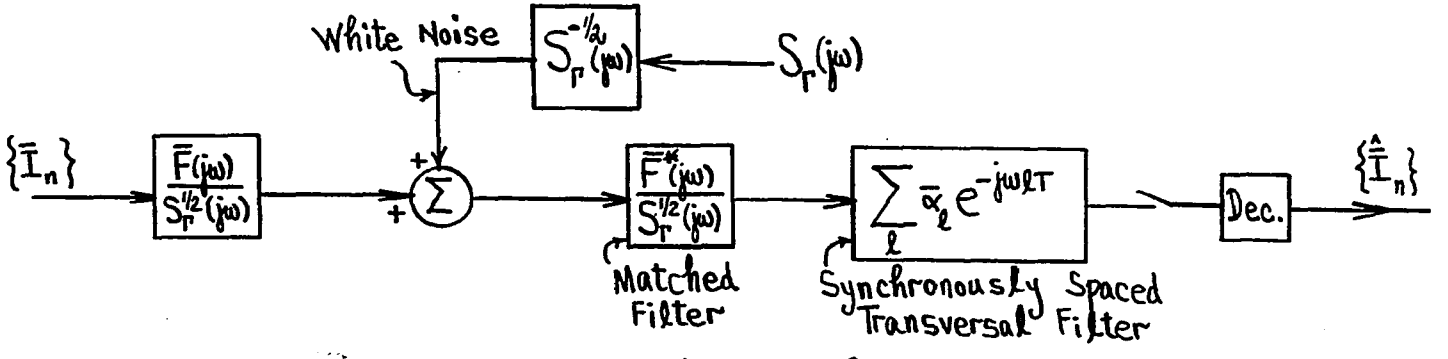

(b) Equivalent Representation of Optimum System (Redistribution of $1/S_r(j\omega)$)

Figure C-2. Interpretation of Optimum Receiver Filter

(noncausal*) synchronously spaced transversal filter architecture of infinite length. Letting

$$\frac{\overline{F}^*(j\omega)}{S_I(j\omega)} \equiv \overline{F}_e^*(j\omega) \multimap \overline{f}_e^*(-t), \text{ where } \overline{F}_e(j\omega) \multimap \overline{f}_e(t), \tag{C-31}$$

the inverse Fourier transformation of equation (C-30) yields

$$\tilde{\overline{g}}(t) = \sum_{\ell} \overline{\alpha}_\ell \overline{f}_e^*(\ell T - t). \tag{C-32}$$

Now, substituting equation (C-32) into equation (C-25) results in

$$\sum_{\ell} \overline{f}^*(\ell T - n) \int_{-\infty}^{\infty} \left(\sum_m \overline{\alpha}_m \overline{f}_e^*(mT-\tau)\right) \overline{f}(\ell T - \tau) d\tau$$

$$+ \frac{1}{\sigma_I^2} \int_{-\infty}^{\infty} \left(\sum_m \overline{\alpha}_m \overline{f}_e^*(mT-\tau)\right) \phi_I(n-\tau) d\tau = \overline{f}^*(-n). \tag{C-33}$$

Rearranging, we have

$$\sum_{\ell} \overline{f}^*(\ell T - n) \sum_m \overline{\alpha}_m \int_{-\infty}^{\infty} \overline{f}(\ell T - \tau) \overline{f}_e^*(mT-\tau) d\tau$$

$$+ \frac{1}{\sigma_I^2} \sum_m \overline{\alpha}_m \int_{-\infty}^{\infty} \overline{f}_e^*(mT-\tau)) \phi_I(n-\tau) d\tau = \overline{f}^*(-n). \tag{C-34}$$

* We note that, in general, both $\overline{F}^*(j\omega)$ and $\sum \overline{\alpha}_\ell e^{-j\omega\ell T}$ represent noncausal systems; this, however, is a mathematical artifice and of no practical concern.

Fourier transforming the above expression with respect to the continuous variable η gives

$$\sum_{\ell}\overline{F}^{*}(j\omega)e^{-j\omega\ell T}\sum_{m}\overline{\alpha}_{m}\overline{\psi}_{f}(\ell T-mT)$$

$$+\frac{1}{\sigma_I^2}\sum_{m}\overline{\alpha}_{m}\int_{-\infty}^{\infty}\overline{f}_{e}^{*}(mT-\tau)S_{\Gamma}(j\omega)e^{-j\omega\tau}d\tau \;=\; \overline{F}^{*}(j\omega), \tag{C-35}$$

where

$$F[\phi_{\Gamma}(n)] \;\equiv\; S_{\Gamma}(j\omega)$$

and

$$\overline{\psi}_{f}(\ell T-mT) \;\equiv\; \int_{-\infty}^{\infty}\overline{f}(\ell T-\tau)\overline{f}_{e}^{*}(mT-\tau)d\tau \;=\; \int_{-\infty}^{\infty}\overline{f}_{e}^{*}(\xi)\overline{f}(\xi+\ell T-mT)d\xi. \tag{C-36}$$

Rewriting equation (C-35) as

$$\overline{F}^{*}(j\omega)\sum_{\ell}\Big(\sum_{m}\overline{\alpha}_{m}\overline{\psi}_{f}(\ell T-mT)\Big)e^{-j\omega\ell T}$$

$$+\frac{1}{\sigma_I^2}S_{\Gamma}(j\omega)\overline{F}_{e}^{*}(j\omega)\sum_{m}\overline{\alpha}_{m}e^{-j\omega mT} \;=\; \overline{F}^{*}(j\omega), \tag{C-37}$$

and dividing through by $\overline{F}^{*}(j\omega)$ yields

$$\sum_{\ell}\Big(\sum_{m}\overline{\alpha}_{m}\overline{\psi}_{f}(\ell T-mT)\Big)e^{-j\omega\ell T}+\frac{1}{\sigma_I^2}\sum_{m}\overline{\alpha}_{m}e^{-j\omega mT} \;=\; 1. \tag{C-38}$$

We now observe that the first term of the left-hand side above represents the Fourier transform of the sequence $\{\sum_m \bar{\alpha}_m \bar{\psi}_f(\ell T - mT)\}$. This sequence, however, is the convolution of $\{\bar{\alpha}_n\}$ and $\{\bar{\psi}_f(nT)\}$, and, hence, the transform of $\{\sum_m \bar{\alpha}_m \bar{\psi}_f(\ell T - mT)\}$ may be evaluated by forming the product of $F[\{\bar{\alpha}_n\}]$ and $F[\{\bar{\psi}_f(nT)\}]$. The transform of the sequence $\{\bar{\psi}_f(nT)\}$ may easily be deduced by observing that (see equation (C-36))

$$\bar{\psi}_f(-nT) = \int_{-\infty}^{\infty} \bar{f}_e^*(\xi)\bar{f}(\xi - t)d\xi \Big|_{t=nT} = \int_{-\infty}^{\infty} \bar{f}(-\mu)\bar{f}_e^*(t-\mu)d\mu \Big|_{t=nT}$$

$$\equiv [\bar{f}(-t) * \bar{f}_e^*(t)]\Big|_{t=nT}. \tag{C-39}$$

Hence, since

$$F[\bar{f}(-t) * \bar{f}_e^*(t)] = \bar{F}(-j\omega)\bar{F}_e^*(-j\omega), \tag{C-40}$$

we conclude, using the result of the sampling theorem (see equation (2-8)), that

$$F[\{\bar{\psi}_f(-nT)\}] = \frac{1}{T}\sum_k \bar{F}(-j\omega + j\frac{2\pi k}{T})\bar{F}_e^*(-j\omega + j\frac{2\pi k}{T}) \tag{C-41}$$

and, consequently, it follows that

$$F[\{\bar{\psi}_f(nT)\}] = \frac{1}{T}\sum_k \bar{F}(j\omega + j\frac{2\pi k}{T})\bar{F}_e^*(j\omega + j\frac{2\pi k}{T}). \tag{C-42}$$

Returning now to equation (C-38), the result of equation (C-42) above may be utilized in solving for the remaining unknown, the Fourier transform of the transversal filter coefficients. We have

$$F[\{\bar{\alpha}_m\}] \equiv \sum_m \bar{\alpha}_m e^{-j\omega mT} = \frac{1}{F[\{\bar{\psi}_f(nT)\}] + \frac{1}{\sigma_I^2}}. \tag{C-43}$$

Finally, we can substitute this result in equation (C-30) to express the optimum minimum MSE receiver filter characteristic solely in terms of the channel and system parameters/characteristics. We have

$$\tilde{\bar{G}}(j\omega) = \frac{\bar{F}_e^*(j\omega)}{\frac{1}{T}\sum_k \bar{F}(j\omega+j\frac{2\pi k}{T})\bar{F}_e^*(j\omega+j\frac{2\pi k}{T}) + \frac{S_I(j\omega)}{\sigma_I^2}} \tag{C-44}$$

We observe that, subject to the simplification of a constant noise power spectral density, $S_I(j\omega) = N_o$, the optimum receiver filter characteristic reduces to[1]

$$\tilde{\bar{G}}(j\omega) = \frac{\bar{F}^*(j\omega)}{\frac{1}{T}\sum_k \left|\bar{F}(j\omega+j\frac{2\pi k}{T})\right|^2 + \frac{N_o}{\sigma_I^2}}. \tag{C-45}$$

As will become evident shortly, a fractionally spaced filter configuration may be utilized to adaptively form the function $\tilde{\bar{G}}(j\omega)$ specified above. This capability of the fractionally spaced filter will be discussed in detail in a later section of this appendix. Suffice it to say, at this point, that the one-sided bandwidth of the function $\bar{F}^*(j\omega)$ (and, hence, the bandwidth of $\tilde{\bar{G}}(j\omega)$) will, in general, exceed $\frac{\pi}{T}$ radians. That is, in general, we will have $|\tilde{\bar{G}}(j\omega)| = 0$ for $\forall|\omega| \geq \omega_M \ni: \omega_M \geq \frac{\pi}{T}$ (with ω_M being greater than $\frac{\pi}{T}$, but less than $\frac{2\pi}{T}$, in practice). Given this, a transversal filter structure with a transfer function of the form $\sum_n \bar{\xi}_n e^{-j\omega nT'}$ must, if it is to form the function $\tilde{\bar{G}}(j\omega)$ via an appropriate choice of its coefficients, be capable of exercising control over the entire bandwidth of $\tilde{\bar{G}}(j\omega)$. Since, by

definition, the bandwidth of $\tilde{\tilde{G}}(j\omega)$ extends from $-\omega_M$ to ω_M and the transversal filter's periodic transfer function has a period of $\frac{2\pi}{T'}$, we must have $\frac{\pi}{T'} \geq \omega_M$ or, equivalently, $\omega_M T' \leq \pi$, which implies that $T' < T$, since $\omega_M > \frac{\pi}{T}$. A transversal filter whose delay between taps (or coefficients) is less than the system's signaling interval is termed fractionally spaced as opposed to synchronously spaced (the term synchronously spaced is reserved for the case where $T' = T$). For the transfer function $\sum_n \overline{\xi}_n e^{-j\omega nT'}$ to converge (in the MSE sense) to the function $\tilde{\tilde{G}}(j\omega)$ over the interval $-\omega_M \leq \omega \leq \omega_M$, we must have

$$\overline{\xi}_n = \frac{T'}{2\pi} \int_{-\pi/T'}^{\pi/T'} \tilde{\tilde{G}}(j\omega) e^{j\omega nT'} d\omega \text{ for } \forall n. \qquad \text{(C-45a)}$$

One technique of adaptively forming (estimating) these optimum coefficients is discussed in paragraph C.4 below.

C.3 A SUBOPTIMAL SOLUTION

We now return to Figure C-1 and impose the additional constraint on the receiver filter that it have a transfer function of the form $\tilde{\tilde{G}}(j\omega) = \sum_k \overline{C}_k e^{-j\omega kT}$ or, equivalently, we require $\tilde{\tilde{g}}(t) = \sum_k \overline{C}_k \delta(t-kT)$, with the coefficient set $\{\overline{C}_k\}$ to be chosen optimally such as to minimize the MSE at the receiver sampling times. A choice of receiver filter architecture such as the one specified above defines the receiver as a synchronously spaced transversal filter configuration. In general, the synchronously spaced transversal filter receiver yields inferior performance as compared with its fractionally spaced counterpart[1]. However, because of the ease with which it lends itself to implementation (particularly in the digital domain),

it enjoys wide usage and is worthy of the following synoptic discussion. Given, therefore, that

$$\tilde{\bar{g}}(t) = \sum_k \bar{C}_k \delta(t-kT), \tag{C-46}$$

the received random process waveform, $\bar{U}(t)$ (see Figure C-1), will be

$$\bar{U}(t) = \int_{-\infty}^{\infty} \left(\sum_m \bar{C}_m \delta(\alpha - mt)\right)\left(\sum_k \bar{I}_k \bar{f}(t-\alpha-kT) + \bar{r}(t-\alpha)\right) d\alpha$$

$$= \sum_m \sum_k \bar{C}_m \bar{I}_k \bar{f}(t-mT-kT) + \sum_m \bar{C}_m \bar{r}(t-mT). \tag{C-47}$$

The value of $\bar{U}(t)$ at the n^{th} sampling instant ($t = nT$) can thus be expressed as

$$\bar{U}_n \equiv \bar{U}(nT) = \sum_m \sum_k \bar{C}_m \bar{I}_k \bar{f}_{n-m-k} + \sum_m \bar{C}_m \bar{r}_{n-m}, \tag{C-48}$$

where

$$\bar{f}_{n-m-k} \equiv \bar{f}(nT-mT-kT) \tag{C-49}$$

and

$$\bar{r}_{n-m} \equiv \bar{r}(nT-mT). \tag{C-50}$$

Substituting $\bar{U}_n$ in the expression of equation (C-9) for the MSE and evaluating yields

$$\varepsilon_n = \sigma_I^2 \sum_m \sum_k \sum_\ell \overline{C}_m \overline{C}_\ell^* \overline{f}_{n-m-k} \overline{f}_{n-\ell-k}^* - \sigma_I^2 \sum_m \overline{C}_m \overline{f}_{-m}$$

$$- \sigma_I^2 \sum_m \overline{C}_m^* \overline{f}_{-m}^* + \sigma_\Gamma^2 \sum_m |\overline{C}_m|^2 + \sigma_I^2, \qquad \text{(C-51)}$$

where

$$\sigma_\Gamma^2 \equiv E[|\overline{\Gamma}_n|^2], \qquad \text{(C-52)}$$

with the discrete time noise process $\{\overline{\Gamma}_n\}$ assumed stationary and of zero mean, and with $\overline{\Gamma}_n$ and $\overline{\Gamma}_m$ statistically independent for $\forall m \neq n$. Note that, in arriving at equation (C-51), the same assumptions leading to equation (C-11) have, once again, been invoked. To find the optimum set of coefficients $\{\overline{C}_k\}$ that minimize ε_n, the gradients of ε_n with respect to $\overline{C}_i$ ($i = \ldots, -1, 0, 1, 2, \ldots$) must be taken, set to zero and then solved for $\{\overline{C}_k\}$. We have

$$\left.\begin{aligned} \frac{\partial \varepsilon_n}{\partial C_{iR}} &= 0 \\ \frac{\partial \varepsilon_n}{\partial C_{iI}} &= 0 \end{aligned}\right\} i = \ldots -1, 0, 1, \ldots, \qquad \text{(C-53)}$$

where, as implied above, we have let

$$\overline{C}_i \equiv C_{iR} + jC_{iI}. \qquad \text{(C-54)}$$

Evaluating equation (C-53) yields

$$\frac{\partial \varepsilon_n}{\partial C_{iR}} = \sigma_I^2\{\sum_m \sum_k \overline{C}_m \overline{f}_{n-m-k} \overline{f}^*_{n-i-k}$$

$$+ \sum_k \sum_\ell \overline{C}^*_\ell \overline{f}_{n-i-k} \overline{f}^*_{n-\ell-k}\}$$

$$- \sigma_I^2 \overline{f}_{-i} - \sigma_I^2 \overline{f}^*_{-i} + \sigma_I^2\{\overline{C}_i + \overline{C}^*_i\} = 0, \tag{C-55}$$

and

$$\frac{\partial \varepsilon_n}{\partial C_{iI}} = \sigma_I^2\{-j\sum_m \sum_k \overline{C}_m \overline{f}_{n-m-k} \overline{f}^*_{n-i-k}$$

$$+ j\sum_k \sum_\ell \overline{C}^*_\ell \overline{f}_{n-i-k} \overline{f}^*_{n-\ell-k}\}$$

$$- j\sigma_I^2 \overline{f}_{-i} + j\sigma_I^2 \overline{f}^*_{-i} + \sigma_I^2\{-j\overline{C}_i + j\overline{C}^*_i\} = 0. \tag{C-56}$$

Multiplying equation (C-56) by j and adding the result to equation (C-55) gives

$$\sigma_I^2 \sum_m \sum_k \overline{C}_m \overline{f}_{n-m-k} \overline{f}^*_{n-i-k} - \sigma_I^2 \overline{f}^*_{-i} + \sigma_I^2 \overline{C}_i = 0. \tag{C-57}$$

Fourier transforming the above with respect to the discrete variable i, we have

$$\sigma_I^2 \sum_m \sum_k \overline{C}_m \overline{f}_{n-m-k} \overline{F}^*(e^{j\omega T}) e^{-j\omega n T} e^{j\omega k T}$$

$$- \sigma_I^2 \overline{F}^*(e^{j\omega T}) + \sigma_I^2 \overline{C}(e^{j\omega T}) = 0. \tag{C-58}$$

Rearranging slightly, we arrive at

$$\overline{F}^*(e^{j\omega T})\sum_m \overline{C}_m \sum_k \overline{f}_{n-m-k} e^{j\omega kT} e^{-j\omega nT}$$

$$+ \frac{\sigma_\Gamma^2}{\sigma_I^2} \overline{C}(e^{j\omega T}) = \overline{F}^*(e^{j\omega T}) \qquad \text{(C-59)}$$

or, equivalently,

$$|\overline{F}(e^{j\omega T})|^2 \overline{C}(e^{j\omega T}) + \frac{\sigma_\Gamma^2}{\sigma_I^2} \overline{C}(e^{j\omega T}) = \overline{F}^*(e^{j\omega T}). \qquad \text{(C-60)}$$

This last equation allows us to solve for the Fourier transform of the optimum transversal filter coefficient set. We have

$$\overline{C}(e^{j\omega T}) = \frac{\overline{F}^*(e^{j\omega T})}{|\overline{F}(e^{j\omega T})|^2 + \frac{\sigma_\Gamma^2}{\sigma_I^2}} \qquad \text{(C-61)}$$

and, hence,

$$\overline{C}_i = \frac{T}{2\pi} \int_{-\pi/T}^{\pi/T} \overline{C}(e^{j\omega T}) e^{j\omega iT} d\omega, \text{ for } \forall i. \qquad \text{(C-62)}$$

C.4 ADAPTIVE FORMATION OF OPTIMUM RECEIVER

A transversal receiver filter structure, as illustrated in Figure C-3, is postulated. The transversal filter is assumed to contain 2N + 1 coefficients, with the spacing (delay) between coefficients specified as T'. As mentioned earlier, if T' is chosen such that $T' \leq \frac{\pi}{\omega_M}$ (where ω_M defines the one-sided baseband equivalent

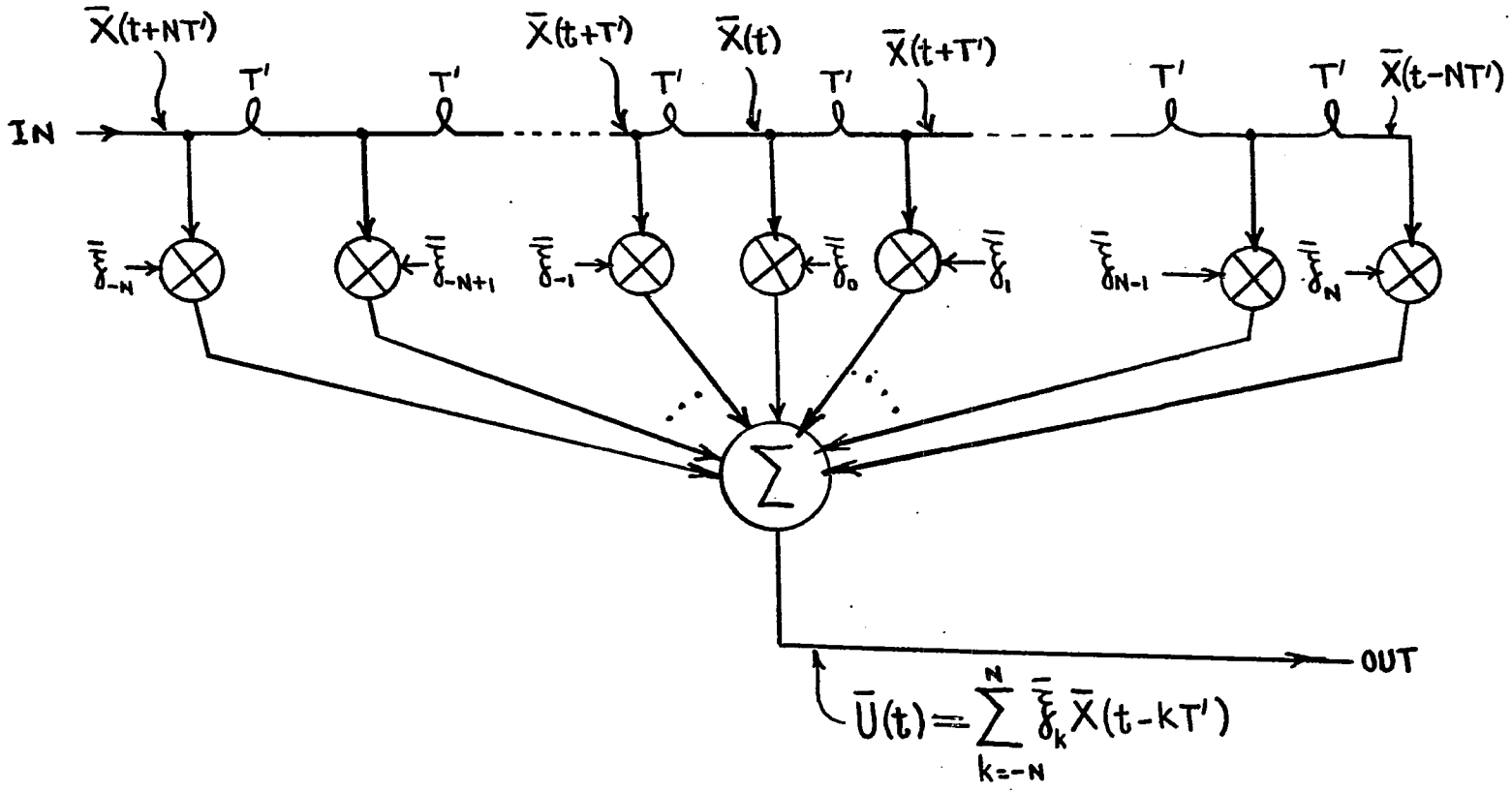

Figure C-3. Transversal Filter with 2N + 1 Coefficients

system bandwidth), the transversal filter periodic transfer function will be capable of exercising control over the entire system band and will thus be able to form the optimum linear receiver characteristic $\tilde{\tilde{G}}(j\omega)$ (as specified by equation (C-44)) via an appropriate choice of the coefficient set $\{\overline{\xi}_i\}$. If, on the other hand, the filter tap spacing T' is not smaller than, or at least equal to, $\frac{\pi}{\omega_M}$, the filter characteristic will, in general, deviate from optimality. If, for example, we set T' = T (where, in general, $T > \frac{\pi}{\omega_M}$), the transversal filter can, at best, form the transfer characteristic given by equation (C-61), which is, in general, suboptimum (in the LMSE sense) to the optimal linear receiver response of equation (C-44).

Independently of the value assigned to the transversal filter tap spacing parameter T', a time domain solution for the filter coefficient set that minimizes the MSE at the receiver sampling times is now sought. As indicated in Figure C-3, the transversal filter output can be expressed in terms of the filter coefficients and the signals residing on the filter delay line as

$$\overline{U}(t) = \sum_{k=-N}^{N} \overline{\xi}_k \overline{X}(t-kT'). \tag{C-63}$$

At the n^{th} receiver sampling time, we have

$$\overline{U}(nT) \equiv \overline{U}_n = \sum_{k=-N}^{N} \overline{\xi}_k \overline{X}(nt-kT') \equiv \underline{\overline{\xi}}^T \underline{\overline{X}}_n, \tag{C-64}$$

where

$$\underline{\bar{\xi}} \equiv \begin{bmatrix} \bar{\xi}_{-N} \\ \bar{\xi}_{-N+1} \\ \vdots \\ \bar{\xi}_0 \\ \bar{\xi}_1 \\ \vdots \\ \bar{\xi}_N \end{bmatrix} \quad \text{and} \quad \underline{\bar{X}}_n \equiv \begin{bmatrix} \bar{X}(nT+NT') \\ \bar{X}(nT+NT'-T') \\ \vdots \\ \bar{X}(nT) \\ \bar{X}(nT-T') \\ \vdots \\ \bar{X}(nT-NT') \end{bmatrix}, \tag{C-65}$$

and where the superscript T as used on a vector denotes transposition.

As seen from the definitions above, the complex-valued (2N + 1)X1 column vector $\underline{\bar{\xi}}$ expresses the transveral filter coefficients, while the complex-valued signal vector $\underline{\bar{X}}_n$ has, as its components, the delay line signal values evaluated at the n^{th} receiver sampling instant. Taking the form of $\bar{U}_n$ as given by equation (C-64) and substituting in the MSE expression of equation (C-9) yields

$$\begin{aligned} \varepsilon_n &= E[\underline{\bar{\xi}}^T \underline{\bar{X}}_n \underline{\bar{X}}_n^{*T} \underline{\bar{\xi}}^*] - E[\bar{I}_n^* \underline{\bar{\xi}}^T \underline{\bar{X}}_n] \\ &\quad - E[\bar{I}_n \underline{\bar{\xi}}^{*T} \underline{\bar{X}}_n^*] + \sigma_I^2 \end{aligned} \tag{C-66}$$

or, equivalently,

$$\begin{aligned} \varepsilon_n &= \underline{\bar{\xi}}^T E[\underline{\bar{X}}_n \underline{\bar{X}}_n^{*T}] \underline{\bar{\xi}}^* - \underline{\bar{\xi}}^T E[\bar{I}_n^* \underline{\bar{X}}_n] \\ &\quad - \underline{\bar{\xi}}^{*T} E[\bar{I}_n \underline{\bar{X}}_n^*] + \sigma_I^2 \\ &\equiv \underline{\bar{\xi}}^T \underline{\bar{r}} \, \underline{\bar{\xi}}^* - \underline{\bar{\xi}}^T \underline{\bar{p}} - \underline{\bar{\xi}}^{*T} \underline{\bar{p}}^* + \sigma_I^2, \end{aligned} \tag{C-67}$$

where

$$\underline{\bar{r}} \equiv E[\underline{\bar{X}}_n \underline{\bar{X}}_n^{*T}] \text{ and } \underline{\bar{p}} \equiv E[\bar{I}_n^* \underline{\bar{X}}_n], \tag{C-68}$$

with the matrix $\underline{\bar{r}}$ easily shown to be Hermitian ($\underline{\bar{r}}^{*T} = \underline{\bar{r}}$).

To find the optimum coefficient vector, $\underline{\bar{\xi}}^0$, that minimizes ε_n, the gradient of ε_n with respect to $\underline{\bar{\xi}}$ must be taken, set to zero and then solved for $\underline{\bar{\xi}}$. We have

$$\nabla_{\underline{\bar{\xi}}} \varepsilon_n = \begin{cases} \nabla_{\underline{\xi}_R} \varepsilon_n = 0 \\ \text{and} \\ \nabla_{\underline{\xi}_I} \varepsilon_n = 0, \end{cases} \tag{C-69}$$

where

$$\underline{\bar{\xi}} \equiv \underline{\xi}_R + j\underline{\xi}_I. \tag{C-70}$$

Furthermore, we have

$$\nabla_{\underline{\xi}_R} \varepsilon_n = 0 \leftrightarrow \frac{\partial \varepsilon_n}{\partial \xi_{R\ell}} = 0; \; \ell = 1, 2, 3, \ldots, 2N + 1; \tag{C-71}$$

and

$$\nabla_{\underline{\xi}_I} \varepsilon_n = 0 \leftrightarrow \frac{\partial \varepsilon_n}{\partial \xi_{I\ell}} = 0; \; \ell = 1, 2, 3, \ldots, 2N + 1. \tag{C-72}$$

Performing the operations indicated above, we find (after some algebraic manipulation)

$$\nabla_{\underline{\xi}_R} \varepsilon_n = 2\mathrm{Re}[\underline{\bar{r}}\, \underline{\bar{\xi}}^*] - \underline{\bar{p}} - \underline{\bar{p}}^* = 0 \tag{C-73}$$

and

$$\nabla_{\underline{\xi}_I} \varepsilon_n = -2\mathrm{Im}[\underline{\bar{r}}\,\underline{\bar{\xi}}^*] - j\underline{\bar{p}} + j\underline{\bar{p}}^* = 0. \tag{C-74}$$

Multiplying equation (C-74) by -j and adding to equation (C-73) produces the result

$$2\underline{\bar{r}}\,\underline{\bar{\xi}}^* - 2\underline{\bar{p}} = 0. \tag{C-75}$$

The optimum, in the LMSE sense, transversal filter coefficient vector is thus defined by the relation

$$(\underline{\bar{\xi}}^o)^* = \underline{\bar{r}}^{-1}\underline{\bar{p}}. \tag{C-76}$$

The best choice of transversal filter coefficients, as defined above, may be found (in the mean) by applying Widrow's Stochastic Gradient Algorithm[2] to the situation at hand. As is shown below, the control law

$$\underline{\bar{\xi}}^*_{k+1} = \underline{\bar{\xi}}^*_k + \mu \bar{E}^*_n \underline{\bar{X}}_n, \tag{C-77}$$

where

$$\bar{E}_n \equiv \bar{I}_n - \bar{U}_n, \tag{C-78}$$

denoting the receiver error at the n^{th} sampling time, finds the complex-valued coefficient vector $\underline{\bar{\xi}}_{k+1}$ such that

$$\lim_{k\to\infty} E[\underline{\bar{\xi}}^*_{k+1}] = (\underline{\bar{\xi}}^o)^* = \underline{\bar{r}}^{-1}\underline{\bar{p}}. \tag{C-79}$$

To show the above, we use

$$\bar{E}_n \equiv \bar{I}_n - \bar{U}_n = \bar{I}_n - \underline{\bar{\xi}}^T_k \underline{\bar{X}}_n \tag{C-80}$$

and substitute into equation (C-77), giving

$$\begin{aligned}\underline{\bar{\xi}}^*_{k+1} &= \underline{\bar{\xi}}^*_k + \mu(I^*_n - \underline{\bar{\xi}}^{*T}_k \underline{X}^*_n)\underline{X}_n \\ &= \underline{\bar{\xi}}^*_k - \mu \underline{\bar{X}}_n \underline{X}^{*T}_n \underline{\bar{\xi}}^*_k + \mu I^*_n \underline{X}_n .\end{aligned} \tag{C-81}$$

Taking the expectation of the above expression yields

$$E[\underline{\bar{\xi}}^*_{k+1}] = E[\underline{\bar{\xi}}^*_k] - \mu \underline{\bar{r}} E[\underline{\bar{\xi}}^*_k] + \mu \underline{\bar{p}}, \tag{C-82}$$

where the relationship

$$E[\underline{\bar{X}}_n \underline{X}^{*T}_n \underline{\bar{\xi}}^*_k] = E[\underline{\bar{X}}_n \underline{X}^{*T}_n] E[\underline{\bar{\xi}}^*_k] \tag{C-83}$$

has been assumed to hold and definitions (C-68) have been used. We point out that the assumption (C-83) is not difficult to justify, particularly when the control law (C-77) is updated once every several baud intervals corresponding to a time span exceeding the memory of the channel.

Since the discrete channel autocorrelation matrix $\underline{\bar{r}}$ appearing in equation (C-82) is Hermitian ($\underline{\bar{r}}^{*T} = \underline{\bar{r}}$), it can be expressed in terms of its corresponding eigenvector and eigenvalue matrices, $\underline{\bar{q}}$ and $\underline{\lambda}$, respectively. We have

$$\underline{\bar{r}} = \underline{\bar{q}}\, \underline{\lambda}\, \underline{\bar{q}}^{-1}, \tag{C-84}$$

where the columns of the eigenvector matrix $\underline{\bar{q}}$ are formed by the normalized eigenvectors of $\underline{\bar{r}}$ and where the real-valued eigenvalue matrix $\underline{\lambda}$ is a diagonal matrix whose main diagonal is made up of the eigenvalues of $\underline{\bar{r}}$. Using the represenттion of equation (C-84) and substituting into equation (C-82), we attain

$$\begin{aligned}E[\underline{\bar{\xi}}^*_{k+1}] &= (\underline{I} - \mu \underline{\bar{q}}\, \underline{\lambda}\, \underline{\bar{q}}^{-1}) E[\underline{\bar{\xi}}^*_k] + \mu \underline{\bar{p}} \\ &= \underline{\bar{q}}(\underline{I} - \mu\underline{\lambda})\underline{\bar{q}}^{-1} E[\underline{\bar{\xi}}^*_k] + \mu \underline{\bar{p}},\end{aligned} \tag{C-85}$$

where $\underline{I}$ denotes the identity matrix. Multiplying both sides of equation (C-85) from the left by $\bar{\underline{q}}^{-1}$ gives

$$E[\bar{\underline{\zeta}}^{*}_{k+1}] = (\underline{I}-\mu\underline{\lambda})E[\bar{\underline{\zeta}}^{*}_{k}] + \mu\bar{\underline{p}}', \tag{C-86}$$

where

$$\bar{\underline{\zeta}}^{*}_{k} \equiv \bar{\underline{q}}^{-1}\bar{\underline{\zeta}}^{*}_{k} \text{ and } \bar{\underline{p}}' \equiv \bar{\underline{q}}^{-1}\bar{\underline{p}}. \tag{C-87}$$

Equation (C-86) is a first order, complex-valued, vector matrix difference equation. It represents 2N + 1 complex-valued scalar difference equations in the transformed coefficients $\{\bar{\zeta}_i\}$, i = -N, -N + 1, ..., -1, 0, 1, ..., N. These equations are all decoupled, owing to the diagonal nature of both $\underline{I}$ and $\underline{\lambda}$, and, hence, they can easily be solved. For the i^{th} such equation, we have

$$E[(\bar{\zeta}_i)^{*}_{k+1}] = (1-\mu\lambda_i)E[(\bar{\zeta}_i)^{*}_{k}] + \mu p'_i, \tag{C-88}$$

where $(\bar{\zeta}_i)_k$ denotes the i^{th} component of $\bar{\underline{\zeta}}_k$, λ_i is the i^{th} eigenvalue of $\bar{\underline{r}}$ (and the diagonal entry of the i^{th} row of $\underline{\lambda}$) and $\bar{p}'_i$ denotes the i^{th} component of $\bar{\underline{p}}'$. Solving equation (C-88), we find

$$E[(\bar{\zeta}_i)^{*}_{k+1}] = (1-\mu\lambda_i)^{k+1}E[(\bar{\zeta}_i)^{*}_{o}] + \mu\bar{p}'_i\left[\frac{1-(1-\mu\lambda_i)^{k}}{1-(1-\mu\lambda_i)}\right]. \tag{C-89}$$

With the step size parameter μ chosen appropriately small such that $0 < \mu\lambda_i < 2$, the first term of equation (C-89) goes to zero in the limit as $k \to \infty$, while the second term approaches $\frac{\bar{p}'_i}{\lambda_i}$. Thus,

$$\lim_{k\to\infty} E[(\bar{\zeta}_i)^*_{k+1}] = \frac{\bar{p}_i'}{\lambda_i} \tag{C-90}$$

or, equivalently,

$$\lim_{k\to\infty} E[\bar{\underline{\zeta}}^*_{k+1}] = \underline{\lambda}^{-1}\bar{\underline{p}}'. \tag{C-91}$$

Finally, using definition (C-87), we conclude

$$\lim_{k\to\infty} E[\bar{\underline{\xi}}^*_{k+1}] = \bar{\underline{q}}\,\underline{\lambda}^{-1}\bar{\underline{q}}^{-1}\bar{\underline{p}} = \bar{\underline{r}}^{-1}\bar{\underline{p}} \equiv (\bar{\underline{\xi}}^o)^*. \tag{C-92}$$

We see that the control law (C-77) has converged, in the mean, to the optimal coefficient vector, which minimizes the ensemble averaged squared error at the receiver sampling instants.

REFERENCES

[1] R. D. Gitlin and S. B. Weinstein, "Fractionally Spaced Equalization: An Improved Digital Transversal Equalizer", Bell System Technical Journal, Feburary 1981, Volume 60, No. 2

[2] B. Widrow, J. M. McCool, M. G. Larimore, and C. R. Johnson, Jr., "Stationary and Nonstationary Learning Characteristics of the LMS Adaptive Filter", Proc. IEEE, Volume 64, No. 8, pages 1151 to 1162, August 1976

APPENDIX D

OPTIMAL LINEAR RECEIVERS IN THE NYQUIST SENSE AND THE ZERO-FORCING ALGORITHM

APPENDIX D

OPTIMAL LINEAR RECEIVERS IN THE NYQUIST SENSE AND THE ZERO-FORCING ALGORITHM

D.1 THE OPTIMAL SOLUTION IN THE NYQUIST SENSE

We begin the analysis by seeking the optimum linear receiver filter which minimizes the thermal noise variance at its output subject to the zero Intersymbol Interference (ISI) constraint. That is, the overall system transfer characteristic, $\overline{X}(j\omega) \equiv \overline{F}(j\omega)\tilde{\tilde{G}}(j\omega)$, is contrained to satisfy equation (2-51) (repeated below for convenience)

$$\sum_k \overline{X}(j\omega + j\frac{2\pi k}{T}) = T \text{ for } |\omega| \leq \frac{\pi}{T}, \tag{D-1}$$

while the receiver filter characteristic is optimally chosen for minimum output thermal noise variance. Clearly, this is a constrained optimization problem which can be handled via the Lagrange multiplier approach. We observe that minimizing a performance index such as the filtered noise mean-squared value subject to the zero ISI constraint also minimizes the probability of error in the system subject to the same constraint.

In reference to Figure D-1, the filtered thermal noise variance (or, equivalently, its mean-squared value, since we assume zero mean statistics) is

$$\sigma_v^2 = E[\overline{V}(t)\overline{V}^*(t)] \equiv E[|\tilde{\tilde{g}}(t) * \overline{r}(t)|^2] \tag{D-2}$$

or, in terms of frequency domain quantities,

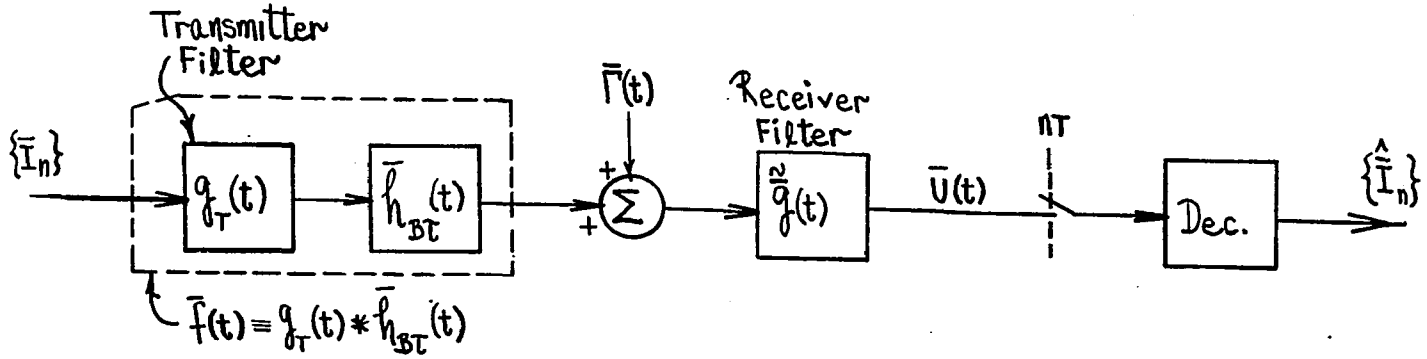

$\bar{h}_{BT}(t) \equiv \bar{h}_B(t+\tau) \equiv \tilde{\bar{h}}(t+\tau)e^{-j\theta}$ = Baseband Equivalent Channel

$\tilde{\bar{h}}(t) \equiv$ Complex Envelope of passband Channel

$\theta \equiv$ Demodulator Carrier phase

$\tau \equiv$ Receiver Sampler Phase

$\bar{\Gamma}(t) \equiv \bar{N}'(t+\tau) \equiv \frac{1}{\sqrt{2}} \tilde{\bar{N}}(t+\tau)e^{-j\theta}$ = Equivalent Thermal Noise

$\tilde{\bar{N}}(t) \equiv$ Complex Envelope of passband Thermal Noise

$\tilde{\bar{g}}(t) \equiv$ Complex Envelope of Passband Receiver Filter

Figure D-1. Baseband Equivalent QAM System Model

$$\sigma_v^2 = \frac{1}{2\pi}\int_{-\infty}^{\infty}|\tilde{\bar{G}}(j\omega)|^2 S_{\bar{\Gamma}}(j\omega)d\omega, \tag{D-3}$$

where $S_{\bar{\Gamma}}(j\omega)$ denotes the power spectral density of the baseband equivalent input thermal noise process $\bar{\Gamma}(t)$.

Equation (D-3) can easily be rearranged and placed in the form of

$$\sigma_v^2 = \frac{1}{2\pi}\int_{-\pi/T}^{\pi/T}[\sum_k|\tilde{\bar{G}}(j\omega+j\frac{2\pi k}{T})|^2 S_{\bar{\Gamma}}(j\omega+j\frac{2\pi k}{T})]d\omega, \tag{D-4}$$

thus providing a statement of the noise variance (to be minimized) in terms of the same frequency band, $|\omega| \leq \frac{\pi}{T}$, over which the constraint equation (equation (D-1)) is valid. Since the quantity σ_v^2 is to be minimized subject to the zero ISI contraint and since the integrand of equation (D-4) is positive (or zero) for every ω within the band $|\omega| \leq \frac{\pi}{T}$, minimizing the integrand at each ω from $-\frac{\pi}{T}$ to $\frac{\pi}{T}$, subject to the constraint, is equivalent to minimizing σ_v^2 subject to the same constraint. Therefore, taking the Lagrange multiplier approach, we define a performance index as[1]

$$J = \sum_k|\tilde{\bar{G}}(j\omega+j\frac{2\pi k}{T})|^2 S_{\bar{\Gamma}}(j\omega+j\frac{2\pi k}{T})$$

$$+ \lambda[\sum_k \bar{F}(j\omega+j\frac{2\pi k}{T})\tilde{\bar{G}}(j\omega+j\frac{2\pi k}{T}) - T] \text{ for } |\omega| \leq \frac{\pi}{T}. \tag{D-5}$$

To minimize J with respect to the unknowns $|\tilde{\bar{G}}(j\omega + j\frac{2\pi\ell}{T})|$ ($\ell = 0, \pm1, \pm2, \ldots$) and λ, the associated partial derivatives must be taken, set to zero and solved. We have

$$\frac{\partial J}{\partial |\tilde{\tilde{G}}(j\omega+j\frac{2\pi\ell}{T})|} = 2|\tilde{\tilde{G}}(j\omega+j\frac{2\pi\ell}{T})|S_r(j\omega+j\frac{2\pi\ell}{T})$$

$$+ \lambda\overline{F}(j\omega+j\frac{2\pi\ell}{T})e^{j\theta(\omega+\frac{2\pi\ell}{T})}$$

$$= 0 \text{ for } |\omega| \leq \frac{\pi}{T} \text{ and } \forall\ell \qquad \text{(D-6)}$$

and

$$\frac{\partial J}{\partial \lambda} = \sum_k \overline{F}(j\omega+j\frac{2\pi k}{T})\tilde{\tilde{G}}(j\omega+j\frac{2\pi k}{T}) - T = 0 \text{ for } |\omega| \leq \frac{\pi}{T}, \qquad \text{(D-7)}$$

where $\theta(\omega)$ denotes the phase characteristic of $\tilde{\tilde{G}}(j\omega)$; that is,

$$\tilde{\tilde{G}}(j\omega) \equiv |\tilde{\tilde{G}}(j\omega)|e^{j\theta(\omega)}. \qquad \text{(D-8)}$$

Rearranging equation (D-6) gives

$$|\tilde{\tilde{G}}(j\omega+j\frac{2\pi\ell}{T})|e^{-j\theta(\omega+\frac{2\pi\ell}{T})} = -\frac{\lambda}{2}\frac{\overline{F}(j\omega+j\frac{2\pi\ell}{T})}{S_r(j\omega+j\frac{2\pi\ell}{T})} \text{ for } |\omega| \leq \frac{\pi}{T} \text{ and } \forall\ell, \qquad \text{(D-9)}$$

and, with the help of definition (D-8), we conclude

$$\tilde{\tilde{G}}(j\omega+j\frac{2\pi\ell}{T}) = -\frac{\lambda}{2}\frac{\overline{F}^*(j\omega+j\frac{2\pi\ell}{T})}{S_r(j\omega+j\frac{2\pi\ell}{T})} \text{ for } |\omega| \leq \frac{\pi}{T} \text{ and } \forall\ell \qquad \text{(D-10)}$$

or, equivalently,

$$\tilde{\bar{G}}(j\omega) = -\frac{\lambda}{2}\frac{\bar{F}^*(j\omega)}{S_r(j\omega)} \text{ for } \forall_\omega. \tag{D-11}$$

In order to solve for the unknown λ, equation (D-10) may be substituted into equation (D-7), giving

$$-\frac{\lambda}{2}\sum_k \frac{|\bar{F}(j\omega+j\frac{2\pi k}{T})|^2}{S_r(j\omega+j\frac{2\pi k}{T})} = T \text{ for } |\omega| \leq \frac{\pi}{T}. \tag{D-12}$$

Solving for $-\frac{\lambda}{2}$ from equation (D-12) and substituting the result into equation (D-11) gives

$$\tilde{\bar{G}}(j\omega) = \frac{\bar{F}^*(j\omega)}{\frac{S_r(j\omega)}{T}\sum_k \frac{|\bar{F}(j\omega+j\frac{2\pi k}{T})|^2}{S_r(j\omega+j\frac{2\pi k}{T})}} \tag{D-13}$$

or, equivalently,

$$\tilde{\bar{G}}(j\omega) = \frac{\bar{F}_e^*(j\omega)}{\frac{1}{T}\sum_k \bar{F}(j\omega+j\frac{2\pi k}{T})\bar{F}_e^*(j\omega+j\frac{2\pi k}{T})}, \tag{D-14}$$

where

$$\bar{F}_e(j\omega) \equiv \frac{\bar{F}(j\omega)}{S_r(j\omega)}. \tag{D-15}$$

Observe that, subject to the simplification of a constant noise power spectral density, $S_r(j\omega) = N_o$, the optimum receiver filter transfer function given by equation (D-14) reduces to

$$\tilde{G}(j\omega) = \frac{\overline{F}^*(j\omega)}{\frac{1}{T}\sum_k |\overline{F}(j\omega + j\frac{2\pi k}{T})|^2} \qquad \text{(D-16)}$$

Furthermore, observe that the optimum solution does force the overall system to be Nyquist, as can readily be seen by straightforward substitution of equation (D-14) into equation (D-1).

The general form of the optimum Nyquist filter may be viewed/interpreted as representing the following two-stage configuration: a first stage comprising a noise whitener/matched filter combination, followed by a second stage representing an infinitely long synchronously spaced transversal filter. The first stage (the noise whitener/matched filter combination) is an interpretation of the numerator term of equation (D-14), while the periodic nature of the denominator naturally lends itself to a transversal filter interpretation/visualization. Figure D-2 further illustrates the structure of the optimum Nyquist filter.

D.2 A SUBOPTIMUM SOLUTION AND ITS ADAPTIVE FORMATION

A suboptimum (and simpler) solution in the Nyquist sense can be derived by allowing the receiver to assume the form of a synchronously spaced transversal filter. With a receiver filter configuration as that shown in Figure D-3, the Nyquist zero ISI constraint of equation (D-1) becomes

$$\tilde{G}(j\omega)\sum_k \overline{F}(j\omega + j\frac{2\pi k}{T}) = T \text{ for } |\omega| \leq \frac{\pi}{T}, \qquad \text{(D-17)}$$

since

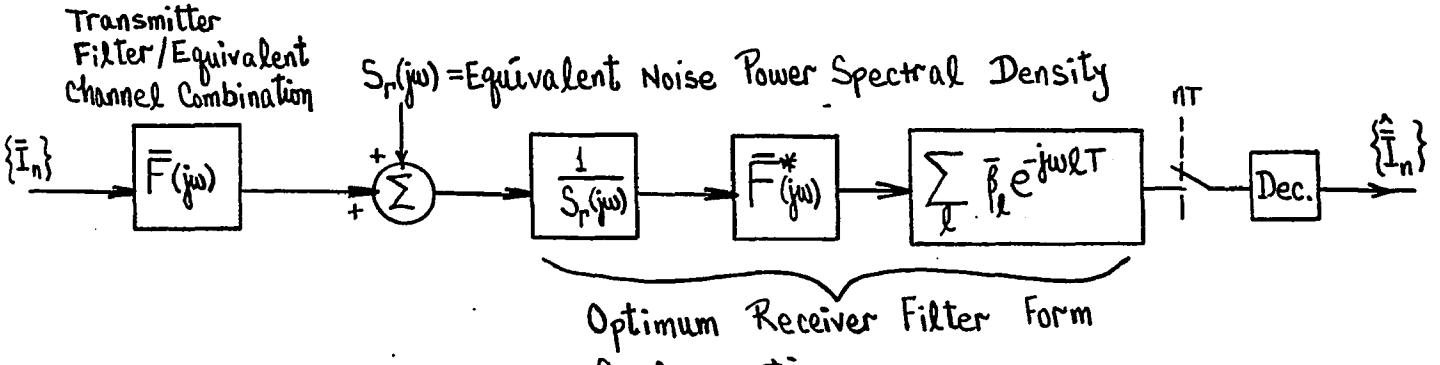

(a) Optimum Receiver Filter Configuration

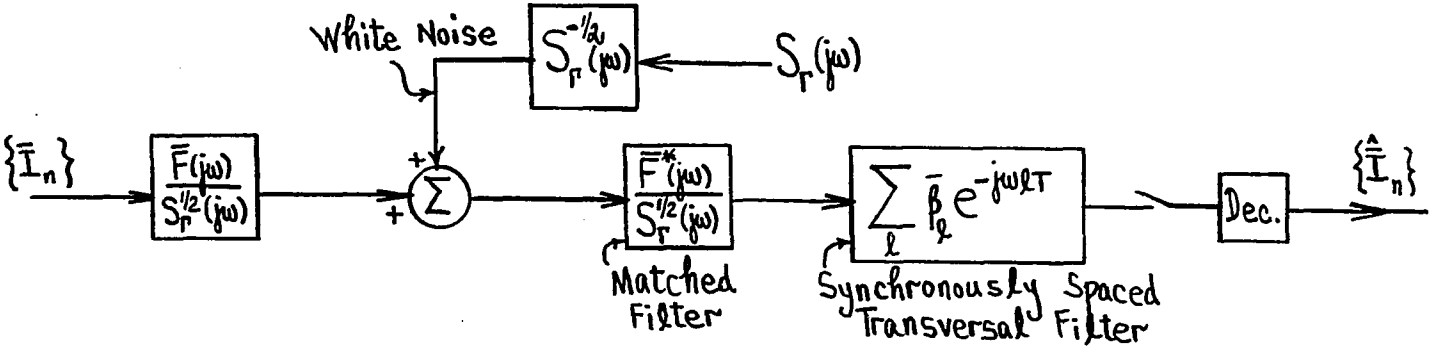

(b) Equivalent Representation of Optimum System (Redistribution of $1/S_r(j\omega)$)

Figure D-2. Interpretation of Optimal Nyquist Receiver Filter

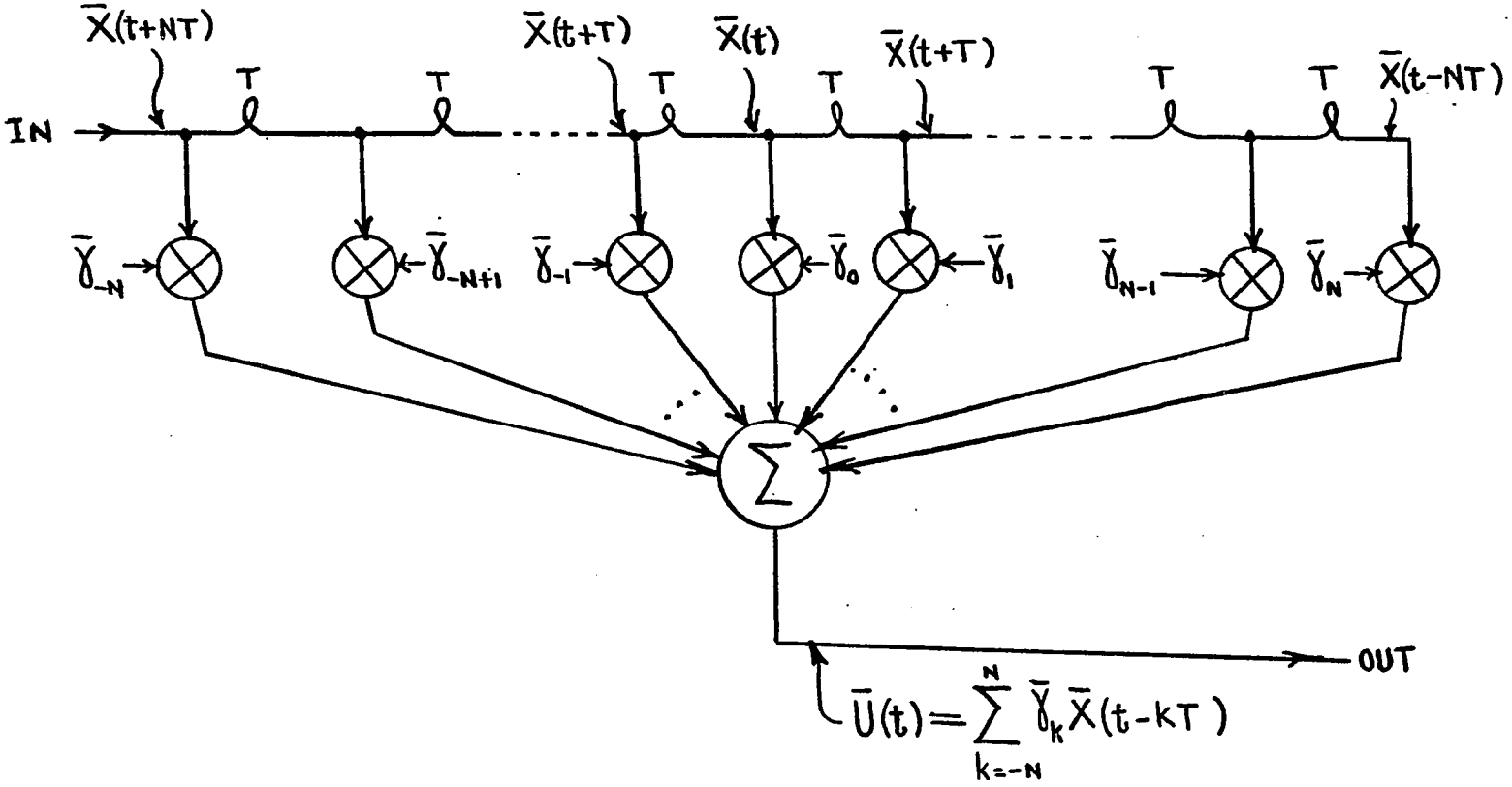

Figure D-3. Transversal Filter with 2N + 1 Coefficients

$$\tilde{\bar{G}}(j\omega) = e^{-j\omega NT} \sum_{i=-N}^{N} \bar{\gamma}_i e^{-j\omega iT} = \tilde{\bar{G}}(j\omega + j\frac{2\pi\ell}{T}); \ \ell = 0, \pm 1, \pm 2, \ldots \tag{D-18}$$

is now a periodic transfer function (see Figure D-3). Solving equation (D-17) for $\tilde{\bar{G}}(j\omega)$, we find

$$\tilde{\bar{G}}(j\omega) = \frac{T}{\sum_{k} \bar{F}(j\omega + j\frac{2\pi k}{T})} \text{ for } |\omega| \leq \frac{\pi}{T}. \tag{D-19}$$

The suboptimum solution found above does force the overall system to be Nyquist. However, it makes no attempt to minimize thermal noise effects. Despite this, it has enjoyed applications in ISI limited channels[2] (operating at fairly large signal-to-noise ratios), owing to its conceptual simplicity and ease of implementation.

Focusing now on Figure D-3, the output waveform, $\bar{U}(t)$, evaluated at the n^{th} sampling instant, may be expressed in terms of the filter coefficients as

$$\bar{U}_n \equiv \bar{U}(nT) = \sum_{i=-N}^{N} \bar{\gamma}_i \bar{X}(nT - iT) \equiv \sum_{i=-N}^{N} \bar{\gamma}_i \bar{X}_{n-i} \tag{D-20}$$

or as

$$\bar{U}_n = \underline{\bar{\gamma}}^T \underline{\bar{X}}_n, \tag{D-20a}$$

where

$$\underline{\overline{Y}} \equiv \begin{bmatrix} \overline{Y}_{-N} \\ \overline{Y}_{-N+1} \\ \vdots \\ \overline{Y}_0 \\ \overline{Y}_1 \\ \vdots \\ \overline{Y}_N \end{bmatrix} \quad \text{and} \quad \underline{X}_n \equiv \begin{bmatrix} X_{n+N} \\ X_{n+N-1} \\ \vdots \\ X_n \\ X_{n-1} \\ \vdots \\ X_{n-N} \end{bmatrix} \tag{D-20b}$$

The waveform at the filter's input, $\overline{X}(t + NT)$, may be written as

$$\overline{X}(t+NT) = \sum_k \overline{I}_k \overline{f}(t-kT) + \overline{r}(t) \tag{D-21}$$

and, therefore,

$$\overline{X}(t) = \sum_k \overline{I}_k \overline{f}(t-NT-kT) + \overline{r}(t-NT). \tag{D-22}$$

Evaluating $\overline{X}_{n-i}$ from the above expression and substituting in equation (D-20) gives

$$\overline{U}_n = \sum_{i=-N}^{N} \overline{\gamma}_i \left[\sum_k \overline{I}_k \overline{f}_{n-i-N-k} + \overline{r}_{n-i-N}\right]$$

$$= \sum_k \overline{I}_k \sum_{i=-N}^{N} \overline{\gamma}_i \overline{f}_{n-i-N-k} + \sum_{i=-N}^{N} \overline{\gamma}_i \overline{r}_{n-i-N}, \tag{D-23}$$

where

$$\overline{f}_{n-i-N-k} \equiv \overline{f}(nT-iT-NT-kT) \text{ and } \overline{r}_{n-i-N} \equiv \overline{r}(nT-iT-NT). \tag{D-24}$$

Since we desire to force the ISI to zero, we require that

$$\sum_{\ell=-N}^{N} \bar{\gamma}_\ell \bar{f}_{n-\ell-N-k} = \begin{cases} 1 \text{ for } k = n \\ 0 \text{ otherwise.} \end{cases} \tag{D-25}$$

The above set of conditions is equivalently expressed by the following complex-valued vector matrix equation:

$$\underline{\bar{f}}\,\underline{\bar{\gamma}} = \underline{u}, \tag{D-26}$$

with $\bar{f}_{N-(i-1)-(j-1)}$ representing the ij^{th} element of the $(2N + 1) \times (2N + 1)$ matrix $\underline{\bar{f}}$ and with $\bar{\gamma}_{-N+(i-1)}$ representing the i^{th} element of the $(2N + 1) \times 1$ column vector $\underline{\bar{\gamma}}$. The vector $\underline{u}$ is a $(2N + 1) \times 1$ column vector with all zero elements, except for its $N + 1$ component, which is 1. The solution of equation (D-26) gives

$$\underline{\bar{\gamma}}^o = \underline{\bar{f}}^{-1}\underline{u} \tag{D-27}$$

or, equivalently,

$$\left.\begin{aligned} \underline{\gamma}_R^o &= (\underline{I} + \underline{f}_R^{-1}\underline{f}_I\underline{f}_R^{-1}\underline{f}_I)^{-1}\underline{f}_R^{-1}\underline{u} \\ \text{and} \\ \underline{\gamma}_I^o &= -\underline{f}_R^{-1}\underline{f}_I\underline{\gamma}_R^o \end{aligned}\right\} \text{(D-27a)}$$

where $\underline{\gamma}_R^o$ and $\underline{\gamma}_I^o$ denote the real and imaginary components of $\underline{\bar{\gamma}}^o$, respectively, and $\underline{f}_R$ and $\underline{f}_I$ represent the real and imaginary parts of $\underline{\bar{f}}$, respectively.

Next, we consider a control law that can adaptively and recursively find an unbiased estimate of $\underline{\bar{\gamma}}^o$. We let

$$\underline{\bar{\gamma}}_{k+1} = \underline{\bar{\gamma}}_k + \mu\bar{E}_n^*\underline{\bar{I}}_n, \tag{D-28}$$

where μ is a constant controlling the algorithm step size,

$$\bar{E}_n \equiv \bar{I}_n - \underline{X}_n^T \underline{\bar{Y}}_k \tag{D-29}$$

denotes the error at the filter output corresponding to the n^{th} receiver sampling instant and

$$\underline{\bar{I}}_n \equiv \begin{bmatrix} \bar{I}_{n-N} \\ \bar{I}_{n-N+1} \\ \vdots \\ \bar{I}_n \\ \bar{I}_{n+1} \\ \vdots \\ \bar{I}_{n+N} \end{bmatrix}. \tag{D-30}$$

Substituting equation (D-29) into equation (D-28) gives

$$\begin{aligned} \underline{\bar{Y}}_{k+1} &= \underline{\bar{Y}}_k + \mu(\bar{I}_n^* - \underline{X}_n^{T*} \underline{\bar{Y}}_k^*)\underline{\bar{I}}_n \\ &= \underline{\bar{Y}}_k + \mu \bar{I}_n^* \underline{\bar{I}}_n - \underline{\bar{I}}_n \underline{X}_n^{T*} \underline{\bar{Y}}_k^*. \end{aligned} \tag{D-31}$$

Taking the statistical expectation of the above yields

$$\begin{aligned} E[\underline{\bar{Y}}_{k+1}] &= E[\underline{\bar{Y}}_k] + \mu E[\bar{I}_n^* \underline{\bar{I}}_n] - \mu E[\underline{\bar{I}}_n \underline{X}_n^{T*} \underline{\bar{Y}}_k^*] \\ &= E[\underline{\bar{Y}}_k] + \mu \sigma_I^2 \underline{u} - \mu E[\underline{\bar{I}}_n \underline{X}_n^{T*}] E[\underline{\bar{Y}}_k^*], \end{aligned} \tag{D-32}$$

where $\sigma_v^2 \equiv E[|\bar{I}_n|^2]$, $E[\bar{I}_n^* \bar{I}_k] = 0$ for $\forall k \neq n$, and $\underline{\bar{Y}}_k^*$ and $\underline{\bar{I}}_n \underline{X}_n^{T*}$ are assumed uncorrelated (an assumption easily justified in practice). The ij^{th} component of the matrix $E[\underline{\bar{I}}_n \underline{X}_n^{T*}]$ can readily be shown to be $\sigma_I^2 \bar{f}_{N-(i-1)-(j-1)}^*$ and, thus, equation (D-32) may be rewritten as

$$E[\bar{Y}_{k+1}] = E[\bar{Y}_k] + \mu\sigma_I^2 \underline{u} - \mu\sigma_I^2 \bar{\underline{f}}^* E[\bar{Y}_k^*]. \tag{D-32a}$$

Letting

$$\bar{\Psi}_k \equiv E[\bar{Y}_{k+1}] \equiv \Psi_R^k + j\Psi_I^k \text{ and } \bar{\underline{f}} \equiv \underline{f}_R + j\underline{f}_I, \tag{D-33}$$

the complex-valued equation (D-32a) may be represented equivalently in terms of the following two real-valued equations:

$$\Psi_R^{k+1} = (\underline{I} - \mu\sigma_I^2 \underline{f}_R)\Psi_R^k + \mu\sigma_I^2 \underline{f}_I \Psi_I^k + \mu\sigma_I^2 \underline{u} \tag{D-34a}$$

and

$$\Psi_I^{k+1} = (\underline{I} + \mu\sigma_I^2 \underline{f}_R)\Psi_I^k + \mu\sigma_I^2 \underline{f}_I \Psi_R^k, \tag{D-34b}$$

or, more compactly, in terms of the following (augmented) vector matrix equation:

$$\left[\begin{array}{c} \Psi_R^{k+1} \\ \hline \Psi_I^{k+1} \end{array}\right] = \left[\begin{array}{c|c} \underline{I} - \mu\sigma_I^2 \underline{f}_R & \mu\sigma_I^2 \underline{f}_I \\ \hline \mu\sigma_I^2 \underline{f}_I & \underline{I} + \mu\sigma_I^2 \underline{f}_R \end{array}\right] \left[\begin{array}{c} \Psi_R^k \\ \hline \Psi_I^k \end{array}\right] + \mu\sigma_I^2 \left[\begin{array}{c} \underline{u} \\ \hline \underline{o} \end{array}\right], \tag{D-35}$$

Rewriting the above as

$$\left[\begin{array}{c} \Psi_R^{k+1} \\ \hline \Psi_I^{k+1} \end{array}\right] = \left[\left[\begin{array}{c|c} \underline{I} & \underline{0} \\ \hline \underline{0} & \underline{I} \end{array}\right] - \mu\sigma_I^2 \left[\begin{array}{c|c} \underline{f}_R & -\underline{f}_I \\ \hline -\underline{f}_I & -\underline{f}_R \end{array}\right]\right] \left[\begin{array}{c} \Psi_R^{k+1} \\ \hline \Psi_I^{k+1} \end{array}\right] + \mu\sigma_I^2 \left[\begin{array}{c} \underline{u} \\ \hline \underline{o} \end{array}\right], \tag{D-36}$$

the following solution is readily arrived at (following the analysis of Appendix C, equations (C-81) through (C-92)):

$$\lim_{k\to\infty}\begin{bmatrix} \underline{\psi}_R^{k+1} \\ \hline \underline{\psi}_I^{k+1} \end{bmatrix} = \left[\begin{array}{c|c} \underline{f}_R & -\underline{f}_I \\ \hline -\underline{f}_I & -\underline{f}_R \end{array}\right]^{-1}\begin{bmatrix} \underline{u} \\ \hline \underline{o} \end{bmatrix}. \tag{D-37}$$

Equation (D-37) is equivalent to the statement

$$\lim_{k\to\infty} E[\underline{\bar{\gamma}}_{k+1}] = \underline{\bar{\gamma}}^o = \underline{\bar{f}}^{-1}\underline{u}, \tag{D-38}$$

thus concluding the argument that the control law of equation (D-28) finds, in the mean, the optimal coefficient vector resulting in an overall Nyquist system (or, equivalently, control law (D-28) finds an unbiased estimate of $\underline{\bar{\gamma}}^o$). The coefficient vector found by control law (D-28), however, although optimal in the Nyquist sense (in terms of forcing ISI to zero), is suboptimal from a residual noise MSE standpoint. The optimal Nyquist solution presented in the first section of this appendix is revisited next, since this solution does force the noise MSE to a minimum while simultaneously maintaining zero ISI. As will be seen, however, the adaptive formation of this (more optimum) solution is substantially more complex and, hence, typically not sought in practice.

D.3 ADAPTIVE FORMATION OF THE OPTIMAL NYQUIST SOLUTION

Figure D-4 illustrates a receiver architecture that can be used to adaptively form the optimum Nyquist characteristic of equation (D-14). As shown in the figure, an overall receiver configuration is postulated comprising a fractionally spaced transversal filter whose coefficients are controlled by the Least Mean-Squared (LMS)

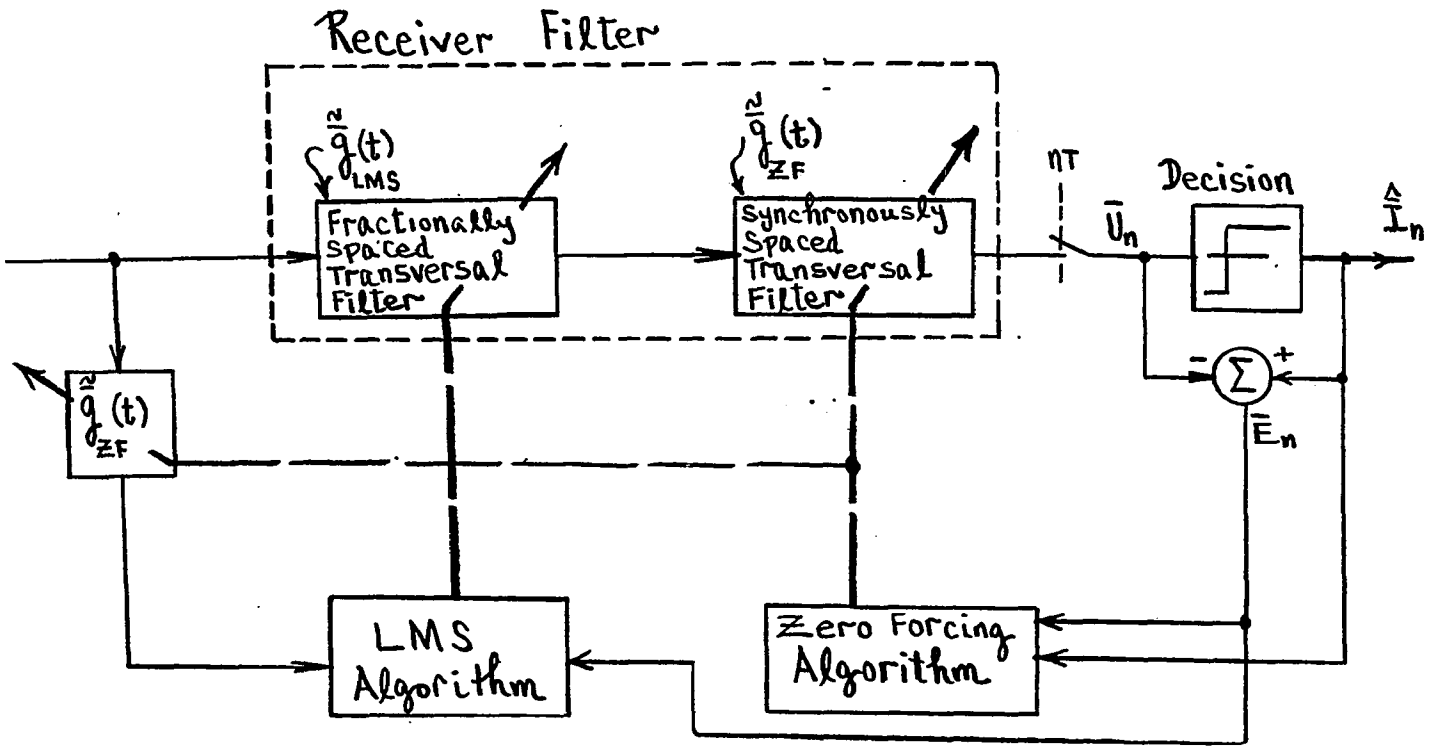

Figure D-4. Optimum Adaptive Receiver Configuration in the Nyquist Sense

error algorithm (as described in Appendix C) followed by a synchronously spaced transversal filter controlled by the Zero-Forcing (ZF) algorithm (as described in the previous section of this appendix). The LMS controlled fractionally spaced filter minimizes the residual noise MSE, while the ZF algorithm controlling the synchronously spaced filter guarantees ISI-free performance. As can readily be seen from equation (D-1) and/or equation (D-17), the optimum synchronously spaced transversal filter transfer function, $\tilde{\tilde{G}}^{o}_{ZF}(j\omega)$, will converge to

$$\tilde{\tilde{G}}^{o}_{ZF}(j\omega) = \frac{T}{\sum_{k}\tilde{\tilde{G}}_{LMS}(j\omega+j\frac{2\pi k}{T})\bar{F}(j\omega+j\frac{2\pi k}{T})}, \quad |\omega| \leq \frac{\pi}{T}, \tag{D-39}$$

while the optimum fractionally spaced filter characteristic, $\tilde{\tilde{G}}^{o}_{LMS}(j\omega)$, will be governed by a coefficient vector, $\underline{\bar{G}}_{LMS}$, defined by

$$\underline{\bar{G}}_{LMS} = (\underline{\bar{R}}^{-1}_{LMS}\underline{\bar{P}}_{LMS})^{*}, \tag{D-40}$$

where

$$\left.\begin{aligned} \underline{\bar{R}}_{LMS} &\equiv E[\bar{Y}_n\bar{Y}_n^{*T}], \\ \underline{\bar{P}}_{LMS} &\equiv E[\bar{I}_n^{*}\bar{Y}_n] \end{aligned}\right\} \tag{D-41}$$

and

$$\underline{\bar{Y}}_n \equiv \begin{bmatrix} \bar{Y}(nT+NT') \\ \bar{Y}(nT+NT'-T') \\ \vdots \\ \bar{Y}(nT) \\ \bar{Y}(nT-T') \\ \vdots \\ \bar{Y}(nT-NT') \end{bmatrix}; \; T' = \frac{T}{2}, \tag{D-42}$$

such that

$$\bar{Y}(t) \equiv \bar{X}(t) * \tilde{\bar{g}}_{ZF}(t). \tag{D-43}$$

The statement made by equation (D-40) can be verified using the techniques of Appendix C. Furthermore, to adaptively converge to the optimum solution of equation (D-40), the following control law must be used to update the fractionally spaced filter coefficient vector:

$$\underline{\bar{G}}_{LMS}^{k+1} = \underline{\bar{G}}_{LMS}^{k} + \mu \bar{E}_n \underline{\bar{Y}}_n^*, \tag{D-44}$$

where

$$\bar{E}_n \equiv \bar{I}_n - \bar{U}_n. \tag{D-45}$$

Using the control law of equation (D-44), it can readily be shown that

$$\lim_{k \to \infty} E[\underline{\bar{G}}_{LMS}^{k+1}] = (\underline{\bar{R}}_{LMS}^{-1} \underline{\bar{P}}_{LMS})^*. \tag{D-46}$$

REFERENCES

[1] R. W. Lucky, J. Salz, and E. J. Weldon, Jr., "Principles of Data Communication", McGraw-Hill, 1968, Chapter 4

[2] J. Fenderson, S. R. Shepard, and M. A. Skinner, "Adaptive Transversal Equalizer for 90-Mb/s 16-QAM System in the Presence of Multipath Propagation", Paper C8.7, ICC'83, June 19 to 22, 1983, Boston, MA

BIBLIOGRAPHY

1. Y. Bar-Ness, J. W. Carlin and M. L. Steinberger, "Bootstrapping Adaptive Cross-Pol Cancelers for Satellite Communications", ICC 1982, pages 4F.5.1 to 4F.5.5

2. A. Benveniste and M. Goursat, "Blind Equalizers", IEEE Transactions on Communications, August 1984, Volume COM-32, No. 8

3. E. Biglieri, A. Gersho, R. D. Gitlin and T. L. Lim, "Adaptive Cancellation of Nonlinear Intersymbol Interference for Voiceband Data Transmission", IEEE Journal on Selected Areas in Communications, September 1984, Volume SAC-2, No. 5

4. M. Emshwiller, "Characterization of the Performance of PSK Digital Radio Transmission in the Presence of Multipath Fading", International Conference on Communications (ICC), 1978

5. D. D. Falconer, "Adaptive Equalization of Channel Nonlinearities in QAM Data Transmission Systems", Bell System Technical Journal, September 1978, Volume 57, No. 7

6. J. Fenderson, S. R. Shepard and M. A. Skinner, "Adaptive Transversal Equalizer for 90-MB/s 16-QAM System in the Presence of Multipath Propagation", International Conference on Communications (ICC), June 19 to 22, 1983, Boston, MA, Paper C8.7

7. A. Gersho and T. L. Lim, "Adaptive Cancellation of Intersymbol Interference for Data Transmission", Bell System Technical Journal, November 1981, Volume 60, No. 9

8. R. D. Gitlin and S. B. Weinstein, "Fractionally Spaced Equalization: An Improved Digital Transversal Equalizer", Bell System Technical Journal, February 1981, Volume 60, No. 2

9. D. N. Goddard, "Self-Recovering Equalization and Carrier Tracking in Two-Dimensional Data Communication Systems", IEEE Transactions on Communications, November 1980, Volume COM-28, No. 11

10. L. J. Greenstein and B. A. Czekaj, "A Polynomial Model for Multipath Fading Channel Responses", Bell System Technical Journal, September 1980, Volume 59, No. 7

11. G. L. Heiter, "Characterization of Nonlinearities in Microwave Devices and Systems", IEEE Transactions on Microwave Theory and Techniques, December 1973, Volume MTT-21, No. 12

12. P. D. Karabinis and F. E. Thau, "An Adaptive Algorithm for Linear/Nonlinear Distortion Cancellation in Digital Communications Systems", ICC, 1990, Volume 4, Paper 337.5

13. P. D. Karabinis, "Asynchronous and Non-Data Decision Directed Equalizer Adjustment", U.S. Patent No. 4,635,276, January 6, 1987

14. P. D. Karabinis, "Suppressed Double-Sideband Communication System", U.S. Patent No. 4,780,884, October 25, 1988

15. S. Komaki, Y. Okamoto and K. Jajima, "Performance of 16-QAM Digital Radio System Using New Space Diversity", ICC, June 8 to 12, 1980, Seattle, WA, Paper 52.2

16. R. W. Lucky, J. Salz and E. J. Weldon, Jr., "Principles of Data Communication", McGraw-Hill, 1968, Chapter 4

17. P. Monsen, "Theoretical and Measured Performance of a DFE Modem on a Fading Multipath Channel", IEEE Transactions on Communications, October 1977, Volume COM-25, No. 10

18. T. Murase, K. Morita and S. Komaki, "200 Mb/s 16-QAM Digital Radio System with New Countermeasure Techniques for Multipath Fading", ICC, 1981, Denver, CO, Paper 46.1

19. J. J. O'Reilly and A. M. de Oliveira Duarte, "Error Propagation in Decision Feedback Receivers", IEE Proceedings, December 1985, Volume 132, Part F, No. 7

20. L. W. Pickering and J. K. DeRosa, "Refractive Multipath Model for Line-of-Sight Microwave Relay Links", IEEE Transactions on Communications, August 1979, Volume COM-27, No. 8, pages 1174 to 1182

21. S. U. H. Qureshi and G. D. Forney, Jr., "Performance and Properties of a T/2 Equalizer", NTC'77

22. S. U. H. Qureshi, "Adaptive Equalization", Proceedings of the IEEE, September 1985, Volume 73, No. 9

23. W. D. Rummler, "A New Selective Fading Model: Application to Propagation Data", Bell System Technical Journal, May to June 1979, Volume 58, No. 5, pages 1037 to 1071

24. A. A. M. Saleh and J. Salz, "Adaptive Linearization of Power Ampifiers in Digital Radio Systems", Bell System Technical Journal, April 1983, Volume 62, No. 4

25. Y. Sato, "A Method of Self-Recovering Equalization for Multilevel Amplitude Modulation Systems", IEEE Transactions on Communications, June 1975, Volume COM-23, pages 679 to 682

26. G. Ungerboeck, "Fractional Tap-Spacing Equalizer and Consequences for Clock Recovery in Data Modems", IEEE Transactions on Communications, August 1976, Volume COM-24, No. 8

27. B. Widrow, J. M. McCool, M. G. Larimore and C. R. Johnson, Jr., "Stationary and Nonstationary Learning Characteristics of the LMS Adaptive Filter", Proc. IEEE, August 1976, Volume 64, No. 8, pages 1151 to 1162